Applied String Theory, Hot and Cold:

A Holographic View on

Quark–Gluon Plasma and Superfluids

Andreas Wilhelm Samberg

Heidelberg, October 2015

Dissertation

submitted to the

Combined Faculties of the Natural Sciences and Mathematics
of the Ruperto-Carola-University of Heidelberg, Germany

for the degree of

Doctor of Natural Sciences

Put forward by

Dipl.-Phys. Andreas Wilhelm Samberg
born in Gronau (Westfalen)

Oral examination: December 21, 2015

Applied String Theory, Hot and Cold:

A Holographic View on

Quark–Gluon Plasma and Superfluids

Angewandte String-Theorie, heiß und kalt: Eine holographische Sicht auf das Quark-Gluon-Plasma und Supraflüssigkeiten

Diese Arbeit befasst sich mit Anwendungen der Eichtheorie-/Gravitations-Dualität auf stark gekoppelte Phänomene im Quark-Gluon-Plasma und in Supraflüssigkeiten fernab des Gleichgewichts. Im ersten Teil suchen wir modellunabhängiges (universelles) Verhalten in verschiedenen nicht-Abelschen Eichtheorie-Plasmen mit chemischem Potential. Dazu betrachten wir stark gekoppelte $\mathcal{N} = 4$ supersymmetrische Yang-Mills-Theorie und drei Klassen von nicht-konformen Deformationen dieser Theorie. Wir untersuchen die freie Energie und zugehörige thermodynamische Größen schwerer Quarks und im Falle von Quark-Antiquark-Paaren zusätzlich die Bindungsenergie. Außerdem untersuchen wir die laufende Kopplung. Wir finden qualitative Übereinstimmung mit Gitter-QCD-Daten. Zusätzlich beobachten wir universelles Verhalten mehrerer Observablen für alle Werte des chemischen Potentials. Im zweiten Teil untersuchen wir die Dynamik einer bosonischen Supraflüssigkeit in zwei Raumdimensionen nach anfänglichen „Quenches", die das System in einen Zustand fernab des Gleichgewichts versetzen, der viele Vortexdefekte und Quantenturbulenz aufweist. Dabei lösen wir die vollen Bewegungsgleichungen des holographisch dualen Abelschen Higgs-Modells im vierdimensionalen Anti-de-Sitter-Raum numerisch. Wir beobachten einen universellen Langzeitverlauf, der durch Potenzgesetz-Verhalten einer Zweipunkts-Korrelationsfunktion und charakteristischer Längenskalen ausgezeichnet ist und den wir als nichtthermischen Fixpunkt interpretieren.

Applied String Theory, Hot and Cold: A Holographic View on Quark–Gluon Plasma and Superfluids

This thesis deals with applications of gauge/gravity duality to strong-coupling phenomena in the quark–gluon plasma and far-from-equilibrium superfluids. In a first part we search for model-independent (universal) behavior in various non-Abelian gauge-theory plasmas at finite temperature and chemical potential. We employ the holographic duals of strongly coupled $\mathcal{N} = 4$ supersymmetric Yang–Mills theory and three one-parameter families of non-conformal deformations thereof, two of which solve the equations of motion of a five-dimensional Einstein–Maxwell–scalar action. We study the free energy and associated thermodynamic quantities of heavy quarks and bound quark–anti-quark ($Q\bar{Q}$) pairs as well as the $Q\bar{Q}$ binding energy and the running coupling. We find qualitative agreement with available lattice QCD data. Moreover, we show that several observables exhibit universal behavior for all values of the chemical potential. In a second part we investigate the real-time dynamics of a bosonic superfluid in two spatial dimensions after initial quenches that take the system to far-from-equilibrium states characterized by many topological vortex defects in association with quantum turbulence. To this end we numerically solve the full equations of motion of the holographically dual Abelian Higgs model on four-dimensional anti-de Sitter space. We observe a universal non-equilibrium late-time regime characterized by power-law behavior in a two-point correlation function and in characteristic length scales, which we interpret as a non-thermal fixed point.

Publications

This thesis contains the results and discussion from the following publication,

- C. Ewerz, T. Gasenzer, M. Karl, and A. Samberg, "Non-Thermal Fixed Point in a Holographic Superfluid," JHEP **1505** (2015) 070.

That publication is the result of collaborative work. To clearly distinguish my work from that of others I declare that I have done the analytical work, and performed all numerical simulations as well as the analysis. I have developed the numerical code jointly with Markus Karl.

Four further publications of the findings discussed in this thesis are planned, based on the results of Chap. 5 (renormalization in the holographic computation of the heavy quark–anti-quark free energy and binding energy and implications thereof, including entropy and internal energy; with C. Ewerz and O. Kaczmarek), the results of Chap. 6 (Taylor expansion coefficients of the heavy quark–anti-quark free energy for small chemical potential; with C. Ewerz), the results of Chap. 7 (running coupling in the plane of chemical potential and temperature; with C. Ewerz), and the results of Chap. 12 (temperature dependence of the non-equilibrium dynamics of the holographic superfluid; with C. Ewerz, T. Gasenzer, and M. Karl).

During my PhD studies, I published the following further article which deals with related topics but whose content is not subject of this thesis,

- N. Callebaut, S. S. Gubser, A. Samberg, and C. Toldo, "Segmented Strings in AdS_3," (submitted to JHEP), arXiv:1508.07311 [hep-th].

Contents

Contents

1 Introduction

One of the main themes in high-energy physics is the quest for unification. The Standard Model of particle physics unifies three – the electromagnetic, weak, and strong – of the four fundamental interactions in Nature into a single theory in the framework of quantum field theory. The fourth – gravity – so far resists unification with the other three fundamental interactions. Rather, it is currently understood in terms of a classical field theory, Einstein's General Relativity. A theory that promises to provide a framework in which a unification of all fundamental interactions becomes possible is string theory. However, while a series of groundbreaking insights into string theory have been obtained in the last three decades, its status as a fundamental theory of nature is debated, and its uniquely 'stringy' predictions elude experimental verification as they are expected to become manifest only at energies many orders of magnitude above the energies attainable in colliders. Nevertheless, research in string theory is a very active field, not least because of the major breakthrough sparked by the work of Maldacena [1] and others [2, 3] in 1997/98, namely the concept of Anti-de Sitter/Conformal Field Theory duality, or *AdS/CFT duality*.

This idea, nowadays understood in broader terms as *gauge/gravity duality*, has opened up new and unexpected relations between non-gravitational quantum field theories, in particular gauge theories, on the one hand, and gravity on the other hand. An exceptional feature of gauge/gravity duality is that it posits an exact equivalence between physical theories defined in spacetimes of different dimensionalities, which is expressed by the alternative name of *holographic duality*, or simply holography. In general, a specific instance of gauge/gravity duality provides a mapping of the complete dynamics of some quantum field theory in a non-dynamical spacetime to the complete dynamics of a gravitational quantum theory in a higher-dimensional spacetime. Practically, the difference in dimensions is often one, and the higher-dimensional spacetime is an (asymptotically) AdS spacetime which has a negative cosmological constant and is called the 'bulk'. The dual quantum field theory 'lives' on the conformal boundary of the bulk spacetime and is hence called the 'boundary theory'. In a particular limit the bulk theory essentially becomes a *classical* gravity theory, while the boundary theory becomes *strongly coupled*. This makes holographic duality a powerful tool for studying physics of systems described by strongly coupled quantum field theory. This will be the way we view and use holographic duality in this thesis. By now, holographic methods are applied to a broad range of physical systems, including heavy-ion collisions (see *e. g.* [4] for a review) and ultracold quantum gases (see *e. g.* [5] for a review), as well as various condensed-matter systems such as high-T_c superconductors or strange metals (see *e. g.* [6, 7] for reviews). Due to being formulated in terms of unusual degrees of free-

dom in unconventional spacetimes, holographic methods can provide new insight into and complementary intuition for the physical systems that they are applied to. In this work, we will apply holographic methods in order to investigate aspects of the physics of strongly correlated quantum fluids.

Such systems have been observed at vastly different temperatures, ranging from the very cold to the very hot. Examples include ultracold Bose [8–10] and Fermi [11–15] quantum gases in the nanokelvins range, superfluid helium-3 [16, 17] below $2.5\,\mathrm{mK}$ and superfluid helium-4 [18, 19] below $2.17\,\mathrm{K}$, as well as various semiconductor-based exciton–polariton condensates (see *e. g.* [20] for a recent review) in the few-kelvin range. On the other end of temperature extremes is the strongly coupled quark–gluon plasma (QGP) that is produced and studied in heavy-ion collision experiments ([21–27]; see *e. g.* [28, 29] for recent reviews), with temperatures exceeding $1.75 \times 10^{12}\,\mathrm{K}$. It is believed that some microseconds after the Big Bang the universe was filled with a QGP.

In this thesis, which comprises two main parts, we deal with both stationary (probes in an equilibrated system) and time-dependent (non-equilibrium dynamics) phenomena in strongly correlated quantum fluids using a holographic approach. There are different possible strategies in the application of holography. We apply a 'bottom-up' approach where one does not start from string theory, as in the derivation of the original AdS/CFT duality, but rather uses general lessons learned from exact gauge/gravity dualities to construct phenomenological models for the physics of interest. The bottom-up approach is motivated by the search for universal features shared by many strongly coupled theories. A famous example is the so-called KSS bound by Kovtun *et al.* [30] on the ratio of the shear viscosity and entropy density of a strongly coupled plasma that has applications to the physics of the QGP, as we will discuss. In a similar spirit, in the first part of this thesis, we will study heavy quarks in a large class of holographic models for the quark–gluon plasma. As another interesting aspect, holographic models are used for exploratory studies of physics at strong coupling. In this vein, in the second part of this work, we apply holographic duality to the non-equilibrium dynamics of a cold strongly coupled bosonic superfluid in two spatial dimensions. We will discuss further details of the physical systems of interest and the motivation for our work at the beginning of each part.

In the following, we give a brief overview of the structure of this thesis. To lay the ground, we will review some background material and the original AdS/CFT duality in Chap. 2, where we will then further discuss the more general holographic dictionary that we use in our investigations.

Hot: Heavy Quarks in Strongly Coupled Plasmas

In the first main part, we study the physics of heavy quarks in strongly coupled plasmas described by holography. In particular, we will focus on heavy quark–antiquark bound states, *i. e.*, quarkonia, and single heavy quarks. These are important probes of the quark–gluon plasma.

We will start in Chap. 3 with a discussion of heavy-ion collisions and the quark–gluon plasma as the motivation for our work. Next, in Chap. 4 we will introduce our various holographic models for the hot strongly coupled plasma. This large class of models includes conformal $\mathcal{N} = 4$ supersymmetric Yang–Mills (SYM) theory and non-conformal deformations of that theory. In particular, all models include a chemical potential that enables us to study finite-density effects. We will further discuss the holographic setup for the description of heavy quarks. Our investigation of a heavy quark–anti-quark pair ($Q\bar{Q}$) is based on the computation of distance-dependent energies, some of which can be interpreted as model potentials. This is the topic of Chap. 5. We thoroughly review the holographic procedure used to compute the free energy of a heavy quark–anti-quark pair in the strongly coupled plasma. We will point out an essential constraint on the necessary renormalization of the free energy and advocate a generally applicable holographic scheme that makes sure that constraint is satisfied. This renormalization scheme differs from the one commonly used in the literature. We will show that the latter scheme does not give rise to the free energy but rather a binding energy. We will then explore the implications of these general arguments which to the best of our knowledge have not been fully discussed in the literature so far. We will find qualitative agreement between the free energy and related thermodynamic quantities computed in our holographic models and in lattice QCD. We will further perform a similar analysis for single heavy quarks in the medium. In lattice QCD, Taylor coefficients of an expansion of the $Q\bar{Q}$ free energy for small chemical potential can be computed, though the so-called sign problem generally impedes access to regimes of non-zero chemical potential. A detailed comparison of the leading non-trivial coefficient in lattice QCD and our holographic models in Chap. 6 will show that our holographic bottom-up chemical potential indeed captures essential aspects of the baryon chemical potential in QCD. Equipped with this result, in Chap. 7 we will study, in the whole plane of chemical potential and temperature, the running coupling $\alpha_{Q\bar{Q}}$ derived from the $Q\bar{Q}$ free energy. $\alpha_{Q\bar{Q}}$ clearly exhibits the effects of the non-conformal deformation and medium-induced screening on the $Q\bar{Q}$ interaction, and allows to study the interplay of these effects. Our holographic models contain a parameter λ related to the coupling strength in the boundary theory. Throughout Part I we will constrain the range of values of λ by comparison of various observables to lattice QCD. We will generally find large values for λ, consistent with general expectations. We summarize our findings regarding heavy quarks in strongly coupled plasmas with non-zero chemical potential in Chap. 8.

Cold: Non-Equilibrium Dynamics in a Holographic Superfluid

In the second part of this thesis, we make use of holographic duality to investigate the non-equilibrium real-time dynamics of a strongly coupled bosonic superfluid in two spatial dimensions. We will study the relaxation of the system from quench-like far-from-equilibrium initial states that contain a large number of quantum vortices which are topological collective excitations of a superfluid and are related to the

phenomenon of superfluid turbulence. In the introductory chapter 9 we discuss the physical motivation for our investigation. In Chap. 10 we introduce the holographic model for the superfluid and discuss its equilibrium properties and the phase transition to the superfluid state. We derive the full equations of motion of the system which are coupled non-linear partial differential equations, and we discuss how they are solved numerically. Results of our numerical simulations of non-equilibrium dynamics are discussed starting in Chap. 11. In particular, we first focus on statistical properties of the vortex distribution in the superfluid, and then on aspects of quantum turbulence visible in the momentum-space occupation number spectrum of microscopic excitations. We conclude that in the late-time stage of the evolution (a notion which we quantify) the system enters a universal non-equilibrium regime irrespective of the details of the initial conditions. We study this universal regime in detail in terms of scaling exponents of observables with respect to momenta and time and interpret it as a so-called non-thermal fixed point in Sec. 11.5. There we also give the first discussion of this general concept from the holographic perspective. While qualitative features of the non-equilibrium dynamics and the characteristics of the universal regime are expected to be independent of the choice of the temperature used in the simulations, in Chap. 12 we assess the robustness of our conclusions by investigating the system at further temperatures within the superfluid phase. Moreover, we estimate the temperature dependence of certain non-universal quantities characterizing the evolution of the vortex distribution. We summarize our findings regarding the non-equilibrium dynamics of a holographic superfluid in Chap. 13.

Finally, Chap. 14 contains a discussion of our main results and an outlook. Various technical details are discussed in four appendices. Appendix A contains our conventions and some identities used in gravity computations. Details concerning the holographic models employed in the investigations in the first part of this thesis and for the computation of an observable studied in that part are given in Appendices B and C, respectively. In Appendix D we give further details regarding our numerical methods for the computation of equilibrium properties and for the simulation of the non-equilibrium dynamics of the holographic superfluid in the second part of this thesis.

2 Holographic Duality

In this chapter, we review the basic features of gauge/gravity or holographic duality that we will need in this thesis.

In the first section 2.1, we introduce basic notions from string theory (Sec. 2.1.1), and motivate (Sec. 2.1.2) the original AdS/CFT correspondence that essentially relates four-dimensional $\mathcal{N} = 4$ supersymmetric $SU(N_c)$ Yang–Mills (SYM) theory, which is a conformal field theory (CFT), to type IIB string theory in five-dimensional anti-de Sitter (AdS) spacetime. We give some details concerning the $\mathcal{N} = 4$ SYM theory and AdS spacetime in Sec. 2.1.3. In this work, however, we will use a generalized notion of gauge/gravity duality as we study deformed holographic models for the physics of four-dimensional strongly coupled plasmas (Part I) and the so-called 'holographic superfluid' model for superfluids in two spatial dimensions (Part II). Therefore, in the second section 2.2 of this chapter we review central concepts of the 'holographic dictionary' that are believed to hold under more general circumstances than those of the prototypical $\mathcal{N} = 4$ SYM/AdS_5 case reviewed in the first section. Let us note here that, despite a large body of evidence for its correctness has been accumulated (see for instance [31] and references therein), the AdS/CFT duality still remains a conjecture, *i.e.*, it is not rigorously proven.

The AdS/CFT duality[a] is a concrete realization of the ideas formulated in the *holographic principle*. This principle has been put forward by 't Hooft [32] and Susskind [33] and holds that it should be possible to describe a theory of quantum gravity in $D+1$ spacetime dimensions (the so-called *bulk*) by a quantum field theory in a related D-dimensional spacetime (generally called the *boundary*), which acts as a 'screen' onto which the bulk dynamics is projected. In general, the degrees of freedom in the higher- and lower-dimensional theories will be different, but the two theories are physically equivalent.

Within gravity, early hints towards holography appeared in the context of a semiclassical treatment of black hole physics. Bekenstein [34] and Hawking [35] discovered that a black hole is a thermodynamic object. In particular, an entropy can be assigned to it [34] which is given by

$$S = \frac{A}{4G_N},\qquad(2.1)$$

where A is the area of the black-hole horizon and G_N is the Newton constant. A very remarkable feature of this equation is that the entropy scales with the area of

---

[a]An alternative name is AdS/CFT correspondence or Maldacena conjecture. More generally, one speaks of gauge/gravity duality, also called gauge/string duality or, encompassing all of the previous cases, holography.

the black hole instead of its volume. This hints at a description of the physics of the black hole in terms of degrees of freedom 'living' on its horizon which has one dimension less than the inside of the black hole.

On the field-theory side, an early indication towards gauge/string duality was found by 't Hooft [36]. He realized that the diagrams of non-Abelian gauge theory with N_c colors organize themselves according to their topology in the limit $N_c \to \infty$ and observed that this bears a close resemblance to the perturbative expansion in a quantized theory of closed strings.

In fact, it was within string theory that the AdS/CFT duality, as the first example of a gauge/string or gauge/gravity duality, has been derived by Maldacena [1]. We will review the essential ideas of this derivation in the following section.

Throughout this thesis we will set the constants $c = \hbar = k_B = 1$, and work in the units thus specified. Occasionally, we will in addition set the so-called AdS radius to unity, $L_{AdS} = 1$. We work with metric signature $(- + \cdots +)$, and use the sign conventions for gravity of Misner, Thorne, and Wheeler [37]. The explicit expressions that we use for the Christoffel symbols and various tensors of general relativity are given in Appendix A.

2.1 AdS/CFT Duality

While we will be using a generalized notion of gauge/gravity duality for our applications in this thesis, the 'cleanest' case is the original AdS/CFT duality conjectured in 1997 by Maldacena [1]. Thus, in this section we focus on that example of a holographic duality.

2.1.1 String Theory

The AdS/CFT duality has been derived in the framework of supersymmetric string (superstring) theory that is formulated in ten-dimensional spacetime (for an introduction, see for instance the textbooks [38–40]). Therefore, to start with, in this section we briefly review those features of string theory that are important for the derivation of the AdS/CFT duality and for our further purposes in this thesis.

Strings come in two topologies, they are either open or closed. There are five different consistent superstring theories that are related to each other through a web of dualities. While string theory has been formulated originally as a theory of quantized one-dimensional strings, it was realized starting from the seminal paper by Polchinski [41] that it also contains higher-dimensional non-perturbative objects called Dirichlet branes (D-branes). These are higher-dimensional 'membranes' in spacetime on which open strings can end, and are dynamical objects themselves. A D-brane with p spatial dimensions is called a Dp-brane for short.

As strings propagate through D-dimensional spacetime[b], they trace out a two-

---

[b]For superstring theory, $D = 10$. We use general D here since we will eventually use the Nambu–Goto action (2.2) for strings in $(D = 5)$-dimensional spacetime.

dimensional *worldsheet* that can be described by an embedding function $X^M(\sigma^a)$ with $M = 0, 1, \ldots, D - 1$ and $a = 0, 1$. In a direct generalization of the physics of a point particle with a one-dimensional worldline, the classical physics of the string follows from demanding that the area of the worldsheet be extremal on the classical trajectory. This gives rise to the *Nambu–Goto action*

$$S_{\mathrm{NG}} = -\frac{1}{2\pi\alpha'} \int \mathrm{d}^2\sigma \sqrt{-\det g_{ab}}\,, \tag{2.2}$$

where $1/(2\pi\alpha')$ is the string tension and g_{ab} is the induced metric on the worldsheet,

$$g_{ab} = g_{MN} \frac{\partial X^M}{\partial \sigma^a} \frac{\partial X^N}{\partial \sigma^b}\,, \tag{2.3}$$

with g_{MN} the metric of the D-dimensional ambient spacetime. Upon quantization[c], the string gives rise to 'towers' of excitations with masses $m^2 \propto 1/\alpha'$, *i. e.*, the parameter α' sets the fundamental energy scale $1/\sqrt{\alpha'}$ (or fundamental length scale l_{s}, writing $\alpha' = l_{\mathrm{s}}^2$) associated with the string. In particular, the excitation towers include massless excitations. String interactions are described by the breaking and merging of string worldsheets, and are controlled by the string coupling g_{s}. In the low-energy or 'decoupling' limit $\alpha' \to 0$ the massive string excitations decouple from the theory as their mass exceeds any finite energy scale. The remaining massless excitations give rise to fields in spacetime and their dynamics can be described by a low-energy effective action. For type IIB string theory which is the basis of the AdS/CFT duality the low-energy effective theory is type IIB supergravity.

In contrast to α', the string coupling g_{s} is not an input parameter but is determined dynamically by the *dilaton ϕ_D* which is one of the massless modes of closed strings (see *e. g.* [39]; a nice discussion is also given in the lecture notes [42]). In particular, a factor involving the dilaton enters the metric that is 'seen' by strings, *i. e.*, the metric in the Nambu–Goto action. In other words, the way we have written the Nambu–Goto action in Eq. (2.2) assumes that the spacetime metric g_{MN} be given in the so-called *string frame*. An alternative frame is the so-called *Einstein frame*. The two frames are related by a dilaton-dependent rescaling of the spacetime metric (see *e. g.* [43]),

$$g_{MN}^{(\mathrm{s})} = \mathrm{e}^{\frac{4}{D-2}\,\phi_D} g_{MN}^{(\mathrm{E})}\,, \tag{2.4}$$

where the superscripts 's' and 'E' indicate the string and Einstein frame, respectively. Now, if we work in Einstein frame, using the Einstein-frame spacetime metric to compute the induced metric on the string worldsheet according to Eq. (2.3), the string dynamics is not governed by the action (2.2), but instead by

$$-\frac{1}{2\pi\alpha'} \int \mathrm{d}^2\sigma\, \mathrm{e}^{\frac{4}{D-2}\,\phi_D} \sqrt{-\det g_{ab}^{(\mathrm{E})}}\,. \tag{2.5}$$

---

[c]We note that for the quantization of the string the Polyakov action is suited better than the Nambu–Goto action (see *e. g.* [39]). It gets rid of the square root in the Nambu–Goto action at the expense of introducing an auxiliary field. At the classical level, the two actions are equivalent. For the computations in this thesis, we will be interested in classical strings, so we can use either action. We will always work with the Nambu–Goto action which is simpler for our purposes.
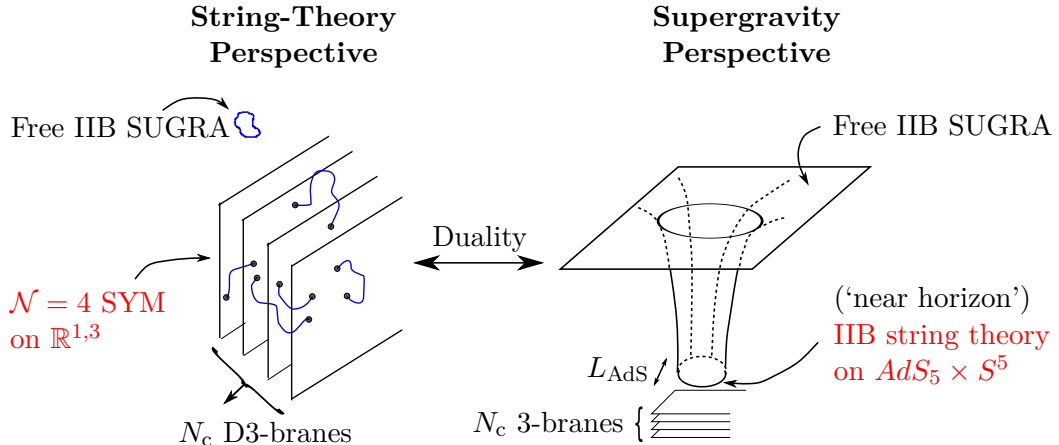
Figure 2.1: Sketch of the derivation of the AdS/CFT duality. There are two per-
spectives on the same physical setup. In the low-energy ('decoupling')
limit that is sketched, from either point of view there are two decoupled
theories, and free type IIB supergravity (SUGRA) is one of these in both
perspectives. The remaining theories on both sides (red) are identified
which yields the AdS/CFT duality. Figure adapted from [45].

Despite more complicated equations of motion due to the dilaton contribution, this
leads to the same string dynamics – the two frames are equivalent, but computations
may be simpler in one or the other. Whereas string dynamics is more naturally
studied in string frame, low-energy effective actions turn out to have a simpler form
in Einstein frame. We will further discuss this in the context of the construction of
our models in Sec. 4.1.

2.1.2 Motivation of the AdS/CFT Duality

Let us now review the basic idea of the derivation of the AdS/CFT duality. Good
reviews of the AdS/CFT duality, or gauge/gravity duality more generally, include
[4, 31, 44].

The AdS/CFT duality arises from taking the low-energy limit in two different
descriptions of D-branes and conjecturing that these are equivalent [1]. We consider
a stack of N_c coincident D3-branes in 10-dimensional Minkowski spacetime. We
have written the subscript 'c' in anticipation of the fact that N_c will turn out to be
the number of colors on the gauge-theory side of the duality. The physical setup is
sketched in Fig. 2.1. The presentation in the figure already assumes the low-energy
limit.

The first perspective is the string-theory perspective. It involves both open and
closed strings. Open strings have to end on the D3-branes, but the two ends of
an open string need not end on the same brane. Rather, for an open string there
are N_c^2 possible combinations for the two ends to connect to D3-branes which is
indicative of the N_c^2 'gluons' of $U(N_c)$. The open strings describe the fluctuations

of the D-branes. There is a finite number of massless modes in the open-string spectrum. Among these, in particular, are non-Abelian gauge fields, *i. e.*, gluons. It turns out [46] that the low-energy effective action of the open strings is the action of $\mathcal{N} = 4$ supersymmetric $U(N_c)$ Yang–Mills theory on the worldvolume of the D3-branes which is $\mathbb{R}^{1,3}$. The group $U(N_c)$ can be written as $U(N_c) = SU(N_c) \times U(1)$, and one can argue that the $U(1)$, which corresponds to the center-of-mass motion of the D3-branes [47], effectively decouples from the dynamics (see for instance [44]). Therefore, in the following we will always consider $\mathcal{N} = 4$ supersymmetric Yang–Mills theory with gauge group $SU(N_c)$. This theory is controlled by the coupling constant g_{YM} which is determined in terms of the string coupling by $g_{\mathrm{YM}}^2 = 4\pi g_s$. The $\mathcal{N} = 4$ supersymmetry gives rise to a global $SU(4)$ so-called R-symmetry. We will say more about this theory below in section 2.1.3. On the other hand, the massless modes of the closed-string spectrum in this description give rise, in the low-energy limit, to type IIB supergravity. Interactions in this low-energy effective action are controlled by the ten-dimensional Newton constant $G_{\mathrm{N}}^{(10)}$ which is given by the string parameters α' and g_s (see *e. g.* [4]),

$$G_{\mathrm{N}}^{(10)} = 8\pi^6 g_s^2 \alpha'^4 \,. \tag{2.6}$$

We see that $G_{\mathrm{N}}^{(10)}$ vanishes in the low-energy limit, so that the supergravity theory becomes free. (Recall that on the string-theory side this limit can be seen as $\alpha' \to 0$.) The Newton constant also controls the interactions between the open- and the closed-string sectors. Consequently, in the low-energy limit the two sectors decouple. To summarize, in the string-theory perspective, after taking the low-energy limit we are left with two decoupled theories (see the left-hand side of Fig. 2.1): (i) $\mathcal{N} = 4$ SYM on the $(3 + 1)$-dimensional worldvolume of the branes, and (ii) free type IIB supergravity in the 'bulk' surrounding the branes.

The other perspective on the same physical setup is the (type IIB) supergravity perspective. Strings will later re-appear in this perspective. First, let us concentrate on the spacetime geometry. The D3-branes are massive objects that distort spacetime. In the supergravity language, the 'D' is usually left out, one speaks of p-branes. The ten-dimensional metric sourced by N_c 3-branes is found [48] to be given by

$$\mathrm{d}s^2 = \frac{1}{\sqrt{H(r)}} \left(-\mathrm{d}t^2 + \mathrm{d}\boldsymbol{x}^2 \right) + \sqrt{H(r)} \left(r^2 + r^2 \,\mathrm{d}\Omega_5^2 \right) , \tag{2.7}$$

$$H(r) = 1 + \frac{L_{\mathrm{AdS}}^4}{r^4} \,, \tag{2.8}$$

where $(t, \boldsymbol{x}) = (t, x^1, x^2, x^3)$ are the coordinates on the worldvolume of the branes, r is the distance to the branes in the six-dimensional transverse space ($r^2 = y_1^2 + \cdots + y_6^2$ with the transverse coordinates y_i), and $\mathrm{d}\Omega_5$ is the solid angle on the five-dimensional sphere S^5. The characteristic length scale L_{AdS} is determined by the string parameters inherited by the supergravity via

$$L_{\mathrm{AdS}}^4 = 4\pi g_s N_c \alpha'^2 \,. \tag{2.9}$$

For $r \gg L_{\text{AdS}}$, *i.e.* far away from the branes, we have $H(r) \approx 1$ and the metric (2.7) reduces to the ten-dimensional Minkowski metric. On the other hand, in the so-called 'near-horizon' region for $r \ll L_{\text{AdS}}$, *i.e.* close to the branes, we have $H(r) \approx L_{\text{AdS}}^4/r^4$, and the metric (2.7) becomes

$$\mathrm{d}s^2 = \left[\frac{r^2}{L_{\text{AdS}}^2} \left(-\mathrm{d}t^2 + \mathrm{d}\boldsymbol{x}^2 \right) + \frac{L_{\text{AdS}}^2}{r^2} \, \mathrm{d}r^2 \right] + L_{\text{AdS}}^2 \, \mathrm{d}\Omega_5^2 = \mathrm{d}s_{AdS_5}^2 + \mathrm{d}s_{S^5}^2 \, . \quad (2.10)$$

In other words, the metric factorizes into the metric of five-dimensional anti-de Sitter spacetime AdS_5 and that of the five-dimensional sphere S^5. Both parts have the same 'radius' L_{AdS}. This geometry is sketched in the right-hand side of Fig. 2.1. While asymptotically flat, the spacetime develops a 'throat' along the radial coordinate r that measures the distance from the branes. Excitations with some fixed energy appear more and more red-shifted from the point of view of an observer in the asymptotically flat region the deeper they are in the throat. Thus, in the low-energy limit, there are two kinds of excitations that survive. On the one hand, there are the supergravity modes in the asymptotically flat region. Their description reduces to free type IIB supergravity. On the other hand, for r approaching zero, *i.e.*, 'zooming into' the near-horizon region, we can have excitations of arbitrary proper energy. These excitations are those of type IIB string theory, the theory that encompasses type IIB supergravity as its low-energy approximation. In the low-energy limit, these two systems decouple from each other [49, 50]. To summarize, in the supergravity perspective, after taking the low-energy limit we are left with two decoupled theories (see the right-hand side of Fig. 2.1): (i) type IIB string theory in the near-horizon region of the 3-branes whose geometry is $AdS_5 \times S^5$, and (ii) free type IIB supergravity in the asymptotically flat region far away from the branes.

If we compare the outcome of taking the low-energy limit in these two perspectives on the stack of D3-branes, we see that from either point of view there are two decoupled theories. One of them is, in each case, free type IIB supergravity. Assuming that the two descriptions of the D3-branes are equivalent, Maldacena conjectured [1] that the remaining theories on both sides are dual, that is equivalent, to each other. Schematically,

$$\mathcal{N} = 4 \, SU(N_\text{c}) \text{ SYM in } \mathbb{R}^{1,3} \longleftrightarrow \text{type IIB string theory in } AdS_5 \times S^5 \, . \quad (2.11)$$

This is the *AdS/CFT duality* conjecture. Let us mention already here that in a certain limit the right-hand side of the above duality will essentially reduce to classical gravity on the AdS_5 part of the full ten-dimensional geometry.

As we will see in the next section below, $\mathbb{R}^{1,3}$ is the boundary of the bulk spacetime AdS_5. Accordingly, $\mathcal{N} = 4$ SYM is called the 'boundary theory' whereas the theory in the bulk is called the 'bulk theory'.

2.1.3 AdS Spacetime and $\mathcal{N} = 4$ Supersymmetric Yang–Mills Theory

Now that we have motivated the AdS/CFT duality, let us have a closer look at each of the two sides of the duality. In this section, we mainly follow [4].

Let us first discuss AdS spacetime. For future reference – anticipating that we will work in AdS_4 in Part II – we consider D-dimensional AdS spacetime. We also introduce the notation $d \equiv D-1$ which is the dimensionality of the boundary theory. For concreteness and the connection to $\mathcal{N} = 4$ SYM, however, for now just think of $D = 5$ and $d = 4$. Let us consider the D-dimensional Einstein–Hilbert action with a cosmological constant,

$$S = \frac{1}{16\pi G_{\mathrm{N}}^{(D)}} \int \mathrm{d}^D x \, \sqrt{-g} \, (\mathcal{R} - 2\Lambda) \,, \tag{2.12}$$

where $G_{\mathrm{N}}^{(D)}$ is the D-dimensional Newton constant, g is the determinant of the metric g_{MN} and $\mathcal{R}$ is the associated Ricci scalar. (See Appendix A for our gravity and index conventions.) The cosmological constant is negative,

$$\Lambda = -\frac{(D-1)(D-2)}{2L_{\mathrm{AdS}}^2} \,. \tag{2.13}$$

This, in particular, yields $\Lambda = -6/L_{\mathrm{AdS}}^2$ for $D = 5$ (AdS_5) and $\Lambda = -3/L_{\mathrm{AdS}}^2$ for $D = 4$ (AdS_4). The equations of motion associated with the action (2.12) are the D-dimensional vacuum Einstein equations with a cosmological constant,

$$\mathcal{R}_{MN} - \frac{1}{2}\mathcal{R} \, g_{MN} + \Lambda \, g_{MN} = 0 \,, \tag{2.14}$$

where $\mathcal{R}_{MN}$ is the Ricci tensor. AdS_D spacetime is their maximally symmetric solution with the metric

$$\mathrm{d}s^2 = \frac{L_{\mathrm{AdS}}^2}{z^2} \left(-\eta_{\mu\nu} \, \mathrm{d}x^\mu \, \mathrm{d}x^\nu + \mathrm{d}z^2 \right) \,, \tag{2.15}$$

where $\eta_{\mu\nu}$ is the d-dimensional Minkowski metric, and $x^\mu = (t, \boldsymbol{x}) = (t, x^1, \ldots, x^{d-1})$. The holographic coordinate z is the 'inverse' of the coordinate r that we used in the AdS_5 metric in Eq. (2.10),

$$z = \frac{L_{\mathrm{AdS}}^2}{r} \,. \tag{2.16}$$

In the further course of this thesis, we will only use the coordinate z. It varies between 0 and infinity. The coordinates employed in Eq. (2.15) are called Poincaré coordinates. The conformal boundary[d] of this spacetime is at $z = 0$ and the metric induced on it is, up to a Weyl rescaling, the standard Minkowski metric which is identified with the metric of the boundary theory.

Note that the metric (2.15) is invariant under the scale transformation

$$(t, \boldsymbol{x}) \to C(t, \boldsymbol{x}) \,, \quad z \to Cz \,, \tag{2.17}$$

---

[d]A mathematical definition of the conformal boundary is somewhat subtle and these details will not be important for us. A definition and further information can for instance be found in [51].

for any constant $C > 0$. This is reflected in scale invariance of the dual theory (think $\mathcal{N} = 4$ SYM). In fact, as is nicely discussed in [4], assuming the existence of a D-dimensional gravity dual of a d-dimensional quantum field theory invariant under Poincaré transformations and the first part of the scale transformation (2.17), the form of the metric (2.15) can already be inferred.

Let us now turn to the other side of the duality (2.11), namely four-dimensional $\mathcal{N} = 4$ maximally supersymmetric $SU(N_c)$ Yang–Mills (SYM) theory. Let us briefly review its essential features, after which we will turn to the relation of its parameters to those of the bulk theory. $\mathcal{N} = 4$ SYM is a non-Abelian gauge theory that has four Weyl spinors and six real scalar fields in addition to the gauge field. All fields transform in the adjoint representation of the gauge group $SU(N_c)$. The theory is conformal, *i. e.*, its β-function vanishes identically and the coupling does not run. The conformal group in four dimensions is $SO(4, 2)$, and this is also the isometry group of AdS_5. Moreover, the $\mathcal{N} = 4$ supersymmetry gives rise to an $SU(4)$ R-symmetry group, and $SO(6) \simeq SU(4)$ is the isometry group of the five-sphere S^5. Under the AdS/CFT duality, these isometries are identified with the symmetries of the dual field theory [1]. For a detailed discussion of $\mathcal{N} = 4$ SYM see for instance the review [31]. We will discuss the question in which sense and to what degree $\mathcal{N} = 4$ SYM can be thought of as a model for QCD in Sec. 4.1.1. It is natural to think of the field theory to 'live' on the boundary of the AdS spacetime which is why it is often called boundary theory.

There are two parameters in $\mathcal{N} = 4$ SYM, the Yang–Mills coupling g_{YM} and the number of colors N_c, but the theory is usually discussed in terms of N_c and the 't Hooft coupling $\lambda \equiv g_{\text{YM}}^2 N_c$. The latter controls the perturbative expansion of the Yang–Mills theory [36]. The boundary-theory parameters can be expressed in terms of bulk parameters (see *e. g.* [4]),

$$g_{\text{YM}}^2 = 4\pi \, g_s \,, \tag{2.18}$$

$$\sqrt{\lambda} = \frac{L_{\text{AdS}}^2}{\alpha'} \,. \tag{2.19}$$

We recall that g_s is the string coupling and α' yields the string tension $1/(2\pi\alpha')$. The first of these relations arises in reducing the open-string spectrum on the D3-branes to its low-energy effective description, see the discussion before Eq. (2.6). The second relation follows from using the first relation and Eq. (2.9).

The strong form of the AdS/CFT duality holds that the duality (2.11) is valid for all values of the parameters λ and N_c (for this statement and discussions of the weaker forms reviewed next see for instance [44]). A somewhat weaker form is that it only holds in the limit $N_c \to \infty$. This is, in fact, a requirement for the supergravity description used in the previous Sec. 2.1.2 to hold. A way to see that is by noting from Eqs. (2.6) and (2.9) that the dimensionless coupling parameter $G_N^{(10)}/L_{\text{AdS}}^8 = \pi^4/(2N_c^2)$. Viewed this way, taking the limit $G_N^{(10)} \to 0$ in which the two theories in the supergravity description decouple entails the limit $N_c \to \infty$. An even weaker form assumes that, besides $N_c \to \infty$, also λ is taken to be large. This is the form that we will use.

As we see from the relation (2.19), $\lambda = L_{\text{AdS}}^4/\alpha'^2 = L_{\text{AdS}}^4/l_{\text{s}}^4$, so this parameter measures the curvature scale of the AdS spacetime in units of the string length scale. If the limit $N_{\text{c}} \to \infty$ is taken and λ is tuned to large values $\lambda \gg 1$, the strings in the dual string theory behave classically and all their massive excitations decouple. We are left with a weakly coupled classical theory of gravity coupled to various matter fields (see for instance [4]). On the other side of the duality, for large λ, the gauge theory is *strongly coupled*, so perturbation theory breaks down. We conclude that the AdS/CFT duality is a *strong/weak* duality. This is what makes it such a powerful tool for applications. For many purposes, the field dynamics in the internal manifold S^5 can be ignored (see for instance [4]). This reduces the duality (2.11) to the duality of large-N_{c}, strongly coupled $\mathcal{N} = 4$ SYM with a gravity theory in AdS_5, and makes manifest its status as a realization of the holographic principle discussed above.

2.2 Elements of the Holographic Dictionary

In the previous section, we have reviewed the basic ideas leading to the AdS/CFT duality as conjectured by Maldacena [1]. Further fundamental properties of the duality were found in [2, 3]. Since those early works, a number of further holographic dualities have been found, see for instance [52–54] and the (early) review [44].

In this thesis, we will work with a generalized notion of gauge/gravity duality. In essence, we will take the generic elements of the AdS/CFT duality, and use them to construct phenomenological models for the physical systems of interest. There is a huge literature on 'bottom-up' holography that is done in this spirit, and this will be discussed further in the context of our applications in the parts I and II. As the crucial feature of the AdS/CFT duality, throughout this thesis we shall always assume that the field theories of interest are strongly coupled and can be described by a dual classical theory of gravity, generally including additional matter fields, in an asymptotically AdS spacetime of one higher dimension.

Let us, then, collect in this section further elements of the 'holographic dictionary' that can be gathered from the prototype AdS/CFT duality discussed in Sec. 2.1, and that we will apply in more general contexts in our work.

UV/IR relation. The first general concept we discuss is the UV/IR relation [1, 55, 56]. Roughly speaking, it holds that the holographic coordinate z in the AdS metric (2.15) can be interpreted as being dual to an energy scale in the boundary theory. UV (IR) physics in the boundary theory is mapped to processes in the bulk at small (large) values of z. Explicitly, physics at a characteristic energy scale E in the boundary theory should be dominated by bulk physics at a characteristic 'depth'

$$z \sim \frac{1}{E} \tag{2.20}$$

in the bulk. We will several times draw on this idea for the interpretation of our results.

Field–operator correspondence. Another important concept is the field–operator correspondence [2, 3, 57]. A field in the bulk is associated with an operator in the boundary theory. In particular, a bulk scalar Φ is dual to a scalar operator $\mathcal{O}$ in the boundary theory, and a bulk vector A_M is dual to a vector operator j^μ. Importantly, if j^μ is the conserved current associated to some global symmetry in the boundary theory, the bulk vector A_M will be a gauge field. Let us in the following illustrate the field–operator correspondence at the example of a scalar field. The mass m_Φ of the bulk scalar field encodes the scaling dimension of the dual operator [2, 3]. For a scalar field/operator, the scaling dimension Δ is generally[e] the larger root of

$$m_\Phi^2 L_{\mathrm{AdS}}^2 = \Delta(\Delta - d)\,, \tag{2.21}$$

where d is the dimension of the boundary theory.

For example, we might introduce a massive dynamical scalar in the bulk action (2.12). Solving the associated coupled Einstein and Klein–Gordon equations we can construct a gravity dual for $\mathcal{N} = 4$ SYM deformed by the operator dual to the bulk scalar (see for instance [44]). If the scaling dimension of the operator is $\Delta < d$, the scalar will approach zero as $z \to 0$ and we will obtain a metric that approaches the AdS metric as $z \to 0$, but deviates from it deeper in the bulk. (We will construct explicit examples in Part I.) We call such a spacetime *asymptotically AdS*. According to the UV/IR relation discussed above, this signifies that in the UV the boundary theory reduces to the undeformed conformal theory but deviates from it for smaller energy scales. In this sense, the gauge/gravity duality can be interpreted as a "geometrization of the renormalization group flow" [4].

An operator with $\Delta < d$ is called a relevant operator since, as we have discussed, it induces a deformation that becomes important in the IR. For further discussion of deformations in the context of gauge/gravity duality see for instance [44]. The condition $\Delta < d$ translates via Eq. (2.21) to $m_\Phi^2 < 0$ for the bulk scalar field. We note that the mass-squared of a scalar field in AdS can be negative without rendering the spacetime unstable, as long as it satisfies the so-called Breitenlohner–Freedman bound [58–60],

$$m_\Phi^2 \geq -\frac{d^2}{4}\,. \tag{2.22}$$

Sources and expectation values. Generally, the value of a bulk field at the boundary $z = 0$ determines (up to a rescaling by z) the value of the source conjugate to the dual operator. Computing the 'response' of an operator in the boundary theory to a given source then translates in the bulk to a boundary-value problem for the equation of motion of the associated bulk field. In general, these equations are partial differential equations, and they are of second order in the holographic coordinate z. We will encounter both these features explicitly in our study of non-equilibrium

---

[e]Under certain conditions [57], one may also choose what is called the 'alternative quantization', and associate to the bulk scalar an operator with scaling dimension equal to the smaller root of Eq. (2.21). In this thesis, however, we will stick with the standard choice.

dynamics in Part II. Besides the boundary condition at $z = 0$ one typically imposes the second boundary condition at the black-hole horizon, to be discussed below. The response of the boundary-theory operator, *i.e.* its one-point quantum expectation value in the presence of the source can now be extracted from the near-boundary behavior of the dual field [61, 62]. The general procedure to derive these relations and higher-order correlators is called holographic renormalization (for a review see [63]), but we will not need these details here.

As an example, let us again consider a bulk scalar field, say Φ. The source η conjugate to the dual operator is determined by the value of the scalar at the $z = 0$ boundary via (see for instance [4]),

$$\eta(x^\mu) = \lim_{z \to 0} z^{\Delta - d} \Phi(x^\mu, z) \,, \tag{2.23}$$

where x^μ are the coordinates of the boundary theory and Δ is determined from Eq. (2.21) as discussed above. Eq. (2.23) projects out of the series expansion of Φ around $z = 0$ the coefficient of the leading-order term (see for instance [4]). The expression for the expectation value involves the coefficient of the next-order subleading term. However, it depends on further details of the bulk action, so we cannot make a general statement here. We will discuss and use an explicit example in Part II, where we study the holographic superfluid defined by the action (10.1).

Non-zero temperature and chemical potential. For the applications of holographic duality that we have in mind, we are not actually interested in the vacuum of the boundary theory. Rather, we want to study physics at non-zero temperature and chemical potential.

The bulk theory can be prepared at non-zero temperature by putting a black hole (often actually a black brane) inside the bulk. The Hawking temperature [35] associated with the black hole is identified with the temperature of the boundary theory [64]. A heuristic explanation for this procedure is that the black hole emits Hawking radiation and thus heats up the boundary where the field theory 'lives'. The Hawking temperature of a black hole can be computed from the formula

$$T = \frac{\kappa}{2\pi} \,, \tag{2.24}$$

where κ is the surface gravity [35]. Alternatively, it can be computed by demanding regularity of the analytic continuation of the metric into the Euclidean-time domain (see for instance [4]). We will make this more concrete in the context of our models for strongly coupled plasmas in Sec. 4.1, where we will explicitly construct (asymptotic) AdS spacetimes with black holes.

A chemical potential, on the other hand, can also be introduced in a straightforward way (see *e.g.* [4]), applying the field–operator correspondence as well as the general relation of boundary values of bulk fields and boundary-theory sources discussed above. We consider a $U(1)$ global symmetry in the boundary theory and want to turn on a chemical potential μ which is a source for the associated charge

density. From what we discussed above, the conserved boundary-theory vector current j^μ corresponding to that symmetry is dual to a $U(1)$ gauge field A_M in the bulk. Thus, to implement a chemical potential in the boundary theory, one adds such a gauge field to the bulk action. Then, the value of the A_0 component (the 'electrostatic' potential) of the bulk gauge field at the $z = 0$ boundary yields the source for the charge density j^0, explicitly

$$\lim_{z\to 0} A_0(z) = \mu\,. \tag{2.25}$$

This should be thought of as a boundary condition to be imposed on the bulk gauge field. Depending on the normalization of the gauge field in the bulk action, a factor L_{AdS} might appear on the right-hand side of Eq. (2.25). Since we will not consider spatially varying chemical potentials, we have suppressed the dependence on the boundary-theory coordinates x^μ. The boundary condition (2.25) generally leads to a non-zero electric flux in the bulk so that there have to be charged sources somewhere in the bulk. In this thesis, we will encounter both charged black holes (Part I) and charged bulk condensates (Part II) as sources for the gauge field.

We now have all necessary ingredients to start applying the gauge/gravity duality to the study of strongly coupled systems. In the following part I we will study holographic models of strongly coupled plasmas to learn about heavy quarks and quarkonia in the quark–gluon plasma, while in Part II we study non-equilibrium dynamics in a holographic superfluid in $2 + 1$ dimensions.

Part I

Hot: Heavy Quarks
in Strongly Coupled Plasmas

3 Introduction and Overview

We now start with our investigation of the physics of strongly coupled systems described by holography. In this part, we focus on strongly coupled plasmas, and in particular study heavy quarks in these media. Our central theme will be the search for universal behavior. We start with a discussion of heavy-ion collisions and the quark–gluon plasma which are the motivation for our work.

3.1 Motivation

When normal matter is heated up to temperatures in excess of about 150 MeV (*i. e.*, above 1.75×10^{12} K, which is five orders of magnitude hotter than the core of the sun) a new state of matter is formed. At lower temperatures, the fundamental degrees of freedom of quantum chromodynamics (QCD), quarks and gluons which carry a charge called 'color', are not observed as single particles but are rather *confined* into color-neutral bound states called hadrons. However, at a temperature around 150–180 MeV a rapid crossover into a new deconfined phase takes place, as is theoretically indicated by studies (*e. g.* [65, 66]) in lattice QCD, a numerical approach to evaluating the partition function of QCD ([67]; see, for instance, [68] for a general introduction and [69, 70] for reviews of finite-temperature lattice QCD). The name 'quark–gluon plasma' associated with this high-temperature phase was introduced by Shuryak [71].

The quark–gluon plasma is experimentally studied by means of ultrarelativistic heavy-ion collisions. Such experiments are currently being undertaken at the Relativistic Heavy Ion Collider (RHIC) in Brookhaven, NY, USA, and at the Large Hadron Collider (LHC) of the European Organization for Nuclear Research CERN in Geneva, Switzerland. While at RHIC gold ions (as well as other ion species) are collided at nucleon–nucleon center-of-mass energies $\sqrt{s_{\mathrm{NN}}}$ around 200 GeV, the LHC has worked with lead ions at much higher energies of $\sqrt{s_{\mathrm{NN}}} = 2.76$ TeV and will soon operate with lead ions at roughly twice that energy.

A heavy-ion collision is sketched in Fig. 3.1. The two colliding heavy nuclei overlap in an almond-shaped region whose size and aspect ratio depend on the impact parameter, the distance between the ions' centers. A lot of energy is deposited inside the overlap region, where a hot and dense medium is produced. It appears that the medium quickly thermalizes at least locally and reaches temperatures of several hundreds MeV, far above the deconfinement crossover temperature. As the medium rapidly expands outwards it cools and undergoes a complicated evolution; eventually, inelastic collisions cease (chemical freezeout). The system hadronizes, and in the detectors surrounding the collision point, many thousands of particles
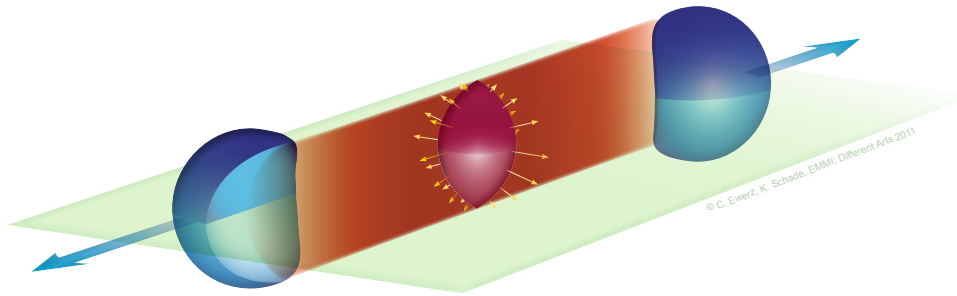
Figure 3.1: Sketch of a heavy-ion collision (figure by C. Ewerz, K. Schade, and Different Arts, 2011). The quark–gluon plasma is produced in the overlapping region of the nuclei, and rapidly expands after the collision, as indicated by the small arrows.

are detected in a single collision for small impact parameters [72]. It is nowadays generally accepted that the heavy-ion collision experiments at RHIC and LHC have in fact succeeded at producing the QGP, and there are indications that, before those experiments, the Super Proton Synchrotron (SPS) at CERN produced the QGP in the 1990's [73–75].

Beyond the thermodynamic regime of the QGP that has been investigated so far by RHIC and LHC, namely very high temperatures but small net baryon density, future lower-energy facilities like for instance the Facility for Antiproton and Ion Research (FAIR) in Darmstadt, Germany, will investigate QCD matter in new regimes, where a significant non-vanishing baryon (or quark) chemical potential can be expected. Moreover, non-zero chemical potential is even currently being explored already in the RHIC beam-energy-scan program at low energies $\sqrt{s_{\mathrm{NN}}} = \mathcal{O}(10\,\mathrm{GeV})$ (see *e. g.* [76]). This is part of an ongoing effort to explore the phase structure of QCD at non-zero baryon chemical potential. A qualitative sketch showing some general expectations regarding the QCD phase diagram is shown in Fig. 3.2. The figure gives a rough idea of the regimes to be explored in future FAIR experiments and also of the regimes explored with high-energy collisions at RHIC and LHC. An important question for those experiments concerns the existence and properties of the critical endpoint, at which the crossover transition from hadronic matter to the QGP is expected to sharpen into a true phase transition.

Huge progress in the experimental study of the properties of the QGP in heavy-ion collisions has been made over the last decade. It was found both at RHIC [21–24] and later at higher energies at the LHC [25, 77–82] that the QGP is *strongly coupled* (also see *e. g.* [83, 84] for discussions from a theoretical perspective; [28, 29] for recent reviews of RHIC and/or LHC results; and [85] for an up-to-date overview of the field of nucleus–nucleus collisions at large). This conclusion rests upon many
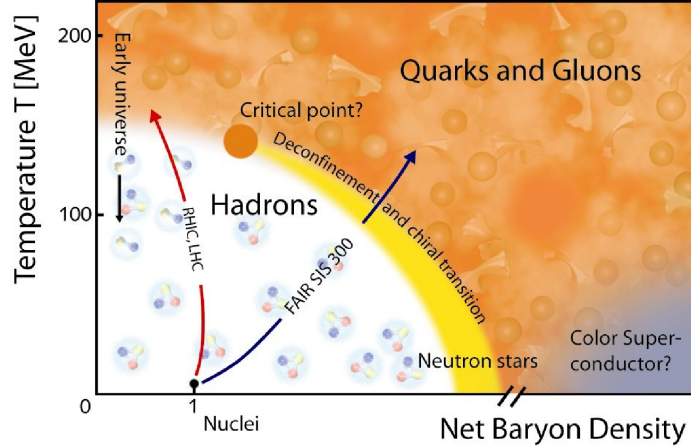
Figure 3.2: Sketch of the phase diagram of QCD (figure by GSI, Darmstadt). The net baryon density is directly related to the baryon chemical potential.

experimental observations and a close interplay with theoretical modeling. Let us just mention two key observations.

Firstly, the bulk evolution of the medium can be modeled by hydrodynamics (see *e. g.* [86] for a recent review) using a very small ratio of the shear viscosity η to entropy density s. This indicates that the medium behaves like a liquid rather than a gas. In fact, the small observed value of η/s hints at an extremely small mean free path of the constituents of the medium (see *e. g.* [87]) which implies that they are strongly interacting, and even calls into doubt a description of the medium based on the concept of quasi-particles. The hydrodynamic behavior manifests itself in collective anisotropic flow [25, 27, 77, 78]. This means that the medium is very efficient at transforming an initial spatial anisotropy, clearly present in collisions with non-zero impact parameter as illustrated in Fig. 3.1 (almond-shaped overlap), into an anisotropy in momentum space which is measured in terms of the Fourier coefficients of the azimuthal distribution of the particle yield.

Secondly, the yield of heavy quarkonia (such as J/ψ or Υ) is strongly suppressed relative to proton–proton collisions [88–91]. The original idea is that the interaction between the valence quarks in the quarkonium is screened by the medium [92] which leads to 'melting' at high temperatures. However, in the study of the physics of actual heavy-ion collisions many complications arise beyond this simple picture (see *e. g.* [93, 94]). There are many open questions regarding the physics of quarkonia and the QGP. In this thesis, as one important aspect, we will investigate the interaction of a heavy quark–anti-quark pair immersed in a strongly coupled plasma. In general, we will also include a non-zero chemical potential in our investigations.

The fact that the quark–gluon plasma that is produced and studied in heavy-ion-collision experiments is strongly coupled makes a theoretical description quite demanding, as many conventional methods rely on a perturbative expansion in terms

of the coupling constant as a small parameter. Holography is ideally suited to deal with strong-coupling physics. There are various further theoretical methods besides holography to deal with strongly coupled physics relevant for the QGP. These include lattice QCD, mentioned above, which relies on a discretization of spacetime and extensive numerical simulations, and functional quantum-field-theory methods like the functional renormalization group ([95], for reviews see *e. g.* [96–98]) or Dyson–Schwinger equations ([99, 100], for reviews see *e. g.* [101, 102]). Functional methods have, for instance, recently been applied for a computation of η/s in finite-temperature Yang–Mills theory [103].

Lattice techniques, while in principle allowing for an *ab initio* approach to QCD, rely on an Euclideanization of the theory and hence only give direct access to static phenomena. Furthermore, including a non-zero chemical potential in lattice studies is notoriously difficult due to the so-called 'sign problem' of the fermion determinant (see *e. g.* [104] for a review). In contrast, in holography it is straightforward to include a chemical potential, as we have reviewed in Sec. 2.2.

Heavy quarks and heavy quarkonia are important probes of the QGP, as heavy quarks are produced early on in the collision and experience the whole evolution of the medium (see *e. g.* [28] and references therein). It is therefore crucial to understand their behavior in a strongly coupled medium, and holography has been applied to many aspects related to heavy quarks. As we will review in Sec. 4.2, in holography a heavy quark in the boundary theory is dual to an open, macroscopic string in the bulk [105] with one endpoint located at the boundary. That endpoint can be pictured as the point-like quark. A bound pair made up of a heavy quark and its anti-quark, as a model for quarkonium, is represented by a string with both endpoints on the boundary. Using this holographic setup, it becomes possible to study many quantities of interest for quark–gluon plasma phenomenology. An example is the screening distance of a quark–anti-quark pair, defined as the length scale where the quark–anti-quark free energy transitions from roughly Coulombic behavior into exponentially screened behavior, to be further discussed below. The screening distance can be computed from the bulk equation of motion of the string connecting the quarks, and a lot of work has been done on this subject in the gauge/gravity literature (see *e. g.* [106–113], and [4] for a review), if mostly at vanishing chemical potential. As another example, one can study the energy loss of a single heavy quark traversing the medium at some finite velocity by studying, in the bulk, the energy flowing down the string whose endpoint on the boundary represent the quark [114, 115]. This setup gives rise to a so-called 'drag force' and has also been widely studied (see *e. g.* [109, 116–124], and [4] for a review).

In this thesis, in the spirit of the so-called universality approach, we study a large class of non-conformal models that are deformations of $\mathcal{N} = 4$ SYM. We generally include a chemical potential. We will discuss our approach and its relation to other approaches that are pursued in the gauge/gravity literature in the following section 3.2, after which we will introduce our models and the holographic description of heavy quarks in Chap. 4. For our models, we have extensively studied the behavior of the $Q\bar{Q}$ screening distance and of the heavy-quark drag force before [45]. We

have found intriguing patterns in a systematic investigation of the effect of non-conformality and chemical potential on these observables. At vanishing chemical potential, it turns out, as found by the authors of [110, 111, 113], that in a large class of non-conformal deformations of $\mathcal{N} = 4$ SYM the screening distance universally increases upon the introduction of non-conformality, such that the screening distance in $\mathcal{N} = 4$ SYM constitutes a lower bound. Now, this continues to hold at small non-zero chemical potential but there are violations of the lower bound in certain models at larger chemical potential which are, however, small [45].

While the screening distance is just a single length scale, more can be learned about the heavy quark–anti-quark interaction and how it is affected by the strongly coupled plasma by studying length-scale-dependent *heavy-quark energies*, and in this thesis we turn to these observables. This will be the topic of Chap. 5. While at zero temperature a systematic framework exists (see for instance [125] for a review) that allows to derive an effective potential to describe the interaction of quarks bound in heavy quarkonia, the situation at non-zero temperature is ambiguous, and it is not fully understood how to determine an effective potential (see *e. g.* the discussion in [4]). Here, we will take a more pragmatic approach and study different energies that can be associated with a heavy quark–anti-quark pair. These are the quark–anti-quark *free energy* and the *binding energy*, as well as the *internal energy*. We will thoroughly discuss the holographic computation of the $Q\bar{Q}$ free energy and the binding energy in Sec. 5.1. There has been, apparently, some confusion in the gauge/gravity literature with respect to the distinction of these two quantities. We will point out an essential property of the free energy and show how to make that manifest in the holographic description. In Secs. 5.2 and 5.3 we will show that the free energy computed in holography with the correct procedure discussed before qualitatively behaves like the one obtained in lattice QCD. Furthermore, we will compare the behavior of the free energy and the binding energy both in conformal and non-conformal models. Having validated the procedure for the holographic computation of the free energy, we make will use of the fact that it is a thermodynamic potential and investigate in Sec. 5.4 the associated $Q\bar{Q}$ internal energy and entropy. After that we turn to single quarks. In Sec. 5.5 we study their free energy, internal energy, and entropy in the strongly coupled plasma. That closes our basic discussion of heavy-quark energies.

The two following chapters 6 and 7 are dedicated to a more detailed study of the quark–anti-quark free energy. The $Q\bar{Q}$ free energy has been computed in lattice QCD for small values of the baryon chemical potential, where it is possible to circumvent the sign problem by a Taylor expansion whose coefficients can be evaluated at vanishing chemical potential. While in holography there is no such restriction on the value of the chemical potential, in Chap. 6 we nevertheless focus on small chemical potentials in holography, too. Comparing the holographic results to the lattice data, we will assess the important question how closely the chemical potential introduced in our holographic models can model the baryon (or quark) chemical potential in QCD that we are ultimately interested in. Such a comparison has not been done in the literature so far. Subsequently, in Chap. 7 we will

return to considering all values of the chemical potential. In that chapter we will study the distance-dependent *running coupling* derived from the $Q\bar{Q}$ free energy. This quantity elucidates the fine details of the quark–anti-quark interaction in the strongly coupled plasma. It has been studied before in $\mathcal{N} = 4$ SYM [126] and in non-conformal models at vanishing chemical potential [113], but a holographic study at non-zero chemical potential is performed here for the first time. In non-conformal models at vanishing chemical potential the running coupling was found to feature a universal maximum [113]. We will study this maximum in detail and quantitatively compare its value to lattice-QCD data at vanishing chemical potential, and then investigate the fate of the maximum at non-zero chemical potential. Finally, we will study the length scale associated with the maximum and compare it to the screening distance.

There are infinitely many possibilities how to construct holographic models that are deformations of $\mathcal{N} = 4$ SYM. Thus, in spite of our including some general features that are known to increase the similarity with QCD (discussed in Sec. 4.1), some arbitrariness in our choice of models necessarily remains. We try to compensate for that by performing a *systematic investigation* of our observables:

1. We will generally start by studying (often reviewing) the conformal case of $\mathcal{N} = 4$ SYM, and then ask:

   - What is the effect of introducing non-conformality?

   - Are there universal properties common to a large class of non-conformal models?

2. We will vary the chemical potential that is included in all our models, and ask:

   - What effect does the chemical potential have on our various observables?

In $\mathcal{N} = 4$ SYM, the 't Hooft coupling λ parametrizes the coupling strength, and it has to be large for the classical-gravity approximation in the bulk to hold, as reviewed in Sec. 2.1.3. In each of our non-conformal holographic models we have a parameter λ that is analogously defined in the bulk, but there is no rigorous interpretation of it in the respective boundary theory. In the course of our investigation, we will compare our observables to lattice data, where available, and from this estimate the value of the parameter λ. Then, comparing the estimates obtained from different observables can serve as a coarse consistency test of our approach.

In this thesis, we will focus entirely on static quarks, but the extension to moving quarks is straightforward along the lines of [106, 108]. We have previously studied in detail the dependence of the screening distance and drag force on the velocity in non-conformal models including a chemical potential [45].

We will close Part I with a summary of our findings in Chap. 8.

3.2 Philosophy

In this section, we set out our approach and compare it to other approaches that are used in studying strongly coupled plasmas via gauge/gravity duality.

We aim at describing physics in a strongly coupled, deconfined gauge theory plasma akin to QCD. The original AdS/CFT correspondence, however, relates gravity on AdS_5 to large-N_c, strongly coupled $\mathcal{N} = 4$ supersymmetric Yang–Mills (SYM) theory which is a supersymmetric and conformal gauge theory. QCD has neither of these properties. Therefore, to come closer to an effective model of QCD, we have to break both supersymmetry and conformal invariance. Supersymmetry is already broken by putting the theory at finite temperature. After introduction of a non-zero temperature T the energy–momentum tensor of $\mathcal{N} = 4$ SYM remains traceless. In this sense, we still call the theory conformal, despite the presence of the scale T. We may break conformality explicitly by introducing in the bulk description a scalar field that is dual to a relevant operator and thus deforms the IR properties of the boundary field theory, as discussed in Sec. 2.2. With this general idea in mind, there are different approaches one can pursue:

- The more rigorous one is called the *top-down approach.* In this setting, one usually starts from string theory and tries to modify the construction that led to the original AdS/CFT correspondence. For instance, one can add additional 'flavor branes' to introduce matter transforming in the fundamental representation of the gauge group in the boundary theory [127]. An advantage of this strategy is that one has relatively good control over the new physical ingredients added to the boundary theory that one eventually wants to study. A disadvantage is that calculations are usually quite complicated in such approaches. Holographic models set up in this way to capture some features of QCD at vanishing and non-zero temperature include [52–54, 128, 129] and [64, 130, 131], respectively.

- Another approach is the *bottom-up approach.* In contrast to the top-down approach, here one typically does not attempt to derive an exact duality from string theoretic arguments. Rather, one directly constructs an effective five-dimensional model such that the dual theory captures the phenomenology of interest. The arena for this are (asymptotically) AdS spacetimes as the original AdS/CFT duality is formulated in AdS_5 (more precisely, $AdS_5 \times S^5$, but the S^5 is usually not considered in bottom-up studies). While such models can be practical in terms of explicit calculations, the downside of this approach is obviously that one loses knowledge of the characteristics of the dual theory to a certain extent. Insight into some properties of the emergent 'boundary theory' has to be gained from explicit calculations in the bulk rather than being fixed *a priori* by construction.

In this thesis, we will be dealing with bottom-up models. Central to the effective five-dimensional model is its geometry, described by the spacetime metric. A simple

and straightforward way to obtain non-trivial models beyond the original AdS/CFT duality is to simply alter the metric 'by hand'. This has been done early on to build holographic models that exhibit various QCD-like phenomena, see *e. g.* [132, 133] and [116, 134–136] for studies at vanishing and non-zero temperature, respectively. Such models, however, have the shortcoming that their thermodynamics is in general not consistent, see for instance the discussion in [136]. Furthermore, in certain models of this type, when considering moving probes inconsistent string configurations can appear [124]. The reason for these issues is ultimately that the metric in these models does not solve the Einstein equations. Therefore a better if more laborious procedure is to derive the metric as a solution of the Einstein equations of a five-dimensional gravity action. In order to construct a non-trivial modification of the original correspondence, one adds additional fields to that action. The choice of additional fields is motivated by the holographic dictionary that we discussed in Sec. 2.2. Studies of this kind relevant to QGP phenomenology include [121, 122, 137–141]. In this thesis, we will consider both an *ad hoc* model where the metric is deformed by hand and various consistent models that we construct from a five-dimensional action, discussed in the next chapter.

No matter how one chooses to construct a holographic model for a non-conformal theory, constructing an exact dual to QCD, if one exists, seems out of reach at present. Therefore, for our investigation we will follow a *universality approach*. This notion is somewhat complementary to the distinction between the bottom-up and top-down approaches. We do not aim primarily at obtaining the closest approximation of QCD possible in a holographic setting, with the various mismatches this necessarily entails as of now. Rather, the idea is to study a large class of holographic models and to search for behavior qualitatively or even quantitatively similar in all of these models. Given that these models share some features with QCD, the hope is that insights obtained in this way can be applied to QCD, too. The approach relies on the observation that despite stark differences in the microscopic degrees of freedom, different strongly correlated systems can give rise to the same collective physics. In this way we argue that holographic models of strongly coupled gauge theory plasmas can yield insight into the properties of the strongly coupled QGP observed in heavy-ion collision experiments. For further discussion of the universality approach see for instance [109, 142, 143].

A famous example for strong-coupling universality, obtained via the gauge/gravity duality, is the universality of the ratio of the shear viscosity η to entropy density s. It was observed that the ratio has the value $\eta/s = 1/(4\pi)$ in quite different field theories with holographic duals [144–147]. Motivated by this and results on the corrections for η/s when relaxing the infinite-coupling limit [148], Kovtun, Son, and Starinets (KSS) conjectured [30] that for all relativistic quantum field theories at non-zero temperature and vanishing chemical potential there is a lower bound, $\eta/s \geq 1/(4\pi)$. The bound should be saturated for theories possessing gravity duals.[f]

---

[f]More precisely, it appears that $\eta/s = 1/(4\pi)$ in all theories with *Einstein* gravity duals. Smaller values have been found for Gauss–Bonnet or more general $\mathcal{R}^2$ gravity [149, 150]. However, it

This result was later extended to non-zero chemical potential [152–155].

The comparison of experimental data and hydrodynamic models of the evolution of the quark–gluon plasma (QGP) indicates that the QGP is the most perfect fluid observed in nature thus far. By now, it is possible to measure flow coefficients up to high order [77, 78]. Based on such data, hydrodynamic models taking into account event-by-event fluctuations in the initial conditions [156, 157] yield estimates around $\eta/s \sim 0.2 \approx 2.5/(4\pi)$, even smaller than the specific viscosities measured in superfluid helium or ultracold atomic gases (see for instance the review [5] and references therein). No known fluid violates the KSS bound. The low experimental value of the QGP's η/s also indicates that holographic results might even allow semi-quantitative insight into the behavior of the QGP, in particular in light of practical difficulties such as sign problems in alternative approaches to strongly coupled gauge theory dynamics.

---

has been shown that for these cases a lower bound is enforced by causality [151].

4 Holographic Models and Holographic Description of Quarks

Having laid out our general philosophy, we now proceed to introducing the bottom-up models we will be concerned with in this thesis. Then, we discuss the holographic description of heavy quarks, and in particular of bound quark–anti-quark pairs.

4.1 The Models

We will discuss our holographic models in terms of the action [158]

$$S = \frac{1}{16\pi G_{\mathrm{N}}^{(5)}} \int \mathrm{d}^5 x \, \sqrt{-g} \left(\mathcal{R} - \frac{1}{2} \partial_M \phi \, \partial^M \phi - V(\phi) - \frac{f(\phi)}{4} F_{MN} F^{MN} \right) , \quad (4.1)$$

where g is the determinant of the metric g_{MN} and $\mathcal{R}$ is the associated Ricci scalar. (See Appendix A for our gravity and index conventions.) $G_{\mathrm{N}}^{(5)}$ is the five-dimensional Newton constant. ϕ is the scalar that induces the deformation away from conformality. Its potential $V(\phi)$ contains the cosmological constant term 2Λ but remains otherwise unspecified for now. F_{MN} is the field strength tensor associated with an Abelian gauge connection A_M. The latter is present in the bulk to implement the desired $U(1)$ symmetry and the corresponding chemical potential in the boundary theory, *cf.* the holographic dictionary in Sec. 2.2. $f(\phi)$ is called the gauge kinetic function and parametrizes the coupling between the gauge field and the scalar.

The five-dimensional Newton constant $G_{\mathrm{N}}^{(5)}$ used in the action (4.1) can be obtained from the ten-dimensional Newton constant $G_{\mathrm{N}}^{(10)}$ given in Eq. (2.6) by dividing by the volume of the 5-sphere with radius L_{AdS}. We can express $G_{\mathrm{N}}^{(5)}$ in different ways in terms of bulk or boundary parameters,

$$G_{\mathrm{N}}^{(5)} = \frac{G_{\mathrm{N}}^{(10)}}{\mathrm{Vol}(S^5[L_{\mathrm{AdS}}])} = (2\pi)^3 \, g_{\mathrm{s}}^2 \, \frac{\alpha'^4}{L_{\mathrm{AdS}}^5} = \frac{\pi}{2} \, \frac{L_{\mathrm{AdS}}^3}{N_{\mathrm{c}}^2} , \quad (4.2)$$

where we have used $\mathrm{Vol}(S^5[L_{\mathrm{AdS}}]) = \pi^3 L_{\mathrm{AdS}}^5$ for the second equality and the relations (2.18) and (2.19) for the third. A caveat here is that the relations (2.18) and (2.19) between bulk and boundary parameters, as well as Eq. (2.6) for the Newton constant in terms of bulk parameters, were derived in the context of the AdS/CFT duality for $\mathcal{N} = 4$ SYM, so by using them we have to assume that they still hold in the present case. However, this is not a real issue here as the Newton constant does not affect the equations of motion of the action (4.1). In the following, $G_{\mathrm{N}}^{(5)}$ will only

appear explicitly in the expression for the entropy density in the boundary theory which will be discussed in Sec. 4.1.4 below. However, even there the exact value will not be important for us.

The equations of motion associated with the action (4.1) are a coupled system of Einstein, Maxwell, and Klein–Gordon equations,

$$\mathcal{R}_{MN} - \frac{1}{2}\mathcal{R}\, g_{MN} = T_{MN}\,, \tag{4.3}$$

$$\nabla_M f(\phi) F^{MN} = 0\,, \tag{4.4}$$

$$\nabla^M \nabla_M \phi = V'(\phi) + \frac{f'(\phi)}{4}\, F_{MN} F^{MN}\,, \tag{4.5}$$

where ∇_M denotes the Levi-Civita covariant derivative associated with the metric g_{MN}, and the bulk energy–momentum tensor is given by

$$T_{MN} = \frac{1}{2}\left[f(\phi)\left(F_{MA}F_N{}^A - \frac{1}{4}\, g_{MN} F_{AB}F^{AB}\right) \right.$$
$$\left. + \left(\partial_M \phi \partial_N \phi - \frac{1}{2}\, g_{MN} \partial_A \phi \partial^A \phi \right) - g_{MN}V(\phi) \right]. \tag{4.6}$$

Furthermore, the antisymmetric field strength tensor F_{MN} is defined as

$$F_{MN} = \nabla_M A_N - \nabla_N A_M\,, \tag{4.7}$$

but let us note that for an antisymmetric tensor the covariant derivatives can be replaced by coordinate derivatives (see *e. g.* [159]).

We do not (yet) specify the full form of the scalar potential $V(\phi)$ (gauge kinetic function $f(\phi)$), except for these limits for vanishing scalar,

$$V(0) = 2\Lambda = -12/L_{\text{AdS}}^2\,, \tag{4.8}$$

$$f(0) = 1\,. \tag{4.9}$$

The cosmological constant $\Lambda = -6/L_{\text{AdS}}^2$ introduces the length L_{AdS} that will control the curvature scale of the resulting spacetime. The cosmological constant thus reappears in the Einstein equations (4.3) as the constant term in the scalar potential $V(\phi)$ in the energy–momentum tensor. In the models with a non-vanishing scalar, rather than specifying the full scalar potential from the start, we will prescribe the bulk profile of the scalar and reconstruct the potential that supports it *a posteriori*. The approach to 'reconstruct' the potential after imposing certain constraints on the solution has been widely used in the construction of bottom-up holographic models (see for instance [137, 138, 141, 160–162]).[g]

---

[g]See also [163] for a similar argument regarding the deformation of AdS_5 in the context of particle-physics model building with extra dimensions.

The most general *ansatz* for the metric [137] compatible with translation symmetry in the boundary directions $(t, \boldsymbol{x}) = (t, x^1, x^2, x^3)$ and $SO(3)$ invariance in $\boldsymbol{x}$ is

$$\mathrm{d}s^2 = \mathrm{e}^{2A(z)} \left(-h(z)\, \mathrm{d}t^2 + \mathrm{d}\boldsymbol{x}^2 \right) + \frac{\mathrm{e}^{2B(z)}}{h(z)}\, \mathrm{d}z^2 \,, \tag{4.10}$$

where z is the fifth-dimensional, holographic coordinate. The metric of all models that we introduce in the next sections can be expressed in this general form. Thus, we will discuss the holographic computation of physical observables in subsequent chapters in terms of this general metric (4.10).

In solving the equations of motion (4.3)–(4.6), we will always demand that the resulting spacetime be asymptotically AdS, *cf.* our discussion in Sec. 2.2. This implies the following boundary conditions at $z = 0$ for the functions A, B, and h in the ansatz (4.10),

$$A(z) \sim \log\left(\frac{L_{\mathrm{AdS}}}{z}\right) \text{ as } z \to 0\,, \tag{4.11}$$

$$B(z) \sim \log\left(\frac{L_{\mathrm{AdS}}}{z}\right) \text{ as } z \to 0\,, \tag{4.12}$$

$$h(z = 0) = 1\,. \tag{4.13}$$

(It is these boundary conditions that enforce the limiting value (4.8) for $V(\phi)$, *i. e.* the re-appearance of the cosmological constant in the scalar potential.) Furthermore, in order not to break isotropy in the dual field theory, we always set the spatial gauge field components A_i to zero, and we can ensure $A_z = 0$ by a gauge choice. Thus, we have

$$A_i(z) = 0\,, \qquad A_z(z) = 0 \text{ for all } z\,. \tag{4.14}$$

Whether or not the 'electrostatic potential' A_0 vanishes determines whether or not we have a chemical potential.

A zero in the 'blackening' function $h(z)$ signals the presence of a black hole (more precisely, a black brane). Note that, with our black holes generally being charged, there will generically be two zeros of h, just as it happens in the case of the charged asymptotically flat, four-dimensional Reissner–Nordström black hole (see for instance [37]). The relevant event horizon is located at the position of the zero closest to the boundary, *i. e.*, the one with smaller coordinate z. We call that position z_{h}. For the general metric (4.10) the Hawking temperature, see Eq. (2.24), is given by [137, 138]

$$T = \frac{\mathrm{e}^{A(z_{\mathrm{h}}) - B(z_{\mathrm{h}})} |h'(z_{\mathrm{h}})|}{4\pi}\,. \tag{4.15}$$

In the course of our studies of physical observables, we will evaluate the Nambu–Goto action describing a macroscopic string propagating in the five-dimensional spacetime. The Nambu–Goto action, see Eq. (2.2), contains the parameter α' and

our general metric, Eq. (4.10), always includes a factor L_{AdS}^2 due to the boundary conditions (4.11) and (4.12) satisfied by all our models. We define

$$\sqrt{\lambda} = \frac{L_{\text{AdS}}^2}{\alpha'} \tag{4.16}$$

for the combination of L_{AdS} and α' that will generically appear in our observables. For vanishing deformation, *i. e.* in the holographic dual of $\mathcal{N} = 4$ SYM, λ agrees with the 't Hooft coupling $\lambda = g_{\text{YM}}^2 N_{\text{c}}$, *cf.* Eq. (2.19). However, when we consider non-conformal models obtained by deformations of the bulk theory we lose the precise mapping between bulk and boundary quantities. Thus we cannot be sure of the exact meaning of λ in the boundary theory. This is not too big an issue since we are not primarily interested in quantitative predictions from our holographic models. In any case, it stands to reason that also in our non-conformal models λ still is a proxy for the coupling strength in the boundary field theory.

We will now proceed to discussing our holographic models in order of increasing complexity of the bulk theory.

4.1.1 $\mathcal{N} = 4$ Supersymmetric Yang–Mills Theory and Its Dual

Let us start with the simplest solution of the equations of motion of the action (4.1) relevant for the purposes of this chapter, the five-dimensional anti-de Sitter-black hole spacetime. Due to the presence of the gauge field, the black hole will in general be charged.

AdS-black hole spacetime arises as a solution of Eqs. (4.3)–(4.6) with vanishing scalar field ϕ. Only the cosmological-constant term 2Λ remains of the potential $V(\phi)$, and $f \equiv 1$, so that we can consider the simplified action

$$S = \frac{1}{16\pi G_{\text{N}}^{(5)}} \int \mathrm{d}^5 x \sqrt{-g} \left(\mathcal{R} + \frac{12}{L_{\text{AdS}}^2} - \frac{1}{4} F_{MN} F^{MN} \right) , \tag{4.17}$$

with the equations of motion

$$\mathcal{R}_{MN} - \frac{1}{2}\mathcal{R}\, g_{MN} + \Lambda\, g_{MN} = \frac{1}{2} \left(F_{MA} F_N{}^A - \frac{1}{4}\, g_{MN} F_{AB} F^{AB} \right) , \tag{4.18}$$

$$\nabla_M F^{MN} = 0 \,. \tag{4.19}$$

At vanishing temperature and vanishing chemical potential (vanishing gauge field), we have discussed the solution in Sec. 2.1.3. It is AdS_5 spacetime, dual to large-N_{c}, strongly coupled $\mathcal{N} = 4$ SYM theory. We have reviewed its particle content and some of its properties in Sec. 2.1.3.

Let us start with non-zero temperature but yet vanishing chemical potential. As reviewed in Sec. 2.2, the bulk theory is 'heated up' by putting a black hole into the bulk. This comes down to demanding that the horizon function $h(z)$ vanishes at some

point $z = z_h$ in the bulk. With this condition and the boundary conditions (4.11)–(4.13) the corresponding solution of the equation of motion (4.18) (with vanishing right-hand side) is the *AdS₅-Schwarzschild* metric

$$\mathrm{d}s^2 = \frac{L_{\mathrm{AdS}}^2}{z^2} \left(-h(z)\,\mathrm{d}t^2 + \mathrm{d}\boldsymbol{x}^2 + \frac{1}{h(z)}\,\mathrm{d}z^2 \right) ,$$
$$h(z) = 1 - \frac{z^4}{z_h^4} .$$

$$(4.20)$$

The coordinate z is bounded from above by z_h. At this position in the bulk there is a planar black-hole (black-brane) horizon. The associated Hawking temperature [35] is obtained from the general formula (4.15),

$$T = \frac{1}{\pi z_h} , \qquad (4.21)$$

and it is identified with the temperature of the boundary theory, *i. e.*, gravity in the AdS_5-Schwarzschild spacetime is dual [64] to large-N_c, strongly coupled $\mathcal{N} = 4$ SYM at non-zero temperature T given by Eq. (4.21). Obviously, in the limit $z_h \to \infty$ where the temperature vanishes, $h \equiv 1$, and the AdS_5-Schwarzschild metric (4.20) reduces to the AdS_5 metric (2.15).

Now we allow a non-vanishing gauge-field component A_0 and impose the boundary condition

$$A_0(z = 0) = \mu L_{\mathrm{AdS}} \qquad (4.22)$$

on it as demanded by the holographic dictionary, see Sec. 2.2. Here, μ is the chemical potential which in the present case of $\mathcal{N} = 4$ SYM is conjugate to an R-charge associated with supersymmetry.[h] In addition we have the boundary conditions (4.11)–(4.13) and require a zero of h at some z_h. A final condition is regularity of the gauge field at the horizon, which means that $\|A_M\,\mathrm{d}x^M\|^2 = g^{tt}A_0^2$ should be finite at z_h, leading to

$$A_0(z = z_h) = 0 . \qquad (4.23)$$

Putting all this together, from the equations of motion (4.18) and (4.19) we obtain

---

[h]Besides the conformal symmetries, the $\mathcal{N} = 4$ SYM theory has an $SO(6)$ global R-symmetry (see for example [31]), as mentioned in Sec. 2.1.3. The parameter μ introduced via Eq. (4.22) is a chemical potential for the charge corresponding to a $U(1)$ subgroup. It will lead to a spacetime with a charged black hole, and can in the string-theoretic context be connected to the properties of branes with angular momentum [164, 165]. These and similar constructions have been studied *e. g.* in [166–169]. We will lose the precise knowledge of the boundary theory, anyway, when we deform the bulk theory, so we will take a more pedestrian approach and generally define the chemical potential as the boundary value of the A_0 gauge-field component as in Eq. (4.22), in accordance with the holographic dictionary discussed in Sec. 2.2. As is typical for a holographic bottom-up approach, we will then only see from studying physical observables that the quantity thus introduced indeed behaves like a chemical potential.

AdS$_5$-Reissner–Nordström (AdS-RN) spacetime with the metric

$$\mathrm{d}s^2 = \frac{L_{\mathrm{AdS}}^2}{z^2}\left(-h(z)\,\mathrm{d}t^2 + \mathrm{d}\boldsymbol{x}^2 + \frac{1}{h(z)}\,\mathrm{d}z^2\right),$$

$$h(z) = 1 - \left(1 + \frac{\mu^2 z_{\mathrm{h}}^2}{3}\right)\frac{z^4}{z_{\mathrm{h}}^4} + \frac{\mu^2 z_{\mathrm{h}}^2}{3}\frac{z^6}{z_{\mathrm{h}}^6}. \tag{4.24}$$

The gauge-field component A_0 is found to be

$$A_0(z) = \mu L_{\mathrm{AdS}}\left(1 - \frac{z^2}{z_{\mathrm{h}}^2}\right). \tag{4.25}$$

In the limit $\mu \to 0$, the *AdS$_5$*-Reissner–Nordström metric reduces to the *AdS$_5$*-Schwarzschild metric, as expected. Using the formula (4.15), the temperature associated with the *AdS$_5$*-Reissner–Nordström metric is obtained,

$$T = \frac{1}{\pi z_{\mathrm{h}}}\left|1 - \frac{1}{2}\frac{\mu^2 z_{\mathrm{h}}^2}{3}\right|. \tag{4.26}$$

The AdS-Reissner–Nordström black hole is charged, thus supporting the electrostatic potential A_0 given in Eq. (4.25). We introduce the charge parameter $Q = \mu z_{\mathrm{h}}/\sqrt{3}$, which allows us to express the temperature (4.26) as

$$T = \frac{1}{\pi z_{\mathrm{h}}}\left(1 - \frac{Q^2}{2}\right), \tag{4.27}$$

with the restriction $0 \leq Q \leq \sqrt{2}$ for Q. Note that this imposes no restriction on the values of the pair (T, μ). Explicitly, given (T, μ) in the boundary theory, the parameters (z_{h}, Q) of the bulk theory are

$$z_{\mathrm{h}}(T, \mu) = 3\pi\frac{T}{\mu^2}\left[\sqrt{1 + \frac{2}{3\pi^2}\left(\frac{\mu}{T}\right)^2} - 1\right], \tag{4.28}$$

$$Q(T, \mu) = \sqrt{3}\pi\frac{T}{\mu}\left[\sqrt{1 + \frac{2}{3\pi^2}\left(\frac{\mu}{T}\right)^2} - 1\right]. \tag{4.29}$$

Note that (by construction, see Eqs. (4.11)–(4.13)) both the AdS-Schwarzschild metric (4.20) and the AdS-Reissner–Nordström metric (4.24) approach the plain-AdS metric (2.15) for small z close to the boundary, *i.e.* the scale-free metric dual to $\mathcal{N} = 4$ SYM at $T = 0, \mu = 0$. This is natural from the point of view of the dual theory since, as discussed in Sec. 2.2, the limit $z \to 0$ in the bulk corresponds to considering the UV in the boundary theory where the scales set by the temperature and/or chemical potential are expected to decouple.

To summarize, we have introduced the holographic duals of $\mathcal{N} = 4$ SYM including non-zero temperature and chemical potential. The general metric is the

AdS$_5$-Reissner–Nordström metric (4.24). This will in general be our starting point for investigating the physics in strongly coupled plasmas, and serve as a reference to compare with our more complicated models. We construct the latter as deformations of the *AdS*$_5$-Reissner–Nordström spacetime, as discussed in the following two sections.

However, before proceeding to these constructions, let us discuss what we have achieved so far, whether control over large-N_c, strongly coupled $\mathcal{N} = 4$ SYM really helps us with our goal of understanding physics relevant for the real-world quark–gluon plasma. Following [107], let us list prominent properties of $\mathcal{N} = 4$ SYM that distinguish it from QCD from which an *ab initio* description of the QGP should in principle start:

- The theory is (maximally) supersymmetric. It includes scalar fields, and all fields 'live' in the adjoint representation. In QCD the quarks transform in the fundamental representation.

- It is conformal, and the coupling does not run, whereas QCD is asymptotically free.

- There is neither confinement nor chiral symmetry breaking.

- In order to use the classical limit in the bulk, we have to send $N_c \to \infty$ in $\mathcal{N} = 4$ SYM. In QCD we have $N_c = 3$.

It might appear hopeless to use the AdS/CFT correspondence as a tool to handle strongly coupled $\mathcal{N} = 4$ SYM theory and attempt to extract lessons applicable to QGP physics from it. However, the above comparison concerns the vacua of the theories and the situation is considerably more favorable at non-zero temperature (and chemical potential), the setting relevant for the QGP. The differences are much smaller in this case:

- Both supersymmetry and conformal invariance of $\mathcal{N} = 4$ SYM are broken at non-zero temperature.

- There is no confinement in QCD above T_c, and no chiral condensate.

- At temperatures somewhat larger than T_c, QCD approaches conformality in the sense that the trace of the energy–momentum tensor becomes small (see *e. g.* [170]).

- There are no well-defined, long-lived quasiparticles at strong coupling and hence it is possible that details concerning the microscopic degrees of freedom do not matter too much, at least for some observables.

We have discussed the last argument concerning the universality at strong coupling in more detail in Sec. 3.2. Furthermore, as also discussed there, we will deform the bulk theory to consider more models for the QGP than only $\mathcal{N} = 4$ SYM. If

behavior common to all these models is found, it might indeed hint to universal features that are potentially shared also by QCD in the temperature range that we are interested in. Finally, let us note that lattice gauge theory studies indicate that QCD-like thermodynamics is remarkably insensitive to value of N_c [170], so that $N_c = 3$ might already be 'large'.

With these encouraging general considerations in mind, let us now proceed to the construction of explicitly non-conformal models.

4.1.2 The SW$_{T,\mu}$ Model

The model that we discuss in this section does not solve the full set of equations of motion that are associated with the action (4.1). Rather, it can be seen as a crude first approximation in which one solves the Einstein–Maxwell part of the action, and then the scalar part with the background metric fixed, thus ignoring the backreaction of the scalar onto the metric.

Ignoring for the moment the gauge field which means to assume vanishing chemical potential, the first step is to solve the pure-gravity problem $\mathcal{L} = (-g)^{1/2}(\mathcal{R} - 2\Lambda)$. Considering the system at non-zero temperature, this gives rise to the AdS-Schwarzschild metric (4.20), as discussed in the previous section. The scalar is interpreted as a dilaton in the present case. As discussed in Sec. 2.1.1, the metric in string frame has an overall exponential warp factor with the dilaton in the exponent. Effectively it will be the string-frame metric that we will need when studying physical observables in the later sections. One often demands a quadratic dilaton, $\phi \propto z^2$. This is motivated by the 'soft-wall' model of [132] that introduced a quadratic dilaton to emulate confinement in the boundary theory at vanishing temperature. Let us stress again that the model we are discussing does not solve equations of motion, so the above discussion of the scalar is somewhat academic. In practice, the model is just *defined* by the AdS-Schwarzschild metric multiplied by a warp factor of the form e^{cz^2} for some deformation parameter c.[i] Such models have been studied for instance in [116, 133, 136, 171, 172] and might be generally called 'SW$_T$' models, for 'soft wall-like models at finite temperature T' [113].

At non-zero chemical potential μ the starting point is the AdS_5-Reissner–Nordström metric (4.24), which is multiplied by a warp factor. Such a model has been first discussed in [173]. Further studies of models of this type include [45, 174–177]. With conventions slightly different from [173] we now *define* the SW$_{T,\mu}$ model by the metric

$$
\begin{aligned}
\mathrm{d}s^2 &= \frac{L_{\mathrm{AdS}}^2 \mathrm{e}^{c^2 z^2}}{z^2}\left(-h(z)\,\mathrm{d}t^2 + \mathrm{d}\boldsymbol{x}^2 + \frac{1}{h(z)}\,\mathrm{d}z^2\right), \\
h(z) &= 1 - \left(1 + \frac{\mu^2 z_{\mathrm{h}}^2}{3}\right)\frac{z^4}{z_{\mathrm{h}}^4} + \frac{\mu^2 z_{\mathrm{h}}^2}{3}\,\frac{z^6}{z_{\mathrm{h}}^6}\,.
\end{aligned}
\tag{4.30}
$$

---

[i] We note in passing that demanding the scalar to be $\phi(z) = cz^2$ in the AdS-Schwarzschild background (4.20) necessitates that the scalar potential be given by $V(\phi)L_{\mathrm{AdS}}^2 = -2\phi^2 - \pi^2(T^2/c)^2\phi^4$ (without including the cosmological-constant term 2Λ in the potential) if the scalar is to solve $\Box\phi = V'(\phi)$. However, note that this neglects the backreaction of the scalar onto the metric.

A warp factor has been included, but the horizon function is taken unchanged from the AdS-Reissner–Nordström metric (4.24). μ is the chemical potential, and c is the deformation parameter which has the dimension of energy. In the limit $c \to 0$, the metric (4.30) reduces to the AdS-Reissner–Nordström black-hole metric. We assume that the Hawking temperature of the latter, which we reproduce here for convenience,

$$T = \frac{1}{\pi z_{\mathrm{h}}} \left(1 - \frac{Q^2}{2} \right) \tag{4.31}$$

with $Q = \mu z_{\mathrm{h}}/\sqrt{3}$ and $0 \leq Q \leq \sqrt{2}$, is the temperature of the boundary theory even at non-zero c, since backreaction of finite c onto the metric is ignored. Then, with T and Q determined as above, the relations (4.28) and (4.29) expressing z_{h} and Q in terms of T and μ apply in this model, too.

We note that the thermodynamics of this model is not consistent since it does not solve the Einstein equations; *cf.* also [45] and a related discussion in [136]. Furthermore, moving probes constitute another example where unphysical behavior seems to arise [124]. This necessitates to consider consistent models that solve equations of motion. Indeed, it turns out that the problems just mentioned do not appear in such models [45, 124]. The construction of specific consistent models is the topic of the next section.

In spite of the aforesaid issues, the present model will be useful to us. Its main virtue is its simplicity. The horizon function remains relatively simple since there is no backreaction. In consequence, the numerics is much simpler in this model than in the more complicated models to be discussed next which solve equations of motion. We will see that often the present model gives answers very similar to those of the more sophisticated models. On the other hand, the comparison of results obtained in the present and the consistent models makes it possible to identify those parameter regimes for which it becomes important to invest the additional effort of using consistent models.

4.1.3 The 1-Parameters Models

Now we proceed to discussing models arising as solutions to the full equations of motion associated with the action (4.1). As mentioned in the previous section, this procedure is generally preferable in the construction of bottom-up models as it is more faithful to the basic ideas of holography, and we call models thus obtained consistent models. Specifically, in our case this amounts to including the backreaction of the scalar onto the metric that was ignored in the construction of the $\mathrm{SW}_{T,\mu}$ model. Constructions of consistent models were performed for instance in [113, 122, 137, 139–141, 160, 178, 179]. The cited models are based on actions of the general form (4.1) *excluding* the gauge field, *i.e.*, they have vanishing chemical potential.

We are concerned with models including a non-zero chemical potential. Models with a gauge field in an action of the type (4.1) have for example been constructed

in [45, 158, 180–182]. Here we use the model that we have first constructed in [45].

For the metric we take the general *ansatz* given in Eq. (4.10) which we reproduce here for convenience together with the *ansätze* for the scalar and the gauge field[j],

$$\mathrm{d}s^2 = \mathrm{e}^{2A(z)}\left(-h(z)\,\mathrm{d}t^2 + \mathrm{d}\boldsymbol{x}^2\right) + \frac{\mathrm{e}^{2B(z)}}{h(z)}\,\mathrm{d}z^2\,, \tag{4.32}$$

$$\phi = \phi(z)\,, \qquad A_M\,\mathrm{d}x^M = \Phi(z)\,\mathrm{d}t\,. \tag{4.33}$$

We have introduced the symbol Φ for the electrostatic potential A_0. The remaining gauge-field components vanish, *cf.* Eqs. (4.14). With these *ansätze*, the equations of motion (4.3)–(4.6) can be brought into the form

$$0 = A'' - A'B' + \frac{1}{6}\,\phi'^2\,, \tag{4.34}$$

$$0 = h'' + (4A' - B')h' - \mathrm{e}^{-2A}f(\phi)\Phi'^2\,, \tag{4.35}$$

$$0 = \Phi'' + (2A' - B')\Phi' + \frac{\mathrm{d}\log f(\phi)}{\mathrm{d}\phi}\,\phi'\Phi'\,, \tag{4.36}$$

$$0 = \phi'' + \left(4A' - B' + \frac{h'}{h}\right)\phi' - \frac{\mathrm{e}^{2B}}{h}\left(\frac{\mathrm{d}V}{\mathrm{d}\phi} - \frac{1}{2}\,\mathrm{e}^{-2(A+B)}\Phi'^2\frac{\mathrm{d}f}{\mathrm{d}\phi}\right)\,, \tag{4.37}$$

$$0 = h\left(24A'^2 - \phi'^2\right) + 6A'h' + 2\mathrm{e}^{2B}V(\phi) + \mathrm{e}^{-2A}f(\phi)\Phi'^2\,. \tag{4.38}$$

These equations are not all independent. In fact, the z-derivative of the right-hand side of the last equation can be expressed as a linear combination of the right-hand sides of all five equations. Thus, if the first four equations are satisfied, the last one is satisfied for all z if it is satisfied at one value of z.

As discussed below Eq. (4.8), we do not specify the scalar potential $V(\phi)$ but rather the bulk profile of the scalar, and reconstruct the potential from the equations of motion. Explicitly, we demand that the scalar have a quadratic dependence on the holographic coordinate z,

$$\phi(z) = \sqrt{\frac{3}{2}}\kappa z^2\,, \tag{4.39}$$

where κ is the deformation parameter that will be discussed below. This choice is motivated by the work of [132] where it turns out that the spectrum of a model with a quadratic scalar (more precisely, a dilaton; we will discuss the interpretation of the scalar later on), a so-called 'soft-wall' model, compares favorably to QCD. The reasons for the choice of the normalization factor will become clear soon. With the choice (4.39), the scalar vanishes as it approaches the boundary. According to our general discussion in Sec. 2.2, it will thus induce a relevant deformation of the conformal UV theory. In fact, from the explicit solution of the equations of motion discussed below, one finds[k] $m^2 = -4$ which translates via Eq. (2.21) into a scaling dimension $\Delta = 2$. For further discussion see [45].

---

[j]One should take care not to confuse the gauge 1-form $A_M(z)\,\mathrm{d}x^M$ with the exponent $A(z)$ in the metric warp factor, nor to confuse the 0-component of the gauge field Φ with the scalar ϕ.

[k]Note that $m^2 = -4$ with $d = 4$ boundary-theory dimensions obeys the Breitenlohner–Freedman bound given in Eq. (2.22).

In addition to the condition (4.39), we specify $A(z)$ as follows,

$$A(z) = \log\left(\frac{L_{\text{AdS}}}{z}\right) \tag{4.40}$$

for all z, which in particular satisfies the asymptotic-AdS boundary condition (4.11) without any deviations from the asymptotic form deeper in the bulk. In this sense, the form (4.40) is a minimal choice for A.

The chemical potential μ is introduced by the first of the two boundary conditions for Φ,

$$\Phi(z = 0) = \mu L_{\text{AdS}}, \tag{4.41}$$

$$\Phi(z = z_{\text{h}}) = 0, \tag{4.42}$$

in accordance with the general prescription discussed in Sec. 2.2. Just like in Sec. 4.1.1 before, the condition (4.42) is a regularity condition. This condition introduces the horizon coordinate z_{h}. The integration constant that eventually appears in the solution for $h(z)$ after imposing Eq. (4.13) can be traded for z_{h}, thus establishing the latter as the position of the black hole horizon.

We have not yet specified the gauge kinetic function $f(\phi)$. It parametrizes the coupling between the gauge field and the scalar. Thus, in the boundary theory, it will affect the interplay of the chemical potential and the deformation. We will mostly work with the expression used in [158] by DeWolfe, Gubser, and Rosen,

$$f_{\text{DWGR}}(\phi) = \frac{\cosh\left(\frac{12}{5}\right)}{\cosh\left(\frac{6}{5}(\phi - 2)\right)}, \tag{4.43}$$

which was chosen there to improve the matching of results to QCD lattice data. However, in order to be able to assess the impact of the choice of the gauge kinetic function on observables we will also solve the equations of motion for the minimal choice

$$f_{\text{min}}(\phi) = 1. \tag{4.44}$$

Given ϕ and A, Eqs. (4.39) and (4.40), respectively, as well as the boundary conditions (4.12), (4.13), (4.41), and (4.42), the equations of motion (4.34)–(4.38) can be solved in closed form one-by-one for $B(z)$, $\Phi(z)$, $h(z)$, and $V(\phi)$, and the relation between the equations of motion discussed after Eq. (4.38) ensures that all five equations are satisfied. The explicit expressions for the solution of the equations of motion are lengthy for both choices (4.43) and (4.44) of the gauge kinetic function. We give the solutions in the appendices B.1 and B.2, respectively. However, let us mention here that the models defined by (4.43) and (4.44), respectively, differ only at $\mu \neq 0$, and coincide for $\mu = 0$. This immediately follows from the action where the gauge kinetic function multiplies the field-strength term which vanishes for $\mu = 0$. We discuss the thermodynamic properties of the models below in Sec. 4.1.4. For an extensive discussion of the equations of motion and their solution we refer to [45].

Eq. (4.39) introduces the *deformation parameter* κ which has mass dimension 2. In the limit $\kappa \to 0$ the solutions reduce to AdS-Reissner–Nordström spacetime. The dimensionful parameter κ introduces a scale in the dual field theory and thereby explicitly breaks the conformal invariance. We collectively refer to the models we have constructed as the *1-parameter models*. For each choice of the gauge kinetic function $f(\phi)$ we have a 1-parameter family of models with the deformation parameter κ. Actually, as we will discuss momentarily, for each choice of $f(\phi)$ we have two 1-parameter families of models. Thus, all in all in this thesis we will study four families of models that we refer to by the term '1-parameter models'.

It turns out that the scalar potential $V(\phi)$ depends not only on the deformation parameter but also on the thermodynamic variables, see the explicit solutions (B.14) and (B.21) in Appendix B. (Recall that, as discussed above, we reconstruct the scalar potential from the equations of motion such that it supports the bulk profile (4.39) of the scalar.) This might spoil the study of the behavior of observables in the 1-parameter models under variation of the temperature and chemical potential because the boundary theory depends on the specific form of the potential and would thus change upon changing the thermodynamic variables. However, a detailed analysis [45] shows that the variation of the potential only affects orders in ϕ higher than quadratic and, moreover, is small in the part of the bulk that is causally connected to the boundary. Therefore, it is in fact meaningful to compare the values of physical observables for different thermodynamic states.

In the following chapters, we will use macroscopic strings as 'probes' in the space-times we have constructed since these can in the boundary theory be interpreted as quarks (as we will explain later). Then, a further choice that one can make in working with the models becomes important, and this will effectively give rise to two different families of models for each choice of the gauge kinetic function, as announced above. We can either view the scalar field ϕ in our models as a dilaton or as 'just' some scalar matter field in which case we assume a trivial dilaton. We take both of these points of view. In case the theory contains a non-trivial dilaton, the spacetime metric depends on whether we work in the Einstein frame or string frame, as discussed in Sec. 2.1.1, see Eq. (2.4). In order to describe string dynamics with the Nambu–Goto action as defined in (2.2), we need to use the string-frame metric. Now, the action (4.1) is given in Einstein frame. That means that a metric that solves its equations of motion is an Einstein-frame metric.

In case we do not view the scalar ϕ as a dilaton and assume a trivial dilaton, the transformation to the string-frame metric that we will use in the Nambu–Goto action is the identity. In other words, we can directly use the metric that is derived from the equations of motion of the action (4.1) in the Nambu–Goto action (2.2).

On the other hand, in case we view the scalar as a dilaton, before using the Nambu–Goto action (2.2), we have to transform the metric obtained from the action (4.1) into the string frame. The transformation is not exactly the one given in Eq. (2.4) because of the normalization of the scalar kinetic term in our action (4.1). In five spacetime dimensions the canonical normalization of the dilaton kinetic term

in low-energy effective string-theory actions is (see *e. g.* [43])

$$S^{(E)} = \frac{1}{16\pi G_N^{(5)}} \int d^5 x \sqrt{-g^{(E)}} \left(\mathcal{R}^{(E)} - \frac{4}{3} \partial_M \phi_5 \, \partial^M \phi_5 + \dots \right) , \tag{4.45}$$

where we have used superscripts 'E' to indicate that this action is written in Einstein frame[1], and have left out all additional terms as these are not important for the present discussion. We see that the scalar ϕ in our action (4.1) is related to the canonically normalized dilaton, denoted by ϕ_5 in the equation above, by

$$\phi = \sqrt{\frac{8}{3}} \, \phi_5 \,. \tag{4.47}$$

Using this, we obtain from Eq. (2.4) the transformation rule between the Einstein-frame metric $g_{MN}^{(E)}$ and the string-frame metric $g_{MN}^{(s)}$,

$$g_{MN}^{(s)} = e^{\sqrt{\frac{2}{3}}\phi} g_{MN}^{(E)} \,. \tag{4.48}$$

The numerical factor in the exponent explains the apparently awkward normalization in our *ansatz* (4.39) for the scalar field. The metric $g_{MN}^{(s)}$ can now be used in the Nambu–Goto action (2.2).

   Following a convention in the literature we call, in a slight abuse of language, the model in which the scalar field is a dilaton the (1-parameter) *string-frame model* and the model in which it is just an additional scalar the (1-parameter) *Einstein-frame model*. As can be seen from the expressions in Appendix B, for either choice of the gauge kinetic function both warp-factor exponents A and B in the metric of the string-frame model contain an additional term $\kappa z^2/2$ that is not present in the corresponding Einstein-frame model. Thus, the exponents in the warp factors of both the 1-parameter string-frame models and the $SW_{T,\mu}$ model have a term quadratic in the holographic coordinate z. This suggests that the string-frame models have a greater similarity to the $SW_{T,\mu}$ model than the Einstein-frame models which lack this quadratic term in the warp factor. When discussing physical observables we will see that this is indeed the case, and we have also observed this in our previous investigation of different observables [45]. Roughly speaking, the 1-parameter string-frame models can be seen as consistent versions of the $SW_{T,\mu}$ model.

4.1.4 Thermodynamics

In this section, we discuss some thermodynamic properties of our models. As our main focus in the present part of this thesis is not on the thermodynamics of the

---

[1]In string frame, using Eq. (2.4), the action can be shown to be

$$S^{(s)} = \frac{1}{16\pi G_N^{(5)}} \int d^5 x \sqrt{-g^{(s)}} e^{-2\phi_5} \left(\mathcal{R}^{(s)} + 4\partial_M \phi_5 \, \partial^M \phi_5 + \dots \right) , \tag{4.46}$$

which nicely illustrates that, as announced in Sec. 2.1.1, for the derivation of the spacetime metric it is simpler to work in Einstein frame where the overall factor $e^{-2\phi_5}$ is absent.

models, we will be brief. Another issue to be addressed here are constraints imposed on the deformation parameters. We will see that there are upper bounds on the range of admissible choices of the deformation parameters. Finally, a certain thermodynamic quantity, the trace of the energy–momentum tensor (scaled by temperature such that it becomes dimensionless), can be used to estimate 'optimal' choices of the deformation parameter for realizing a concrete model in physical units. These estimates are based on a comparison to lattice-QCD results at vanishing chemical potential, which has been performed for the ($\mu = 0$)-limits of our models in [113]. We will briefly review this comparison. We start with the $\text{SW}_{T,\mu}$ model, and then proceed to the 1-parameter models. On the way, we also comment on the (simple) thermodynamics of $\mathcal{N} = 4$ SYM.

The $\text{SW}_{T,\mu}$ Model

The thermodynamics in the ($\mu = 0$)-limit of the $\text{SW}_{T,\mu}$ model, *i. e.*, in the SW_T model, has been studied in many works including the early references [135, 136, 171]. Before discussing the thermodynamics of the $\text{SW}_{T,\mu}$ model, we should raise the caveat that its thermodynamics cannot be expected to be consistent, see for instance [136]. The reason for this is that the $\text{SW}_{T,\mu}$ model does not solve gravity equations of motion, so this problem will be cured in the 1-parameter models, which do solve equations of motion. With this caveat in mind, let us nevertheless proceed and see what lessons we can learn about the $\text{SW}_{T,\mu}$ model from thermodynamic quantities.

The temperature in the $\text{SW}_{T,\mu}$ model is given by Eq. (4.31). A central thermodynamic quantity is the entropy density. By the holographic dictionary, the entropy density of the black hole is identified with the entropy density in the boundary theory. The entropy of a black hole can be computed from the Bekenstein–Hawking formula [34, 35], which in the case at hand reads

$$S = \frac{A_3}{4G_{\text{N}}^{(5)}} \, , \tag{4.49}$$

where A_3 is the three-dimensional 'area' of the black-hole horizon and $G_{\text{N}}^{(5)}$ is the five-dimensional Newton constant. While A_3 is actually divergent since we have an infinitely extended black-brane horizon, the entropy density s is well-defined. For the SW_T model, *i. e.*, at $\mu = 0$, the entropy density was first computed in [136]. Using the definition (4.49) and Eq. (4.2) for the five-dimensional Newton constant[m],

---

[m]In light of the caveat discussed after Eq. (4.2) – and the additional caveat that the $\text{SW}_{T,\mu}$ model does not even solve the full equations of motion of the action (4.1) – the prefactor in the expression (4.50) for the entropy density should be taken with a grain of salt. However, the value of the prefactor does not affect the position of the maximum of the quantity $(\epsilon - 3p)/T^4$ (discussed below) which we are ultimately after here.

one readily derives[n]

$$s = \frac{N_c^2}{2\pi} \frac{\exp\left(-\frac{3}{2}c^2 z_h^2\right)}{z_h^3} \, . \tag{4.50}$$

In this form this equation holds for both vanishing and non-zero chemical potential with z_h given by Eq. (4.28).

Let us now turn to the (dimensionless) trace of the boundary theory's energy–momentum tensor. In an isotropic homogeneous system, it is given by $\epsilon - 3p$, where ϵ is the energy density and p the pressure, and it is made dimensionless by dividing by T^4. The resulting quantity $(\epsilon - 3p)/T^4$ is often called the 'trace anomaly', and can be computed in QCD at vanishing chemical potential via lattice QCD (see for instance [186, 187]). Since in a conformal theory $p = \epsilon/3$, and accordingly $(\epsilon - 3p)/T^4$ vanishes, a non-vanishing trace is a measure of the deviation from scale invariance. In QCD, lattice studies indicate that the trace anomaly is strongly peaked at T_c (*e. g.* [186, 187]). Ref. [113] has computed the dimensionless trace of the energy–momentum tensor from the entropy density for the ($\mu = 0$)-limits of both the $\mathrm{SW}_{T,\mu}$ and the 1-parameter models and found good qualitative agreement with lattice-QCD data. It turns out that the non-conformal holographic models have a strong peak in $(\epsilon - 3p)/T^4$ at a certain temperature. (On the other hand, the energy–momentum tensor of $\mathcal{N} = 4$ SYM has vanishing trace even at non-zero temperature.) This temperature is identified with T_c in accordance with lattice QCD studies. In this work, we adopt the results from [113], and use the value

$$T_c/c = 0.494 \tag{4.51}$$

for the $\mathrm{SW}_{T,\mu}$ model.[o] The position of the maximum of the dimensionless trace of the energy–momentum tensor just fixes the ratio T_c/c, and we still have to choose the value of T_c to make contact with physical units. Again following [113], we take $T_c = 176\,\mathrm{MeV}$, an estimate which is based on an analysis [188] of particle

---

[n] A comment is in order here. To derive Eq. (4.50) from the metric (4.30) of the $\mathrm{SW}_{T,\mu}$ model, one has to flip the sign in the argument of the exponential in the metric. In fact, the authors of [136] who first derived (4.50) in the SW_T model actually start out with a metric with a negative sign in the exponent, which is assumed to be the Einstein-frame metric that should be used to study thermodynamics. It is then assumed that the model involves a non-trivial dilaton. Strings 'see' the so-called string-frame metric which contains a contribution from the dilaton, as discussed in Sec. 2.1.1. In the course of the analysis of [136], it turns out that the relative strength of the dilaton is such that in the string frame the exponent in the metric switches sign which ultimately yields a string-frame metric of the form (4.30). Following the argument of [136] we use the sign-flipped version of the metric (4.30) for the thermodynamics. However, in the rest of this thesis, we will only be concerned with the physics of strings in the $\mathrm{SW}_{T,\mu}$ model, and will assume that the metric as written in Eq. (4.30) is the appropriate, *i. e.* string-frame metric. For further discussion of various sign choices (in the context of soft-wall models at vanishing temperature), see for instance [183–185].

[o] For consistency with our choice in the 1-parameter model, to be discussed below, in the $\mathrm{SW}_{T,\mu}$ model we use the value for T_c/c as determined from the maximum of the dimensionless trace. We note, however, that Ref. [136], which first studied the thermodynamics of the SW_T model in detail, fixes the critical temperature based on a different procedure resulting in the slightly different $T_c/c = 0.434$.

ratios measured at RHIC with a statistical thermal model (see for instance [189]). This choice translates into $c = 356\,\text{MeV}$ as the 'optimal' value of the deformation parameter that makes sure that the maximum of the dimensionless trace of the energy–momentum tensor lies at $T = 176\,\text{MeV}$.[p]

In general, however, we are not so much interested in fixing a specific model, but will rather explore the behavior of our observables in a class of models parametrized by the deformation parameter. Typically, we will make it dimensionless by normalizing it to some fixed temperature and will often denote that dimensionless ratio $\delta = c/T$. Thus, the question arises what range of deformation parameters is sensible to consider. The authors of Ref. [109] have calculated various observables in the SW_T model and conclude that the range of deformations[q] $0 \le c/T \lesssim 2.5$ is most relevant for a comparison with QCD. In this thesis, we will also use that range of deformations for our $\text{SW}_{T,\mu}$ model. This restriction of c also avoids inconsistencies we have found previously [45, 124] that appear in the model at somewhat larger deformations ($c/T > 5.06$).

The 1-Parameter Models

In the 1-parameter models, first of all we need to discuss the temperature. The formula (4.15) can be used for both the Einstein- and the string-frame model. Using the metric (4.32) and the expressions given in Appendix B.1, we find, for the models defined by the choice (4.43) of the gauge kinetic function,

$$
T = \frac{1}{\pi z_{\text{h}}} \frac{\kappa^2 z_{\text{h}}^4}{4} \frac{\text{e}^{\kappa^2 z_{\text{h}}^4/4}}{\text{e}^{\kappa^2 z_{\text{h}}^4/4} - 1} \, \mathcal{S}^{-2}\left(\kappa z_{\text{h}}^2\right) \left| \mathcal{S}^2\left(\kappa z_{\text{h}}^2\right) + \frac{\mu^2}{\kappa} \theta \left[\mathcal{S}\left(\kappa z_{\text{h}}^2\right) - \iota \widetilde{\mathcal{S}}\left(\kappa z_{\text{h}}^2\right) \right] \right| ,
$$
(4.52)

where we have defined the constants

$$
\theta = \frac{2}{\sqrt{\pi}} \text{e}^{-54/25}\left(1 + \text{e}^{24/5}\right) \approx 15.94\,, \qquad \iota = \frac{\text{e}^{-27/25}}{\sqrt{2}} \approx 0.24\,,
$$
(4.53)

and have used the functions $\mathcal{S}$ and $\widetilde{\mathcal{S}}$ defined in the appendix in Eqs. (B.7) and (B.9), respectively.

For the alternative 1-parameter models defined by the minimal choice (4.44) of the gauge kinetic function $f(\phi)$, we find, again independently of whether we consider

---

[p]We note that there have been varied estimates for the transition temperature T_{c} in QCD (actually, crossover temperature) throughout the years. Recent lattice studies [65, 66] favor a value around $T_{\text{c}} \sim 154\,\text{MeV}$. For LHC data measured by the ALICE experiment, an estimate of $156\,\text{MeV}$ for the chemical-freeze-out temperature is found [190] with a statistical thermal model. Since we will use the specific choice of the deformation parameter of the holographic model based on the value for T_{c} only for a rough estimate of our model parameter λ, as will be discussed later, a difference of $\sim 20\,\text{MeV}$ for the value of T_{c} does not matter, so we stay with $T_{\text{c}} = 176\,\text{MeV}$.

[q]Ref. [109], following [136], uses a normalization of the deformation parameter different from ours. For the cited range, we have translated the ratio of deformation parameter and temperature to our conventions.
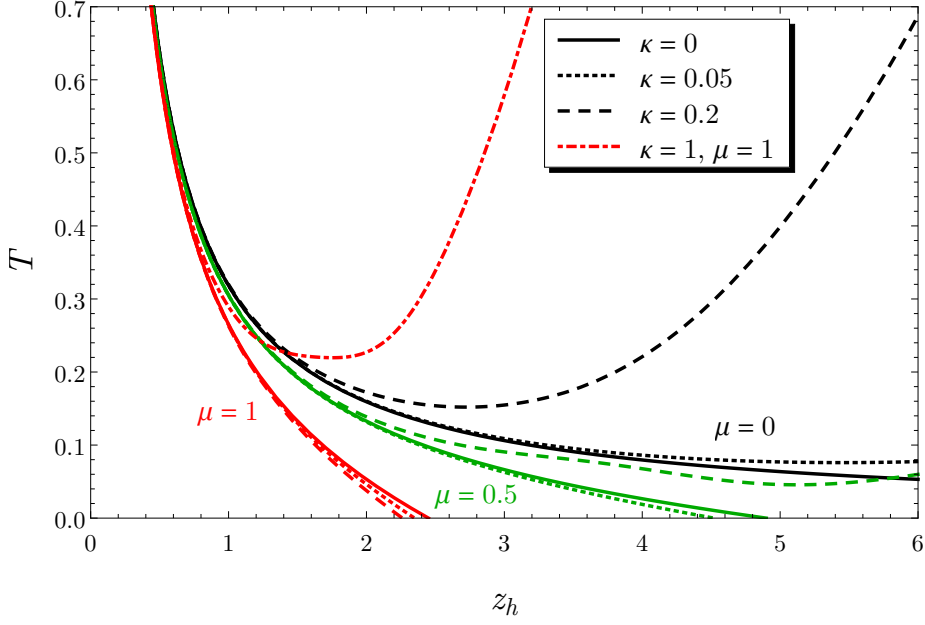
Figure 4.1: Temperature in the 1-parameter models with $f(\phi)$ chosen according to Eq. (4.43). Different colors indicate different choices of the chemical potential, while the linestyle encodes the choice of the deformation parameter. In making this plot, we have ignored the absolute value in Eq. (4.52). Thus, the curves that reach $T = 0$ at some z_h would actually rise again for larger z_h. However, as explained in the text, the rising parts are not important and hence are left our here. Figure adapted from [45].

the Einstein- or the string-frame model,

$$T = \frac{1}{\pi z_h} \frac{\kappa^2 z_h^4}{4} \frac{e^{\kappa^2 z_h^4/4}}{e^{\kappa^2 z_h^4/4} - 1} \operatorname{erf}^{-2}\left(\frac{\kappa z_h^2}{2}\right)$$

$$\times \left| \operatorname{erf}^2\left(\frac{\kappa z_h^2}{2}\right) - \frac{\mu^2}{\kappa}\sqrt{\frac{2}{\pi}}\left[\sqrt{2}\operatorname{erf}\left(\frac{\kappa z_h^2}{2}\right) - \operatorname{erf}\left(\frac{\kappa z_h^2}{\sqrt{2}}\right)\right] \right|. \tag{4.54}$$

The definition of the error function erf used here is given in Eq. (B.10).

We plot the temperature function (4.52) for the 1-parameter models (string-frame and Einstein-frame models) with the choice (4.43) for the gauge kinetic function in Fig. 4.1 where we vary the chemical potential μ and the deformation parameter κ. The behavior in the alternative models defined by Eq. (4.44) is similar. We observe three important features of the curves $T = T(z_h)$ that are shared by the $T(z_h)$ in the alternative models. First, for small z_h (equivalent to considering large

temperatures in the boundary theory) the chemical potential and the deformation parameter only induce small corrections to the relation $T = 1/(\pi z_h)$ that holds in AdS_5-Schwarzschild. We can see this immediately from (4.52) or (4.54), respectively. Second, if κ is sufficiently large compared to μ (roughly $\sqrt{\kappa} \gtrsim \mu$) the temperature curve does not reach $T = 0$ but rather has some non-zero minimum $T_{\min}$. Third, and related to the second observation, there are parts where T rises with increasing z_h. Besides the curves that have a non-zero $T_{\min}$, also those that reach $T = 0$ actually have a rising part due to the absolute value in Eq. (4.52). For clarity, we have left out these parts in Fig. 4.1.

The third observation implies that there are generally two solutions for z_h that yield a prescribed T with some fixed μ and κ. The question arises which solution to take. Computing the entropy density in these models can provide guidance. Applying the formula (4.49) to the present models and using again Eq. (4.2) for the five-dimensional Newton constant[r] (2.18) and (4.2) we find

$$s = \frac{N_c^2}{2\pi} \frac{1}{z_h^3} \,, \tag{4.55}$$

which looks similar to Eq. (4.50) but lacks the warp factor. However, note that the relation between the gravity parameter z_h and the boundary-theory parameters T and μ encoded in Eq. (4.52) is quite different from the one in the $SW_{T,\mu}$ model. We see from Eq. (4.55) that s decreases monotonically with z_h. Now, starting out at $z_h = 0$ and $T = \infty$ and increasing z_h, once we reach a branch of the temperature curve that increases with z_h, the derivative $T \partial s/\partial T = T(\partial z_h/\partial T)(\partial s/\partial z_h)$ becomes negative. This means that the heat capacity $T \partial s/\partial T$ is negative, indicating an instability of the black hole. This leads us to exclude those branches of the temperature curves. In other words, for a given T we always take the smaller solution z_h, which is the one that is on the branch where T decreases with increasing z_h. See Ref. [45] for further discussion of this matter.

Having thus established a unique relation between the temperature T and the horizon position z_h for given μ and κ, it remains to discuss the implications of the fact that we have a set of values μ, κ with minimal temperatures $T_{\min} > 0$. We constructed our bulk theories as models for a deconfined gauge-theory plasma, so it should not be too big a surprise (or problem) that we cannot reach arbitrarily low values of the temperature or chemical potential. It often seems to be the case that in the gravity duals of theories that undergo a phase transition the spacetime dual to the low-temperature phase is qualitatively different from the black-hole spacetime dual to the high-temperature phase[s], and our ansatz for the scalar and the warp-factor exponent might be too restrictive to find solutions corresponding to lower

---

[r] We recall the caveat discussed after Eq. (4.2) concerning the expression of $G_N^{(5)}$ in terms of N_c (and L_{AdS}, the natural length scale in the bulk). Since these issues only concern the normalization of the entropy density, they are not important for the present argument. *Cf.* also footnote (m).

[s] For instance, in a typical holographic model [135] of the deconfinement/confinement phase transition, on the gravity side the transition is of the Hawking–Page type [191], and the low-temperature phase is described by a thermal-AdS spacetime in which there is no black hole.
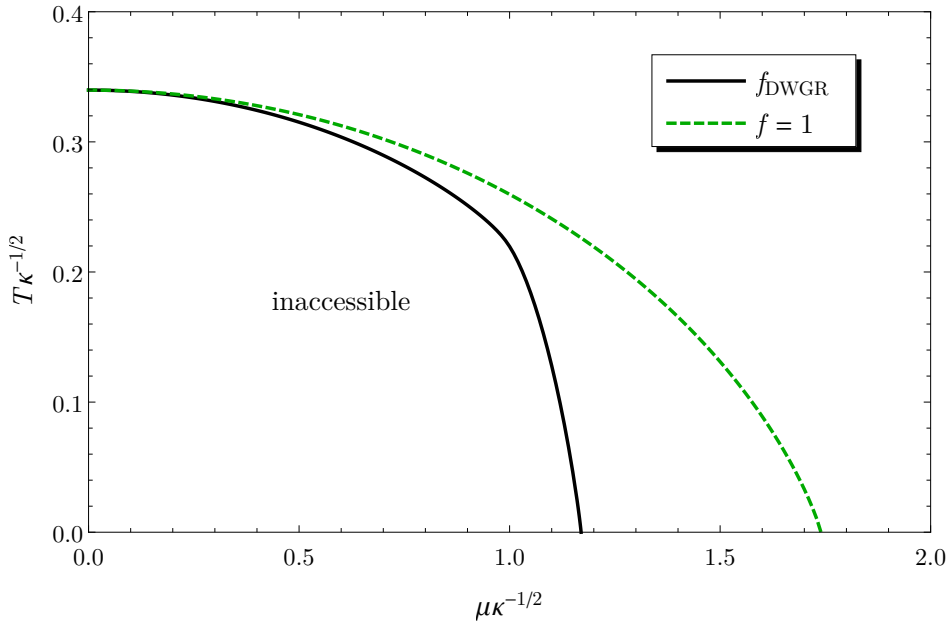
Figure 4.2: Region in the (μ, T)-plane inaccessible in the 1-parameter models. μ and T are normalized to $\sqrt{\kappa}$ with κ the deformation parameter. Shown are the inaccessible regions for both choices of the gauge kinetic function, f_{DWGR} as used by DeWolfe, Gubser, and Rosen [158], and the minimal choice $f = 1$, see Eqs. (4.43) and (4.44), respectively. Figure adapted from [45].

temperatures.

More explicitly, a numerical analysis [45] shows that a region including the origin in the (μ, T)-plane is not accessible by any of our 1-parameter models. This statement can be made independent of the choice of the deformation parameter by considering the dimensionless ratios $T/\sqrt{\kappa}$ and $\mu/\sqrt{\kappa}$, see Fig. 4.2. The precise form of the curve bounding the inaccessible region is dependent on the choice of the gauge kinetic function $f(\phi)$, but for both choices considered in this thesis the minimal attainable (dimensionless) temperature at vanishing chemical potential is $T_{\min}/\sqrt{\kappa} = 0.34$. Turning this around, the maximal deformation in units of the temperature is $\sqrt{\kappa_{\max}}/T = 2.94$. We can infer from Fig. 4.2 that the maximal deformation in units of the temperature increases with increasing μ. However, when we are going to consider physical observables at non-zero chemical potential, we usually want to make contact with the physics at $\mu = 0$. Therefore, in this work

---

On the other hand, apparently this need not always be the case. In the model constructed in [158] from an Einstein–Maxwell–scalar bulk action similar to Eq. (4.1) also the low-temperature phase is described by black-hole spacetimes. Differences to our models include the fact that the scalar potential is fixed instead of reconstructed, and, probably more importantly, a different treatment of the scalar field.

we restrict ourselves to deformations that always allow us to go back to $\mu = 0$. In short, we only consider deformations with $\sqrt{\kappa}/T < 2.94$. As for the $\mathrm{SW}_{T,\mu}$ model, the dimensionless ratio of the deformation parameter and the temperature will often be denoted by δ, *i. e.* $\delta = \sqrt{\kappa}/T$. The distinction between the δ in different models will always be clear from the context.

To close this section, we review the result of the analysis performed in [113] concerning the dimensionless trace $(\epsilon - 3p)/T^4$ of the energy–momentum tensor of the 1-parameter model at $\mu = 0$. As in the case of the $\mathrm{SW}_{T,\mu}$ model discussed above, the position of the maximum of the dimensionless trace of the energy–momentum tensor is identified with T_c which leads to

$$T_c/\sqrt{\kappa} = 0.394 \,. \tag{4.56}$$

This yields $\kappa \approx 0.200 \,\mathrm{GeV}^2$ as the value realizing $T_c = 176 \,\mathrm{MeV}$.

Now we have all prerequisites in place to start with the analysis of physical observables in our holographic models. In the next section, we will discuss the holographic representation of heavy quarks in the hot medium of the boundary theory, and then study in the remaining chapters of the present part of this thesis the binding energy and the free energy of heavy quark–anti-quark pairs as well as their entropy and internal energy. We will also discuss the free energy, entropy and internal energy of single quarks in the deconfined medium, and finally analyze the free energy of quark–antiquark pairs in more detail by studying its derivatives.

4.2 The Quark–Anti-Quark System

In this section, we will introduce the basic setup that we will be concerned with for the rest of this chapter, namely a heavy quark–anti-quark ($Q\bar{Q}$) pair immersed in the strongly coupled plasmas described by our holographic models. We will describe the kinematic setup and holographic description of the system in this section, and discuss the screening distance as a physical observable that has been studied extensively in holography. A review of this subject can be found *e. g.* in [4], and we will mostly follow this reference here. In the next chapter, we will discuss in detail the computation and renormalization of boundary-theory Wegner–Wilson loops from the holographic models. From expectation values of these loops and a related quantity, we compute the $Q\bar{Q}$ free energy and binding energy, respectively. Most of our further investigations in this part of this thesis are based on the free energy.

Let us begin with the holographic description of a $Q\bar{Q}$ pair in a strongly coupled plasma. Here we consider static, infinitely heavy quarks. An extension to quarks with non-zero velocity in the medium is straightforward; detailed studies of the dependence of the screening distance and the $Q\bar{Q}$ binding energy on the velocity have been performed for instance in [106, 108, 110] and [45] in non-conformal models at vanishing and non-zero chemical potential, respectively. As we will see below, as a natural consequence of the holographic prescription [105] for the computation of expectation values of Wegner–Wilson loops, infinitely heavy quarks in the boundary
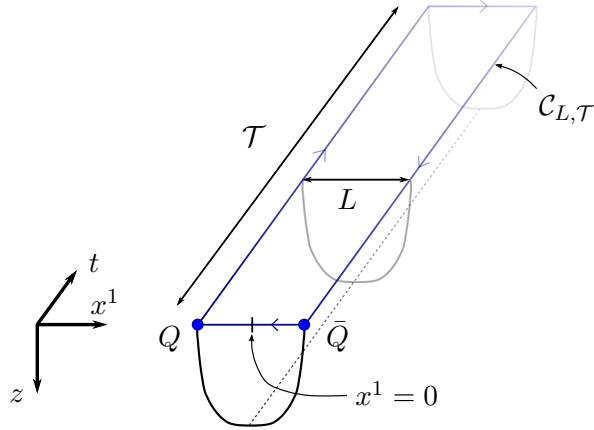
Figure 4.3: Sketch of a static quark–anti-quark pair separated by a distance L along the boundary coordinate direction x^1. The quarks' worldlines are parallel to the time direction t. Also shown is the bulk coordinate direction z and sketches of spacelike slices of the worldsheet of the string connecting the quarks. For later reference, we have also indicated the integration contour $\mathcal{C}_{L,\mathcal{T}}$ used in the integration for the Wegner–Wilson loop (5.1). Its timelike edges are of length $\mathcal{T}$ and coincide with the worldlines of the quarks. Eventually, the limit $\mathcal{T} \to \infty$ will be taken.

theory can be modeled by an open string in the bulk with the endpoints on the four-dimensional boundary. The endpoints can be viewed as point-like quarks.[t] In accordance with the UV/IR relation (2.20) discussed in Sec. 2.2, the quarks' mass is inversely related to the coordinate z of the endpoints of the string and thus diverges if the string endpoints are situated on the boundary $z = 0$. The setup is sketched in Fig. 4.3. The string connecting the quarks 'hangs' into the bulk. As our quarks are static their worldlines are parallel to the time direction t, separated by a spatial distance we call L. The worldlines coincide with the boundary of the string worldsheet.

The dynamics of the string is described by the Nambu–Goto action (2.2) which we reproduce here for convenience,

$$S_{\mathrm{NG}} = -\frac{1}{2\pi\alpha'} \int \mathrm{d}^2\sigma \sqrt{-\det g_{ab}} \,. \tag{4.57}$$

The integral extends over the worldsheet. $1/(2\pi\alpha')$ is the string tension and g_{ab} the induced metric on the worldsheet,

$$g_{ab} = g_{MN} \frac{\partial X^M}{\partial \sigma^a} \frac{\partial X^N}{\partial \sigma^b} \,, \qquad a,b = 0,1 \,, \tag{4.58}$$

---

[t]This treatment is sufficient in our bottom-up models. In a top-down construction, one would introduce 'flavor branes' to which the quarks are confined [127]. One then has to study the embedding of the branes into the ambient spacetime. For a review of this approach see for instance [192].

where g_{MN} is the spacetime metric. We use static gauge for the worldsheet coordinates σ^0, σ^1, *i. e.* $\sigma^0 = t, \sigma^1 = x$, and parametrize the worldsheet as follows,

$$X^M = (t, x, 0, 0, z(x)) \,, \tag{4.59}$$

with boundary conditions (see Fig. 4.3)

$$z(\pm L/2) = 0 \,. \tag{4.60}$$

Working in the general metric (4.10), we derive the following explicit form of the Nambu–Goto action (4.57),

$$S_{\mathrm{NG}} = -\frac{\mathcal{T}}{2\pi\alpha'} \int_{-L/2}^{L/2} \mathrm{d}x \, \mathrm{e}^{2A} \sqrt{h \left(1 + \frac{\mathrm{e}^{2B-2A}}{h} z'^2 \right)} \,, \tag{4.61}$$

where A, B, and h depend on $z(x)$ and we have performed the trivial t-integration. As the Lagrangian in Eq. (4.61) does not depend explicitly on the coordinate x, there is a first integral of the equation of motion associated with the conservation of the Hamiltonian,

$$\xi \equiv \mathrm{const} = \mathcal{H} = z' \frac{\partial \mathcal{L}}{\partial z'} - \mathcal{L} = -\frac{\mathrm{e}^{4A}h}{\mathcal{L}} \,, \tag{4.62}$$

which can be solved for z'. The string configuration will be symmetric with respect to $x \to -x$. It starts out at $x = -L/2, z = 0$, descends into the bulk, and turns around at $x = 0$. In particular, $z'(0) = 0$. We call the coordinate $z(0)$ the turning point, and denote it by z_{t}. Due to the symmetry, to obtain the string configuration it suffices to consider that half of the string which rises up again from its turning point in the bulk at $x = 0, z = z_{\mathrm{t}}$. For that half of the string, we derive from Eq. (4.62) the equation of motion for the embedding $z(x)$,

$$z' = -\mathrm{e}^{A(z)-B(z)} \sqrt{h(z) \left(\frac{\mathrm{e}^{4A(z)}h(z)}{\mathrm{e}^{4A(z_{\mathrm{t}})}h(z_{\mathrm{t}})} - 1 \right)} \,, \tag{4.63}$$

where we have used $z'(0) = 0$ to trade ξ for z_{t}.

In general, Eq. (4.63) has to be solved numerically. Typical solutions are shown in Fig. 4.4, where we plot the string configurations in AdS-Schwarzschild for three different quark separations in the dual $\mathcal{N} = 4$ SYM at vanishing chemical potential. The qualitative properties of the string solutions are the same in all our non-conformal models and at non-zero chemical potential.

As first observed in [193, 194], it turns out that one cannot arbitrarily prescribe the value of the interquark separation L of a bound quark–anti-quark pair. In fact, as can be seen in Fig. 4.4, there is a special value L_{s}. For $Q\bar{Q}$ pairs with $L < L_{\mathrm{s}}$ there are always two string configurations solving the string equations of motion with the boundary conditions (4.60) induced from the position of the quarks. We can uniquely parametrize the possible string configurations using the turning point
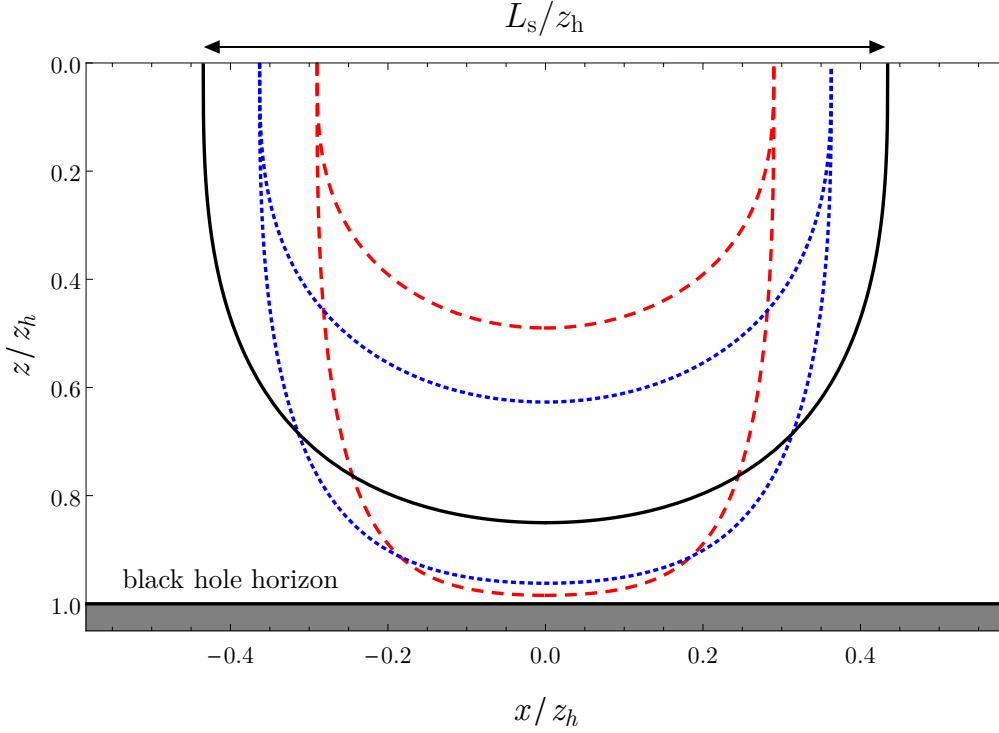
Figure 4.4: String configurations in AdS-Schwarzschild, dual to a heavy quark–anti-quark pair in $\mathcal{N} = 4$ SYM. The quarks can be imagined to be situated at the endpoints of the strings at $z = 0$. For all quark separations L smaller than the screening distance L_{s} there are two string solutions. There is only one for $L = L_{\mathrm{s}}$, and no real solution for $L > L_{\mathrm{s}}$, where the quark interaction is entirely screened. Shown are quark separations $L = 2L_{\mathrm{s}}/3$ (red dashed strings), $L = 5L_{\mathrm{s}}/6$ (blue dotted strings), and $L = L_{\mathrm{s}}$ (black solid string). In $\mathcal{N} = 4$ SYM, $L_{\mathrm{s}} = 0.86912/(\pi T)$ with the temperature T.

z_{t}. Using Eq. (4.63), the distance L is easily expressed as a function of the turning point z_{t},

$$
L(z_{\mathrm{t}}) = 2 \int_0^{L/2} \mathrm{d}x = 2 \int_0^{z_{\mathrm{t}}} \frac{\mathrm{d}z}{-z'} = 2 \int_0^{z_{\mathrm{t}}} \mathrm{d}z \, \mathrm{e}^{B-A} \left[h \left(\frac{\mathrm{e}^{4A} h}{\mathrm{e}^{4A_{\mathrm{t}}} h_{\mathrm{t}}} - 1 \right) \right]^{-1/2} . \tag{4.64}
$$

Here, functions with a subscript 't' are to be evaluated at the turning point z_{t}. We have suppressed in our notation all additional parameters on which the metric functions, and thereby L, can depend, *viz.* temperature, chemical potential, and deformation parameter. The turning point can be located at any depth in the bulk, *i. e.*, z_{t} can take any value between the boundary ($z = 0$) and the black hole horizon

$(z = z_t)$.[u]

As we see in Fig. 4.4, for increasing distance L the turning points of the two string configurations sharing this L approach each other. The string configurations become one degenerate configuration at $L = L_s$. For all $L > L_s$ no real solutions of the string equations of motion exist. In the boundary theory this means that no bound $Q\bar{Q}$ states exist beyond L_s. We therefore call L_s the *screening distance*.[v] The screening distance has been studied extensively, see *e. g.* [45, 107, 108, 110], and, at vanishing chemical potential, enjoys the remarkable universal property that, starting from $\mathcal{N} = 4$ SYM, consistent non-conformal deformations always lead to an increase of its value. In this context, by 'consistent deformation' we mean deformations of AdS_5-Schwarzschild that solve coupled gravity–scalar equations of motion. This was observed numerically in [110] and analytically proven for a large class of small deformations in [113]. At non-zero chemical potential, we have found numerically that said universal behavior continues to hold for small chemical potential, but deviations appear at larger values [45].

It turns out, as we will explicitly verify later, that for given $L < L_s$ the string configuration that has the smaller z_t is thermodynamically preferred over the one with the same L but larger z_t. Thus, the turning point corresponding to the string configuration with $L = L_s$, call it $z_{t,max}$, is the 'deepest' turning point that still yields a stable string configuration. For instance, in Fig. 4.4, the stable string configurations are the black string configuration and all string configurations on its 'inside', *i. e.* closer to the boundary. We will in the following concentrate on the string configurations with $z_t \leq z_{t,max}$. We emphasize that this does not imply any restriction on the admissible values of L.

Now that we have laid out the holographic description of the string connecting the $Q\bar{Q}$ pair, in the next chapter we begin with our discussion of physical observables. We will extract the $Q\bar{Q}$ free energy and binding energy from the bulk string configuration, and in particular discuss in detail the necessary renormalization of the Wegner–Wilson loop on the gravity side.

---

[u]The turning point could no longer be chosen freely on $[0, z_h]$ if we were to consider moving quarks here. For further details in the context of our models see [45].

[v]The screening distance should not be confused with the (Debye) screening *length*. The latter is defined as the inverse of the Debye screening mass and parametrizes the exponential fall-off of the free energy that is seen for instance in lattice studies (*e. g.* [195, 196]). A holographic determination of the screening length in $\mathcal{N} = 4$ SYM can be performed by analyzing the spectrum of supergravity modes that can be exchanged between well-separated strings in the bulk [197]. However, for our deformed, non-conformal models an unique, well-defined prescription is not known.

5 Heavy-Quark Energies

In the previous section 4.2, we have summarized the basic holographic description of a heavy quark–anti-quark pair. We now study different energies associated with the interaction of the heavy quark–anti-quark pair. In the first section 5.1, we discuss the holographic computation of the free energy of this system. A second observable related to a heavy $Q\bar{Q}$ pair is a quantity often called a potential in the gauge/gravity literature. As we will discuss, this observable can be thought of as the binding energy of the $Q\bar{Q}$ pair. It can be computed holographically in a similar way to the free energy, and we will study these computations in detail. In the course of these computations, some renormalization has to be performed to extract finite quantities. In practice, one has to subtract two bulk quantities that diverge due to their near-boundary behavior. There are different ways in which this subtraction is done in the gauge/gravity literature. We will briefly review these procedures, and point out a crucial property that any subtraction scheme used for the computation of the free energy must obey. We will then advocate a subtraction scheme that can be used in any holographic model whose metric is asymptotically AdS, and use it to compute the free energy. Furthermore, to illustrate these general considerations, in Secs. 5.2 and 5.3 we will compare the free energy to lattice QCD calculations on the one hand, and to the binding energy on the other hand. Moreover, in those sections we will study the dependence of the free and binding energies on the chemical potential as well as the impact of the introduction of non-conformality on these observables.

In the subsequent section 5.4 we will use the fact that the free energy is a thermodynamic potential and compute the associated entropy and internal energy. Finally, in Sec. 5.5 we will study the free energy and the associated entropy and internal energy of single heavy quarks in the strongly coupled plasmas described by our models. In both of these sections, we will in particular investigate the changes relative to the behavior in $\mathcal{N} = 4$ SYM introduced by the deformation, searching for indications of universal behavior.

5.1 Free Energy versus Binding Energy

Let us start with the discussion of the heavy quark–anti-quark free energy on the field theory side. We are interested in the expectation value of a Wegner–Wilson-loop operator in the gauge-theory medium, defined as

$$W(\mathcal{C}) = \operatorname{tr} \mathcal{P} \exp \left(\mathrm{i} \oint_{\mathcal{C}} \mathrm{d}x^{\mu} A_{\mu}(x) \right) . \tag{5.1}$$

Here, $\mathcal{C}$ is a closed contour in spacetime, $A_\mu(x) = A_\mu^a(x)T^a$ is the non-Abelian gauge field where T^a are the generators in the representation that the trace tr is taken over. $\mathcal{P}$ denotes path ordering. For our purposes, the integration contour to consider is a rectangular contour $\mathcal{C}_{L,\mathcal{T}}$, made up by the worldlines of length $\mathcal{T}$ of the heavy quarks and two small segments along the spacelike direction in which they are separated by the distance L, see Fig. 4.3. The Wegner–Wilson loop is a gauge-invariant object that in particular encodes the free energy of the $Q\bar{Q}$ pair. To wit, in the limit of infinite temporal extent of the contour, $\mathcal{T} \to \infty$, we have the relation

$$\langle W(\mathcal{C}_{L,\mathcal{T}}) \rangle \sim \exp\left(-\mathrm{i}F_{Q\bar{Q}}(L)\mathcal{T}\right), \qquad \mathcal{T} \to \infty, \tag{5.2}$$

where $F_{Q\bar{Q}}(L)$ is the $Q\bar{Q}$ free energy [198–200].[w] The expectation value is to be taken for a thermal state of the medium surrounding the quarks. This introduces the dependence of $F_{Q\bar{Q}}$ in Eq. (5.2) on the temperature and chemical potential that characterize the medium. The relation (5.2) holds up to an infinite renormalization constant that we will discuss in the context of the holographic computation below.

Obviously, the problem now is to compute the expectation value of the Wegner–Wilson loop on the gravity side. The basic prescription was given by Maldacena [105]; see also [204]. From the bulk perspective, the integration contour $\mathcal{C}$ coincides with the boundary of the worldsheet of the string dual to the quarks, *cf.* our discussion in Sec. 4.2. Then, the expectation value of the Wegner–Wilson loop is related to the on-shell string action by

$$\langle W(\mathcal{C}) \rangle \sim \exp\left(\mathrm{i}S_{\mathrm{NG}}[\mathcal{C}]\right), \tag{5.3}$$

with $S_{\mathrm{NG}}[\mathcal{C}]$ the extremal Nambu–Goto action of the string. This is the saddle-point approximation of the more general statement where on the right-hand side we would have a path integral over all string configurations in the bulk with the prescribed boundary conditions [105].

From the equations (5.2) and (5.3) it follows that the $Q\bar{Q}$ free energy can be computed holographically from

$$F_{Q\bar{Q}}(L) \sim -\frac{S_{\mathrm{NG}}[\mathcal{C}_{L,\mathcal{T}}]}{\mathcal{T}}, \qquad \mathcal{T} \to \infty. \tag{5.4}$$

This relation still needs to be renormalized. Let us now discuss the procedure on the gravity side. For our system, an expression for $S_{\mathrm{NG}}[\mathcal{C}_{L,\mathcal{T}}]$ can be obtained by plugging $z'(x)$ from the equation of motion (4.63) into the action functional (4.61).

---

[w]More precisely, recent studies starting with [201] have argued that in QCD the real-time Wegner–Wilson loop in the limit $\mathcal{T} \to \infty$ gives rise to an effective quark potential that is in general complex. However, the real part of this potential appears to coincide [202] with the $Q\bar{Q}$ (singlet) free energy that is defined from a Euclidean-time Wegner–Wilson loop. Indeed, this seems to be confirmed by lattice QCD calculations which reconstruct the real-time potential from the Euclidean-time spectral function (see *e. g.* [203]). Therefore, we call the quantity extracted from the real-time Wegner–Wilson loop via the holographic procedure discussed in the following the $Q\bar{Q}$ free energy, and, in accordance with the literature, interpret it as such.

After rewriting the integration over the worldsheet coordinate x as an integration over the bulk coordinate z we obtain

$$S_{\text{NG}}[\mathcal{C}_{L,\mathcal{T}}] = -\frac{\mathcal{T}}{\pi\alpha'} \int_0^{z_t} dz\, e^{A(z)+B(z)} \sqrt{\frac{e^{4A(z)}h(z)}{e^{4A(z)}h(z) - e^{4A(z_t)}h(z_t)}}\,. \tag{5.5}$$

Recall from Eq. (4.64) that the turning point z_t is directly related to the $Q\bar{Q}$ distance L. As it stands, this expression is divergent. For all our models, and in fact for all models whose metric approaches the AdS metric asymptotically, as $z \to 0$, the first factor e^{A+B} is asymptotic to L_{AdS}^2/z^2, whereas the square root approaches unity asymptotically. Thus, we have a divergence from the lower integral limit, which can be regularized by restricting the integration to start a small distance ε away from the boundary. We thus write for the regularized action

$$S_{\text{NG}}^{(\text{reg})}[\mathcal{C}_{L,\mathcal{T}}] = -\frac{\mathcal{T}}{\pi\alpha'} \int_\varepsilon^{z_t} dz\, e^{A+B} \sqrt{\frac{e^{4A}h}{e^{4A}h - e^{4A_t}h_t}} \sim -\frac{\mathcal{T} L_{\text{AdS}}^2}{\pi\alpha'} \left(\frac{1}{\varepsilon} + \dots\right)\,, \tag{5.6}$$

using a subscript 't' on functions to indicate their evaluation at the turning point z_t. The divergence is a pole $\sim 1/\varepsilon$. It appears because the string endpoints are situated at the boundary $z = 0$, the holographic realization of the infinite-quark-mass limit, *cf.* our discussion in Sec. 4.2 above. Subtracting an appropriate (infinite) quantity ΔS, we can cast Eq. (5.4) in an operational form for the computation of the renormalized free energy,

$$F_{Q\bar{Q}}^{(\text{ren})}(L) = \lim_{\mathcal{T}\to\infty} \left(-\frac{S_{\text{NG}}^{(\text{reg})}[\mathcal{C}_{L,\mathcal{T}}] - \Delta S}{\mathcal{T}}\right)\,. \tag{5.7}$$

This expression tacitly includes the limit $\varepsilon \to 0$ that removes the regulator. Henceforth, we will drop the specification 'ren' and simply write $F_{Q\bar{Q}}$ for the renormalized free energy; likewise, we will drop the superscript 'reg'. It remains to specify the subtraction ΔS.

There are different choices for ΔS that have been used in the literature so far:

- Refs. [193] and [194] first computed expectation values of Wilson loops at finite temperature in AdS/CFT. They subtract twice the action of a straight string stretching from the boundary at $z = 0$ to the black hole horizon at $z = z_h$. This is the commonly used procedure in the literature, also in non-conformal theories, see for instance the review [4] and references therein.

- In contrast to this method, in Ref. [205] the real part of the Nambu–Goto action for infinite $Q\bar{Q}$ distance L is subtracted. Given that there are no real solutions to the string equation of motion for $L > L_s$, the authors of [205] continue the string configuration into the complex domain. This procedure was recently applied *e. g.* in [206].

These two procedures differ from each other only at non-zero temperature. Thus, for $T \to 0$ both reduce to the procedure used in the first papers on the computation of the heavy-quark free energy (or heavy-quark potential, at $T = 0$) in AdS/CFT [105, 204] which work at zero temperature and where subtracting ΔS indeed amounts to subtracting the infinite quark-mass contribution.

We argue in the following that neither of these procedures is appropriate for the calculation of the $Q\bar{Q}$ free energy. Before we introduce the subtraction that we are going to use to compute the free energy, let us discuss our expectations for this quantity on the field theory side. For small distances L, we expect the thermodynamic variables T and μ, as well as a possible deformation scale, to have negligible effect on the $Q\bar{Q}$ interaction. This argument is backed by data from lattice QCD, *e. g.* [195, 196], where indeed for $LT \ll 1$ the free energy becomes independent of T, see also [207]. Now consider Eq. (5.7) for the holographic computation of the free energy. Effectively, the first term $S_{\mathrm{NG}}[\mathcal{C}_{L,\mathcal{T}}]$ becomes independent of any scale other than L for very small L. This is straightforward to see in the bulk picture for all spacetimes that are asymptotically AdS, which in particular includes all our models. Note that small L means a small turning point z_{t}. (Recall that of the two string configurations corresponding to given a L, we choose the one with the turning point closer to the boundary, *i. e.* the one with smaller z_{t}. We will explicitly verify below that indeed that string configuration is thermodynamically preferred over the one with larger z_{t}.) Thus, a string corresponding to very small L only probes the part of the spacetime that is essentially fixed by the boundary conditions and does not depend on the temperature or chemical potential, or a possible deformation parameter, which all manifest themselves significantly only deeper in the bulk. We will numerically verify this bulk argument when discussing the free energy in the following sections.

Now, if $F_{Q\bar{Q}}$ should not depend for small L on T and μ, or a potential deformation scale, the subtraction ΔS should not depend on these scales either. (Moreover, ΔS should not depend on L.) We therefore advocate a minimal choice ΔS_{min} that just subtracts the $1/\varepsilon$ pole in the regularized Nambu–Goto action (5.6), explicitly,

$$\Delta S_{\mathrm{min}} \equiv -\frac{\mathcal{T}L_{\mathrm{AdS}}^2}{\pi\alpha'} \int_\varepsilon^\infty \frac{\mathrm{d}z}{z^2} = -\frac{\mathcal{T}L_{\mathrm{AdS}}^2}{\pi\alpha'} \frac{1}{\varepsilon} \,. \tag{5.8}$$

This can be used in all our models, and more generally, in any model for which the metric asymptotically reduces to AdS. The choice (5.8) makes sure that right-hand side of Eq. (5.7) does in fact yield the free energy, and that the latter does not depend on T and μ (and neither on a possible deformation scale) for small $Q\bar{Q}$ distances L. We note that essentially equivalent subtractions have been used before in the finite-temperature context ([134, 172, 208–210], but despite a thorough literature review that list may not be exhaustive), and the authors of [197] comment as a side remark that using a temperature-dependent renormalization is not correct. However, to the best of our knowledge the full implications of the details of the renormalization procedure and the distinctions of the quantities derived by different procedures have not yet been discussed in the literature so far. We fill this apparent

gap in the literature and, in particular, we will study thermodynamic quantities related to the free energy that crucially require the use of a temperature-independent renormalization.

Finally, using formula (5.7) with the subtraction (5.8) we find the following relation for the free energy in our general metric,

$$
\frac{\pi F_{Q\bar{Q}}(z_\mathrm{t})}{\sqrt{\lambda}} = \int_0^{z_\mathrm{t}} \mathrm{d}z \left[\frac{\mathrm{e}^{A+B}}{L_\mathrm{AdS}^2} \sqrt{\frac{\mathrm{e}^{4A} h}{\mathrm{e}^{4A} h - \mathrm{e}^{4A_\mathrm{t}} h_\mathrm{t}}} - \frac{1}{z^2} \right] - \frac{1}{z_\mathrm{t}} \, . \tag{5.9}
$$

Here, we have used the abbreviation $\sqrt{\lambda} = L_\mathrm{AdS}^2/\alpha'$, see Eq. (4.16).

The quantity computed via the commonly used subtraction procedure (the first one in the list above), the difference of the string action of the 'U'-shaped string connecting the quarks and twice the string action of a straight string stretching from the boundary to the horizon,

$$
E_{Q\bar{Q}}(L) = \lim_{\mathcal{T} \to \infty} \left(-\frac{S_\mathrm{NG}[\mathcal{C}_{L,\mathcal{T}}] - 2 S_\mathrm{NG}[\text{straight string}]}{\mathcal{T}} \right), \tag{5.10}
$$

can be understood as a difference of free energies. Namely, by inserting a 0 in the form $-\Delta S_\mathrm{min} + \Delta S_\mathrm{min}$ with the minimal ΔS_min defined in Eq. (5.8) we can reinterpret this quantity as

$$
\begin{aligned}
E_{Q\bar{Q}}(L) &= \lim_{\mathcal{T} \to \infty} \left[-\frac{(S_\mathrm{NG}[\mathcal{C}_{L,\mathcal{T}}] - \Delta S_\mathrm{min}) - (2 S_\mathrm{NG}[\text{straight string}] - \Delta S_\mathrm{min})}{\mathcal{T}} \right] \\
&= F_{Q\bar{Q}} - F_{Q\,;\,\bar{Q}} \, ,
\end{aligned}
\tag{5.11}
$$

where we have used Eq. (5.7) and the analogous relation for the free energy of two non-interacting heavy quarks, which we have denoted by $F_{Q\,;\,\bar{Q}}$. The latter quantity can be written as $F_{Q\,;\,\bar{Q}} = 2 F_Q$ where we might call F_Q the free energy of a single heavy quark. More explicitly, in our general metric we define F_Q by the relation

$$
\frac{\pi F_Q}{\sqrt{\lambda}} = \frac{1}{2} \left[\int_0^{z_\mathrm{h}} \mathrm{d}z \left(\frac{\mathrm{e}^{A+B}}{L_\mathrm{AdS}^2} - \frac{1}{z^2} \right) - \frac{1}{z_\mathrm{h}} \right], \tag{5.12}
$$

where we have again used the abbreviation $\sqrt{\lambda} = L_\mathrm{AdS}^2/\alpha'$. We will discuss the single-quark free energy further in Sec. 5.5.

Let us turn back to $E_{Q\bar{Q}}(L)$. We see from Eq. (5.11) that $E_{Q\bar{Q}}(L)$ is an energy difference. It vanishes when the free energy of the interacting $Q\bar{Q}$ pair equals the free energy of a pair of free quarks. We can thus interpret $E_{Q\bar{Q}}(L)$ (or more precisely, its negative) as the binding energy of the $Q\bar{Q}$ pair. Explicitly, for the binding energy we obtain the relation

$$
\frac{\pi E_{Q\bar{Q}}(z_\mathrm{t})}{\sqrt{\lambda}} = \int_0^{z_\mathrm{t}} \mathrm{d}z \, \frac{\mathrm{e}^{A+B}}{L_\mathrm{AdS}^2} \left[\sqrt{\frac{\mathrm{e}^{4A} h}{\mathrm{e}^{4A} h - \mathrm{e}^{4A_\mathrm{t}} h_\mathrm{t}}} - 1 \right] - \int_{z_\mathrm{t}}^{z_\mathrm{h}} \mathrm{d}z \, \frac{\mathrm{e}^{A+B}}{L_\mathrm{AdS}^2} \, . \tag{5.13}
$$

The binding energy has been extensively studied as a finite-temperature quark–anti-quark potential by means of the gauge/gravity duality, see for instance [107, 109, 110, 112, 134, 162, 193, 194, 211]. These references include investigations in $\mathcal{N} = 4$ SYM (in the strict limit of infinite 't Hooft coupling λ as well as including first-order corrections in an expansion in $1/\lambda$ [112]) and in deformed models, at vanishing and non-zero temperature, and with the $Q\bar{Q}$ pair stationary or moving with respect to the rest frame of the background medium (including analyses of the dependence of the free energy on the angle of the $Q\bar{Q}$ dipole to its velocity [107, 110]). Furthermore, $E_{Q\bar{Q}}$ has been studied in holographic models of anisotropic strongly coupled plasma [212–214], as well as at non-zero chemical potential in $\mathcal{N} = 4$ SYM [108]. Within our non-conformal models, we have previously undertaken a systematic study of possible universal behavior of $E_{Q\bar{Q}}$ at non-zero chemical potential [45].

We will see in the following sections that the behavior of the binding energy is fundamentally different from that of the free energy. Moreover, we will find that the free energy in $\mathcal{N} = 4$ SYM, as in the non-conformal models, behaves qualitatively like the $Q\bar{Q}$ free energy computed in lattice QCD, whereas the binding energy does not. This corroborates our general arguments for the use of the subtraction (5.8) for the computation of the free energy.

5.2 Free Energy and Binding Energy in $\mathcal{N} = 4$ Supersymmetric Yang–Mills Theory

In the previous section, we have defined the $Q\bar{Q}$ free energy $F_{Q\bar{Q}}$ and binding energy $E_{Q\bar{Q}}$ in general holographic models, see Eqs. (5.9) and (5.13), respectively. Before proceeding to a discussion of these quantities in our non-conformal models, in this section we will make the general discussion and formulae more concrete by studying the simplest case, $\mathcal{N} = 4$ SYM. Furthermore, we will compare the free energy obtained in $\mathcal{N} = 4$ SYM to lattice data and find qualitative agreement.

For vanishing chemical potential, we can evaluate the integrals in the formulae for $F_{Q\bar{Q}}$, $E_{Q\bar{Q}}$, and L explicitly, so let us start with the case $\mu = 0$. Using the formula (5.13) for the binding energy $E_{Q\bar{Q}}(L)$ with the AdS-Schwarzschild metric (4.20), we obtain

$$\frac{\pi E_{Q\bar{Q}}(z_\mathrm{t})}{\sqrt{\lambda}} = -\frac{\sqrt{\pi}\,\Gamma\left(\frac{3}{4}\right)}{\Gamma\left(\frac{1}{4}\right)}\, {}_2\mathrm{F}_1\left(-\frac{1}{2}, -\frac{1}{4}; \frac{1}{4}; \frac{z_\mathrm{t}^4}{z_\mathrm{h}^4}\right)\frac{1}{z_\mathrm{t}} + \frac{1}{z_\mathrm{h}}, \tag{5.14}$$

where ${}_2\mathrm{F}_1$ is the (Gaußian) hypergeometric function. An equivalent formula has been obtained in [215]. Note that, working in $\mathcal{N} = 4$ SYM, $\sqrt{\lambda}$ which we defined as a shorthand for the ratio of bulk quantities L_AdS^2/α' is in fact the 't Hooft coupling $\sqrt{\lambda} = g_\mathrm{YM}^2 N_\mathrm{c}$. The temperature is determined by $T = 1/(\pi z_\mathrm{h})$, see Eq. (4.21).

The temperature-dependent term $1/z_\mathrm{h}$ in Eq. (5.14) is entirely due to the contribution $2S_\mathrm{NG}[\text{straight string}]$ of the straight strings stretching from the boundary to the horizon, see Eq. (5.10). It is due to this term that $E_{Q\bar{Q}}$ depends on T for small interquark distances. As discussed at length above, this should not be the case

for the free energy $F_{Q\bar{Q}}$, and $F_{Q\bar{Q}}$ indeed lacks that term. Explicitly, we find from Eq. (5.9) with the AdS-Schwarzschild metric (4.20),

$$\frac{\pi F_{Q\bar{Q}}(z_\mathrm{t})}{\sqrt{\lambda}} = -\frac{\sqrt{\pi}\,\Gamma\left(\frac{3}{4}\right)}{\Gamma\left(\frac{1}{4}\right)}\, {}_2\mathrm{F}_1\left(-\frac{1}{2}, -\frac{1}{4}; \frac{1}{4}; \frac{z_\mathrm{t}^4}{z_\mathrm{h}^4}\right)\frac{1}{z_\mathrm{t}}\,, \tag{5.15}$$

valid for non-zero temperature but vanishing chemical potential. Since the positive term $1/z_\mathrm{h}$ is absent, $F_{Q\bar{Q}}$ will be smaller than $E_{Q\bar{Q}}$ for any $T>0$. In the limit $T\to 0$, which is $z_\mathrm{h}\to\infty$ on the gravity side, $F_{Q\bar{Q}}$ and $E_{Q\bar{Q}}$ coincide.

We have expressed both the binding energy and the free energy in terms of the turning point z_t. The latter is related to the interquark distance L via the explicit relation

$$L(z_\mathrm{t}) = \frac{2\sqrt{\pi}\,\Gamma\left(\frac{7}{4}\right)}{3\,\Gamma\left(\frac{5}{4}\right)}\sqrt{1-\frac{z_\mathrm{t}^4}{z_\mathrm{h}^4}}\; {}_2\mathrm{F}_1\left(\frac{1}{2}, \frac{3}{4}; \frac{5}{4}; \frac{z_\mathrm{t}^4}{z_\mathrm{h}^4}\right)z_\mathrm{t}\,, \tag{5.16}$$

derived from the general expression (4.64). This explicit form has also been obtained in [215].

Before discussing the case of non-zero chemical potential, let us consider the vacuum $T=0, \mu=0$. As discussed above, in this limit the free energy and the binding energy coincide. For $T=0, \mu=0$ it is possible to explicitly solve Eq. (5.16) for z_t and compute $V_{Q\bar{Q}}(L) \equiv F_{Q\bar{Q}}(L) = E_{Q\bar{Q}}(L)$, the heavy quark–anti-quark potential, as a function of L,

$$V_{Q\bar{Q}}(L) = -\frac{4\pi^2\sqrt{\lambda}}{\Gamma^4\left(\frac{1}{4}\right)L}\,, \tag{5.17}$$

which has been first obtained by Maldacena [105]. The strict proportionality $V_{Q\bar{Q}} \propto 1/L$ reflects the absence of any other dimensionful scale at $T=0, \mu=0$.

Let us now study the general case $T\neq 0, \mu\neq 0$ and investigate how the free energy behaves as opposed to the binding energy. We can no longer evaluate the integrals in Eqs. (4.64), (5.9), and (5.13) explicitly, but they can easily be evaluated numerically. We have used the `NIntegrate` routine of MATHEMATICA. In Fig. 5.1, we plot $F_{Q\bar{Q}}(L)$ and $E_{Q\bar{Q}}(L)$ in $\mathcal{N}=4$ SYM for varying temperature and chemical potential. Both $F_{Q\bar{Q}}(L)$ and $E_{Q\bar{Q}}(L)$ actually have two values for every distance L smaller than the screening distance L_s, *i.e.*, both functions have two branches. This is a consequence of the fact that there are two string configurations for every distance $L < L_\mathrm{s}$, as discussed in Sec. 4.2. The inset in the upper panel in Fig. 5.1a displays the full $F_{Q\bar{Q}}(L)$ and $E_{Q\bar{Q}}(L)$, showing their lower and upper branches. The lower branches correspond to the string configurations that stay closer to the boundary. Since their free energy is smaller than that of the string configurations protruding farther into the bulk, they are thermodynamically preferred. In addition, it turns out that the solutions that protrude farther into the bulk possess runaway modes when subjected to small perturbations whereas the string configurations that stay closer to the boundary are stable against such perturbations [216]. From now on,
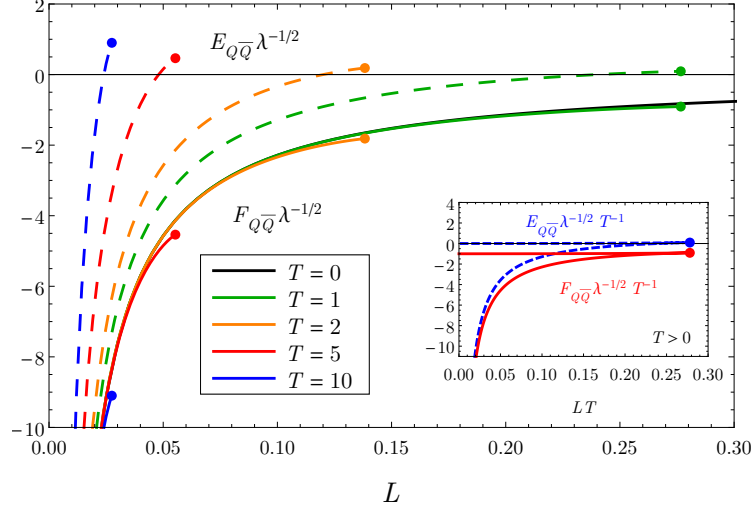
(a) Free energy (solid lines) and binding energy (dashed lines) for varying temperature T and vanishing chemical potential, restricted to the stable branch (main plot) and including both the stable and the unstable branch (inset, $T > 0$), see text. For $T = 0$, both $F_{Q\bar{Q}}$ and $E_{Q\bar{Q}}$ reduce to the same Coulombic potential (solid black curve) given by Eq. (5.17). In the main plot, we express all dimensionful quantities in AdS units specified by $L_{\mathrm{AdS}} = 1$, and in the inset in units of temperature.
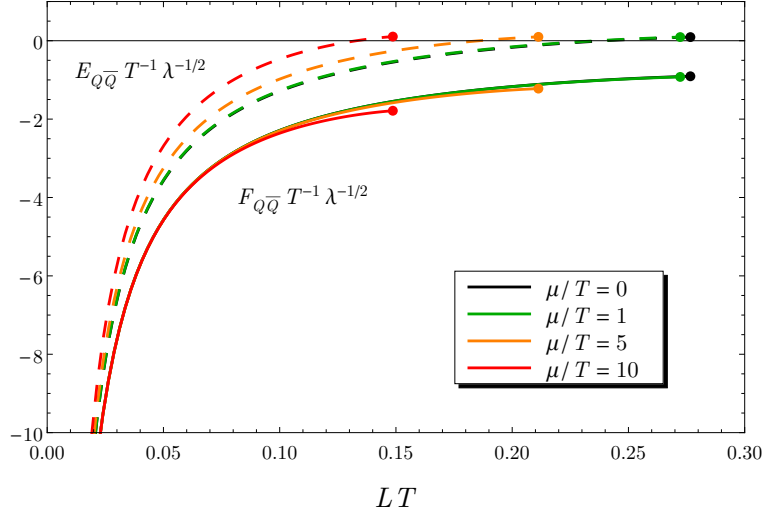
(b) $F_{Q\bar{Q}}(L)/\sqrt{\lambda}$ (solid lines) and $E_{Q\bar{Q}}(L)/\sqrt{\lambda}$ (dashed lines) for fixed temperature and varying chemical potential μ. All dimensionful quantities are expressed in units of the temperature.

Figure 5.1: Free energy $F_{Q\bar{Q}}(L)$ and binding energy $E_{Q\bar{Q}}(L)$ in $\mathcal{N} = 4$ SYM under variations of the thermodynamic variables. Except for the plot in the inset, we have reduced both $F_{Q\bar{Q}}$ and $E_{Q\bar{Q}}$ to their stable branches. The dots on the endpoints of the curves mark the screening distance.

we will always restrict ourselves to the stable, lower branches of both $F_{Q\bar{Q}}$ and $E_{Q\bar{Q}}$, and accordingly we have not plotted the upper branches in the main plots in Fig. 5.1.

For any value of T and μ both $F_{Q\bar{Q}}$ and $E_{Q\bar{Q}}$ become Coulombic at small interquark distances. This signals a restoration of conformality in the UV as the medium-induced scales T and μ decouple. However, as we can nicely see from Fig. 5.1, the free energy becomes independent of the thermodynamic variables T and μ for small L, whereas the binding energy does not. As anticipated, it contains an L-independent but T- and μ-dependent piece. We now turn to a more detailed comparison. In Fig. 5.1a the dependence of $F_{Q\bar{Q}}$ and $E_{Q\bar{Q}}$ on the temperature at vanishing chemical potential is shown. The qualitative behavior of the two energies is different. For $T = 0$, both $F_{Q\bar{Q}}(L)$ and $E_{Q\bar{Q}}(L)$ reduce to the same function, namely the zero-temperature potential given in Eq. (5.17). However, for increasing T, the free energy at fixed distance L becomes smaller as compared to the $(T = 0)$-limit, whereas $E_{Q\bar{Q}}$ increases. In Fig. 5.1b the free energy and binding energy are shown at a fixed temperature and varying chemical potential. We observe that the effect of increasing the chemical potential is qualitatively analogous to the effect of increasing the temperature seen in Fig. 5.1a. The free energy decreases whereas $E_{Q\bar{Q}}$ increases. However, the quantitative effect of increasing μ appears to be smaller than that of increasing T, as we will make more explicit later on. The behavior of $E_{Q\bar{Q}}$ is consistent with our interpretation of it as a (negative) binding energy. Increasing T or μ at a fixed distance L, the modulus of the binding energy decreases. In other words, the binding of the quarks becomes weaker. This is natural since we would expect a hotter or denser medium to lead to stronger screening of the interaction. Accordingly, also the screening distance becomes smaller for increasing T or μ.

For any non-zero temperature or chemical potential, at some value $L_c < L_s$ of the interquark separation, the binding energy vanishes, $E_{Q\bar{Q}}(L_c) = 0$. Thus, at this distance the free energy of the bound $Q\bar{Q}$ pair equals the free energy of an unbound $Q\bar{Q}$ pair, while for larger distances the free energy of an unbound pair is smaller than that of a bound pair. However, this does not necessarily imply that the $Q\bar{Q}$ pair dissociates at this length scale. In fact, the dynamic evolution of the string configurations is beyond the approximation underlying Eq. (5.3) which is our starting point. The $Q\bar{Q}$ pair might well be metastable even beyond L_c. For further discussion of this issue see, *e. g.*, [110, 216].

At this point, it is sensible to compare the qualitative behavior of the free energy in $\mathcal{N} = 4$ SYM to that of QCD. In lattice QCD, the heavy-quark free energy can be extracted from a correlator of Polyakov loops. This is done for instance in [195, 196]; we show data from quenched lattice QCD [195] simulations in Fig. 5.2. The temperature is varied and all chosen temperatures are above T_c. We note two characteristics of the behavior of the free energy. First, for small interquark distances r (L in our notation) the free energy becomes independent of the temperature. Second, the free energy decreases with increasing T, *i. e.*, data points for some $T_2 > T_1$ always lie below those for T_1. Both these characteristics are also present in the free energy computed in $\mathcal{N} = 4$ SYM, as discussed above. Furthermore, they are also present
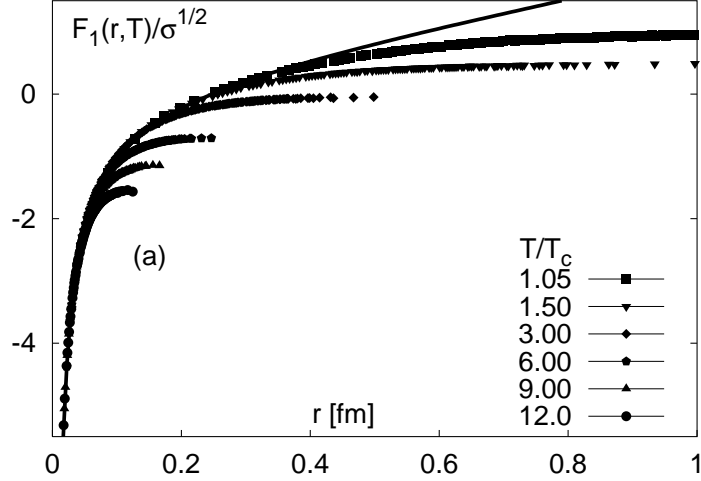
Figure 5.2: Heavy-quark free energy at various temperatures above T_c, computed in quenched lattice QCD; the figure is taken from [195]. The solid line is the ($T = 0$) heavy-quark potential. The string tension σ is chosen as $\sqrt{\sigma} = 420\,\text{MeV}$.

in our non-conformal models that will be discussed in the next section. In contrast to this, the quantity $E_{Q\bar{Q}}$ behaves differently. It rather increases with increasing T. These findings further substantiate our general arguments regarding the choice (5.8) of the subtraction ΔS. Using it in Eq. (5.7) we indeed obtain the proper $Q\bar{Q}$ free energy.

5.3 Free Energy and Binding Energy in Non-Conformal Models

In the previous section, we have compared the behavior of the free energy and the binding energy in strongly coupled $\mathcal{N} = 4$ SYM at non-zero temperature and chemical potential which is dual to AdS gravity with a Reissner–Nordström black brane. We have validated the procedure that we have advocated in Sec. 5.1 for the holographic calculation of the $Q\bar{Q}$ free energy. In this section we study the free energy in all our non-conformal models both at vanishing and non-zero chemical potential. Moreover, we compare the free energy and the binding energy in one of our non-conformal models in order to explore the consequences of our general arguments in a more complicated bulk theory than AdS_5-Reissner–Nordström discussed in the previous section.

In Fig. 5.3 we show the free energy in our non-conformal models at a fixed temperature and a large value $\delta = 2.5$ of the dimensionless ratios of the deformation parameters and the temperature, $\delta = c/T$ and $\delta = \sqrt{\kappa}/T$ for the $\text{SW}_{T,\mu}$ model and the 1-parameter models, respectively. We vary the chemical potential over a substantial range. For comparison, we have also plotted $F_{Q\bar{Q}}$ in $\mathcal{N} = 4$ SYM (black
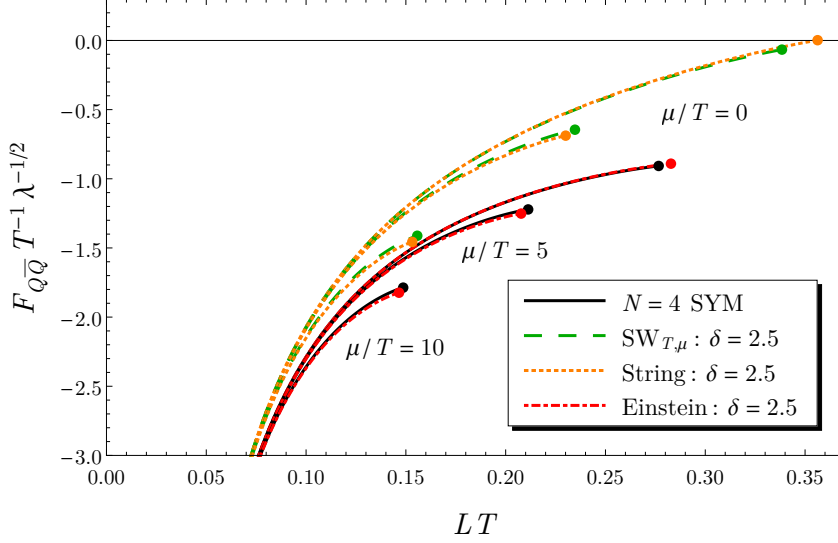
Figure 5.3: Free energy $F_{Q\bar{Q}}/(\sqrt{\lambda}T)$ in $\mathcal{N} = 4$ SYM and non-conformal models at large dimensionless deformation-parameter-to-temperature ratios δ, for a fixed temperature and varying chemical potential. The different models are color-coded. The four curves with the rightmost endpoints correspond to $\mu/T = 0$, those four with the middle endpoints to $\mu/T = 5$, and the remaining four curves to $\mu/T = 10$. To be able to discern details of the free energy close to the screening distance (marked by dots), we do not show the curves for very small distances. For small LT, all shown curves converge to one universal curve.

curves).

First of all, we note that in all non-conformal models the qualitative behavior of the free energy upon an increase of the chemical potential is the same as in $\mathcal{N} = 4$ SYM which we discussed in the previous section. For a given quark separation LT the free energy decreases, and the curves for different μ approach one universal curve for small distances. Furthermore, for quark separations L somewhat smaller than those shown in Fig. 5.3, which we have left out of the plot to not obscure the details close to the screening distance (marked by the dots), even for different models the free energy approaches a single, apparently universal curve. That curve is given by the vacuum potential $V_{Q\bar{Q}}$ of $\mathcal{N} = 4$ SYM, see Eq. (5.17). This verifies our argument using the bulk picture in our general discussion in Sec. 5.1.

Since the curves for all our models approach a single universal curve for small quark separation, we can sensibly compare the free energy in different theories.[x] Thus, let us compare the different non-conformal models to $\mathcal{N} = 4$ SYM. First

---

[x]*A priori*, the free energy is only defined up to an overall constant offset. However, by demanding that the free energy approaches the vacuum potential $V_{Q\bar{Q}}$ for small distances this ambiguity is fixed.

we note that the 1-parameter Einstein-frame model is very robust against non-conformal deformation. The free energy changes only little from $\mathcal{N} = 4$ SYM even at the relatively large deformation considered here. As a side remark, in Fig. 5.3 we can also nicely see a peculiarity of the 1-parameter Einstein-frame models (it also occurs in the one with the minimal choice of the gauge kinetic function) that we have discovered in [45]. For large chemical potentials (roughly if $\mu > \sqrt{\kappa}$) the screening distance is smaller in the consistently deformed 1-parameter Einstein-frame model than in $\mathcal{N} = 4$ SYM at the same temperature and chemical potential. In accordance with this observation and the generic behavior of the free energy that we have seen so far, we further observe that the free energy in the Einstein-frame model at large chemical potential ($\mu/T = 5$ and 10 in the figure) is smaller than in $\mathcal{N} = 4$ SYM. However, the deviation is pretty small.

On the other hand, in both the $\mathrm{SW}_{T,\mu}$ and 1-parameter string-frame models the free energy increases above its value in $\mathcal{N} = 4$ SYM upon introducing non-conformality. This is true both at vanishing and non-zero chemical potential. Combining this with the robustness observed in the Einstein-frame model, $F_{Q\bar{Q}}$ in $\mathcal{N} = 4$ SYM seems to be an approximate lower bound for estimating the free energy of a heavy quark–anti-quark pair, if the latter is normalized such that for small distances it reduces to the $(T = 0)$-potential given in Eq. (5.17).

We now turn to a comparison of the free energy $F_{Q\bar{Q}}$ and the binding energy $E_{Q\bar{Q}}$ in the 1-parameter string-frame model as an example of a consistent non-conformal deformation of $\mathcal{N} = 4$ SYM. This will also allow us to check the statement we just made about the approximate lower bound for the free energy at smaller values of the deformation. In Fig. 5.4 we plot $F_{Q\bar{Q}}$ and $E_{Q\bar{Q}}$ in the 1-parameter string-frame model at vanishing chemical potential for varying dimensionless deformation parameter $\sqrt{\kappa}/T$. We see that in the 1-parameter string-frame model the free energy gradually increases with increasing deformation. Thus, it indeed always stays above its value in $\mathcal{N} = 4$ SYM, even for smaller deformations. The figure also shows that, as mentioned above, the free energy in different theories (corresponding to different values of the deformation) converges upon a single universal curve for small quark separations L.

In contrast to the behavior of the free energy, $E_{Q\bar{Q}}$ decreases with increasing deformation. Thus, the binding of the $Q\bar{Q}$ pair at a given L becomes stronger (recall that $E_{Q\bar{Q}}$ is actually the negative binding energy). We will not study the behavior of the binding energy with respect to the deformation in our other non-conformal models here, as that has been studied in detail in [45]. Let us just note that, as seen in Fig. 5.3 for the free energy, the binding energy $E_{Q\bar{Q}}$, too, behaves very similarly in the $\mathrm{SW}_{T,\mu}$ model and in the 1-parameter string-frame model for which we have shown $E_{Q\bar{Q}}$ in Fig. 5.4. Furthermore, this quantity is very robust in the 1-parameter Einstein-frame model, staying quantitatively close to its counterpart in $\mathcal{N} = 4$ SYM for all values of the deformation parameter. Also, the feature that clearly distinguishes the two quantities $F_{Q\bar{Q}}$ and $E_{Q\bar{Q}}$ from each other turns out to be robust among our non-conformal models: Whereas $F_{Q\bar{Q}}(L)$ at fixed L increases
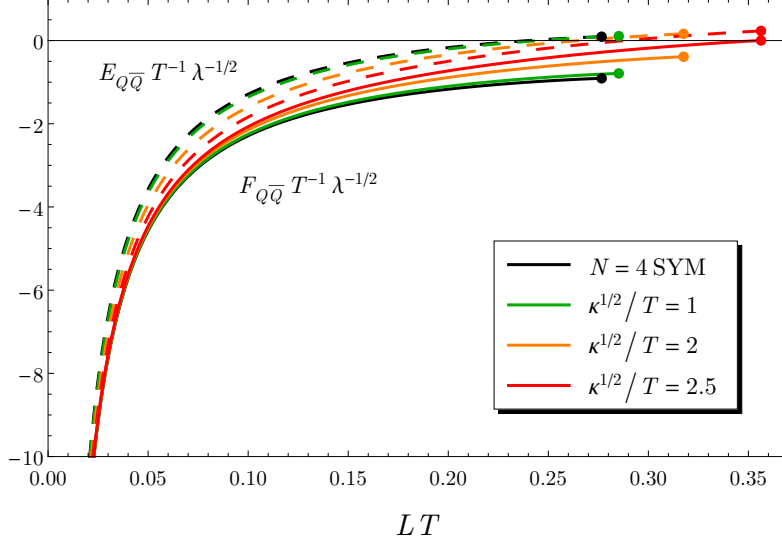
Figure 5.4: Free energy $F_{Q\bar{Q}}$ and binding energy $E_{Q\bar{Q}}$ in $\mathcal{N} = 4$ SYM (black curves) and the 1-parameter string-frame model at fixed temperature and vanishing chemical potential for varying deformation parameter. All dimensionful quantities are measured in units of the temperature.

with increasing non-conformality, $E_{Q\bar{Q}}(L)$ decreases, except for the case of the 1-parameter Einstein-frame model where both quantities almost do not change at all.

This concludes our comparative analysis of the free energy and the binding energy of a heavy quark–anti-quark pair in a hot and dense strongly coupled medium. In the following, we will focus on the free energy. In the next section we will study thermodynamic quantities associated with the free energy, namely the $Q\bar{Q}$ entropy and internal energy. Thereafter, in section 5.5 we will put to use Eq. (5.12) that we derived in our general discussion of the $Q\bar{Q}$ free energy as a definition of the *single-quark* free energy F_Q, and study F_Q and the associated entropy and internal energy. Then, in the subsequent chapters 6 and 7 we will analyze μ- and L-derivatives of the free energy both of which are interesting physical observables on their own.

5.4 Heavy-Quark Entropy and Internal Energy

In previous sections, we have discussed how one computes the heavy-quark free energy holographically and have studied its basic properties in our holographic models. Moreover, we have verified that the quantity we have computed indeed behaves like the free energy computed in lattice QCD. In this section, we will derive formulae for two observables that can be derived from the free energy, *viz.* the heavy-quark entropy and internal energy. Obviously, this crucially depends on the use of the correct subtraction in Eq. (5.7) to in fact obtain the free energy instead of the binding

energy.

Both of these quantities can be computed using standard thermodynamic relations. For simplicity, we will work at vanishing chemical potential in this section. In this case, barring the dependency on the deformation parameter which we always assume to be held constant, the heavy-quark free energy $F_{Q\bar{Q}}(L,T)$ discussed in Sec. 5.1 depends on the interquark distance L and the temperature T of the surrounding medium. Following the definition used in lattice QCD (see for instance [217]), the entropy can be computed as the derivative

$$S_{Q\bar{Q}}(L,T) = -\frac{\partial F_{Q\bar{Q}}(L,T)}{\partial T} \,. \tag{5.18}$$

With the entropy in hand, the internal energy can be obtained from the standard thermodynamic relation

$$U_{Q\bar{Q}}(L,T) = F_{Q\bar{Q}}(L,T) + TS_{Q\bar{Q}}(L,T) \,. \tag{5.19}$$

The explicit computation in our holographic models, where we have the parametric expressions (5.9) for $F_{Q\bar{Q}}$ and (4.64) for the distance L in terms of the bulk length scales z_{t} and z_{h}, is not entirely straightforward. We give details on the computation and an explicit formula for the derivative $\partial F_{Q\bar{Q}}/\partial T$ in Appendix C.

Both the free and the internal energy are phenomenologically interesting as candidates for model potentials for the interaction of heavy quarks in a finite-temperature medium. Model potentials are used for the computation of properties of heavy quarkonia from Schrödinger-like equations in the spirit of potential non-relativistic QCD (pNRQCD; see [125] for a review, and *e. g.* [218] for more recent work including finite-temperature effects). At zero temperature, pNRQCD provides a systematic framework for the derivation of an effective $Q\bar{Q}$ potential. At non-zero temperature the choice of a potential to model the heavy-quark interaction is ambiguous. The internal and the free energy differ from each other due to the entropy contribution, and it is thus worth exploring the behavior of both heavy-quark energies. See also [217, 219, 220] for discussions of heavy-quark energies and potentials in the context of lattice QCD.

Let us now begin with the computation of the $Q\bar{Q}$ entropy and internal energy in our holographic models. In $\mathcal{N} = 4$ SYM, the above formulae (5.18) and (5.19) can be evaluated explicitly based on the expressions (5.15) and (5.16) for $F_{Q\bar{Q}}(z_{\mathrm{t}})$ and $L(z_{\mathrm{t}})$, plugged into Eq. (C.4) in the Appendix. We find the following parametric expressions,

$$\frac{S_{Q\bar{Q}}(z_{\mathrm{t}})}{\sqrt{\lambda}} = \frac{2\sqrt{\pi}\,\Gamma\left(\frac{3}{4}\right)}{\Gamma\left(\frac{1}{4}\right)}\,\frac{z_{\mathrm{h}}}{z_{\mathrm{t}}}\,\frac{5\left(1-\frac{z_{\mathrm{t}}^4}{z_{\mathrm{h}}^4}\right)f_{\mathrm{a}}^2 + \left[3\left(1-\frac{z_{\mathrm{t}}^4}{z_{\mathrm{h}}^4}\right)f_{\mathrm{b}} - 5f_{\mathrm{a}}\right]f_{\mathrm{c}}}{5\left(\frac{z_{\mathrm{h}}^4}{z_{\mathrm{t}}^4}-3\right)f_{\mathrm{a}} + 6\left(1-\frac{z_{\mathrm{t}}^4}{z_{\mathrm{h}}^4}\right)f_{\mathrm{b}}} \,, \tag{5.20}$$

and

$$\frac{U_{Q\bar{Q}}(z_{\mathrm{t}})}{\sqrt{\lambda}} = -\frac{5\,\Gamma\left(\frac{3}{4}\right)}{\sqrt{\pi}\,\Gamma\left(\frac{1}{4}\right)}\frac{1}{z_{\mathrm{t}}}\frac{\left(1 - \frac{z_{\mathrm{t}}^4}{z_{\mathrm{h}}^4}\right)f_{\mathrm{a}}f_{\mathrm{d}}}{5\left(1 - 3\frac{z_{\mathrm{t}}^4}{z_{\mathrm{h}}^4}\right)f_{\mathrm{a}} + 6\frac{z_{\mathrm{t}}^4}{z_{\mathrm{h}}^4}\left(1 - \frac{z_{\mathrm{t}}^4}{z_{\mathrm{h}}^4}\right)f_{\mathrm{b}}}\,, \tag{5.21}$$

where f_{a}, f_{b}, f_{c}, and f_{d} depend on $z_{\mathrm{t}}^4/z_{\mathrm{h}}^4$: we define them as shorthand notation for the functions

$$f_{\mathrm{a}}\left(\frac{z_{\mathrm{t}}^4}{z_{\mathrm{h}}^4}\right) = {}_2\mathrm{F}_1\left(\frac{1}{2}, \frac{3}{4}; \frac{5}{4}; \frac{z_{\mathrm{t}}^4}{z_{\mathrm{h}}^4}\right)\,, \tag{5.22}$$

$$f_{\mathrm{b}}\left(\frac{z_{\mathrm{t}}^4}{z_{\mathrm{h}}^4}\right) = {}_2\mathrm{F}_1\left(\frac{3}{2}, \frac{7}{4}; \frac{9}{4}; \frac{z_{\mathrm{t}}^4}{z_{\mathrm{h}}^4}\right)\,, \tag{5.23}$$

$$f_{\mathrm{c}}\left(\frac{z_{\mathrm{t}}^4}{z_{\mathrm{h}}^4}\right) = {}_2\mathrm{F}_1\left(-\frac{1}{2}, -\frac{1}{4}; \frac{1}{4}; \frac{z_{\mathrm{t}}^4}{z_{\mathrm{h}}^4}\right)\,, \tag{5.24}$$

$$f_{\mathrm{d}}\left(\frac{z_{\mathrm{t}}^4}{z_{\mathrm{h}}^4}\right) = {}_2\mathrm{F}_1\left(-\frac{1}{2}, \frac{3}{4}; \frac{1}{4}; \frac{z_{\mathrm{t}}^4}{z_{\mathrm{h}}^4}\right)\,. \tag{5.25}$$

The entropy $S_{Q\bar{Q}}$ vanishes identically in the limit $T \to 0$. This can be verified analytically in $\mathcal{N} = 4$ SYM from formula (5.20). This implies that for $T = 0$ the internal energy coincides with the free energy. As we have seen before, in this case the free energy, and thus also the internal energy, is given by the zero-temperature potential $V_{Q\bar{Q}}$, see Eq. (5.17).

Let us now have a look at the entropy and internal energy in more detail. To begin with, in Fig. 5.5 we plot the internal energy $U_{Q\bar{Q}}$ and the free energy $F_{Q\bar{Q}}$ in $\mathcal{N} = 4$ SYM for increasing temperature (in AdS units set by $L_{\mathrm{AdS}} = 1$) starting at $T = 0$. An inset shows the entropy $S_{Q\bar{Q}}$ for any $T > 0$ as a function of the dimensionless product LT. Note that in $\mathcal{N} = 4$ SYM, due to the absence of any further scales the dimensionless entropy $S_{Q\bar{Q}}$ necessarily only depends on LT. The black solid curve in Fig. 5.5 shows $V_{Q\bar{Q}}$.

At $T > 0$, the internal and free energies start to differ from each other and their common $(T = 0)$-limit $V_{Q\bar{Q}}$ at intermediate L (compared to the screening distance, which in the figure is marked by a dot on the respective curve's endpoint). We have discussed the behavior of the free energy in Secs. 5.2 and 5.3, so let us focus now on the entropy and the internal energy. As seen in the inset in Fig. 5.5, the entropy increases monotonically with the quark separation L. A heuristic physical explanation of this observation might be that, as the size of the $Q\bar{Q}$ bound state increases, it has a growing overlap with the regime of the (thermal) length scales $L_{\mathrm{th}} \sim 1/T$ of the surrounding medium. Therefore, the $Q\bar{Q}$ state can couple to an increasing number of modes of the medium, thus increasing its associated phase-space volume which leads to an increase in entropy. In contrast to the free energy, the internal energy increases for fixed L upon increasing the temperature. It is always larger than the free energy due to the positive entropy contribution $TS_{Q\bar{Q}}(L) > 0$.
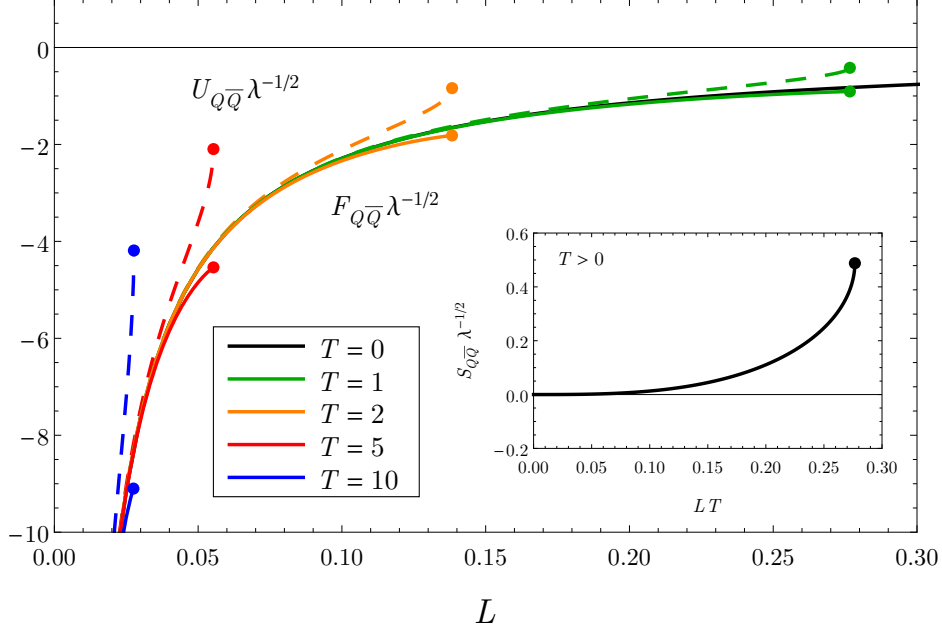
Figure 5.5: Internal energy $U_{Q\bar{Q}}(L)/\sqrt{\lambda}$ (dashed lines) and free energy $F_{Q\bar{Q}}(L)/\sqrt{\lambda}$ (solid lines) for varying temperature in $\mathcal{N} = 4$ SYM. The inset shows the entropy $S_{Q\bar{Q}}/\sqrt{\lambda}$ for an arbitrary fixed $T > 0$ as a function of LT. The dots on the endpoints of the curves mark the screening distance. For very small L, the entropy approaches zero and both $U_{Q\bar{Q}}$ and $F_{Q\bar{Q}}$ approach a universal, Coulombic curve, given by Eq. (5.17).

Interestingly, the internal energy has an inflection point and curves upward close to the screening distance. Since the entropy approaches zero for small distances L, the internal energy approaches the free energy and shares with it the independence of T for small L.

Having gained an understanding of the behavior of the entropy and internal energy in $\mathcal{N} = 4$ SYM, next we investigate their behavior in our non-conformal models where the entropy, and subsequently the internal energy, are computed numerically from the free energy via Eq. (C.4) in the appendix. The qualitative dependence on temperature is similar to the one we discussed in $\mathcal{N} = 4$ SYM above. To study the impact of the deformation in more detail, in Fig. 5.6 we show the internal energy as a function of the quark separation at fixed temperature in our non-conformal models for a large value $\delta = 2.5$ of the dimensionless ratios of the deformation parameters and the temperature, $\delta = c/T$ and $\delta = \sqrt{\kappa}/T$ in the SW$_T$ and 1-parameter models, respectively. In the inset, we plot the entropy as a function of LT using the same deformation parameters. For comparison, we also display the internal energy and entropy in $\mathcal{N} = 4$ SYM (black curves). We see that the entropy behaves similarly as in $\mathcal{N} = 4$ SYM discussed above, *cf.* the inset in Fig. 5.5. While $S_{Q\bar{Q}}$ vanishes
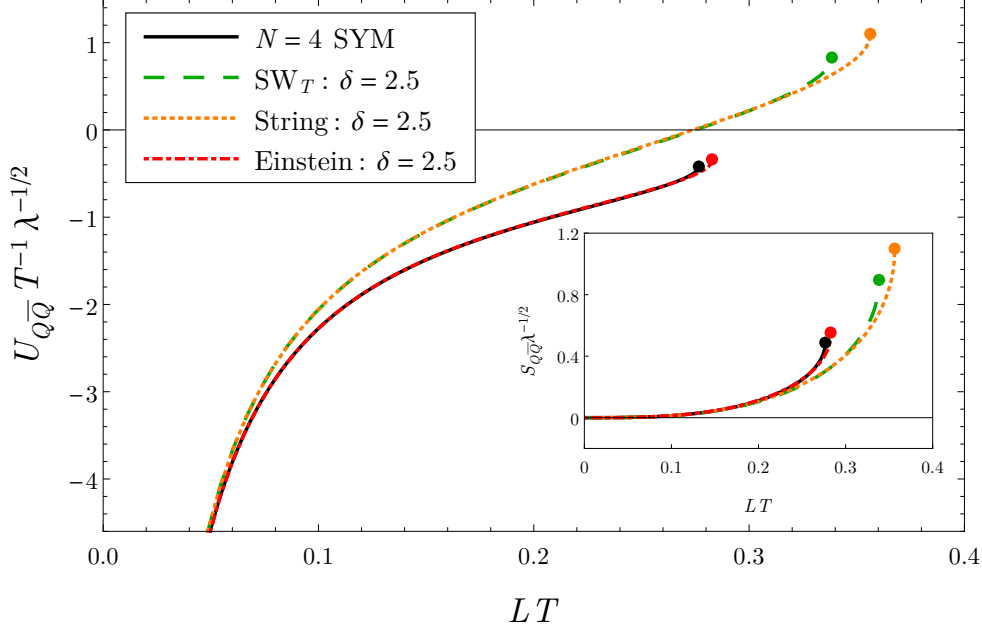
Figure 5.6: Internal energy $U_{Q\bar{Q}}(L)/(T\sqrt{\lambda})$ at fixed temperature in $\mathcal{N}=4$ SYM and non-conformal models at large deformations $\delta=2.5$ with $\delta=c/T$ and $\delta=\sqrt{\kappa}/T$ for the SW_T and 1-parameter models, respectively. The inset shows the entropy $S_{Q\bar{Q}}/\sqrt{\lambda}$ as a function of LT. For very small L, the entropy approaches zero in all models and $U_{Q\bar{Q}}$ in all models converges to a universal, Coulombic curve.

for $L=0$, it increases monotonically for increasing L towards its maximum at the screening distance. The internal energy $U_{Q\bar{Q}}(L)$ in the non-conformal models has a shape similar to that in $\mathcal{N}=4$ SYM. In particular, its slope increases towards the screening distance L_{s}, too, which can be traced back to the strong increase of $S_{Q\bar{Q}}$ towards L_{s}.

For small distances L, the behavior of the internal energy is dominated by that of the free energy because the entropy approaches zero in all our models. Accordingly, like the free energy discussed in Sec. 5.3, also the internal energy in all non-conformal models converges to one universal curve for small L, namely the one in $\mathcal{N}=4$ SYM given by the zero-temperature potential $V_{Q\bar{Q}}$ in Eq. (5.17).

Differences between the behavior of the internal energy in our non-conformal models and the behavior in $\mathcal{N}=4$ SYM generally appear at intermediate and large L. As we have seen before in the context of other observables, the 1-parameter Einstein-frame model is very robust against non-conformal deformation, and both $S_{Q\bar{Q}}$ and $U_{Q\bar{Q}}$ stay very close to their respective values in $\mathcal{N}=4$ SYM for all distances L. On the other hand, in both the SW_T and 1-parameter string-frame models the entropy at fixed distance decreases relative to its value in $\mathcal{N}=4$ SYM for the chosen
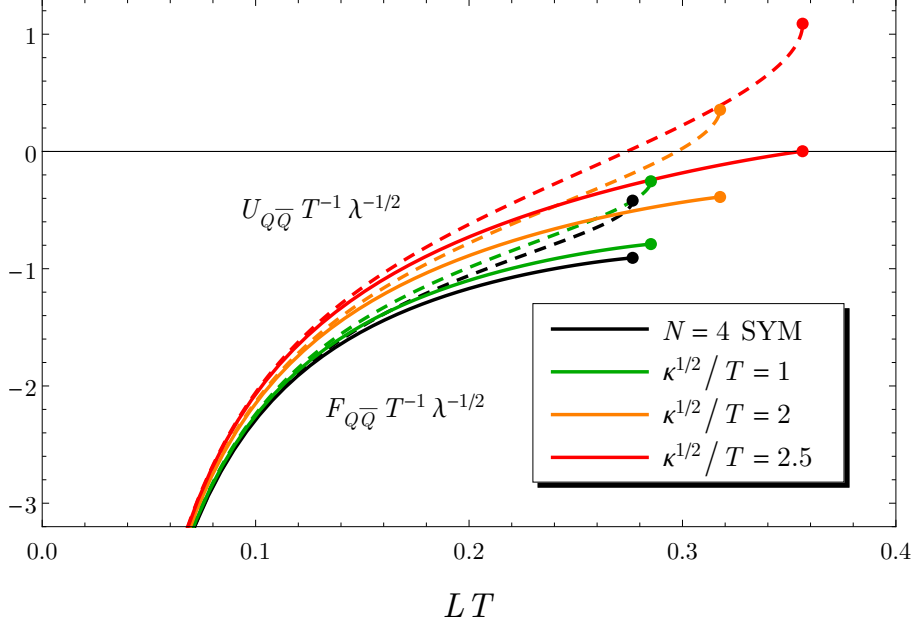
Figure 5.7: Internal energy $U_{Q\bar{Q}}(L)/(T\sqrt{\lambda})$ (dashed lines) and free energy $F_{Q\bar{Q}}(L)/(T\sqrt{\lambda})$ (solid lines) at fixed temperature in $\mathcal{N} = 4$ SYM (black curves) and the 1-parameter string-frame model for varying deformation parameter. For very small L, both $U_{Q\bar{Q}}$ and $F_{Q\bar{Q}}$ approach a universal, Coulombic curve.

degree of non-conformality. In the overall effect on the internal energy, however, the increase in the free energy that we have seen in Sec. 5.3 obviously overwhelms the decrease in the entropy in $U_{Q\bar{Q}} = F_{Q\bar{Q}} + TS_{Q\bar{Q}}$, such that the internal energy in the SW_T and 1-parameter models is larger than in $\mathcal{N} = 4$ SYM. This and the robustness observed for the Einstein-frame model indicate that $U_{Q\bar{Q}}$ in $\mathcal{N} = 4$ SYM might constitute an approximate lower bound on the internal energy at least for our class of non-conformal deformations of this theory.

To not clutter the presentation, we have refrained in Fig. 5.6 from also showing the free energy. To gain a better understanding of the relative behavior of the free and the internal energy in a non-conformal model, we now focus on the 1-parameter string-frame model as an example of a consistent deformation of AdS_5-Schwarzschild. Moreover, in this way we can check whether the internal energy in the deformed model is larger than the corresponding internal energy in $\mathcal{N} = 4$ SYM also for smaller values of the deformation. In Fig. 5.7 we show the dependence of the internal energy and free energy on the deformation parameter in the 1-parameter string-frame model, starting from the undeformed theory, *i. e.* $\mathcal{N} = 4$ SYM (black curves). Like the free energy, the internal energy increases with increasing deformation parameter, and indeed is larger than in $\mathcal{N} = 4$ SYM for all deformations. Just as in $\mathcal{N} = 4$ SYM,

also in the non-conformal model the internal energy approaches the free energy for small quark separation L. As the entropy approaches zero for small L in all our non-conformal models, *cf.* the inset in Fig. 5.6, this is a robust observation, *i.e.*, the internal energy approaches the free energy for small L in all our models. Thus, in all of our models the internal and free energy differ only for intermediate and large quark separations. This also seems to be the case in lattice simulations [217] within in the range of quark separations studied in that work. The changes of the internal energy with respect to $\mathcal{N} = 4$ SYM induced by non-conformality are very small (Einstein-frame model) or positive, *i.e.*, $U_{Q\bar{Q}}$ increases above its value in $\mathcal{N} = 4$ SYM (SW_T and 1-parameter string-frame model). Finally, we find that at small quark separations, $F_{Q\bar{Q}}$ and $U_{Q\bar{Q}}$ in all theories approach as a common limit the free energy in $\mathcal{N} = 4$ SYM, which in turn approaches the zero-temperature potential $V_{Q\bar{Q}}$ for small L.

In the derivation of the holographic formula for the $Q\bar{Q}$ free energy in Sec. 5.1, we have obtained as a by-product a definition of the free energy of a single quark in the hot medium described by our holographic models. In the next section, we will study this quantity and, in analogy to the current section, the associated entropy and internal energy.

5.5 Single-Quark Free Energy, Entropy, and Internal Energy

In this section, we will put the relation (5.12) to use that we obtained in the derivation of the free energy of the bound heavy quark–anti-quark pair. It yields the free energy of a single heavy 'test' quark in the strongly coupled plasmas dual to our holographic models. We will also study the entropy and internal energy associated with the free energy. As in the previous section, we will continue to work at vanishing chemical potential. An analysis of these single-quark quantities in our class of non-conformal models, with a focus on the impact of non-conformal deformations of $\mathcal{N} = 4$ SYM, has not been performed in the literature so far.[y]

We have defined the free energy F_Q in Eq. (5.12), and again define the entropy and internal energy by standard thermodynamic relations,

$$S_Q = -\frac{\partial F_Q}{\partial T}\,, \tag{5.26}$$

$$U_Q = F_Q + T S_Q\,. \tag{5.27}$$

Let us start with $\mathcal{N} = 4$ SYM. In this case, Eq. (5.12) can easily be explicitly evaluated, using the AdS-Schwarzschild metric (4.20). We obtain for the single-quark

---

[y]Previous work with different focus includes Ref. [209] which studies the single-quark free energy in a bottom-up framework tuned to model Yang–Mills thermodynamics, and the very recent work [221] that computes the single-quark free energy and entropy in the so-called 'improved holographic QCD' model of [178, 179]. For a general discussion of single-quark thermodynamics in holographic models see [222].

free energy, entropy, and internal energy,

$$F_Q = -\frac{\sqrt{\lambda}}{2}T \,, \qquad S_Q = \frac{\sqrt{\lambda}}{2} \,, \qquad U_Q = 0 \,. \qquad (5.28)$$

These values have also been obtained in [222]. Since $\mathcal{N} = 4$ SYM is a conformal theory, at $T > 0$ only the temperature itself is available as a dimensionful quantity for the problem at hand. Thus, the relation $F_Q \propto T$ already follows from dimensional analysis. The non-analytic square-root dependence on the 't Hooft coupling is, however, a non-trivial outcome of the computation. Interestingly, the free energy is entirely determined by the entropic contribution as the internal energy vanishes.

We can analytically compute the above quantities also in the SW_T model and the 1-parameter Einstein-frame model. Unfortunately, we did not find a closed-form expression for it in the 1-parameter string-frame model. Let us start with the SW_T model. Due to the simple relation of the temperature and the horizon position, $z_\mathrm{h} = 1/(\pi T)$, we can explicitly express F_Q as a function of T and compute the entropy and internal energy. We find

$$F_Q = -\frac{\sqrt{\lambda}}{2\pi} \exp\left(\frac{c^2}{\pi^2 T^2}\right) \left[\pi T - 2c \mathcal{F}\left(\frac{c}{\pi T}\right)\right] \,, \qquad (5.29)$$

$$S_Q = \frac{\sqrt{\lambda}}{2} \exp\left(\frac{c^2}{\pi^2 T^2}\right) \,, \qquad (5.30)$$

$$U_Q = \frac{\sqrt{\lambda}}{2\sqrt{\pi}} \, c \, \mathrm{erfi}\left(\frac{c}{\pi T}\right) \,, \qquad (5.31)$$

where $\mathcal{F}$ is the Dawson integral and erfi the 'imaginary' error function defined by $\mathrm{erfi}(x) = -\mathrm{i}\,\mathrm{erf}(\mathrm{i}x)$.[z] Here, λ denotes the bulk quantity defined by $\sqrt{\lambda} = L_\mathrm{AdS}^2/\alpha'$, and is a proxy for the coupling strength in the boundary theory, *cf.* Eq. (4.16) and the discussion thereof. As we will see explicitly below, for high temperatures, F_Q, S_Q, and U_Q approach their values in $\mathcal{N} = 4$ SYM from above. However, as T is lowered they significantly increase above the conformal values.

In the 1-parameter Einstein-frame model, we can only find closed-form expressions for F_Q, S_Q, and U_Q as functions of z_h, as we cannot analytically invert the

---

[z]The Dawson integral is defined by

$$\mathcal{F}(x) = \mathrm{e}^{-x^2} \int_0^x \mathrm{d}y \, \mathrm{e}^{y^2} \,,$$

see [223]. See Eq. (B.10) for the definition of the error function erf. The latter is related to the Dawson integral by $\mathcal{F}(x) = \sqrt{\pi}\mathrm{e}^{-x^2}\,\mathrm{erfi}(x)/2$.

temperature function $T(z_{\mathrm{h}})$ (not even at $\mu = 0$) in Eq. (4.52). We find

$$F_Q(z_{\mathrm{h}}) = -\frac{\sqrt{\lambda}}{8\sqrt{2}\pi}\sqrt{\kappa}\left[4\,\Gamma\left(\frac{3}{4}\right) + \gamma\left(-\frac{1}{4}, \frac{\kappa^2 z_{\mathrm{h}}^4}{4}\right)\right], \qquad (5.32)$$

$$S_Q(z_{\mathrm{h}}) = \frac{2\sqrt{\lambda}}{3}\frac{1}{\kappa^2 z_{\mathrm{h}}^4}\frac{\exp\left(-\frac{1}{2}\kappa^2 z_{\mathrm{h}}^4\right)\left[\exp\left(\frac{1}{4}\kappa^2 z_{\mathrm{h}}^4\right) - 1\right]^2}{1 - \exp\left(\frac{1}{4}\kappa^2 z_{\mathrm{h}}^4\right) + \frac{1}{3}\kappa^2 z_{\mathrm{h}}^4}, \qquad (5.33)$$

$$U_Q(z_{\mathrm{h}}) = \frac{\sqrt{\lambda}}{6\pi}\left\{\frac{1}{z_{\mathrm{h}}}\frac{1 - \exp\left(-\frac{1}{4}\kappa^2 z_{\mathrm{h}}^4\right)}{1 - \exp\left(\frac{1}{4}\kappa^2 z_{\mathrm{h}}^4\right) + \frac{1}{3}\kappa^2 z_{\mathrm{h}}^4}\right.$$

$$\left. -\frac{3\sqrt{2}}{8}\sqrt{\kappa}\left[4\,\Gamma\left(\frac{3}{4}\right) + \gamma\left(-\frac{1}{4}, \frac{\kappa^2 z_{\mathrm{h}}^4}{4}\right)\right]\right\}, \qquad (5.34)$$

where γ is the incomplete Γ-function.[aa] Although we are not able to express these quantities symbolically in terms of the temperature T, it is straightforward to analyze their behavior numerically.

For the 1-parameter string-frame model, the additional terms in the warp factors prohibit a solution of the integrals for F_Q, S_Q, and U_Q in closed form. Nevertheless, we can numerically evaluate the definition (5.12) for the free energy, and easily compute the entropy and internal energy from it.

We plot the free energy, entropy and internal energy as functions of the temperature in $\mathcal{N} = 4$ SYM and all our non-conformal models in Figs. 5.8, 5.9, and 5.10, respectively. In order to be able to sensibly compare the temperatures, we scale the temperatures in each model to the temperature T_{c}, defined as the position of the maximum of the dimensionless trace of the energy–momentum tensor, as discussed in Sec. 4.1.4. We have $T_{\mathrm{c}}/c \approx 0.494$ and $T_{\mathrm{c}}/\sqrt{\kappa} \approx 0.394$ in the SW$_T$ model and 1-parameter models, respectively, and choose $T_{\mathrm{c}} = 176\,\mathrm{MeV}$ to introduce physical units. As our models are constructed to describe a deconfined gauge-theory plasma, we focus on the temperature range $T/T_{\mathrm{c}} \geq 1$. Let us note that qualitative conclusions do not change if we vary the ratios of T_{c} and the deformation parameters around the values given above. To exhibit the behavior of F_Q in Fig. 5.8 more clearly, we scale out the dominant T-dependence $F_Q \sim T$. Note that in all our models F_Q/T is negative, *i.e.*, F_Q decreases with increasing T. We recall that in $\mathcal{N} = 4$ SYM the trace of the energy–momentum tensor vanishes identically for all temperatures, so there is no way to define T_{c}. Thus, the choice $T_{\mathrm{c}} = 176\,\mathrm{MeV}$ is

---

[aa]The incomplete Γ-function is defined by

$$\gamma(a, x) = \int_x^\infty \mathrm{d}t\, t^{a-1}\mathrm{e}^{-t},$$

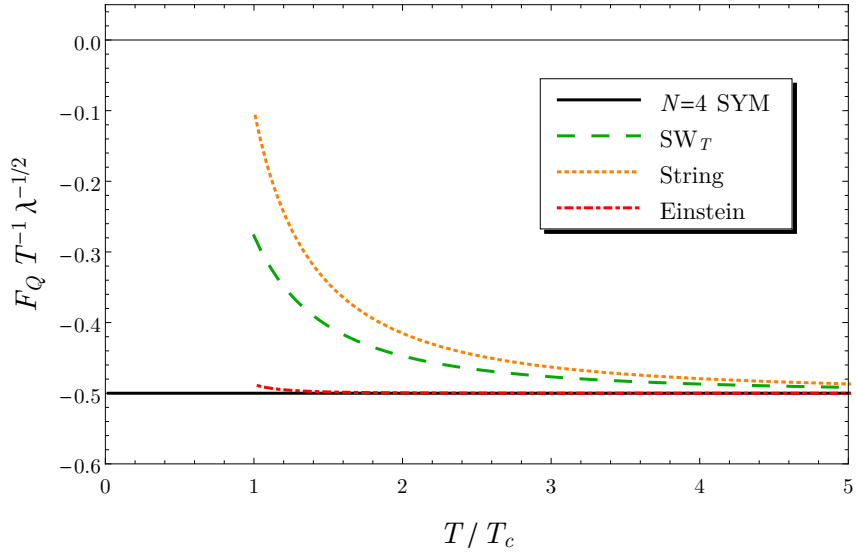see [223]. It is related to the ordinary Γ-function by $\gamma(a, 0) = \Gamma(a)$.

Figure 5.8: Single-quark free energy as a function of temperature in $\mathcal{N} = 4$ SYM and our non-conformal models. We have scaled out the dominant T-dependence of F_Q. See the text for an explanation of the scale T_c used here.
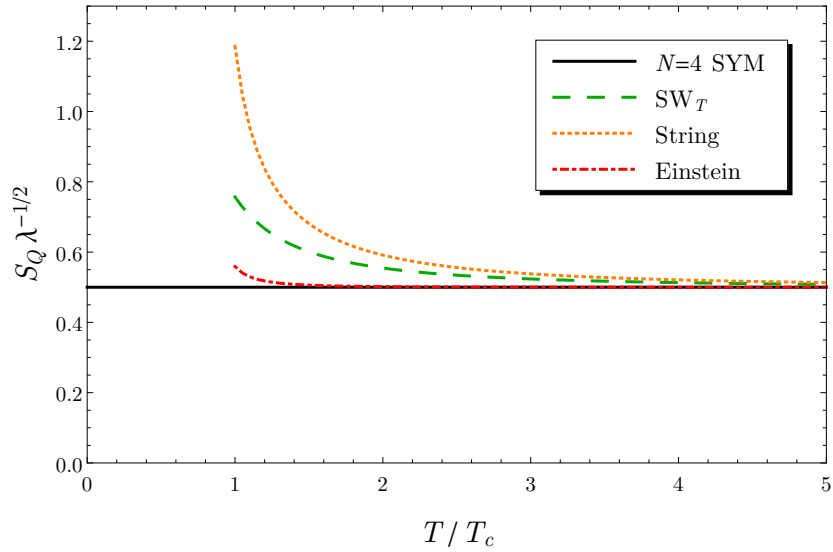

Figure 5.9: Single-quark entropy as a function of temperature in $\mathcal{N} = 4$ SYM and our non-conformal models. See the main text for an explanation of the scale T_c used here.
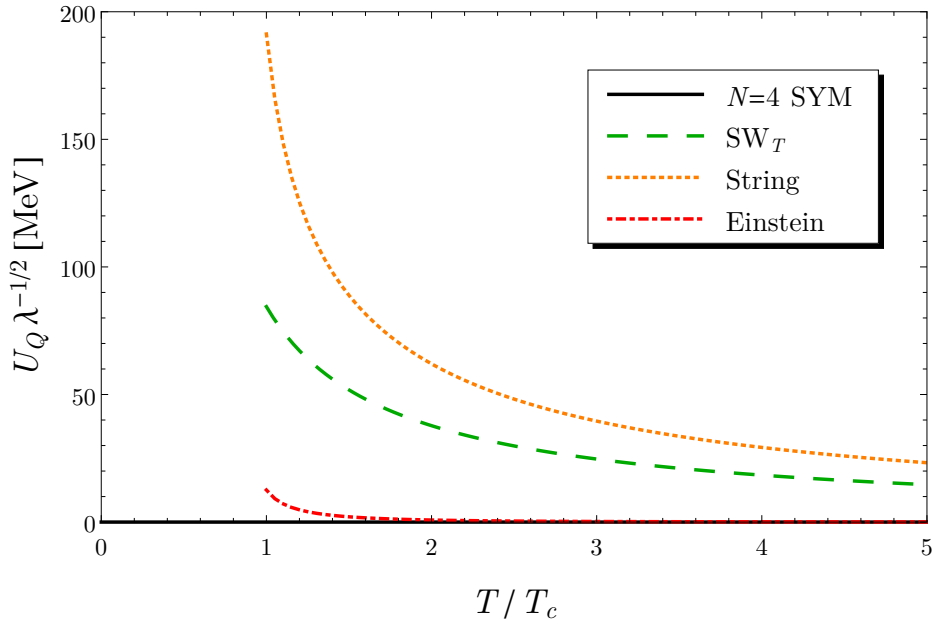
Figure 5.10: Single-quark internal energy as a function of temperature in $\mathcal{N} = 4$ SYM and our non-conformal models, in physical units set by the choice $T_c = 176\,\mathrm{MeV}$ (see the text). Note that the internal energy vanishes identically in $\mathcal{N} = 4$ SYM.

completely arbitrary in this case. In any case, the way we scaled F_Q, S_Q, and U_Q in the figures makes the dependence on T trivial for $\mathcal{N} = 4$ SYM.

We have seen before that the 1-parameter Einstein-frame model is very robust and stays quantitatively close to $\mathcal{N} = 4$ SYM. The quantities F_Q, S_Q, and U_Q are no exception, and are very close to their respective values in $\mathcal{N} = 4$ SYM for almost all T, as seen in the three figures. All three quantities exhibit a stronger dependence on the temperature in both the SW_T model and the 1-parameter string-frame model. The latter deviates farthest from the behavior seen in $\mathcal{N} = 4$ SYM. For large temperatures, F_Q, S_Q, and U_Q approach their values in $\mathcal{N} = 4$ SYM from above. This implies an interesting universal behavior. In all our non-conformal models, F_Q, S_Q, and U_Q are larger than their respective values in $\mathcal{N} = 4$ SYM for all temperatures. Even choosing a different procedure to normalize the temperature scale in each model would not change this observation, so it appears that it is a robust conclusion.

Computations of the single-quark free energy in lattice QCD have been performed for instance in [217, 224, 225] (see also [207]) for a temperature range including T_c. In these studies, the single-quark free energy is defined from the large-distance behavior of the expectation value of a Polyakov loop correlator. The latter yields the free energy of a heavy $Q\bar{Q}$ pair at large quark separation, where the $Q\bar{Q}$ free energy

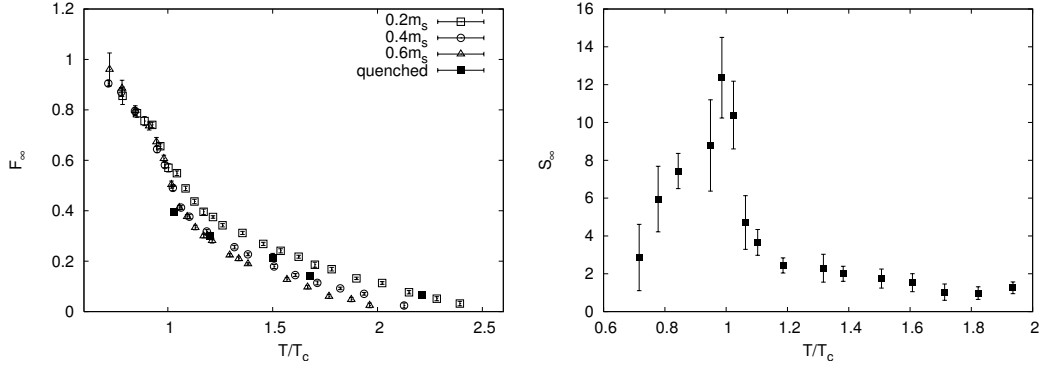Figure 5.11: Asymptotic values of the free energy (F_∞, left panel) and entropy (S_∞, right panel) of a $Q\bar{Q}$ pair obtained in lattice QCD. Above T_c, these can be interpreted as twice the single-quark free energy and entropy, respectively. Note, however, that the free energy is only defined up to a constant shift. In the left panel, different symbols correspond to different values of the dynamic-quark masses used in the lattice simulations. Figures taken from [224].

in fact approaches a constant value F_∞. At least in the deconfined phase where the far-separated quarks are screened from each other, one can interpret that free energy as twice the single-quark free energy, $F_\infty = 2F_Q$. Our holographic models should be compared to lattice data for the deconfined phase, $T \geq T_c$. The free energy is only defined up to an arbitrary, constant shift. Thus, we cannot compare the overall scale of F_Q. However, we may compare the behavior of F_Q as a function of temperature. In the following, for concreteness, we will compare to the results reported in [224]. The qualitative behavior that we are going to compare to is the same in the other lattice studies cited above. The left panel in Fig. 5.11 shows F_∞ obtained in the lattice QCD study of Ref. [224] with dynamic quarks. The different symbols correspond to different choices of the mass of the dynamic quarks; as we only aim at a qualitative comparison, these details do not matter for us. Somewhat above T_c we observe an approximately linear decrease of $F_\infty = 2F_Q$ with T, while closely above T_c the free energy $F_\infty(T) = 2F_Q(T)$ is convex. The free energy F_Q in our holographic models exhibits very similar behavior, see Fig. 5.8; note that in that figure, we have shown F_Q/T, and this ratio is negative such that F_Q in fact decreases with T. The decrease is linear in T for large T. Moreover, in the SW_T and 1-parameter string-frame models, $F_Q(T)$ is also clearly convex.

For a more quantitative comparison let us now focus on the single-quark entropy. Lattice data from Ref. [224] on the entropy S_∞ computed as $S_\infty = -(\partial F_\infty(T))/(\partial T)$ is shown in the right panel in Fig. 5.11. The interpretation of the free energy F_∞ as twice the single-quark free energy implies $S_\infty = 2S_Q$. The entropy S_∞ computed on the lattice is peaked at $T = T_c$. We focus on the deconfined phase, $T \geq T_c$. The entropy is a T-independent constant in $\mathcal{N} = 4$ SYM, clearly illustrating the need to

introduce non-conformality to model QCD physics at $T \gtrsim T_c$. Indeed, in our non-conformal models we find an increase of S_Q as T is lowered towards T_c, qualitatively similar to the lattice results. A heuristic explanation for the decrease of the entropy with temperature above T_c might be as follows. As the temperature increases, the screening length in the medium decreases and the quark interacts with a smaller volume around it. Thus, its phase space and accordingly its entropy decreases (*cf.* also the discussion in [224]).

The entropy, as a derivative of the free energy, is not affected by the ambiguity concerning the overall normalization that we discussed above. We can thus use it in order to produce a rough estimate for the parameter λ. From the lattice data shown in Fig. 5.11, we take a representative value $S_Q = S_\infty/2 \approx 6$ at $T = T_c$. We can easily evaluate S_Q in our holographic models at (a caricature of) T_c, *cf.* Fig. 5.9 and the discussion regarding the choice of T_c in Sec. 4.1.4. Comparing the holographic values to the lattice value $S_Q \approx 6$, we obtain estimates $\sqrt{\lambda} \approx 7.9, 10.7, 5.1$, *i.e.*, $\lambda \approx 63, 115, 26$, for the SW$_T$, the 1-parameter Einstein-frame, and the 1-parameter string-frame models, respectively. However, given the size of the uncertainty in the lattice data shown in Fig. 5.11, as well as the spread of the values $S_\infty(T_c)$ obtained in different lattice studies, large relative uncertainties should be assumed for these estimates of λ. For instance, the data of Ref. [217] yield representative values $S_Q = S_\infty/2 \approx 6$ for quenched simulations, and $S_Q \approx 7.5$ for simulations with dynamic quarks, both at $T \approx T_c$. Then, if we assume, from the spread of lattice data, a relative uncertainty of $\pm 25\,\%$ for our estimates of $\sqrt{\lambda}$, by standard propagation of uncertainty we obtain a relative uncertainty of $\pm 50\,\%$ for λ. In any case, since we have used classical gravity in the bulk, which is strictly obtained only in the limit $\lambda \to \infty$,[ab] it is reassuring that we need large values for the parameter λ to reproduce data from a theory that is presumably similar to the boundary theories dual to our holographic models.

Finally, let us briefly turn to the internal energy. It is affected by the same normalization ambiguity as the free energy, so we do not compare numerical values to lattice data. On the lattice [224], like for S_Q, a strong peak at $T = T_c$ is found for $U_\infty = 2U_Q$. In Fig. 5.10 we see that, while U_Q vanishes identically for all temperatures in $\mathcal{N} = 4$ SYM, in the SW$_T$ and 1-parameter string-frame models due to the introduction of non-conformality the internal energy exhibits a strong increase as T is lowered, in qualitative similarity to the internal energy in lattice QCD.

In closing this section, we should caution that our holographic models are constructed as a model description of the deconfined phase of QCD, so the numerical comparison performed should be taken with a grain of salt as we have made the comparison at the very boundary of that phase. Moreover, we cannot expect to see a peak and a subsequent decrease of S_Q as T is lowered past the temperature we

---

[ab]More strictly speaking, we can only be sure about this in the case of $\mathcal{N} = 4$ SYM where we known the dual interpretation of the parameter $\lambda = L_{\mathrm{AdS}}^4/\alpha'^2$ that we have introduced as a shorthand for a bulk quantity.

have called T_{c} in our holographic models. In fact, in our models we can decrease the temperature somewhat further than the temperature we have set to be T_{c}, *cf.* our discussion in Sec. 4.1.4, but in doing so we do not observe a qualitative change in the temperature dependence of F_Q, S_Q, and U_Q. Nevertheless, our non-conformal models seem to capture important features of the physics of the strongly coupled, deconfined QCD medium also in the single-quark sector.

6 Free Energy Taylor Expansions

In the previous chapter, we have studied various energies associated with a heavy quark–anti-quark ($Q\bar{Q}$) pair in a hot strongly coupled plasma. In particular, we have thoroughly reviewed the renormalization procedure involved in the holographic computations, and we have clarified how to holographically compute the $Q\bar{Q}$ free energy making sure that it does not depend on the temperature or chemical potential at small quark separations. We have studied the behavior of the $Q\bar{Q}$ free energy in detail both in $\mathcal{N} = 4$ SYM (Sec. 5.2) and in non-conformal models (Sec. 5.3), and have demonstrated that it qualitatively agrees with the free energy computed in lattice QCD.

It is a simple matter to include a chemical potential in holographic models, and we have done this for all our models. However, since we are working in a bottom-up setup, once we deform AdS_5-Reissner–Nordström spacetime and thus move away from $\mathcal{N} = 4$ SYM as the dual theory, we lose knowledge about the exact meaning of the chemical potential in the boundary theory. Furthermore, in $\mathcal{N} = 4$ SYM itself, we know that the chemical potential we introduced is conjugate to a charge density associated with supersymmetry, as discussed in Sec. 4.1.1. These points raise the question: How closely can the chemical potential in our holographic models mimic the baryon chemical potential in QCD that we are ultimately interested in?

In order to assess this, in this chapter we will compare the dependence of the $Q\bar{Q}$ free energy on the chemical potential in our holographic models and in lattice QCD. In lattice QCD, the evaluation of the $Q\bar{Q}$ free energy at non-zero μ is plagued by the sign problem (see *e. g.* [104] for a review). However, it is possible to compute the Taylor coefficients of an expansion of the free energy in powers of μ/T,

$$F_{Q\bar{Q}}(L; T, \mu) = \sum_{n=0}^{\infty} f^{(n)}(L; T) \left(\frac{\mu}{T}\right)^n . \tag{6.1}$$

On the lattice, the coefficients $f^{(n)}$ can be computed at $\mu = 0$. This has been done up to sixth order in [226]; see also [227, 228] for more recent work that uses different lattice actions for the quarks. In [226], the expansion coefficients $f^{(n)}$ for color-singlet and color-averaged free energies are computed as functions of the interquark distance and the temperature. It is most appropriate to compare our holographic results to the results on the color-singlet free energy and the associated coefficients.

In the first section, we will describe our procedure to compute the expansion coefficients $f^{(n)}$ in our holographic models. In the following sections, we will discuss the behavior of these coefficients in our different holographic models, as well as the temperature dependence. Finally, we will compare the results to those obtained in lattice QCD.

6.1 Holographic Computation

Let us first discuss the computation of the expansion coefficients of the free energy in our holographic models. From the defining equation (6.1) we readily see that

$$f^{(n)}(L;T) = \frac{1}{n!}\, T^n \left. \frac{\partial^n}{\partial \mu^n} F_{Q\bar{Q}}(L;T,\mu) \right|_{\mu=0} . \tag{6.2}$$

This immediately raises an issue since our expression (5.9) for the free energy is formulated in the bulk and depends on z_t and z_h instead of L and T. We have an explicit relation for $z_h = z_h(T,\mu)$ for $\mathcal{N} = 4$ SYM and the SW$_{T,\mu}$ model, see Eq. (4.28). Moreover, in the 1-parameter models we can straightforwardly determine z_h numerically for given T and μ from the relation $T = T(z_h,\mu)$, given in Eq. (4.54). Therefore, we have $F_{Q\bar{Q}}(z_t;T,\mu) \equiv F_{Q\bar{Q}}(z_t;z_h(T,\mu),\mu)$, and the only argument of $F_{Q\bar{Q}}$ left to discuss further is z_t. In all our models, $L = L(z_t;z_h(T,\mu),\mu) \equiv L(z_t;T,\mu)$ depends only weakly on μ for small μ. One might therefore be tempted to conclude that we can compute the derivatives in Eq. (6.2) at constant z_t instead of constant L. However, explicit numerical calculations show that, while such a conclusion is justified for the first derivative (which can also be shown analytically), at higher order $\partial^n F_{Q\bar{Q}}(L;T,\mu)/\partial \mu^n$ differs from $\partial^n F_{Q\bar{Q}}(z_t;T,\mu)/\partial \mu^n$. The upshot is that we need to numerically invert the relation $L = L(z_t;T,\mu)$. By adjusting $z_t = z_t(L;T,\mu)$ to keep L constant, for every L and T (and deformation parameter) we then sample $F_{Q\bar{Q}}(L;T,\mu)$ at different values of μ in the range $0 \leq \mu \leq 1/10$. Now, we use MATHEMATICA's interpolation and differentiation routines to compute $f^{(n)}$ using Eq. (6.2). To test this algorithm, we have compared the results for $f^{(1)}$ and $f^{(2)}$ with results obtained by using a finite-difference formula for the first and second derivatives, thereby circumventing the use of interpolation. Indeed, the values obtained from these different methods are approximately equal. Our numerical procedure becomes increasingly noisy as we increase the order n of the coefficients $f^{(n)}$. For $n \geq 4$ the data is too noisy to extract reliable results.

Up to numerical noise, the coefficients $f^{(1)}$ and $f^{(3)}$ appear to vanish in all our models. We surmise that, more generally, all coefficients of odd order vanish. Evidence for this conjecture comes from noting that μ enters all quantities involved in the computation of the $f^{(n)}$ only quadratically. This can be seen from the equations (5.9) and (4.64) for $F_{Q\bar{Q}}$ and L, respectively. μ appears in the horizon function h and implicitly in $z_h = z_h(T,\mu)$. Both h and $T = T(z_h,\mu)$ do not contain μ but rather μ^2 in all of our models, see Sec. 4.1. It seems reasonable to assume that the series representation of $z_h = z_h(T,\mu)$ in powers of T contains only coefficients involving even powers of μ, and we indeed verify this for the first few terms. In a proof, an analogous argument would have to be made for $z_t = z_t(L;T,\mu)$. Finally, one would conclude that a series expansion of $F_{Q\bar{Q}}(L;T,\mu)$ only contains even powers of μ. Then, odd-order derivatives of $F_{Q\bar{Q}}$ vanish at $\mu = 0$, and thus all expansion coefficients $f^{(n)}$ with n odd in Eq. (6.2) vanish.

In QCD, on the other hand, it follows from a general argument [229] that the odd orders of the (μ/T)-expansion of the heavy-quark free energy vanish [226]. It
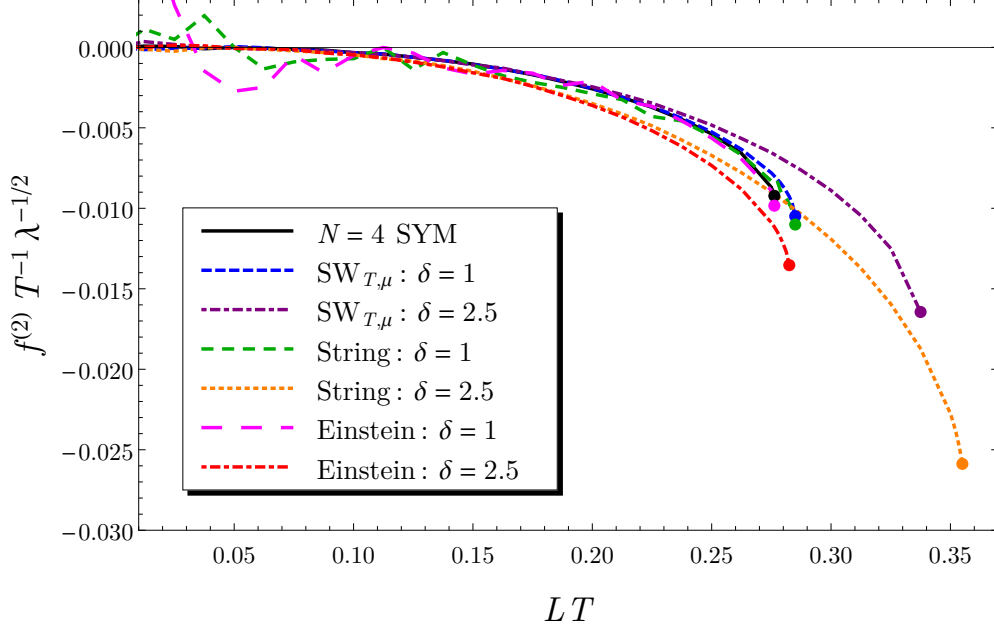
Figure 6.1: Second-order coefficient $f^{(2)}$ of the expansion in μ/T of the $Q\bar{Q}$ free energy $F_{Q\bar{Q}}$ as a function of the quark separation, plotted at fixed temperature T and varying dimensionless non-conformality parameter δ (see text) in our non-conformal models. For comparison, the black solid line shows $f^{(2)}$ in $\mathcal{N} = 4$ SYM. The dots on the endpoints of the curves mark the screening distance. The non-monotonic, noisy behavior of the curves for $\delta = 1$ in the 1-parameter Einstein- and string-frame models is an artifact of the numerics.

is not obvious *a priori* that this should also be the case in our holographic models. The fact that the odd coefficients appear to vanish in all our holographic models thus indicates that the chemical potential which we introduced might be physically similar to the quark or baryon chemical potential in real-world QCD. In the next section, we will study the first non-trivial coefficient $f^{(2)}$ in holography in detail. After that, we will compare it to the lattice results from [226].

6.2 Effect of Non-Conformality

First of all, let us study the first non-vanishing coefficient of the correction due to finite chemical potential, $f^{(2)}$, within holography. We will compare our various non-conformal models with one another and with $\mathcal{N} = 4$ SYM and try to discern common behavior.

We compute $f^{(2)}(L)$ numerically as outlined in the previous section. Figure 6.1 shows the results. $f^{(2)}$, normalized to $T\sqrt{\lambda}$, is plotted in $\mathcal{N} = 4$ SYM and our

non-conformal models at a fixed temperature T as a function of the dimensionless combination LT with L the quark separation. As before, λ is a shorthand for $\lambda = L_{\text{AdS}}^4/\alpha'^2$, and so is a bulk quantity. We only have a precise mapping to $\lambda = g_{\text{YM}}^2 N_{\text{c}}$, the 't Hooft coupling, for the undeformed case of $\mathcal{N} = 4$ SYM. Turning back to Fig. 6.1, the respective deformation parameter in the non-conformal models is made dimensionless by dividing by T, writing $\delta = c/T$ and $\delta = \sqrt{\kappa}/T$ for the SW$_{T,\mu}$ and 1-parameter models, respectively. For each non-conformal model, we plot $f^{(2)}$ for two values of δ. Recall that all our models reduce to $\mathcal{N} = 4$ SYM in the limit $\delta \to 0$.

First of all, we notice that the second-order coefficient tends to zero for small quark separations, irrespective of the temperature T and the model considered. This is due to the fact that the free energy $F_{Q\bar{Q}}$ becomes independent of the thermodynamic variables, and in particular of μ, for small distances, as discussed in Sec. 5.1. This would not have been the case had we used $E_{Q\bar{Q}}$ instead of $F_{Q\bar{Q}}$ in Eq. (6.2). Next, in all models the coefficient $f^{(2)}$ is negative. Since $f^{(2)}$ is the leading non-trivial coefficient in the (μ/T)-expansion, this means that for small μ the free energy decreases with increasing chemical potential. This is in line with the results in Chap. 5, and is in fact true for intermediate and large μ as well.

We see that the Einstein-frame model is robust with respect to the non-conformal deformation. In this model, the curve for $\delta = 1$ is almost on top of that in $\mathcal{N} = 4$ SYM. Even for the relatively large deformation $\delta = 2.5$, the overall magnitude of the coefficient $f^{(2)}$ stays comparable with that in $\mathcal{N} = 4$ SYM, and the screening distance increases only moderately. Interestingly, for $\delta = 2.5$ at fixed L, the deviation from the value of $f^{(2)}$ in $\mathcal{N} = 4$ SYM appears to be slightly larger in the Einstein-frame model than in the other two non-conformal models. This is in contrast to our general findings that the Einstein-frame model is the most robust among our non-conformal models. Nevertheless, in the overall picture the SW$_{T,\mu}$ model and the 1-parameter string-frame model exhibit stronger variations when increasing the deformation parameter: The screening distance increases further and accordingly $f^{(2)}$ assumes larger values in magnitude at larger L. Also, in the string-frame model, there is no single direction in which $f^{(2)}$ evolves upon introducing non-conformality. $f^{(2)}$ increases from its value in $\mathcal{N} = 4$ SYM for small and intermediate deformation (see the green curve for $\delta = 1$), but decreases for large deformation (see the orange curve for $\delta = 2.5$).

However, the stronger variations of $f^{(2)}$ in the sense just discussed in the SW$_{T,\mu}$ and string-frame models are apparently mainly due to the increase of the screening distance. Considering a fixed distance L, the coefficient $f^{(2)}$ is remarkably robust with respect to the deformation in all our non-conformal models. This means that the effect of the chemical potential on the free energy is only mildly moderated by the deformation. Apparently, the quark interaction at small chemical potential is similar in all our models, even at relatively large non-conformal deformations. This is a remarkable result since the temperature, the deformation, and the quark separation are all of roughly comparable magnitude here, so there is not a single

dominant scale at work such that one could argue that all results necessarily have to be close to $\mathcal{N} = 4$ SYM.

In the next two sections, we will study the variation of $f^{(2)}$ with temperature, and investigate how closely our holographic models can mimic QCD behavior as found on the lattice.

## 6.3 Taylor Coefficients at Varying Temperature

In this section we investigate the temperature dependence of the second-order coefficient $f^{(2)}$ of the (μ/T)-expansion of the $Q\bar{Q}$ free energy computed via holography, in preparation for a comparison of our results with data from lattice QCD.

Figure 6.2a displays $f^{(2)}/\sqrt{\lambda}$ as a function of the quark separation L, plotted for three different temperatures in $\mathcal{N} = 4$ SYM and each of our non-conformal models. We have reinstated physical units in the plot. To this end, we have set the deformation parameters to their 'optimal' values, as discussed in Sec. 4.1.4, so that the dimensionless trace of the energy–momentum tensor assumes its maximum at $T = 176\,\mathrm{MeV}$, which we call T_c. Note that in $\mathcal{N} = 4$ SYM the trace vanishes identically also at non-zero temperature, and in the present problem there are no dimensionful parameters other than L and T. For that theory, to set the scale we just use $T = \{T_\mathrm{c}, 1.5\,T_\mathrm{c}, 2\,T_\mathrm{c}\}$ with $T_\mathrm{c} = 176\,\mathrm{MeV}$ for the three black curves in the plot. Then, since for $\mathcal{N} = 4$ SYM the combination $f^{(2)}/(\sqrt{\lambda}T)$ is given by a universal function of LT, the three curves for $\mathcal{N} = 4$ SYM in the plot could be trivially scaled onto one another. This is not the case for the non-conformal models.

Considering a fixed quark separation L, the magnitude of $f^{(2)}$ increases with increasing temperature. However, this does not necessarily mean that the effect of the chemical potential on the free energy becomes larger with increasing temperature. Recall that $f^{(2)}$ is the first non-trivial coefficient in an expansion in the ratio μ/T. Therefore, going for example from $T = T_\mathrm{c}$ to $T = 2\,T_\mathrm{c}$ while keeping μ constant, besides the change in $f^{(2)}$ the first correction term to the free energy contains an additional factor $1/4$ from the change in μ/T. Next, except for the case of the string-frame model, the larger the temperature the larger is the absolute value of $f^{(2)}$ at the screening distance. This, combined with the decrease of the screening distance with increasing temperature leads to a much stronger variation of $f^{(2)}$ with L for larger temperatures. Finally, as the temperature gets larger, $f^{(2)}$ in our different models becomes less varied and approaches the value in $\mathcal{N} = 4$ SYM. This is natural since we adjusted the deformations in such a way that the strongest effect, at least for the dimensionless trace of the energy–momentum tensor, manifests itself around T_c. Going to larger temperatures, the deformation scale begins to decouple and the temperature dominates.

In the next and final section on the coefficients of the (μ/T)-expansion of the free energy we will compare our holographic results to data from lattice QCD.
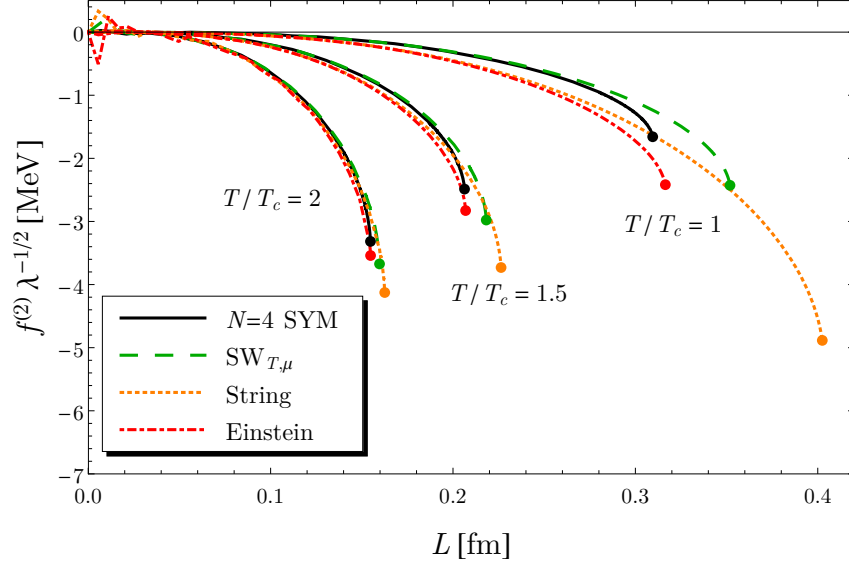
(a) $f^{(2)}/\sqrt{\lambda}$ in $\mathcal{N} = 4$ SYM and our three non-conformal models. See the text for an explanation of the scale T_c used here. The noisy behavior for small L is a numerical artifact. Note the smaller range in L as compared to the lattice data (lower panel).
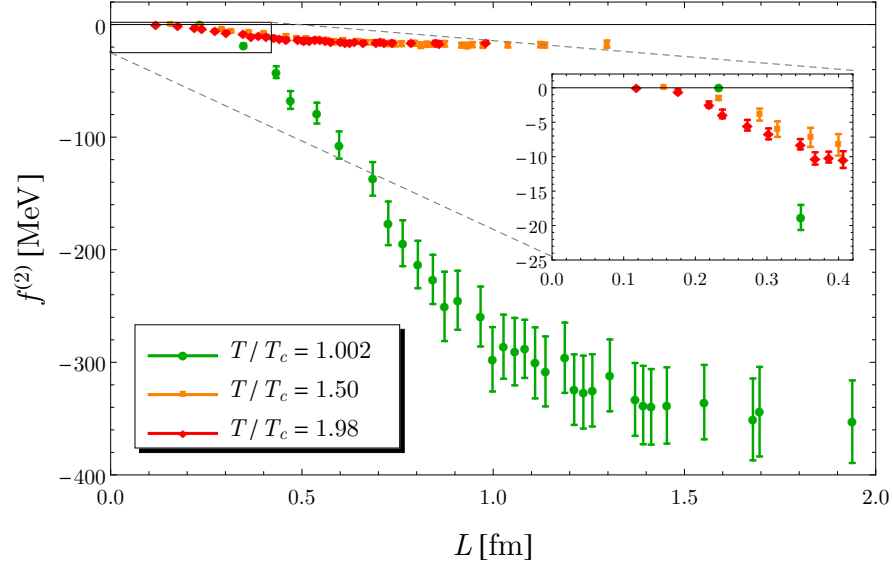
(b) $f^{(2)}$ in 2-flavor lattice QCD [226]. We have chosen from the data of [226] the three temperatures closest to the ones used in the holographic models (upper panel), and converted the data to physical units by using $\sqrt{\sigma} = 420\,\text{MeV}$ for the string tension.

Figure 6.2: Comparison of the second-order coefficients $f^{(2)}$ of the expansion in μ/T of the $Q\bar{Q}$ free energy as functions of the quark separation for varying temperature, computed in holography (upper panel) and lattice QCD (lower panel).

6.4 Comparison with Lattice Results

In Ref. [226] the first coefficients of the (μ/T)-expansion of the color-singlet free energy are computed in 2-flavor QCD. In this section, we want to qualitatively compare these lattice data with our results obtained in holography in order to assess what properties of the quark chemical potential in QCD are captured by the chemical potential in our holographic models.

Both on the lattice and in our holographic models, the first non-vanishing coefficient of the small-(μ/T) corrections to the $Q\bar{Q}$ free energy is $f^{(2)}$. In Fig. 6.2 we show the coefficient $f^{(2)}$ as a function of the quark separation L for three different temperatures in the range T_c to $2\,T_c$, computed in holography (upper panel, Fig. 6.2a) and in lattice QCD [226] (lower panel, Fig. 6.2b).[ac] In both subfigures we have reinstated physical units. For Fig. 6.2a, we have explained the procedure in the previous Sec. 6.3. The data of [226] is given in units of the string tension σ. For Fig. 6.2b, we have converted these data to physical units by choosing $\sqrt{\sigma} = 420\,\mathrm{MeV}$.

First of all, we note that on the lattice, like in holography, $f^{(2)} < 0$ is found. Thus, the overall effect of the chemical potential is the same, it leads to a reduction of the free energy. Therefore, the chemical potential that we use in our holographic models passes an important check. Furthermore, in the limit $L \to 0$ the coefficient $f^{(2)}(L)$ computed on the lattice vanishes. Thus, at small quark separation L the $Q\bar{Q}$ free energy becomes independent of the thermodynamic variables T and μ. We have found the same result in the holographic computation.

Despite the qualitative similarities, there are significant differences between our holographic results for $f^{(2)}$ and the lattice data. First, let us discuss the different ranges in the quark separation L in Figs. 6.2a and 6.2b. In the leading-order holographic computation, we can only describe the $Q\bar{Q}$ free energy up to the screening distance. Beyond that separation, additional string configurations become important on the right-hand side of Eq. (5.3), and additional supergravity modes that mediate interactions between strings have to be taken into account. This has so far been done only for $\mathcal{N} = 4$ SYM [197]. It is not in general clear how to achieve this in deformed bottom-up models (see, however, [209] for a recent investigation of that issue). In particular, in our treatment we do not reach a potential exponential approach of $F_{Q\bar{Q}}$ to a constant value, *i. e.*, Debye screening. Working holographically in strongly coupled $\mathcal{N} = 4$ SYM, corrections of the type just discussed have to be taken into account to compute the free energy on length scales where Debye screening becomes dominant [197]. Therefore, we do not expect to describe the free energy in the Debye-screening regime in our models. It is, however, reached in the lattice data shown in Fig. 6.2b, where the Debye screening length for $T = T_c$ (at vanishing chemical potential) is roughly given by $0.4\,\mathrm{fm}$, and decreases only moderately when approaching $2\,T_c$ [226]. For all three temperatures shown in Fig. 6.2b, the coefficient $f^{(2)}(L)$ appears to have an inflection point, and approaches a constant value for larger L.

[ac]We thank O. Kaczmarek for providing the data of Ref. [226].

In contrast, we do not see an inflection point nor an approach to a constant value of $f^{(2)}(L)$ in any of our holographic models. $f^{(2)}$ might possibly show such behavior at larger distance L, but exploring this would require at least the inclusion of the corrections discussed above. For the time being, let us therefore restrict the comparison of the coefficient $f^{(2)}(L)$ to the range of quark separations covered by our holographic models using the leading-order string configurations in the sense discussed above. To this end, in the inset in Fig. 6.2b we zoom into the lattice data for the range 0–0.42 fm. Unfortunately, on that range of distances there are only very few lattice data points to compare to our holographic results. However, we can discern, at least for $T/T_c = 1.5$ and 1.98, that at these distances the absolute value of $f^{(2)}$ increases with temperature. This qualitatively agrees with the behavior computed from holography.

Let us finally use the lattice data to estimate the value of the parameter λ which is left undetermined in the holographic computation. In light of the scarcity of lattice data points on the relevant length scales, this can only yield a very rough estimate. Working on the range of distances $L = 0$–0.42 fm, we take a typical value 5–10 MeV for the lattice data, and 2–$4\sqrt{\lambda}$ MeV for the holographic data, without further specifying the model. (Let us recall that only for the undeformed AdS-black hole spacetime do we know the exact meaning of λ in the dual boundary theory, $\mathcal{N} = 4$ SYM, where λ is the 't Hooft coupling.) Comparing the two, this yields $\sqrt{\lambda} \sim 2.5$, or $\lambda \sim 6$. This is somewhat smaller than the value obtained by comparing our holographic computation for the single-quark entropy to lattice data in Sec. 5.5. We will discuss our various estimates for λ further in the summary in Chap. 8. In any case, let us caution again that the present comparison gives only an order-of-magnitude estimate.

In the next chapter, we will study another quantity that can be derived from the $Q\bar{Q}$ free energy, the running coupling. For this quantity, too, lattice data are available, if only at vanishing chemical potential $\mu = 0$. We will again, and more reliably than in the case of the coefficient $f^{(2)}$ estimate the parameter λ from a comparison to the lattice data. Then, however, we will go beyond the thermodynamic regime accessible in lattice QCD, and study the running coupling for non-zero and large μ as well.

7 Running Coupling

So far we have discussed a procedure for the holographic computation of the free energy of a heavy quark–anti-quark pair in a strongly coupled plasma. We have verified that in our models this quantity qualitatively behaves as expected from lattice QCD, and have studied various quantities related to the free energy. Furthermore, we have studied in detail the behavior of the free energy at small chemical potential and compared it to lattice QCD, finding that the chemical potential used in our holographic models captures essential properties of the baryon chemical potential in QCD. Holography is a powerful tool for the investigation of physics in strongly coupled plasmas, and in light of the encouraging results that we have found, in this final chapter of Part I we want to analyze the free energy in even more detail. In particular, we focus on the characteristics of its dependence on the quark separation L. A quantity that is very well-suited for this study is the *running coupling* that is obtained from the L-derivative of the free energy. It clearly exhibits the distance-dependence of the free energy and is an interesting physical observable in itself.

We define the distance-dependent running coupling $\alpha_{Q\bar{Q}}(L)$ from the $Q\bar{Q}$ free energy $F_{Q\bar{Q}}$ by

$$\alpha_{Q\bar{Q}}(L) \equiv \frac{3}{4}L^2 \frac{\mathrm{d}F_{Q\bar{Q}}(L)}{\mathrm{d}L}. \tag{7.1}$$

This definition follows Refs. [195, 196] where this quantity is studied in lattice QCD. Note that the running coupling $\alpha_{Q\bar{Q}}$ defined in Eq. (7.1) is not the coupling that one is used to from perturbative QCD, $\alpha_{\mathrm{s}} = g^2/(4\pi)$, which 'runs' with the momentum scale (see for instance the textbook [230]). However, it is shown in [195] that $\alpha_{Q\bar{Q}}$ reduces to its perturbative counterpart for small interquark separations. We will see that the situation in our holographic models is analogous. To distinguish $\alpha_{Q\bar{Q}}$ from the perturbative running coupling, Ref. [231] calls it the *effective* running coupling. For simplicity, we will refer to the quantity $\alpha_{Q\bar{Q}}$ defined in Eq. (7.1) as the 'running coupling'.

Let us give a physical interpretation of the definition (7.1). In the vacuum of a conformal theory the only length scale present in the study of a heavy quark–anti-quark pair is the quark separation L, so on dimensional grounds it should be possible to write the $Q\bar{Q}$ free energy $F_{Q\bar{Q}}$ in the purely Coulombic form $F_{Q\bar{Q}}(L) = -\alpha/L$ with some constant α. Differentiating by L and multiplying by L^2 projects out this α. If conformality is broken, there will be other scales present and α will generically vary with L. For instance, this will already be the case at non-zero temperature. Thus, $\alpha_{Q\bar{Q}}$ as defined in (7.1) is a measure for the deviation from conformality.

The additional factor 3/4 in Eq. (7.1) is the inverse of the Casimir factor that appears in the static potential in QCD. In our holographic models we do not know the exact field content of the boundary theories, so we cannot state the analogous factors. However, as we will mainly be interested in the qualitative behavior of $\alpha_{Q\bar{Q}}$ this is not too big an issue. For concreteness, then, we include the factor 3/4 in Eq. (7.1), thus matching the definition used in the lattice studies [195, 196]. Besides this factor, in the holographic computation we have in addition the parameter $\sqrt{\lambda}$ that appears as a bulk quantity in the formula (5.9) and which we will discuss further below.

In the following, we will first review what has been found regarding the running coupling in lattice QCD. To get some intuition for the physics of $\alpha_{Q\bar{Q}}$ in holography, we will then study it in $\mathcal{N} = 4$ SYM, both at vanishing chemical potential, and, for the first time, at non-zero chemical potential. We will then proceed to studying non-conformal models. The running coupling gives rise to two further interesting physical observables, namely its maximum value and the associated length scale. We will generally analyze the physical observables in the whole (μ, T)-plane. Besides this exploratory investigation, at vanishing chemical potential we will quantitatively compare the maximum value of the running coupling to lattice QCD data, and thus estimate the value of the parameter $\sqrt{\lambda}$, similarly to estimates for it that we based on different observables in the previous chapters.

7.1 Running Coupling in Lattice QCD

Before we turn to the analysis of the running coupling in our holographic models we want to have a look into what has been found in lattice QCD studies. Lattice QCD can currently only determine this quantity at vanishing chemical potential due to the notorious sign problem (see *e. g.* [104] for a review). Thus, we will be able to compare our holographic results to lattice results only at $\mu = 0$.

In Fig. 7.1 we show results on the running coupling from [195]. In this work, the heavy quark–anti-quark free energy is investigated in quenched lattice QCD, *i. e.* in a purely gluonic plasma. A later study [196] has computed the running coupling in 2-flavor lattice QCD with qualitatively similar results. The figure shows the running coupling for six different temperatures above the deconfinement temperature T_c. For all of these temperature, $\alpha_{Q\bar{Q}}$ increases monotonically with the distance r between the quarks (L in our notation) up to a certain point. It then reaches a maximum and subsequently falls off. [196] has a nice argument for the appearance of the maximum at intermediate distances. In the small-distance limit, medium effects become unimportant, so $\alpha_{Q\bar{Q}}$ reflects the logarithmic decrease of the vacuum coupling with decreasing length scale (the thin solid curve in Fig. 7.1 shows the $T = 0$ vacuum value). On the other hand, for large distances color screening exponentially suppresses the coupling. Therefore, a maximum has to appear for intermediate distances.

The situation will necessarily be somewhat different in our holographic models.
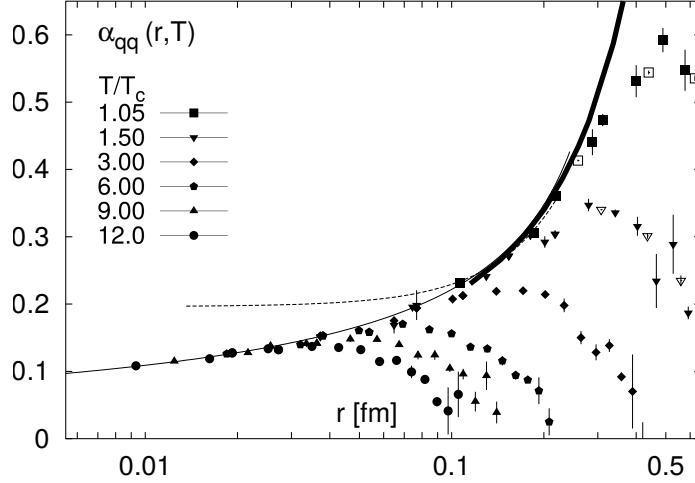
Figure 7.1: Running coupling $\alpha_{Q\bar{Q}}$ (denoted by α_{qq} in the figure) as a function of the interquark distance r at various temperatures, computed in quenched lattice QCD; the figure is taken from [195]. Open and filled symbols represent data computed with different grid spacings. The thin and thick solid black lines, as well as the dashed black line, represent various limits or approximations of the running coupling and are not important for our purposes, see [195] for a discussion.

For one thing, there is no asymptotic freedom, so this argument for a decrease of $\alpha_{Q\bar{Q}}$ for small distances does not apply. Also, using classical gravity in the bulk in the holographic models, we do not expect to describe a potential exponential flattening of the free energy, as discussed in Sec. 6.4. Given these differences of the asymptotic behavior of the running coupling in QCD and holographic models, it is not *a priori* clear whether, at least for intermediate distances, the running coupling can be sensibly compared in holographic models and in QCD.

7.2 Running Coupling in $\mathcal{N} = 4$ SYM

To start with our holographic investigation, we first analyze the behavior of the running coupling in $\mathcal{N} = 4$ SYM. The running coupling for $\mathcal{N} = 4$ SYM was first discussed in the context of gauge/gravity duality in [126]. In this section, in contrast to [126], we include non-zero chemical potential.

For a start, let us review the situation in $\mathcal{N} = 4$ SYM in vacuum, *i. e.*, at $T = 0$ and $\mu = 0$. As discussed in Sec. 5.2, Maldacena [105] has first obtained the heavy quark–anti-quark potential which we repeat here for convenience,

$$V_{Q\bar{Q}}(L) = -\frac{4\pi^2 \sqrt{\lambda}}{\Gamma^4\left(\frac{1}{4}\right) L} ,\tag{7.2}$$

where λ is the 't Hooft coupling. $V_{Q\bar{Q}}$ coincides with the free energy $F_{Q\bar{Q}}$ at $T = 0$.
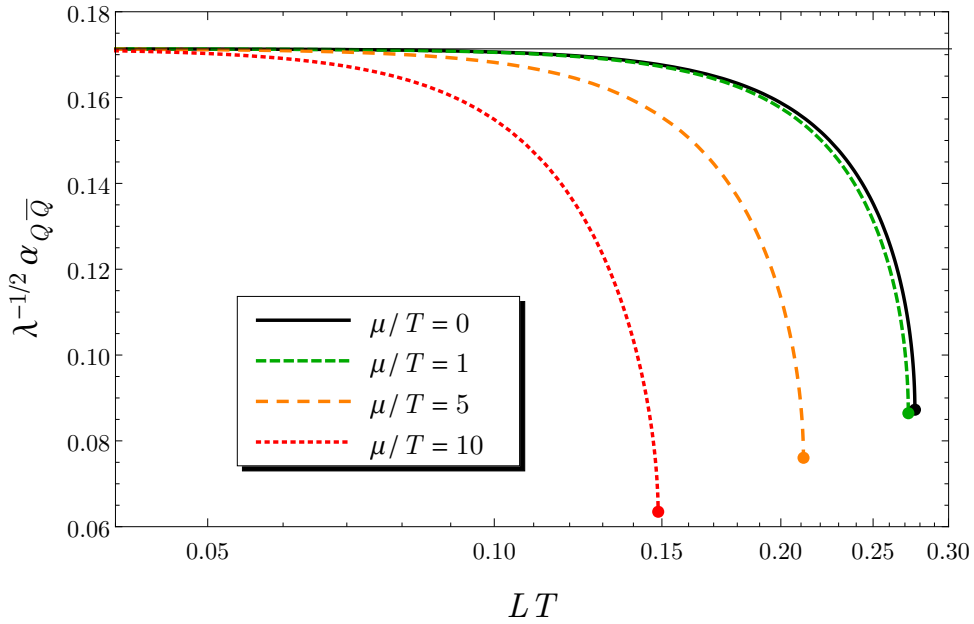
Figure 7.2: Running coupling $\alpha_{Q\bar{Q}}(L)/\sqrt{\lambda}$ in $\mathcal{N} = 4$ SYM at fixed temperature and varying chemical potential. All dimensionful quantities are expressed in units of the temperature. The thin solid line indicates the UV value (7.3) of the coupling. Note that the scale on the LT-axis is logarithmic. The dots on the endpoints of the curves mark the screening distance.

Applying the definition (7.1) yields the constant

$$\alpha_{Q\bar{Q}}^{T=0} = \frac{3\pi^2 \sqrt{\lambda}}{\Gamma^4\left(\frac{1}{4}\right)} \approx 0.171\,\sqrt{\lambda}\,. \tag{7.3}$$

At non-zero temperature and chemical potential, we have to compute the running coupling numerically. To this end, we sample the parametric functions $L(z_t)$ and $F_{Q\bar{Q}}(z_t)$, see Eqs. (4.64) and (5.9), respectively, for regularly spaced values of z_t using MATHEMATICA's routine `NIntegrate`. We reduce the free energy $F_{Q\bar{Q}}$ to its stable branch (*cf.* the discussion in Sec. 5.2) and interpolate the resulting data points to obtain $F_{Q\bar{Q}}(L)$. Finally, we directly apply the definition (7.1) on this interpolating function. Note that for the calculation of the running coupling one can also use the binding energy, Eq. (5.13), instead of the free energy, Eq. (5.9), in the formula (7.1) since the difference between these two energies does not depend on L and thus drops out when taking the L-derivative at fixed temperature (and chemical potential).

In Fig. 7.2 we plot $\alpha_{Q\bar{Q}}(L)$ in finite-temperature $\mathcal{N} = 4$ SYM at varying chemical potential. We note the following generic points about the behavior of the running coupling. These findings concerning the behavior of $\alpha_{Q\bar{Q}}$ hold in all our holographic models.

- Conformality – in the sense of the $Q\bar{Q}$ free energy being $F_{Q\bar{Q}}(L) \propto 1/L$ which implies $\alpha_{Q\bar{Q}}(L) = $ const – is broken by interaction with the medium. The presence of the thermal medium introduces length scales associated with T and μ. As L becomes comparable to them, the medium starts to screen the $Q\bar{Q}$ interaction and consequently $\alpha_{Q\bar{Q}}$ drops as L increases.

- In the UV, *i.e.*, as $L \rightarrow 0$, the running coupling becomes constant. This signals a restoration of conformality in the above sense in the UV where the thermal scales become negligible compared to the energy scales considered. The constant UV value is the vacuum value $\alpha_{Q\bar{Q}}/\sqrt{\lambda} \approx 0.171$, see Eq. (7.3).

- The effect of the chemical potential is a decrease of the running coupling. This is likely due to the increased charge density in the surrounding medium leading to stronger screening. This finding is in line with the observations we made for the binding energy, *cf.* Fig. 5.1b and the discussion thereof in Sec. 5.2.

For every curve in Fig. 7.2, we have marked the screening distance L_s with dots. It decreases with increasing chemical potential. The thermal scale L_{th} associated with the presence of the medium sets the fall-off scale of $\alpha_{Q\bar{Q}}(L)$, *cf.* the first point in the list above. It is in turn determined by $L_{th} \sim 1/T$ at vanishing chemical potential [113]. In the figure we see that in $\mathcal{N} = 4$ SYM at $\mu = 0$ the coefficient of $1/T$ in L_{th} is on the order of 0.1. At non-zero chemical potential, L_{th} is determined by two scales. However, we see from Fig. 7.2 that, at least in $\mathcal{N} = 4$ SYM, L_{th} depends only weakly on μ as compared to the dependence on T.

Comparing with the lattice data shown in Fig. 7.1, we observe two key differences: Firstly, the UV behavior differs, as was to be expected from the discussion in Sec. 7.1. As the quark separation becomes small, the running coupling in $\mathcal{N} = 4$ SYM becomes constant, in contrast to the asymptotically free behavior in QCD seen in the data displayed in Fig. 7.1 (and also in studies including dynamical quarks like [196]). Secondly, while the screening effect of the thermal medium is clearly seen in the drop-off of $\alpha_{Q\bar{Q}}$ in Fig. 7.2, there is no maximum of the coupling before the fall-off, unlike in the case of QCD. The first difference is intrinsic to our approach and we cannot overcome it by just considering deformations of the holographic dual of $\mathcal{N} = 4$ SYM theory within asymptotically AdS spacetimes. The reason is that in the UV all such deformations reduce to conformal $\mathcal{N} = 4$ SYM. However, the second difference can be addressed by considering explicitly non-conformal models that deviate from $\mathcal{N} = 4$ SYM at larger distance scales. In fact it has been found in [113] that a certain non-conformal model can fit the lattice data from [195] quite well. In the next section, we will extend these analyses and investigate the behavior of the running coupling in the strongly coupled plasma at non-zero chemical potential. For the case of non-vanishing chemical potential, no lattice data is available. Holography is one of the few methods by which we can gain computational access in this regime.

7.3 Running Coupling in Non-Conformal Holographic Models

In this section, we discuss the behavior of $\alpha_{Q\bar{Q}}$ in non-conformal holographic models, asking in particular how it is affected by the chemical potential. The first and, to the best of our knowledge, so far only study of the running coupling in non-conformal holographic models has been performed in [113], which works at vanishing chemical potential.

In Figs. 7.3 and 7.4 we show results for the running coupling in the $\mathrm{SW}_{T,\mu}$ and 1-parameter string-frame models at a fixed temperature T. We render all dimensionful quantities dimensionless by multiplying or dividing by T. We will briefly comment on the 1-parameter Einstein-frame model at the end of this section. The panels in the figures show data for chemical potentials $\mu/T = 0, 1$ and $\mu/T = 5, 10$, respectively.[ad] Within every panel, we further vary the deformation parameter over a large range, starting with $\mathcal{N} = 4$ SYM for vanishing deformation (black curves). In the figures, the variable δ stands for the dimensionless ratio of the deformation parameter and the temperature, *i. e.*, $\delta = c/T$ for the $\mathrm{SW}_{T,\mu}$ model and $\delta = \sqrt{\kappa}/T$ for the 1-parameter string-frame model.

First of all, we note that in both models the introduction of non-conformality leads to the appearance of a maximum in $\alpha_{Q\bar{Q}}$. Non-conformality apparently strengthens the interaction between the quarks. The qualitative behavior is similar to the one found in lattice QCD, *cf.* Fig. 7.1. Furthermore, $\alpha_{Q\bar{Q}}$ reduces to conformality for small L in both non-conformal models shown, *i. e.*, the coupling becomes constant. The constant value is independent of the deformation, and it equals the value found in (the vacuum of) $\mathcal{N} = 4$ SYM, see Eq. (7.3). The increase of $\alpha_{Q\bar{Q}}$ above the constant UV value is clearly seen in both non-conformal models. Such a universal increase of $\alpha_{Q\bar{Q}}$ was observed for vanishing chemical potential in [113]. We can now conclude that this property holds in the entire (μ, T)-plane for the two models considered in Figs. 7.3 and 7.4 – we will comment on the 1-parameter Einstein-frame model at the end of the section. Even for large chemical potentials, there still is a small increase above the UV value.

Holographic models can only be expected to approximate QCD behavior at intermediate distances that are neither too small nor too large. There is, in fact, no *a priori* reason for the appearance of a maximum in $\alpha_{Q\bar{Q}}$ in our holographic models. The fact that we see a maximum indicates that, on length scales on the order of the maximum, our holographic models indeed capture essential physics of QCD and we may meaningfully compare results from our models with lattice studies, which we

---

[ad]We emphasize that care must be taken in translating a given value μ/T from holographic models to QCD. We do presently not know what factors might be involved in modeling the baryon (or quark) chemical potential in QCD by the chemical potential in our various holographic models. In light of this uncertainty, it is possible that the range of values for μ/T considered here reaches beyond the range of interest for QGP phenomenology. In any case, it is certainly interesting to also explore the regime of large chemical potentials within our holographic models besides $\mu/T \sim 1$.
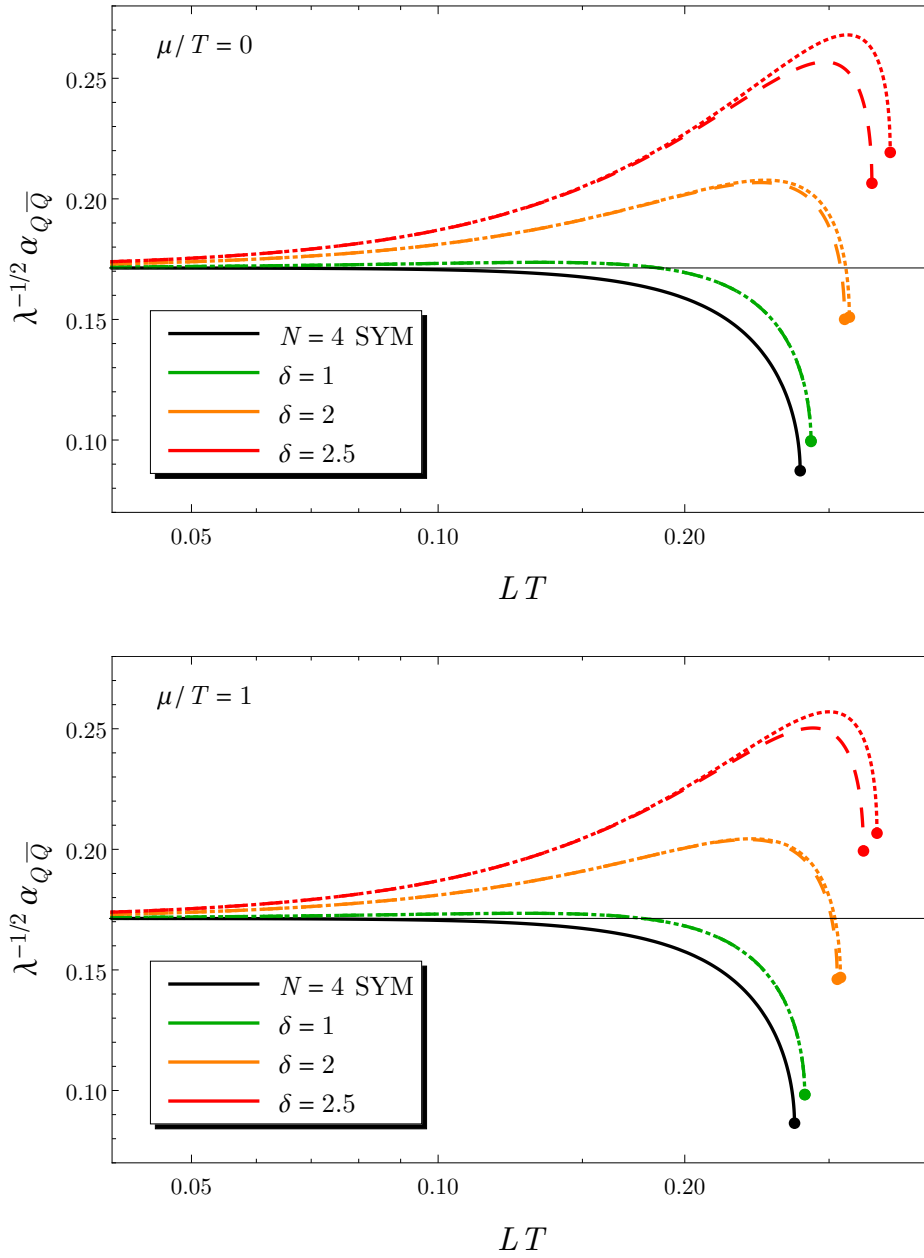
Figure 7.3: Running coupling in the SW$_{T,\mu}$ model (dashed) and in the 1-parameter string-frame model (dotted) at fixed temperature and chemical potential $\mu/T = 0$ (upper panel) and $\mu/T = 1$ (lower panel), for varying deformation parameter δ. The dimensionless deformation parameter is $\delta = c/T$ for the SW$_{T,\mu}$ model and $\delta = \sqrt{\kappa}/T$ for the 1-parameter string-frame model. The thin solid line indicates the UV value, Eq. (7.3), of the coupling in $\mathcal{N} = 4$ SYM. Note the logarithmic LT-axis.
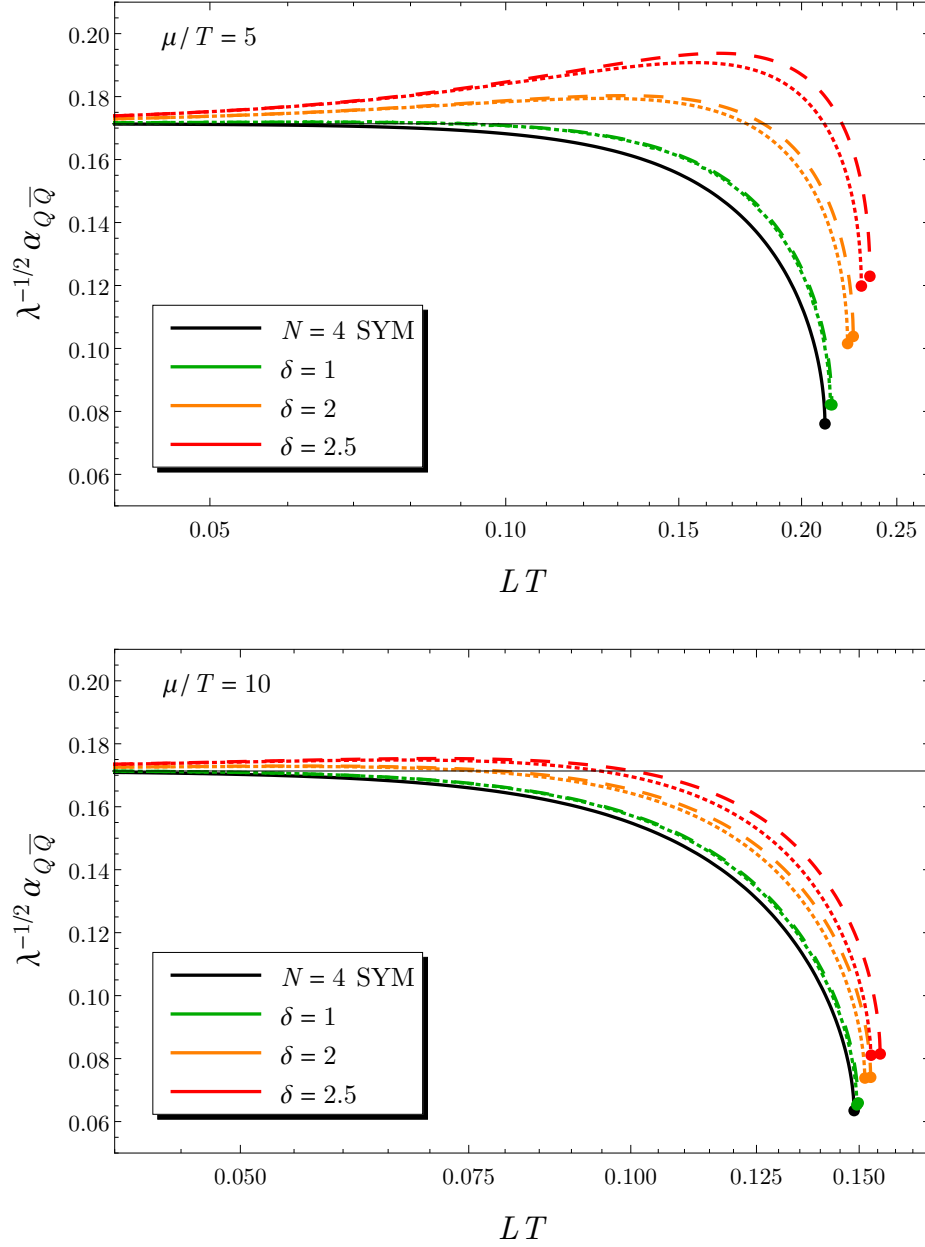
Figure 7.4: Running coupling $\alpha_{Q\bar{Q}}$ in the $\mathrm{SW}_{T,\mu}$ model (dashed) and in the 1-parameter string-frame model (dotted) at fixed temperature and chemical potential $\mu/T = 5$ (upper panel) and $\mu/T = 10$ (lower panel), for varying deformation parameter δ. The dimensionless deformation parameter is $\delta = c/T$ for the $\mathrm{SW}_{T,\mu}$ model and $\delta = \sqrt{\kappa}/T$ for the 1-parameter string-frame model. The thin solid line indicates the UV value, Eq. (7.3), of the coupling in $\mathcal{N} = 4$ SYM. Note the logarithmic LT-axis and the different ranges of the LT axis in the two plots.

will do in the following Sec. 7.4.

Let us now focus on the effect of the chemical potential on $\alpha_{Q\bar{Q}}$. First of all, we notice that the UV value of the coupling is not affected by non-zero μ. This is natural since μ is a scale characterizing the thermal medium surrounding the quarks which becomes unimportant in the UV. Secondly, we observe from the sequence of plots in Figs. 7.3 and 7.4 that an increased chemical potential leads to a decrease in the coupling for intermediate and large distances. In particular, the maximal value of $\alpha_{Q\bar{Q}}$ decreases, as does the screening distance. Apparently, a larger net density of the charge conjugate to μ effectively screens the quarks from each other and weakens their interaction. For large chemical potentials, see the lower panel in Fig. 7.4, the thermal effects set in before the increase in the coupling due to the non-conformality can manifest itself. The maximum almost completely 'melts' away.

Next we turn to a comparison of the impact of the deformation on the behavior of $\alpha_{Q\bar{Q}}$ in the SW$_{T,\mu}$ and 1-parameter string-frame models. We have already noted above that the qualitative behavior of $\alpha_{Q\bar{Q}}$ is similar in the two models. Even the quantitative behavior of $\alpha_{Q\bar{Q}}$ is similar in the two models, *i. e.*, the models yield approximately equal values for the running coupling for equal values of δ. This similarity is somewhat lifted by the inclusion of the chemical potential, as we observe from comparing Figs. 7.3 and 7.4. Overall, the 1-parameter string-frame model is more sensitive to changes in the chemical potential. While for small to intermediate chemical potentials (Fig. 7.3) the running coupling at fixed interquark distance L is slightly larger in the 1-parameter string-frame model than in the SW$_{T,\mu}$ model for all choices of the deformation parameter, this relation is inverted for intermediate to large chemical potentials (Fig. 7.4).

Finally, we note that $\alpha_{Q\bar{Q}}$ computed in the 1-parameter Einstein-frame model is extremely robust under the non-conformal deformation, in accordance with our earlier findings for the physics of this model. Fig. 7.5 shows the running coupling in this model. We have chosen $\mu/T = 1$ as a representative value; the picture is similar for all choices of the chemical potential. We have included the running coupling in $\mathcal{N} = 4$ SYM (black curve), and show the running coupling in the 1-parameter Einstein-frame model for two values of the deformation parameter, $\sqrt{\kappa}/T = 2.5, 2.9$. Note that the latter deformation is very close to the maximally possible deformation for the chosen value of μ, as discussed in Sec. 4.1.4. We see that, despite the fact that for large deformation parameter the running coupling at distances close to the screening distance (slightly) increases from its value in $\mathcal{N} = 4$ SYM, no maximum at intermediate distances is visible. Unfortunately, we cannot decide whether a maximum is present at smaller distances because of increasing numerical imprecision. In any case, even for maximal deformation $\alpha_{Q\bar{Q}}$ in the 1-parameter Einstein-frame model stays very close to the running coupling in $\mathcal{N} = 4$ SYM. The robustness we observe here for $\alpha_{Q\bar{Q}}$ in this model is in line with results on the $Q\bar{Q}$ binding energy in this model obtained in [45].
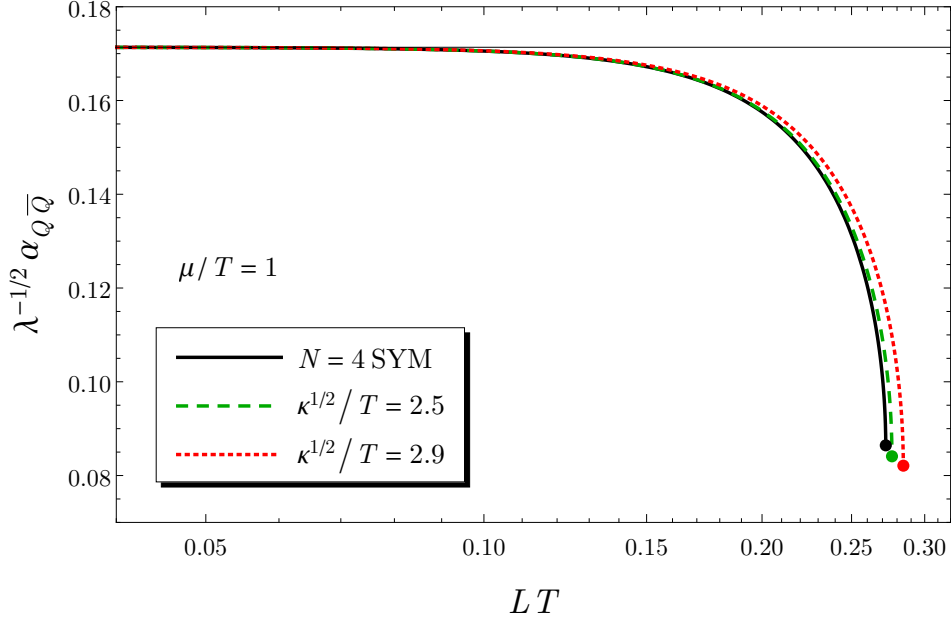
Figure 7.5: Running coupling $\alpha_{Q\bar{Q}}$ in $\mathcal{N} = 4$ SYM and the 1-parameter Einstein-frame model at fixed temperature and chemical potential with $\mu/T = 1$, for $\sqrt{\kappa}/T = 2.5$ and $\sqrt{\kappa}/T = 2.9$, which is close to the maximally possible deformation at the present value of μ. The thin solid line indicates the UV value (7.3) of the coupling in $\mathcal{N} = 4$ SYM.

7.3.1 Robustness With Respect to Choice of Gauge Kinetic Function

Before closing this section, we assess to what degree our results for $\alpha_{Q\bar{Q}}$ depend on the choice of the gauge kinetic function $f(\phi)$ that appears in the action (4.1) from which we have derived the 1-parameter models in Sec. 4.1.3. There, we made two different choices for $f(\phi)$. The explicit solutions for the 1-parameter models can be found in Appendix B. So far, we have studied the models defined by the choice (4.43). Now we compare results to the model defined by the alternative choice (4.44).

Given that $f(\phi)$ couples the scalar field to the gauge field, it can only have an effect in the deformed models at non-zero chemical potential. We have seen above that $\alpha_{Q\bar{Q}}$ shows the strongest dependency on the chemical potential in the 1-parameter string-frame model. In Fig. 7.6 we therefore plot the running coupling $\alpha_{Q\bar{Q}}(L)$ in the 1-parameter string-frame model at fixed temperature and for a large value of the deformation parameter, varying the chemical potential from $\mu/T = 0$ up to $\mu/T = 10$. For each set of parameters, we plot $\alpha_{Q\bar{Q}}$ for both choices of $f(\phi)$. At vanishing chemical potential (black curve), $\alpha_{Q\bar{Q}}$ is insensitive to the choice of the gauge kinetic function, as expected. For all values of the chemical potential chosen in the figure, we observe only small differences between the values for $\alpha_{Q\bar{Q}}$ computed with the different choices of $f(\phi)$. Thus, we conclude that the results obtained
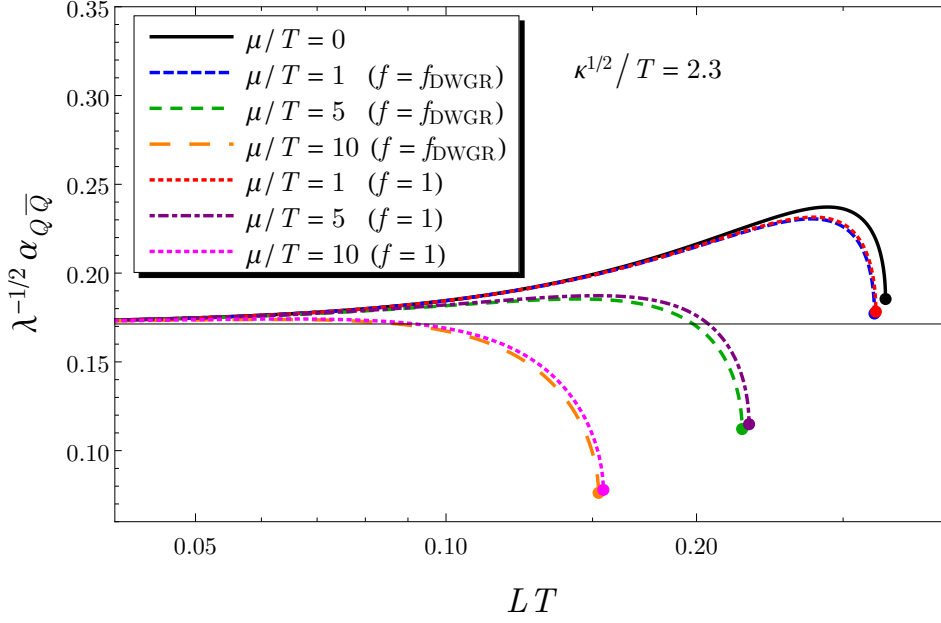
Figure 7.6: Running coupling $\alpha_{Q\bar{Q}}$ in the 1-parameter string-frame model for fixed temperature and deformation with $\sqrt{\kappa}/T = 2.3$, and varying chemical potential. For all parameter choices, we plot $\alpha_{Q\bar{Q}}$ for two choices of the gauge kinetic function, the one used by DeWolfe *et al.*, see Eq. (4.43), and the minimal choice $f(\phi) = 1$. The thin solid line indicates the UV value (7.3) of the coupling in $\mathcal{N} = 4$ SYM.

in this chapter are robust with respect to the choice of the gauge kinetic function. Moreover, as $\alpha_{Q\bar{Q}}$ characterizes the L-dependence of the $Q\bar{Q}$ free energy, this implies that all our results concerning the $Q\bar{Q}$ interaction as described by the free energy should be robust with respect to the choice of $f(\phi)$.

7.4 Maximal Coupling Strength

After our investigation of the running coupling at non-zero chemical potential, we now want to focus on a particular observable at $\mu = 0$ that has not been studied in holography so far. As we have seen, in non-conformal holographic models the running coupling exhibits a maximum. A maximum is also observed on the lattice and it is studied in some detail in [195, 196], so it is worthwhile to compare holographic results on this observable to lattice data. Thus, we are going to investigate the quantity

$$\frac{\alpha_{\max}(T)}{\sqrt{\lambda}} = \max_{L} \left[\frac{\alpha_{Q\bar{Q}}(L, T)}{\sqrt{\lambda}} \right] . \tag{7.4}$$

This quantity depends on temperature and can be understood as a measure of the effective coupling strength at the scale where the thermal medium starts to screen the $Q\bar{Q}$ interaction [231]. We study $\alpha_{\max}$ as a function of the dimensionless temperature ratio $T/T_c \geq 1$. We fix T_c in the holographic models in the same fashion as before, *cf.* Sec. 4.1.4. As we want to compare to lattice data, we work at $\mu = 0$. In our holographic calculation, we focus on the SW_T and 1-parameter string-frame models because, as we have seen above, $\alpha_{Q\bar{Q}}$ in the 1-parameter Einstein-frame model is very robust so we cannot extract a maximal value. In Eq. (7.4), the constant $\sqrt{\lambda}$ is again defined by $\sqrt{\lambda} = L_{\mathrm{AdS}}^2/\alpha'$ and thus has no *a priori* meaning in the boundary theory in the non-conformal models. We will estimate the value of $\sqrt{\lambda}$ from the comparison with lattice data.

In Fig. 7.7 we compare $\alpha_{\max}$ computed in our holographic models with data from lattice QCD. Fig. 7.7a shows $\alpha_{\max}$ in the holographic models, whereas in Fig. 7.7b lattice data from quenched and unquenched simulations are collected ([231], and references therein). In both cases, a temperature range from $T = T_c$ to $T = 3\,T_c$ is plotted. We observe that the increase of $\alpha_{\max}$ as T approaches T_c from above that is seen in the lattice data is reproduced by the holographic models. This increase it stronger in the consistent 1-parameter string-frame model than in the *ad hoc* SW_T model. At larger T, there is a qualitative difference between holography and lattice QCD: Whereas $\alpha_{\max}$ on the lattice decreases continuously with increasing temperature, it approaches some constant value in the holographic models. This can be understood from our discussion in Sec. 7.3. We have seen that the thermal medium tends to decrease the coupling strength of the quarks. At higher T, the screening by the medium sets in at smaller distance, so that the maximum in $\alpha_{Q\bar{Q}}$ due to the non-conformality gradually 'melts' away and $\alpha_{\max}$ decreases. Since for small distances in all of our models $\alpha_{Q\bar{Q}}$ reduces to its value in the vacuum of $\mathcal{N} = 4$ SYM this vacuum value is a lower bound for $\alpha_{\max}$, which is approached from above as the temperature increases. To illustrate this, we have marked the value of $\alpha_{Q\bar{Q}}$ in the vacuum of $\mathcal{N} = 4$ SYM, see Eq. (7.3), by a thin black line in Fig. 7.7a.

By quantitatively comparing our holographic results to the lattice data, we can produce a rough estimate for the value of the constant λ that we have left undetermined in our holographic models. From the lattice data shown in Fig. 7.7b, we read off a typical value $\alpha_{\max} \sim 0.7$ for temperatures slightly above T_c. On the holographic side, for temperatures slightly above T_c we obtain $\alpha_{\max}/\sqrt{\lambda} \sim 0.2$ in the SW_T model, and $\alpha_{\max}/\sqrt{\lambda} \sim 0.25$ in the 1-parameter string-frame model. Comparing, we arrive at $\sqrt{\lambda} \sim 3.5$ and $\sqrt{\lambda} \sim 2.8$, or equivalently $\lambda \sim 12$ and $\lambda \sim 7.8$, for the SW_T model and 1-parameter string-frame model, respectively. The lattice data for $\alpha_{\max}$ from the different lattice simulations shown in Fig. 7.7b are scattered around our reference value 0.7, with deviations of approximately $25\,\%$ in either direction. As in our estimate of λ based on the single-quark entropy S_Q in Sec. 5.5, we take this spread of the lattice data as the relative uncertainty for our estimates of $\sqrt{\lambda}$. This results in a relative uncertainty of $\pm 50\,\%$ for λ. In [126], a value $\lambda = 5.5$ was determined as a representative value from a range of values that, according to that work,
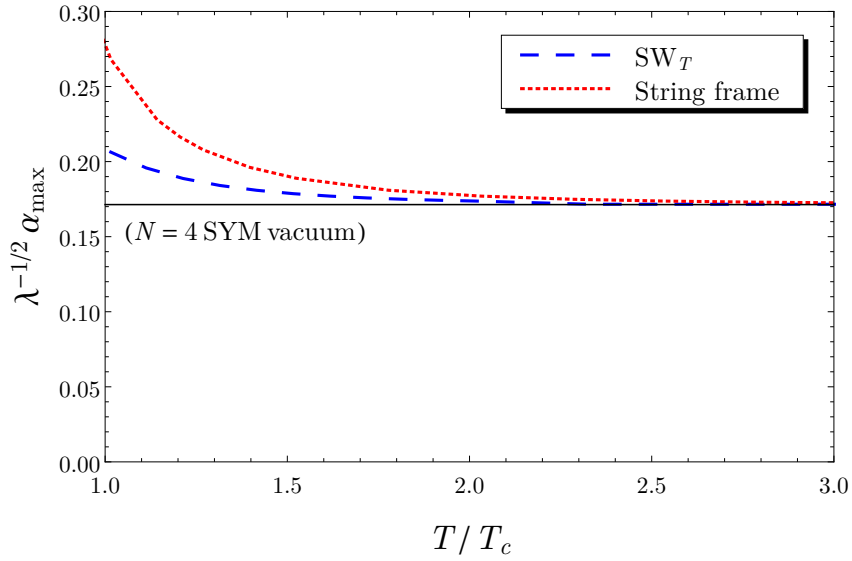
(a) Maximum of the running coupling in the SW_T and 1-parameter string-frame models. We have set $\mu = 0$ for this plot. The straight thin black line indicates the value of the running coupling in the $T = 0$ vacuum of $\mathcal{N} = 4$ SYM for comparison.
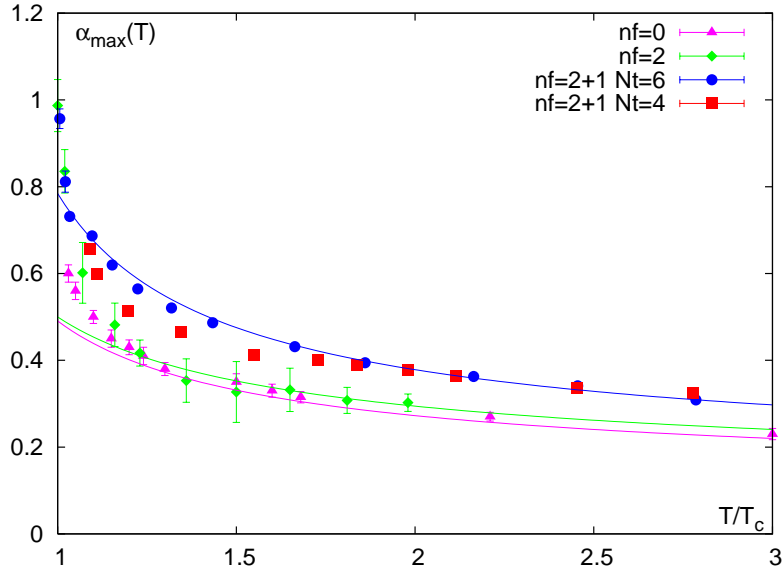
(b) Maximum of the running coupling in various lattice studies without (magenta symbols) and with (green, blue, red symbols) dynamical quarks. Figure taken from [231]. The solid lines are fits that are not important for our purposes.

Figure 7.7: Comparison of the maximum $\alpha_{\max}$ of the running coupling as a function of temperature in our holographic models (upper panel) and lattice QCD studies (lower panel).

should be used in $\mathcal{N} = 4$ SYM calculations for the closest-possible approximation of QGP physics. That estimate is roughly consistent with our estimates, obtained in non-conformal models. Interestingly, there seems to be a tendency towards larger values of λ in non-conformal models.

As before, we take the fact that λ is estimated considerably larger than 1 as an indication for self-consistency of the computational framework employed, in particular the use of the classical approximation in the bulk. The present estimates are in between our previous estimates on the basis of the single-quark entropy in Sec. 5.5 on the one hand, and on the basis of the coefficient $f^{(2)}$ in the (μ/T)-Taylor expansion of the $Q\bar{Q}$ free energy in Sec. 6.4 on the other.

7.5 Distance of Maximal Coupling

In the previous section, we have studied the maximal value of the running coupling and its dependence on temperature at vanishing chemical potential, where we could compare to lattice-QCD data. In this section, we investigate the behavior of the associated length scale $L_{\max}$ at which the running coupling assumes its maximum value, and we return to studying the full μ-dependency. We have seen above that, at least in the $SW_{T,\mu}$ and 1-parameter string-frame models, introducing non-conformality tends to increase the coupling and leads to a maximum in $\alpha_{Q\bar{Q}}$, whereas thermal effects associated with the scales T and μ decrease the coupling. We surmise that $L_{\max}$ can broadly be understood as the scale at which the effects of the thermal medium become more important than the non-conformality. Note that this does not imply that at this scale the thermal effects already dominate the behavior of $\alpha_{Q\bar{Q}}$.

To set the stage, let us first discuss the behavior of $L_{\max}$ at vanishing chemical potential. The author of Ref. [113] finds in the SW_T model that $L_{\max} \sim T^{-2}$. On dimensional grounds it follows that this leading-order scaling behavior can be refined as $L_{\max} \sim c/T^2$ with c the deformation parameter. This makes manifest the fact that the appearance of the maximum is an effect of the non-conformality. In fact, it appears that at least in the SW_T model the relative magnitude of the subleading terms in c/T are small. Similarly, we find that the leading-order scaling in the 1-parameter string-frame model is $L_{\max} \sim \sqrt{\kappa}/T^2$. In lattice QCD, the scaling of $L_{\max}$ is different from the behavior in our holographic models. To wit, [195] finds $L_{\max} \sim 1/T$ for temperatures up to $12\,T_c$. This might be taken as a hint that there is a different mechanism at work that leads to the appearance of the maximum in the holographic models as compared to QCD. Indeed, in QCD the rise of the coupling with increasing distance is, at least for small distances, a perturbative phenomenon, whereas in our strongly coupled non-conformal holographic theories it is likely of non-perturbative origin.

In any case, $L_{\max}$ is an interesting scale for the physics of our models, so let us study its behavior at non-zero chemical potential. We note from Figs. 7.3 and 7.4 that, like at $\mu = 0$, also at non-zero μ the distance $L_{\max}$ increases with increasing
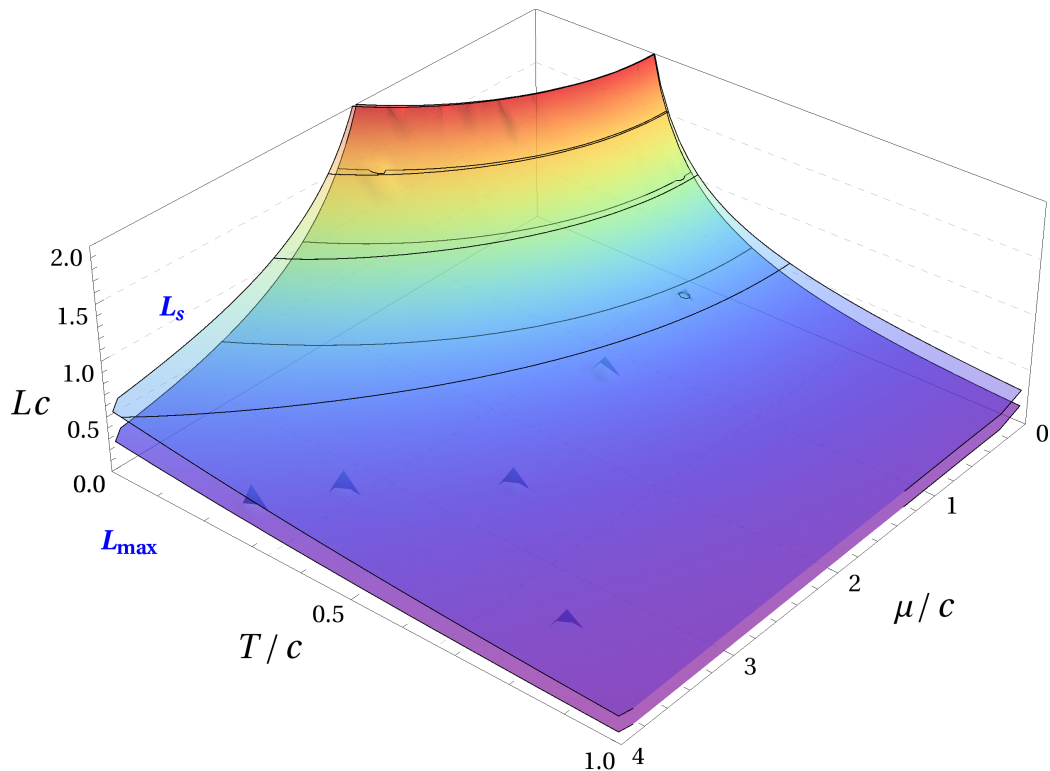
Figure 7.8: Distance of maximum $Q\bar{Q}$ coupling $L_{\max}$ (lower surface) and screening distance L_{s} (upper surface) as functions of the temperature and chemical potential in the $\mathrm{SW}_{T,\mu}$ model at fixed deformation c, in units of which we have expressed all dimensionful quantities. Note the different range of the T/c- and μ/c-axis.

non-conformality. For a quantitative investigation in the (μ, T)-plane we focus on the $\mathrm{SW}_{T,\mu}$ model because, while the numerical cost for computing $L_{\max}(T, \mu)$ is still large in this model, it is considerably smaller than in the consistent models. Moreover, from the discussion of our data in Figs. 7.3 and 7.4 we expect that the results obtained in the $\mathrm{SW}_{T,\mu}$ model will be robust and qualitative conclusions will also hold in the 1-parameter string-frame model. Figure 7.8 shows the distance $L_{\max}$ and, for comparison, the screening distance L_{s} in the (μ, T)-plane for fixed deformation c. Both L_{s} and $L_{\max}$ decrease with the thermodynamic variables T and μ. We observe that for all μ and T the screening distance L_{s} is larger than the distance of maximal coupling $L_{\max}$, as the latter decreases more quickly with T and μ. Phrased differently, our holographic models resolve, in the whole (μ, T)-plane, the increase and subsequent decrease of the running coupling before the screening distance is reached, at which point further string configurations in the basic equation (5.3) would be required as discussed in Sec. 6.4. Since thermal effects clearly dominate at the screening distance, this is evidence supporting our interpretation of $L_{\max}$ as
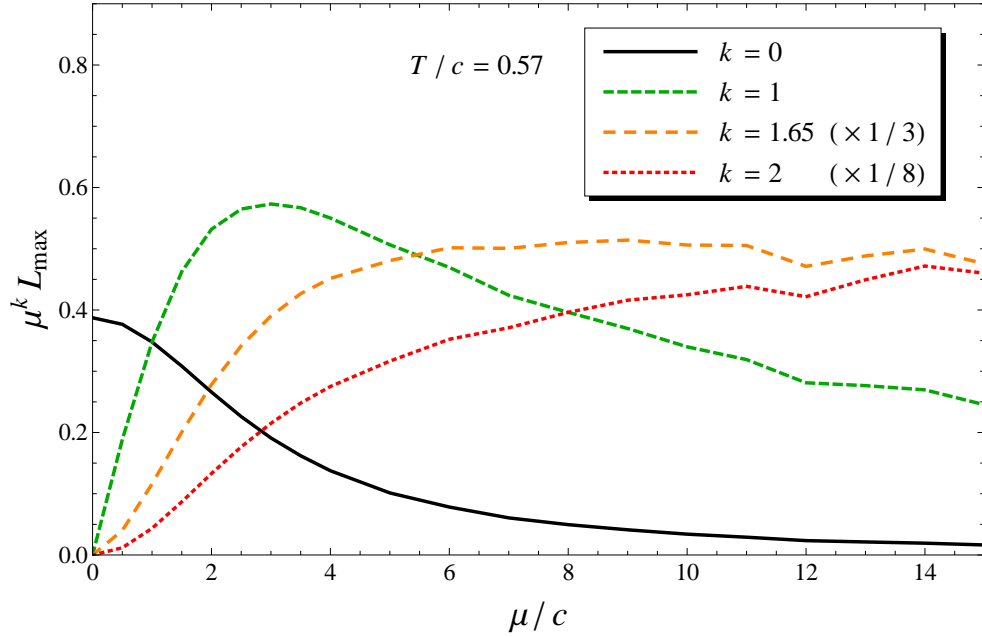
Figure 7.9: The length scale L_{max} in the $\text{SW}_{T,\mu}$ model as a function of the chemical potential at fixed temperature and deformation, scaled by various powers of the chemical potential, as given by the exponent k. Note that we have rescaled the curves for $\mu^{1.65}L_{\text{max}}$ (orange dashed) and $\mu^2 L_{\text{max}}$ (red dotted) by $1/3$ and $1/8$, respectively.

the scale at which thermal effects become more important than the effect of the non-conformality.

Not only T, as discussed above, but also μ appears to have a parametrically stronger impact on L_{max} than on L_{s}. We have found in [45] that for very large chemical potential, $\mu \gg T$, the screening distance behaves universally like $L_{\text{s}} \sim \mu^{-1}$ at fixed T. Fig. 7.8 indicates that the leading-order dependence of L_{max} on μ is stronger than $\sim \mu^{-1}$. Let us investigate the dependence of L_{max} on μ in more detail. To this end, we plot in Fig. 7.9 the scale L_{max} scaled by various powers of the chemical potential at fixed temperature and deformation c as a function of μ/c. The black solid curve shows the decrease of the unscaled L_{max} with the chemical potential. The green dashed curve represents μL_{max}. From it we see that the possibility of a large-μ scaling of the form $L_{\text{max}} \propto \mu^{-1}$ is ruled out, so that the decrease of L_{max} with μ is in fact stronger than that of the screening distance. This explains the behavior seen in Fig. 7.8. The red dotted curve shows $\mu^2 L_{\text{max}}$. We have explored a large range of values for μ in Fig. 7.9, ranging from $\mu/T = 0$ to $\mu/T \approx 26$.[ae] Over this range $\mu^2 L_{\text{max}}$ does not approach a constant value but rather continues to increase. This is opposed to the case of the scaling for large

---

[ae]Regarding the interpretation of such large values for μ/T, *cf.* our remarks in footnote (ad).

temperature, where we find that $L_{\max}T^2$ is near-constant for $T/c \gtrsim 1$. The non-integer scaling $L_{\max} \sim \mu^{-1.65}$, found by manually varying the exponent, appears to parametrize the large-μ behavior of $L_{\max}$ best, but in fact that might change at still larger μ. While it would certainly be interesting to explore this in more detail, we were unfortunately not able to extend the numerics to larger values of the chemical potential in order to test these findings under more extreme conditions. In any case, a robust conclusion appears to be that, while the temperature strongly affects $L_{\max}$ and an asymptotic range where it dominates the behavior of $L_{\max}$ is reached quickly, the effect of μ is weaker in the sense that an asymptotic scaling regime appears to be reached only at large μ/c, or equivalently, large μ/T.

This concludes our discussion of the running coupling $\alpha_{Q\bar{Q}}$ derived from the heavy quark–anti-quark free energy. The running coupling in non-conformal models is found to be either very robust, deviating little from the case of $\mathcal{N} = 4$ SYM (1-parameter Einstein-frame model), or it increases above the value in $\mathcal{N} = 4$ SYM, giving rise to a maximum at intermediate quark separations ($\mathrm{SW}_{T,\mu}$ and 1-parameter string-frame models). The latter two models are in this respect qualitatively similar to QCD. For these models, for vanishing chemical potential we have compared the maximum value of the running coupling to lattice QCD data and found a reasonable estimate for the parameter λ in the holographic models. At non-zero chemical potential, we have found that the increase above the UV value of the coupling persists such that $\alpha_{Q\bar{Q}}$ always assumes a maximum. Furthermore, we have studied the scaling of the length scale $L_{\max}$ associated with the maximum of the running coupling in the (μ, T)-plane. The overall picture is that the impact of the chemical potential on $\alpha_{Q\bar{Q}}$ is considerably weaker than that of the temperature.

8 Summary

In the first part of this thesis, we have studied heavy quarks as probes of a strongly coupled, deconfined gauge-theory plasma, with the quark–gluon plasma as the corresponding real-world system in mind. We have studied both single quarks and bound quark–anti-quark pairs which are models of heavy quarkonia like J/ψ or Υ, using $\mathcal{N} = 4$ SYM theory and a large class of non-conformal holographic models that we have constructed in Chap. 4 as deformations of $\mathcal{N} = 4$ SYM. Generally, we have included a chemical potential and have studied its effect on our physical observables.

We started in Chap. 5 with a thorough review of the holographic computation of energies associated with the interaction of a heavy quark–anti-quark pair (Sec. 5.1). Regarding this computation there has apparently been some confusion in the literature. The calculation involves the renormalization of the UV-divergent, $i.\,e.$ near-boundary-divergent, extremal Nambu–Goto action of a bulk string representing the bound $Q\bar{Q}$ pair. We have studied a general renormalization scheme which we have argued can be used to compute the $Q\bar{Q}$ free energy in any asymptotically AdS spacetime. Using this scheme, the free energy becomes independent of the thermodynamic variables for small distances L as expected on physical grounds. Indeed, we have verified that when increasing the temperature the free energy that we have computed for all our holographic models from the advocated renormalization scheme (Secs. 5.2 and 5.3) qualitatively behaves like the $Q\bar{Q}$ free energy that has been obtained in lattice QCD studies. Moreover, going beyond the thermodynamic regime accessible in lattice QCD, we have found in our models that the chemical potential has an effect on the free energy that is analogous to that of the temperature, $i.\,e.$, the free energy decreases upon increasing the chemical potential.

We have shown that the procedure commonly used in the literature for the aforementioned renormalization of the extremal Nambu–Goto action does not give rise to the $Q\bar{Q}$ free energy. Rather, it leads to a quantity that can be interpreted as a binding energy as we have demonstrated by studying its dependence on the thermodynamic variables T and μ. Increasing either of these scales leads to a reduced binding energy for a fixed quark separation. This nicely leads to a picture of melting induced by increasing chemical potential in analogy to the picture of 'melting' at high temperature [92]. In fact, this finding of the impact of the chemical potential is robust and holds in all our models. Interestingly, we have furthermore found that the qualitative behaviors of the free energy $F_{Q\bar{Q}}$ and the binding energy $E_{Q\bar{Q}}$ under non-conformal deformation are opposites of one another. Whereas $F_{Q\bar{Q}}(L)$ at fixed L increases with increasing non-conformality, $E_{Q\bar{Q}}(L)$ decreases. This is a clear distinction of the two quantities. Another important difference is that, unlike the free energy, the binding energy manifestly depends on temperature and chemical poten-

tial at small quark separations which precludes its interpretation as an effective $Q\bar{Q}$ potential.

For small quark separation L, the free energy becomes independent of the model that we consider and approaches a universal, Coulombic curve, namely the vacuum potential $V_{Q\bar{Q}}(L)$ given in Eq. (5.17) which was first obtained in [105]. Given this common small-L behavior, we can compare the free energy in different models. Under non-conformal deformations, we have found that the free energy changes only very little in the 1-parameter Einstein-frame models. In the $\mathrm{SW}_{T,\mu}$ and 1-parameter string-frame models, on the other hand, the free energy increases above its value in $\mathcal{N} = 4$ when switching on the non-conformality. Thus we conclude that the free energy in $\mathcal{N} = 4$ SYM constitutes an approximate lower bound in a large class of non-conformal models. The internal energy that we have derived from the free energy exhibits an analogous behavior (Sec. 5.4). Here, too, the value in $\mathcal{N} = 4$ SYM seems to mark an approximate lower bound among all our models.

Analogously, we have computed the free energy, entropy, and internal energy associated with single heavy quarks in the strongly coupled plasmas described by our models, and have systematically studied the impact of the non-conformality (Sec. 5.5), an analysis which has not been done so far in the literature. In $\mathcal{N} = 4$ SYM, those three quantities are either temperature-independent (entropy and internal energy) or depend trivially on temperature (free energy $F_Q \propto T$), in accordance with conformal invariance. In non-conformal models, however, a non-trivial temperature dependence arises which is qualitatively similar to lattice QCD results for the deconfined phase, $T \geq T_c$. Moreover, for all temperatures we have found a universal increase of all three quantities above the respective value in $\mathcal{N} = 4$ SYM in all our non-conformal models.

Furthermore, in Chap. 6 we have studied a Taylor expansion of the free energy in powers of (μ/T) and have compared the leading non-trivial coefficient $f^{(2)}$ to lattice QCD data. Such a comparison has not been done before in the literature. We have found that in our holographic models $f^{(2)}$ is remarkably robust under non-conformal deformation. This implies that, as the effect of the chemical potential on the free energy is only mildly moderated by the deformation, the effect of the chemical potential on the quark interaction is similar in all our models, at least for small μ. We might thus hope that this is a universal feature that applies to QCD as well. Now, in comparing $f^{(2)}$ from our holographic models to lattice data on $f^{(2)}$, we have found that the overall features of $f^{(2)}$ compare qualitatively well. We conclude that the simple 'holographic' chemical potential indeed models important aspects of the baryon (or quark) chemical potential in QCD.

In the last chapter 7, we have investigated the running coupling $\alpha_{Q\bar{Q}}(L)$ as a means to clearly expose the distance dependence of the heavy quark–anti-quark interaction. Non-conformal models at vanishing chemical potential exhibit a maximum in $\alpha_{Q\bar{Q}}(L)$ [113], as does the analogous quantity in lattice QCD. While for the $\mathrm{SW}_{T,\mu}$ and 1-parameter string-frame models we have clearly found that this maximum continues to exist at non-zero chemical potential, $\alpha_{Q\bar{Q}}(L)$ in the 1-parameter Einstein-frame turns out to be so robust against non-conformal deformation that the

Table 8.1: Rough estimates for the parameter λ in non-conformal models from comparisons of three different observables with lattice-QCD data. The values are associated with considerable relative uncertainties (see text). There is no estimate for λ from $\alpha_{\max}$ in the 1-parameter Einstein-frame model because we cannot identify a clear maximum in $\alpha_{Q\bar{Q}}(L)$ in that model due to its robustness.

	observable		
model	$S_Q(T_c)$	$f^{(2)}(L \sim L_s)$	$\alpha_{\max}(T \sim T_c)$
SW_T	63	~ 6	12
1-parameter string	26	~ 6	7.8
1-parameter Einstein	115	~ 6	—

question of whether $\alpha_{Q\bar{Q}}$ assumes a maximum could not be settled. Generally, as the chemical potential increases, the maximum seen in the $\mathrm{SW}_{T,\mu}$ and string-frame models 'melts' away which clearly indicates a screening effect due to the charge density associated with the chemical potential. We furthermore have studied the maximal value of the running coupling and the associated length scale. We have investigated the scaling of the latter with temperature and chemical potential, which corroborates the overall picture that has emerged from our study of $\alpha_{Q\bar{Q}}(L)$, namely that in all of our models the impact of the chemical potential on the heavy quark–anti-quark interaction is considerably weaker than that of the temperature. As we have found this in a large class of non-conformal models for strongly coupled plasma, it seems to be a robust conclusion with potential applications to QCD.

Finally, in the non-conformal models we have a parameter λ, defined in the bulk, that has no *a priori* meaning in the boundary theory, but can tentatively be thought of as controlling the coupling strength of the boundary theory, as in the undeformed case, *i.e.* $\mathcal{N} = 4$ SYM. Throughout Part I we have compared three different observables computed in our non-conformal models to data from lattice QCD and thus produced a number of estimates for the value of λ. These observables are the single-quark entropy S_Q at T_c (Sec. 5.5), the Taylor coefficient $f^{(2)}$ close to the screening distance (Sec. 6.4), and the maximal value of the running coupling $\alpha_{\max}$ close to T_c (Sec. 7.4), all of them evaluated for vanishing chemical potential, where lattice data are available. The estimates we have found are summarized in Table 8.1. No estimate for λ could be obtained from $\alpha_{\max}$ in the 1-parameter Einstein-frame model because that model does not exhibit a clear maximum, $\alpha_{Q\bar{Q}}(L)$ remaining very close to $\mathcal{N} = 4$ SYM even for large non-conformal deformation. As discussed in the determination of the estimates, they are associated with large relative uncertainties. From the spread of the lattice data on S_Q and $\alpha_{\max}$, we have estimated a relative uncertainty of λ of $\pm 50\,\%$ in both cases. On qualitative grounds, we expect the relative uncertainty in the determination of λ from $f^{(2)}$ to be at least of the same size, given

the few lattice data points to which we have compared our holographic data, *cf.* the discussion in Sec. 6.4. Focusing then on the SW_T and 1-parameter string-frame models and the two observables other than $f^{(2)}$, we see that within either model the two estimates for λ are within a factor $\lesssim 6$ of each other. For an exact holographic dual of QCD, within the uncertainty we would expect the same estimated value for λ for all observables. In this sense, our 1-parameter string-frame model appears to be most QCD-like, while the very robust 1-parameter Einstein-frame model stays close to $\mathcal{N} = 4$ SYM and thus appears to be least QCD-like. The $SW_{T,\mu}$ model, despite arising from an *ad hoc* deformation of the metric, is in-between the other two models in the above sense. For all models, interpreting λ as a measure of the coupling strength, the values found are sufficiently large as to pass an important self-consistency check of our approach: Working in the classical-gravity limit in the bulk implies a strongly coupled boundary theory, and with interpreting λ as a proxy for coupling strength (this identification is exact for $\mathcal{N} = 4$ SYM) the boundary theories indeed are strongly coupled.

Part II

Cold: Non-Equilibrium Dynamics in a Holographic Superfluid

9 Motivation and Overview

Now we switch gears and apply gauge/gravity duality to another class of extreme matter, namely cold superfluids. We will focus on systems in two spatial dimensions. Systems that one should have in mind include oblate, quasi-2D ultracold atomic gases (see *e. g.* [232]) or semiconductor-based exciton–polariton condensates (see *e. g.* [20] for a review), in the nanokelvin or few-kelvin temperature range, respectively. We consider a holographic model for a strongly correlated superfluid and study the non-equilibrium dynamics ensuing after an initial quench that takes the system to a far-from-equilibrium state.

The non-equilibrium time evolution of a $(2 + 1)$-dimensional holographic superfluid without imposing symmetries which effectively reduce the dimensionality of the system has been studied so far in [233–236]. The present Part II of this thesis is mainly based on our publication [235] which is the first study of the holographic superfluid in view of possible long-time non-equilibrium universality. Some of the material has been rearranged and extended.

Let us now discuss the motivation for our work in more detail. Studies of far-from-equilibrium time evolution of quantum many-body systems have intensified considerably during recent years, driven mainly by new technological possibilities. For example, strongly non-linear dynamics has been observed in ultracold atomic gases [237–242], or semiconductor exciton–polariton superfluids [243–246]. Moreover, high-energy heavy-ion collision experiments have brought up many questions concerning the thermalization of the quark–gluon plasma, *cf.* [247] and references cited therein. Interactions between the constituents of these systems can lead to strong correlations, which render the description of the long-time dynamics intricate and give rise to non-trivial many-body states far from equilibrium. In the case of strong interactions, a quantitative description of dynamical evolution is typically plagued by the absence of suitable approximation techniques, or by technical difficulties such as sign problems when evaluating the dynamics by means of numerical methods. Similarly complicated situations can arise even when a weakly interacting system becomes strongly correlated. In such cases, non-linear excitations can dominate the system's dynamics such as solitary waves or topological defects. In quantum many-body systems the massive appearance of such excitations and their interactions can give rise to quantum turbulence phenomena, *i. e.*, to states the statistical properties of which bear resemblance to correlations observed in classical turbulent systems.

Holographic methods have in recent years opened new vistas on strongly correlated quantum systems, as they allow one to study the dynamical real-time evolution of a strongly correlated many-body quantum system in a genuinely non-perturbative

framework. Remarkably, the intricate dynamics of the system – including its far-from-equilibrium behavior – is entirely captured by a classical gravitational system. Evidently, the holographic description therefore offers the potential to address phenomena in the quantum system which are notoriously difficult to access by other methods. It even carries the promise to discover new phenomena that are unique to strong-coupling situations. Accordingly, holographic methods have in recent years been applied to various condensed-matter quantum systems, for reviews see for instance [5–7]. A particularly interesting discovery is that there are gravitational systems which have a dual interpretation in terms of superconductors or superfluids in $2+1$ dimensions [248–250]. Here, the dual gravitational description is in terms of an Abelian Higgs model on and coupled to a $(3+1)$-dimensional spacetime of negative cosmological constant, an anti-de Sitter spacetime. The breaking of the Abelian $U(1)$ symmetry at low temperature is associated with the condensation of an order-parameter field and can be interpreted as the emergence of superconductivity or superfluidity.

In this thesis, we will consider a holographic superfluid of this kind at finite temperature and with a chemical potential for the $U(1)$ charge. In this system, vortex excitations exist in the superfluid phase without the presence of an external magnetic field.[af] The system we consider is a $(2+1)$-dimensional relativistic superfluid. Studies of various aspects of that particular holographic superfluid include [251–253]. A study of its time-evolution as it relaxes from a far-from-equilibrium initial state, corresponding to an ensemble of vortex defects, was performed in [233]. There, the authors numerically solve the gravitational Einstein–Maxwell–scalar system dual to this superfluid. They have identified a certain regime in the evolution in which the superfluid exhibits Kolmogorov scaling. In this thesis, we perform a similar numerical analysis of the same system. As in [233] we treat the holographic superfluid in the so-called probe limit in which the AdS spacetime in the dual gravitational description is kept fixed. Our numerical methods are sufficiently fast to allow us to investigate three new aspects of the far-from-equilibrium evolution of the superfluid. Firstly, we follow the system's evolution for a very long time. Secondly, we study various initial conditions, in particular, we choose random distributions as well as lattices of vortex defects of different densities. This makes it possible to clearly identify the time scales at which the system enters a universal regime. Thirdly, we vary the thermodynamic parameters of the system in order to explore the dynamics for different temperatures within the superfluid phase.

In particular the investigation of the late-time behavior of the system leads us to a very interesting observation. Following the propagation and annihilation of the quantum vortices in time, we are able to observe a stage of universal critical dynamics arising in the late-time evolution of the superfluid when the quantum turbulent ensemble relaxes towards equilibrium. More specifically, we observe how

---

[af]This is opposed to the case of a holographic superconductor. For a more detailed discussion of the differences between holographic superfluids and holographic superconductors in view of the corresponding vortex solutions see for example [251].

the system approaches a non-thermal fixed point, *i. e.*, a far-from-equilibrium field configuration exhibiting universal scaling behavior [254, 255]. We will demonstrate how the approach to this fixed point can be related to the dynamics of vortex defects in the order-parameter field. Non-thermal fixed points were identified, in quantum field theory, as stationary solutions of non-perturbative equations of motion for Green functions [254, 256, 257]. In the context of non-relativistic Bose gases as well as of relativistic scalar and gauge theories it was shown that superfluid turbulence, related to characteristic distributions of vortex defects [258, 259] or more general non-linear excitations [260–262], can be interpreted in terms of non-thermal fixed points. General universality classes of such non-thermal fixed points are expected to emerge from a renormalization-group analysis which includes scaling in space and time [263, 264].

While non-thermal fixed points have been discussed in various contexts their properties in strongly coupled systems have not yet been explored before. The present work is the first analysis of the holographic, strongly coupled, superfluid in view of the approach to a non-thermal fixed point, comparing universal and non-universal stages of the superfluid's evolution. It opens a new and exciting perspective on time evolution as described in a holographic setting, in particular on the mutual implications of such universal dynamics on both the gravity and the boundary-theory sides.

This part of this thesis is organized as follows. In Chap. 10 we discuss the definition and the properties of the Einstein–Maxwell–scalar gravity model dual to the superfluid, as well as the implementation of the resulting equations within our numerical approach. Chap. 11 contains the details about the different initial conditions considered and summarizes basic properties of vortices in superfluids. Further in that chapter, we present our numerical results on the evolution of the vortex characteristics and of the statistical properties of the ensembles, in particular on occupation number spectra of the boundary theory. Then we discuss the holographic perspective on the non-thermal fixed point in the superfluid's evolution. The non-equilibrium dynamics takes place on top of a heat bath with a well-defined temperature and chemical potential, as we shall explain. To study general properties of the system's dynamics, in Chap. 11 we fix the temperature and chemical potential to one particular set of values. In Chap. 12 we assess the robustness of our results and the temperature dependence of certain observables by studying three further choices of the thermodynamic parameters of the heat bath. We summarize our results in Chap. 13.

10 Holographic Superfluid

In this chapter, we set out the holographic framework for describing the dynamics of a superfluid in $2+1$ dimensions by means of a gravitational dual in a $(3+1)$-dimensional (generally asymptotically) AdS spacetime. We first review the standard holographic-superfluid model (Sec. 10.1). Then, we discuss in detail the construction of thermal solutions associated with the model as well as the full system of equations of motion that encode the non-equilibrium physics (Secs. 10.2–10.4).

10.1 Gravity Model Dual to the Superfluid

The holographic framework for superfluidity was laid down in [248–250]. A scalar field is dynamically coupled to an Abelian gauge theory and gravity on a $(3+1)$-dimensional spacetime with a negative cosmological constant. We use the action

$$S = \frac{1}{16\pi G_{\mathrm{N}}^{(4)}} \int \mathrm{d}^4 x \sqrt{-g} \left(\mathcal{R} - 2\Lambda + \frac{1}{q^2} \mathcal{L}_{\mathrm{matter}} \right) ,$$

$$\mathcal{L}_{\mathrm{matter}} = -\frac{1}{4} F_{MN} F^{MN} - |D_M \Phi|^2 - m^2 |\Phi|^2 .$$

(10.1)

Here, $G_{\mathrm{N}}^{(4)}$ is the Newton constant in four dimensions, and the cosmological constant is $\Lambda = -3/L_{\mathrm{AdS}}^2$, *cf.* Eq. (2.13) and our general discussion of D-dimensional AdS spacetime in Sec. 2.1.3. L_{AdS} sets the curvature scale of the spacetime which arises as a solution of the corresponding Einstein equations. $\mathcal{R}$ is the Ricci scalar constructed from the metric g_{MN}, and g is the determinant of that metric. (See Appendix A for our gravity and index conventions.) The Lagrangian density $\mathcal{L}_{\mathrm{matter}}$ accounts for the gauge field A_M, with the associated field-strength tensor $F_{MN} = \nabla_M A_N - \nabla_N A_M$, and for the scalar field Φ. Here, ∇_M denotes the covariant derivative associated with the Levi-Civita connection. The local $U(1)$ gauge symmetry of the Lagrangian is implemented by upgrading ∇_M to the gauge-covariant derivative $D_M = \nabla_M - \mathrm{i}A_M$.

By the holographic dictionary reviewed in Sec. 2.2, the gauge potential A_M in the bulk induces a global $U(1)$ symmetry of the dual field theory. The operator dual to A_M is the conserved $U(1)$ current j^μ which arises from that symmetry. Finally, the complex scalar field Φ has mass m and charge q which, by suitable rescaling of the fields, has been pulled out of $\mathcal{L}_{\mathrm{matter}}$. If the gravity is taken to be dynamic, q thus quantifies the coupling between the gravity and gauge–matter parts of the model.

Solving the gravity model (10.1) allows us to obtain information about the dynamical evolution of a superfluid described by the boundary theory. A superfluid is commonly described by a complex scalar field ψ which, in the symmetry-broken

phase, assumes a non-vanishing expectation value $\langle\psi\rangle \neq 0$ reflecting the presence of a Bose–Einstein condensate. In our holographic model, the field operator ψ is dual to the scalar field Φ, as we explain in detail in Sec. 10.2 below. The solutions of the equations of motion of the model (10.1) are subject to boundary conditions in the holographic direction. These conditions determine the temperature and the chemical potential for the $U(1)$ charge density j^0 in the $(2+1)$-dimensional boundary theory, as discussed in Sec. 2.2. In particular, the temperature and chemical potential can be chosen such that the boundary theory is in the symmetry-broken phase with a condensate, $\langle\psi\rangle \neq 0$ [248], as we will discuss in detail in Sec. 10.3. Holography allows us to compute the time evolution of the quantum expectation value $\langle\psi\rangle$ starting from various far-from-equilibrium states by solving the classical dynamics of (10.1). In fact, we also have access to the phase angle of the complex field $\langle\psi\rangle$ the spatial variation of which encodes information about the superfluid flow. We will use this to construct far-from-equilibrium initial states.

In this work, we consider the so-called probe limit of the action (10.1) in which the backreaction of the fields Φ and A_M on the metric is neglected. This is a good approximation for large scalar charge q, as is clear from the rescaled form of the action (10.1), with $1/q^2$ entering as a small pre-factor of the gauge–matter Lagrangian, see for example [249, 265]. We can thus treat the gravity and matter parts separately.

Ignoring for the moment the gauge–matter part of the model, the vacuum Einstein equations,

$$\mathcal{R}_{MN} - \frac{1}{2}\mathcal{R}\,g_{MN} + \Lambda\,g_{MN} = 0\,, \tag{10.2}$$

are solved by an AdS_4 spacetime with a planar Schwarzschild black hole, in complete analogy to the AdS_5-Schwarzschild black-hole spacetime discussed in Sec. 4.1.1. The respective metric reads, in Poincaré coordinates indicated by a subscript 'P' on the time,

$$\mathrm{d}s^2 = \frac{L_{\mathrm{AdS}}^2}{z^2}\left(-h(z)\,\mathrm{d}t_{\mathrm{P}}^2 + \mathrm{d}\boldsymbol{x}^2 + \frac{1}{h(z)}\,\mathrm{d}z^2\right)\,, \tag{10.3}$$

with the horizon function

$$h(z) = 1 - \left(\frac{z}{z_{\mathrm{h}}}\right)^3\,. \tag{10.4}$$

Here, $(t_{\mathrm{P}}, \boldsymbol{x}) = (t_{\mathrm{P}}, x, y)$ are the coordinates of the spacetime on which the boundary field theory is defined, and $z \geq 0$ is the coordinate of the holographic direction. It is often useful to think of the dual field theory dynamics to take place at the boundary $z = 0$. However, we stress that the physics of the boundary theory is more than just a restriction of the bulk fields to the $(z = 0)$-slice. It really is a 'projection' where the entire bulk information encodes the physics of the dual theory, *cf.* our general discussion in Sec. 2.2. The black-hole horizon is situated at $z = z_{\mathrm{h}}$, and the associated temperature is

$$T = \frac{3}{4\pi z_{\mathrm{h}}}\,. \tag{10.5}$$

Instead of the Poincaré coordinates employed in Eq. (10.3), for non-equilibrium holography a different set of coordinates is usually preferable [266], namely Eddington–Finkelstein (EF) coordinates. Expressing the metric in those coordinates enables one to use a so-called 'characteristic formulation' of the gravity equations (see *e. g.* [266, 267], and references cited therein). Despite the fact that we do not consider a dynamical metric here, the use of EF coordinates is still advantageous as it simplifies the equations of motion of the gauge–matter part of the action. Thus, following [233], we will use the following metric,

$$\mathrm{d}s^2 = \frac{L_{\mathrm{AdS}}^2}{z^2}\left(-h(z)\,\mathrm{d}t^2 + \mathrm{d}\boldsymbol{x}^2 - 2\,\mathrm{d}t\,\mathrm{d}z\right), \qquad (10.6)$$

that is equivalent to the metric given in Eq. (10.3), and is related to it by a transformation of the time coordinate,

$$\mathrm{d}t = \mathrm{d}t_{\mathrm{P}} - \frac{\mathrm{d}z}{h(z)}. \qquad (10.7)$$

In Eqs. (10.6) and (10.7), $h(z)$ is the horizon function given by Eq. (10.4). At the boundary at $z = 0$ the EF time t coincides with the Poincaré time t_{P} up to a constant that we can set to zero. Thus t is, like t_{P}, identified with the time in the boundary theory.

Working, then, with the fixed background metric (10.6), one is left with the equations of motion for the matter part, *i. e.*, the generally covariant Maxwell and Klein–Gordon equations which are coupled to each other through the bulk electromagnetic current. As the background metric, together with the gauge coupling, allows for spontaneous symmetry breaking in the scalar sector, the problem has thus been reduced to solving a classical Abelian Higgs model on the curved background (10.6). The equations of motion for A_M and Φ, obtained by varying the action (10.1), take the form

$$\nabla_M F^{MN} = J^N, \qquad (10.8)$$

$$\left(-D^2 + m^2\right)\Phi = 0, \qquad (10.9)$$

with the current

$$J^N = \mathrm{i}\left(\Phi^* D^N \Phi - \Phi\left(D^N\Phi\right)^*\right). \qquad (10.10)$$

Recall that ∇_M denotes the metric covariant derivative and $D_M = \nabla_M - \mathrm{i}A_M$ the combined metric- and gauge-covariant derivative. We fix the gauge freedom by choosing the axial gauge, $A_z = 0$. The dual field theory can be tuned to be in the symmetry-broken phase by adjusting the horizon temperature and the chemical potential, to be discussed further below, if the mass m is suitably chosen. Our choice $m^2 = -2/L_{\mathrm{AdS}}^2$ is within the range of permissible values.[ag] For convenience we henceforth set $L_{\mathrm{AdS}} \equiv 1$.

[ag]Further note that the choice $m^2 = -2/L_{\mathrm{AdS}}^2$ with $d = 3$ boundary-theory dimensions obeys the Breitenlohner–Freedman bound given in Eq. (2.22).

The holographic model captures important aspects of Tisza's two-fluid model of superfluidity [268], for a review see for instance [269]. More specifically, it has been shown that in the hydrodynamic expansion, to an order which includes only non-dissipative terms, the boundary theory reduces to a relativistic version of the two-fluid model [270]. We point out that our treatment of the holographic model captures more than the effective hydrodynamic limit of the boundary theory. In fact, the holographic description is valid at all scales. Nevertheless, it can still be useful to think of the dynamics of the superfluid in terms of two distinct components. In the probe limit, the presence of the static black hole at $z = z_h$ translates, by the AdS/CFT dictionary, to a static heat bath of temperature $T = 3/(4\pi z_h)$ in the boundary theory, see Eq. (10.5). Loosely speaking, this can be viewed as the normal component of the fluid. Similarly, the fields Φ and A_M holographically represent the superfluid component. The superfluid component is coupled to the normal component and can dissipate energy and momentum to it. Thus, the model naturally incorporates dissipation to a thermal bath. Further details of the interpretation of the probe limit can be found in [233]. We remark that our formalism is manifestly relativistic. The superfluidity described by the boundary field theory appears in the non-relativistic low-energy limit [233].

In the following section, we discuss the holographic dictionary for the holographic superfluid and the boundary conditions that we impose on the equations of motion. In particular, we discuss how the bulk scalar field Φ encodes the quantum expectation value $\langle\psi\rangle$ of the dual operator. In the sections thereafter, we make the compactly written equations of motion (10.8)–(10.10) more explicit. We will first specialize to equations for static fields homogeneous in the boundary-theory spatial directions. Their solution gives rise to equilibrium states and we will discuss their physical properties. Then we proceed to discussing the full equations of motion that need to be solved to study non-equilibrium dynamics.

10.2 Holographic Dictionary and Boundary Conditions

In this section, we briefly discuss the holographic dictionary for the holographic superfluid. We have reviewed generalities of the gauge/gravity dictionary in Sec. 2.2. Intimately connected to the bulk–boundary relations given by the holographic dictionary, we also discuss the boundary values that we impose on our fields in the solution of the equations of motion. Our general setup follows [233].

As reviewed in Sec. 2.2, the limiting value of the electrostatic component A_t of the gauge field at the conformal boundary $z = 0$ sets the chemical potential in the dual theory,

$$A_t(t, \boldsymbol{x}, z) = \mu + \mathcal{O}(z). \tag{10.11}$$

In this thesis, we always work with a chemical potential constant in space and time, which is why we have not written $\mu(t, \boldsymbol{x})$. Our units are fixed by setting $z_h = 1$ in the metric (10.6), which also fixes the black-hole temperature, Eq. (10.5). Then, in these units the temperature in the boundary theory is $T = 3/(4\pi)$. We still have

the freedom to choose the value of μ. With T fixed, the choice of μ determines the ratio T/T_{c} that expresses the temperature of the system (thinking of an equilibrium state) in units of the superfluid phase-transition temperature T_{c}. We will discuss the precise relation further below in Sec. 10.3. At the black-hole horizon $z = z_{\mathrm{h}}$, we need $A_t(z_{\mathrm{h}}) = 0$ for regularity of A_M. We do not want to switch on sources for the spatial parts of the $U(1)$ current dual[ah] to A_M because these would break isotropy, so we impose the vanishing of A_x, A_y at the boundary. For the static problem, in addition we impose $A_x(z_{\mathrm{h}}) = 0 = A_y(z_{\mathrm{h}})$ at the horizon.

Let us now turn to the scalar field Φ dual to the operator ψ in the boundary theory. Close to the boundary, Φ behaves as

$$\Phi(t, \boldsymbol{x}, z) = \eta(t, \boldsymbol{x})z + \mathcal{O}(z^2)\,, \tag{10.12}$$

which can be derived by plugging a series *ansatz* into the equations of motion. Here, η is the source field conjugate to the boundary-theory operator ψ. *A priori*, $\eta(t, \boldsymbol{x})$ can be chosen freely. Since we want the scalar operator ψ to form a condensate due to spontaneous symmetry breaking we choose $\eta(t, \boldsymbol{x}) = 0$. Then, the expectation value $\langle \psi(t, \boldsymbol{x}) \rangle$ of the operator dual to Φ can be identified with the coefficient of the quadratic term in the expansion,

$$\Phi(t, \boldsymbol{x}, z) = \langle \psi(t, \boldsymbol{x}) \rangle z^2 + \mathcal{O}(z^3)\,. \tag{10.13}$$

To summarize, the boundary conditions for the gauge fields A_μ are

$$\begin{aligned}
A_t(t, \boldsymbol{x}, z = 0) &= \mu, & A_t(t, \boldsymbol{x}, z = z_{\mathrm{h}}) &= 0\,, \\
A_x(t, \boldsymbol{x}, z = 0) &= 0, & A_x(z = z_{\mathrm{h}}) &= 0\,, \\
A_y(t, \boldsymbol{x}, z = 0) &= 0, & A_y(z = z_{\mathrm{h}}) &= 0\,,
\end{aligned} \tag{10.14}$$

where μ is the chemical potential. The conditions on A_i at the black-hole horizon need only be imposed in the static problem. There is one explicit boundary condition for the scalar field Φ, namely $\eta = 0$, which can be expressed as

$$\partial_z \Phi(t, \boldsymbol{x}, z)|_{z=0} = 0\,. \tag{10.15}$$

The second boundary condition for Φ is a behavioral one: Φ be regular at the horizon. Physically, due to our choice of coordinates, this represents the infalling boundary condition [271]. We will use these boundary conditions for the construction of equilibrium solutions and for the full equations of motion.

10.3 Homogeneous Solutions and Phase Transition

We start with a discussion of static solutions, spatially homogeneous in x and y, of the equations of motion (10.8)–(10.10). These bulk solutions are dual to thermal

---

[ah]The expectation value $\langle j^\mu \rangle$ of the current dual to A_M is defined via $\langle j^\mu \rangle = -\lim_{z \to 0} \sqrt{-g} F^{z\mu}$, *cf.* [233].

states in the dual theory. For certain choices of the thermodynamic parameters the system is in the superfluid phase. In this section, we will discuss the relation between the temperature and chemical potential on the one hand and the superfluid order parameter on the other hand. Later on, to study non-equilibrium dynamics of the system, we will construct our initial far-from-equilibrium states by superimposing perturbations on thermal superfluid background states described by the solutions discussed in this section.

With a fixed background metric, *i. e.* in the probe limit, static homogeneous solutions of Eqs. (10.8)–(10.10) have first been obtained in the seminal paper [249]. The same authors have studied static homogeneous solutions of the equations of motion associated with the action (10.1) without taking the probe limit in [272].[ai]

In deriving the explicit equations of motion in terms of partial derivatives, we use identities well-known from general relativity that are given in Appendix A. Taking the fields A_M and Φ independent of the coordinates x, y, and t, we obtain from Eqs. (10.8)–(10.10) with the metric (10.6) a set of equations second order in derivatives with respect to the holographic coordinate z. For the gauge field, they read

$$0 = z^2 A_t'' + 2\,\mathrm{Im}(\Phi'\Phi^*)\,, \tag{10.16}$$

$$0 = z^2(hA_i'' + h'A_i') - 2|\Phi|^2 A_i\,, \tag{10.17}$$

$$0 = 2A_t|\Phi|^2 - \mathrm{i}h\left(\Phi^*\Phi' - \Phi^{*\prime}\Phi\right)\,, \tag{10.18}$$

where $i = x, y$ and the prime denotes the derivative with respect to z. The last equation originates from the dynamic equation for A_z and remains as a gauge constraint to ensure the chosen axial gauge $A_z = 0$. For the scalar field we find

$$0 = z^2 h\Phi'' - z\left(-2\mathrm{i}zA_t + 2h - zh'\right)\Phi' - \left(2\mathrm{i}zA_t - \mathrm{i}z^2 A_t' + z^2 \boldsymbol{A}^2 + m^2\right)\Phi \tag{10.19}$$

with $\boldsymbol{A} = (A_x, A_y)$.

We have thus obtained a system of coupled non-linear ordinary differential equations on the compact domain $0 \leq z \leq z_\mathrm{h}$, and have to solve a boundary-value problem, with the boundary values discussed in the previous Sec. 10.2. We solve this boundary value problem[aj] by using a pseudospectral method (see *e. g.* [273]).

[ai]In Refs. [249] and [272], the solutions are used as backgrounds to study fluctuations of the bulk gauge field, and the results are interpreted in terms of superconductivity rather than superfluidity.

[aj]To solve the background problem, we eventually found it easier in practice to use the metric (10.3) given in Poincaré coordinates. For the interested reader, we give the equations that determine static solutions homogeneous in x and y in the spacetime charted with Poincaré coordinates in Appendix D.4, along with the relations for the transformation of solutions obtained in Poincaré coordinates to Eddington–Finkelstein (EF) coordinates. We have implemented numerical solvers for both Eqs. (10.16)–(10.19) (EF coordinates) and Eqs. (D.2), (D.3), and (D.7) in the appendix (Poincaré coordinates) which yield identical results after transforming the solutions according to the rules given in the appendix. We have used Eqs. (10.16)–(10.19) (EF coordinates) in the construction of initial conditions for the dynamical simulations discussed in the following.

We use a basis of 32 Chebyshev polynomials and 32 grid points in z. Further details on the numerical methods can be found in Appendix D.1.

Varying the thermodynamic parameters T and μ, one finds [248, 249] that starting at some critical values the scalar operator ψ forms a condensate $\langle\psi\rangle \neq 0$. More precisely, the phase transition is just controlled by the dimensionless parameter μ/T, and we have $\langle\psi\rangle \neq 0$ above some critical value for μ/T. Using Eq. (10.5), we can express this ratio in terms of μz_{h}, which is the parameter we actually vary. For clarity, in the present discussion we briefly reinstate the horizon position z_{h} which we have chosen as $z_{\mathrm{h}} = 1$. Varying μz_{h}, we numerically find the critical value for the phase transition,

$$(\mu z_{\mathrm{h}})_{\mathrm{c}} \approx 4.06371\,, \tag{10.20}$$

which is consistent with the literature (see *e. g.* [250]). For $\mu z_{\mathrm{h}} < (\mu z_{\mathrm{h}})_{\mathrm{c}}$ the scalar field Φ vanishes identically in the bulk, and hence $\langle\psi\rangle = 0$ via Eq. (10.13). On the other hand, for $\mu z_{\mathrm{h}} > (\mu z_{\mathrm{h}})_{\mathrm{c}}$, we find $\Phi(z) \neq 0$ and $\langle\psi\rangle \neq 0$. Using Eq. (10.5) to express z_{h} in terms of T, we obtain from Eq. (10.20) the relation

$$\frac{T}{T_{\mathrm{c}}} = \frac{4.06371}{\mu z_{\mathrm{h}}} \equiv \frac{\mu_{\mathrm{c}}}{\mu}\,. \tag{10.21}$$

From now on, we again drop z_{h}. The temperature is fixed at $T = 3/(4\pi)$. The parameter that effectively controls the thermodynamic state of our system is μ, and the phase transition occurs at the critical value $\mu_{\mathrm{c}} = 4.06371$. One can show that the phase transition is of second order and has mean-field critical exponents [250, 274]. It appears reasonable that the critical exponents assume mean-field values due to a suppression of fluctuations in the boundary theory by some large-N_{c} limit that is implicit in using a classical bulk theory (see *e. g.* [274], or [158] in a different context). Moreover, this argument explains why the $U(1)$ symmetry of the holographic superfluid, which lives in two spatial dimensions, can be spontaneously broken, in spite of the Mermin–Wagner theorem [275]; see [276] for further discussion of this point. However, as the holographic-superfluid model defined by the action (10.1) is a 'bottom-up' model, the exact boundary theory is not known and so there is no clear understanding of what the large-N_{c} limit actually is. Furthermore, there are in fact more complicated holographic superfluid models whose critical exponents deviate from mean-field theory (see *e. g.* [277–279]).

In Fig. 10.1 we show the numerically determined dependence of $|\langle\psi\rangle|$ (the order parameter is complex) on μ, along with the ratio T/T_{c} corresponding to μ via Eq. (10.21). In this thesis, we will use the values $\mu = 4.5, 6, 7.5, 9$ in our simulations of non-equilibrium dynamics. In the figure we have marked these values of the chemical potential. Most of our work is done for $\mu = 6$ which corresponds to $\mu/T = 8\pi$, and puts the system into the superfluid phase at a temperature $T/T_{\mathrm{c}} \approx 0.68$.[ak]

Let us briefly discuss the bulk picture of the phase transition. Above T_{c}, the bulk scalar Φ vanishes, and Eq. (10.16) with the boundary conditions given in Eq. (10.14)

[ak]The values of T/T_{c} for all four choices of μ considered in this work can be found in Table 12.1 in Chap. 12 below, and will be further discussed in that chapter.
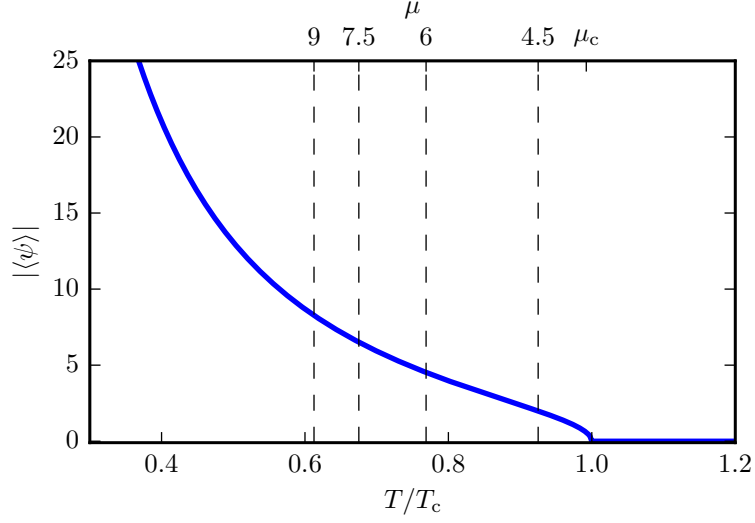
Figure 10.1: Relation between the modulus of the order parameter $|\langle\psi\rangle|$ and the thermodynamic parameters. There is a one-to-one relation between T/T_c and μ, see the text. Above T_c, the order parameter $|\langle\psi\rangle|$ vanishes. We have marked the values of μ that we use in our simulations (dashed lines).

immediately yields, with z_h reinstated for clarity,

$$A_t = \mu \left(1 - \frac{z}{z_h}\right) . \tag{10.22}$$

Actually, the black hole must be charged to support the non-zero electric flux associated with A_t, but we just have an uncharged AdS_4-Schwarzschild black hole with metric given by Eq. (10.6). This shortcoming is due to the probe limit that we use where we ignore the backreaction of the gauge–matter sector onto the metric. The 'proper' solution above T_c (see *e. g.* [272]) is an AdS_4-Reissner–Nordström black hole with A_t given above and the metric analogous to the AdS_5-Reissner–Nordström black hole given in Eq. (4.24).

Let us now turn to the superfluid phase below T_c which is the phase that we are interested in in this thesis. In the equilibrium phase below T_c, the scalar $\Phi(z)$ has a non-trivial bulk profile which via Eq. (10.13) gives rise to the boundary-theory condensate. Φ is charged. Thus, as can be seen by computing the bulk charge density $\sqrt{-g}J^0$ from Eq. (10.10), the bulk condensate manifests itself as a charged 'cloud' in the bulk which sources the electrostatic potential A_t, *cf.* the discussion in, *e. g.*, Ref. [233]. Note that below T_c, the field A_t deviates from the form given in Eq. (10.22) and there is no closed-form solution. The spatial components A_i of the gauge field vanish in the static equilibrium states. We illustrate the configuration of the bulk fields in the superfluid phase in Fig. 10.2. In the profile of the charge density $\sqrt{-g}J^0$ we can clearly discern the charged cloud in the bulk.
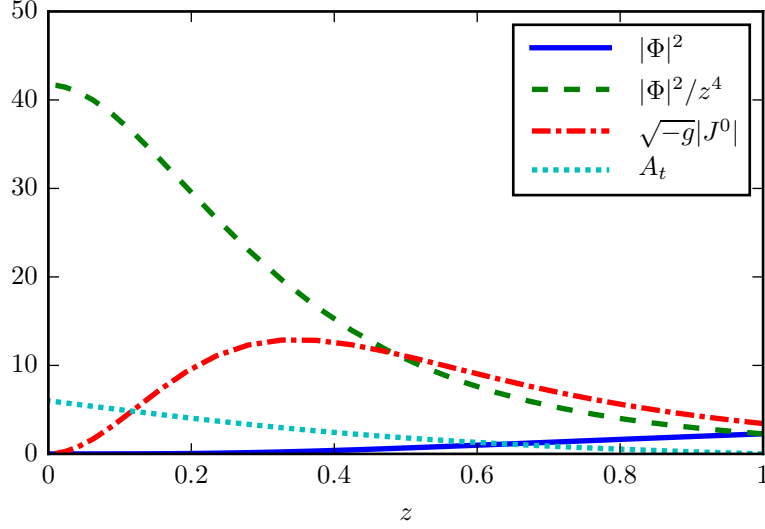
Figure 10.2: Illustration of the bulk field configuration for an equilibrium state in the superfluid phase. Here we have chosen $\mu = 6$. Shown are the modulus-squared of the bulk scalar field $|\Phi|^2$ (blue solid line), the quantity $|\Phi|^2/z^4$ (green dashed), the bulk charge density $\sqrt{-g}\,|J^0|$ (red dot-dashed), and the gauge-field component A_t (turquoise dotted). At the boundary, $|\Phi|^2/z^4$ reduces to the superfluid density $n = |\langle\psi\rangle|^2$. Here, $n \approx 41.7$.

The density of the superfluid order parameter is given by the absolute-value-squared of the condensate $\langle\psi\rangle$. We denote it by $n = |\langle\psi\rangle|^2$. For the case $\mu = 6$ which we will mostly use throughout this work the equilibrium value for the density is $n_0 \approx 41.7$, *cf.* Fig. 10.2.

10.4 Full Equations of Motion and Their Implementation

In this thesis, we want to consider the time evolution of the superfluid starting from a far-from-equilibrium situation. Thus, we now turn to the explicit form of the equations of motion (10.8)–(10.10) for the gauge and matter fields in the fixed curved background specified by the metric (10.6), without further assuming any symmetry in the field configurations.

In light of the near-boundary expansion (10.12) it is convenient for numerics to rescale the scalar field Φ by $1/z$ and work with $\tilde{\Phi} \equiv \Phi/z$. Using the 'lightcone derivative'

$$\nabla_+ X = \partial_t X - \frac{h(z)}{2}\partial_z X \qquad \text{for} \qquad X = A_x, A_y, \tilde{\Phi} \tag{10.23}$$

and with $\boldsymbol{\nabla} = (\partial_x, \partial_y)$ we eventually obtain from Eqs. (10.8)–(10.10) the following

system of equations to solve:

$$\partial_z^2 A_t = \partial_z \boldsymbol{\nabla} \cdot \boldsymbol{A} - 2\operatorname{Im}(\tilde{\Phi}^* \partial_z \tilde{\Phi}) \,, \tag{10.24}$$

$$\partial_z \nabla_+ A_x = \frac{1}{2}\left(\partial_y^2 A_x + \partial_x(\partial_z A_t - \partial_y A_y)\right) - |\tilde{\Phi}|^2 A_x + \operatorname{Im}(\tilde{\Phi}^* \partial_x \tilde{\Phi}) \,, \tag{10.25}$$

$$\partial_z \nabla_+ A_y = \frac{1}{2}\left(\partial_x^2 A_y + \partial_y(\partial_z A_t - \partial_x A_x)\right) - |\tilde{\Phi}|^2 A_y + \operatorname{Im}(\tilde{\Phi}^* \partial_y \tilde{\Phi}) \,, \tag{10.26}$$

$$\partial_z \nabla_+ \tilde{\Phi} = \frac{1}{2}\boldsymbol{\nabla}^2 \tilde{\Phi} - \mathrm{i}\boldsymbol{A} \cdot \boldsymbol{\nabla}\tilde{\Phi} + \mathrm{i}A_t \partial_z \tilde{\Phi} - \frac{\mathrm{i}}{2}\left(\boldsymbol{\nabla} \cdot \boldsymbol{A} - \partial_z A_t\right)\tilde{\Phi} - \frac{1}{2}\left(z + \boldsymbol{A}^2\right)\tilde{\Phi} \,. \tag{10.27}$$

In deriving these equations, we evaluate the left-hand sides of Eqs. (10.8) and (10.9) by using relations following from standard general-relativity identities, see Appendix A.

Our aim is to describe the dynamical evolution of inhomogeneous solutions of the above equations, describing, *e. g.*, vortex excitations of the dual superfluid. The equations of motion (10.24)–(10.27) form a system of coupled non-linear partial differential equations, which makes their solution challenging. However, the structure of the equations is remarkably simple: On a fixed timeslice, at every point (x, y) the equations (10.25)–(10.27) can be integrated with boundary values imposed at $z = 0$, yielding $\nabla_+ A_x$, $\nabla_+ A_y$, and $\nabla_+ \tilde{\Phi}$. Subsequently, we can obtain the time-derivatives $\partial_t A_x$, $\partial_t A_y$, and $\partial_t \tilde{\Phi}$ by undoing the shifts (10.23), and finally integrate Eq. (10.24) to obtain A_t.

We recall that we have chosen the axial gauge $A_z = 0$. With this gauge choice, the z-component of the Maxwell equations (10.8) which we have not written above reads

$$0 = \partial_t \partial_z A_t - \boldsymbol{\nabla}^2 A_t + \partial_t \boldsymbol{\nabla} \cdot \boldsymbol{A} - h\partial_z \boldsymbol{\nabla} \cdot \boldsymbol{A} + 2|\tilde{\Phi}|^2 A_t - 2\operatorname{Im}\left(\tilde{\Phi}^* \partial_t \tilde{\Phi} - h\tilde{\Phi}^* \partial_z \tilde{\Phi}\right) \,. \tag{10.28}$$

This equation is not independent of the equations (10.24)–(10.27). There is a linear differential equation relating the right-hand side of Eq. (10.28) and the right-hand sides of equations of the form $0 = (\dots)$ equivalent to Eqs. (10.24)–(10.27). From this relation it can be shown that if the latter equations are satisfied, Eq. (10.28) will be satisfied in the whole bulk if it is satisfied on one slice of constant z. Thus, Eq. (10.28) can be interpreted as a constraint equation. Alternatively, one could interpret Eq. (10.24) as a constraint, and Eq. (10.28) as a dynamic equation. In practice, as discussed above, we use Eq. (10.24) as a dynamic equation and compute A_t from it in every timestep. We have checked explicitly that Eq. (10.28) remains satisfied during the non-equilibrium evolution.

As we aim at studying universal aspects of the superfluid, we consider different types of initial conditions for the equations of motion, containing topological defects, the details of which are discussed in Sec. 11.1 below. Moreover, we study the system for different choices of the chemical potential μ which corresponds to states at

different values of $T/T_{\rm c}$. To study general properties of the system's time evolution, we choose $T/T_{\rm c} = 0.68$ ($\mu = 6$).

We put the system in a finite volume and take the (x, y) directions to be periodic. We use a pseudo-spectral basis for the fields. In order to be able to properly do statistics and suppress finite-volume effects we need to choose our numerical grid sufficiently large. Specifically, we study grid sizes of 352×352 as well as 504×504 points in the (x, y) plane. The data from these different grid sizes are qualitatively consistent. Thus, by using 504×504 points in the (x, y) plane we do indeed efficiently suppress finite-volume effects. Since observables computed on the larger grids are considerably less noisy, all data presented in the following were produced on 504×504 grids. We use a basis of 32 Chebyshev polynomials and 32 grid points in the holographic direction. We use an explicit time-stepping scheme for the propagation. We point out that the timestep τ used in our numerics is much smaller than one unit of time, $\tau \ll 1$. A more detailed discussion of our choice of numerical methods and parameters is given in Appendix D.

For technical reasons, each of our initial conditions depends on some random data. To get more robust results that do not depend on the precise values of these random data in a specific realization, we average statistical observables discussed in the following chapter 11 over ten runs for each type of initial condition (random distributions and lattices of vortices, see Sec. 11.1). For the additional simulations reported on in Chap. 12, which are performed for choices of $T/T_{\rm c}$ different from $T/T_{\rm c} = 0.68$, we average statistical observables over five runs for each choice of $T/T_{\rm c}$, as will be further discussed in that chapter.

11 Holographic Non-Equilibrium Dynamics and Non-Thermal Fixed Point

We now begin our investigation of the non-equilibrium dynamics of the superfluid described by our holographic model. In the following section 11.1, we discuss the different types of initial conditions that we employ to induce non-equilibrium behavior of the superfluid. Specifically, our initial conditions are characterized by ensembles of topological vortex defects. In the subsequent sections 11.2–11.4, we analyze the evolution of the system in terms of the distribution statistics of the defects. Furthermore, we consider the occupation spectra of the momentum modes of the superfluid order parameter. Finally, in Sec. 11.5 we discuss our findings in the context of non-thermal fixed points.

The basis of the construction of the initial conditions are static homogeneous solutions which we have discussed in Sec. 10.3. (These states are of course no longer homogeneous, nor static, once perturbed by the introduction of vortices.) In this chapter we investigate the system's non-equilibrium behavior for the choice $T/T_c = 0.68$, putting the system in the superfluid phase. This choice corresponds to a choice of the chemical potential $\mu = 6$ in units specified by the condition $z_h = 1$, *cf.* Eq. (10.21), and was also employed in Ref. [233]. In that work, only one type of initial conditions was studied, on short to intermediate evolution time scales in a sense that will become clear below. For $T/T_c = 0.68$ and with our choice of the grid constant, see Appendix D.1, the dimensionless product LT of the extent of the (x, y)-domain and the temperature is $LT = 34.4$. To be able to properly assess the genuine late-time behavior of the system we let it evolve to time $t_f = 4000$ in the aforementioned units, or $t_f T = 955$ in units of temperature.

Later on, in Chap. 12, in order to assess to what extent our findings are robust with respect to the choice of thermodynamic parameters, we will study non-equilibrium dynamics in the superfluid phase for three further choices of T/T_c, using initial conditions analogous to the ones employed in the present chapter.

11.1 Initial conditions

For the quantum systems we have in mind, quenches, especially across a or in the vicinity of a phase transition, are being studied intensively, both experimentally and theoretically. A quench in the usual sense involves the rapid change of either a thermodynamic parameter, such as temperature, or a Hamiltonian parameter,

127

for example interaction strength. Temperature quenches across a superfluid phase transition were recently studied in the holographic approach, in the context of the Kibble–Zurek scenario [234, 280]. Novel techniques developed for ultracold quantum gases and exciton–polariton superfluids allow to rapidly change parameters of the Hamiltonian. Using these, ensembles of vortex defects can be created in the superfluid [237–246]. The generic consequence of both types of quenches for superfluids in two spatial dimensions is the nucleation of quantized vortices. This behavior was also observed in simulations of both relativistic [261, 262] and non-relativistic [258–260, 281, 282] Bose systems. Here, we directly prepare ensembles of vortices as quench-like initial conditions for the superfluid's time evolution. For simplicity, we refer to our initial conditions as quenches in the following.

The structure of the core of a vortex, as well as collective properties of the ensemble, are specific characteristics of the superfluid system. The local phase structure of the superfluid order parameter around a vortex defect, however, is determined by topology. The presence of a local vortex with quantization $w \in \mathbb{Z}\backslash\{0\}$ requires that the phase angle $\varphi = \arg(\langle\psi\rangle)$ of the superfluid order parameter has winding number w around the vortex, *i. e.*, $\oint \mathrm{d}\varphi = 2\pi w$, where the integration contour encircles the particular defect. This property can be used to prepare the initial-time order-parameter field to bear a set of vortices ($w > 0$) and anti-vortices ($w < 0$). We do this by 'multiplying' a localized vortex into the phase of the thermalized superfluid, $\langle\psi\rangle \rightarrow \langle\psi\rangle \cdot \mathrm{e}^{\mathrm{i}w\phi_\mathrm{v}}$ with an appropriate polar angle ϕ_v. During the initial propagation of the equations of motion, the appropriate density profile $|\langle\psi\rangle|^2$ around the defect builds up in a short time, providing us with an ensemble of vortices on top of a previously equilibrated system. Technical details can be found in Appendix D.1. Previous studies of vortex solutions in holographic superfluids include [251, 252].

In Fig. 11.1 we show example realizations of different types of initial conditions we prepare, with a random distribution of vortices and anti-vortices (left column) and a regular lattice distribution (right column). The graphs in the first row show the phase angle field $\varphi(\boldsymbol{x})$. After imprinting the phase winding of the vortices the system reacts by building up vortex cores and, on a longer time scale, by redistributing the defects, as a consequence of interactions in the superfluid. Thus, the short-time outcome of the respective quench is defined by choosing number, quantization, and spatial distribution of the vortices. The second row in Fig. 11.1 shows that indeed vortex cores are built up shortly after the winding phases have been imprinted. This procedure resembles the well-established technique of imprinting vortices by 'stirring' a Bose–Einstein condensed dilute atomic gas with the help of a laser [283, 284]. Experimental methods have been refined for creating vortices in cold atomic gases [232, 241, 242, 285] and exciton–polariton superfluids [244, 245].

In this work, we study two classes of initial vortex distributions: class $\mathcal{A}$ consists of random distributions of elementary vortices of winding numbers ± 1, while class $\mathcal{B}$ comprises regular 12×12 lattices of non-elementary vortices with absolute winding numbers $|w| > 1$, alternating in sign from site to site. For examples from each class see Fig. 11.1. We observe that a non-elementary vortex of absolute winding number w quickly decays into w elementary vortices of the same sign. Therefore, there
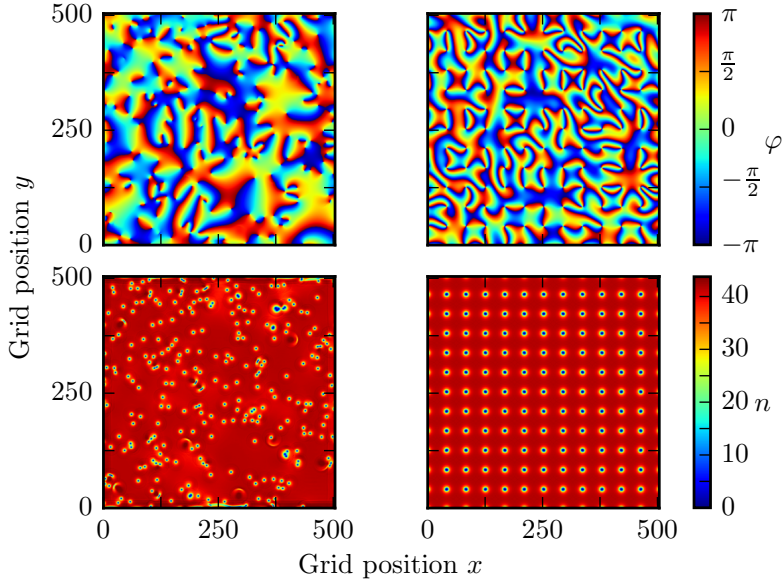
Figure 11.1: Illustration of two classes of initial conditions we have chosen in this work. Left column: random distribution with an equal number of elementary vortices of either sign. Right column: vortex lattice with winding numbers ± 2 alternating from site to site. Shown are single-run snapshots of the phase-angle distributions $\varphi(\boldsymbol{x}) = \arg(\langle\psi(\boldsymbol{x})\rangle)$ (first row) and densities $n(\boldsymbol{x}) = |\langle\psi(\boldsymbol{x})\rangle|^2$ (second row) of the superfluid order-parameter field $\langle\psi(\boldsymbol{x})\rangle$ at time $t = 0$ when the vortex cores are fully developed. The noise that is at this time added onto the phase distribution for the vortex lattices is clearly visible in the upper right panel.

are strong correlations built into the initial vortex positions for initial conditions in class $\mathcal{B}$, insofar as after the decay of the non-elementary vortices the like-sign singly quantized vortices are clustered. On the other hand, within the limitations of the finite grid, the initial vortex positions in class $\mathcal{A}$ are completely uncorrelated. For each class of initial conditions, we vary the number of vortices by randomly distributing $144, 432,$ or 720 vortices of either sign in class $\mathcal{A}$, and choosing winding numbers $\pm 2, \pm 6,$ or ± 10 in class $\mathcal{B}$. This choice implies that after the decay of the non-elementary vortices the total number of elementary vortices is the same in the corresponding cases of both classes. In this way, we vary the initial vortex correlations and the mean separation of vortices, considering both as quench parameters. The resulting six different initial conditions are summarized in Table 11.1. Note that in all cases the net vorticity is zero.

The vortex phases are imprinted at a time $t = t_{\mathrm{i}} < 0$. After starting the simulation, stable vortex cores develop quickly, typically after $\Delta t = 5$ and $\Delta t = 10$ for

Table 11.1: Vortex numbers and winding numbers for the six different types of
initial distributions used in the simulations. Class $\mathcal{A}$ consists of ran-
dom distributions of three different numbers of elementary vortices and
anti-vortices, while class $\mathcal{B}$ comprises regular 12×12 square lattices
of alternating-sign non-elementary vortices with three different winding
numbers. See Fig. 11.1 for example realizations of types $\mathcal{A}$ I and $\mathcal{B}$ I.

		I	II	III
$\mathcal{A}$	random distribution	2×144	2×432	2×720
$\mathcal{B}$	vortex lattice (12×12)	± 2	± 6	± 10
# elementary vortices		288	864	1440

quenches of class $\mathcal{A}$ and $\mathcal{B}$, respectively. We t_{i} such that at $t = 0$ the vortex cores
are fully developed. For class $\mathcal{B}$ (vortex lattices), we furthermore perturb the phase
of the bulk scalar field at time $t = 0$ with random noise to induce variations in the
decay pattern. This is illustrated in the upper right panel in Fig. 11.1. For class $\mathcal{A}$
(random distribution) it is not necessary to add phase noise due to the randomness
of the vortex positions.

11.2 General Considerations on Vortex Dynamics in a Superfluid

It will be useful to discuss the real-time dynamics of our holographic superfluid in
the framework of an effective description that is well known from other superfluid
systems. In this effective picture of quantum turbulence the vortices appear as
collective excitations of the order-parameter field. In addition to the vortices the
system contains sound waves. These also mediate the effective interaction of the
vortex defects. The sound waves can usually be treated in a good approximation as
linear perturbations of the order-parameter field.

In this section we summarize a few basic properties of the effective descrip-
tion known to characterize vortices and their dynamics in two-dimensional non-
relativistic superfluids. For reviews in the context of superfluid helium and cold
atomic gases see, *e. g.*, [286–288]. The time evolution of an undamped dilute non-
relativistic superfluid carrying vortex defects is understood to be well described
by the non-linear Schrödinger or Gross–Pitaevskii equation (GPE) [289, 290], the
classical field equation for the order parameter $\langle \psi \rangle$ with Schrödinger-type free and
quartic-interaction parts. The potential field $\boldsymbol{v} \sim \boldsymbol{\nabla} \varphi$ derives from the order param-
eter's phase angle $\varphi = \arg(\langle \psi \rangle)$ and describes the local velocity of the superfluid.
The velocity field is thus curl free. Vorticity is carried rather by the vortex defects
at which the order-parameter field vanishes, permitting a finite circulation of the
phase around it.

In studies of two-dimensional turbulence, important observables are the kinetic energy spectrum $\propto \langle [\boldsymbol{v}(\boldsymbol{k})]^2 \rangle$ and the distribution of vorticity $\omega = \partial_x v_y - \partial_y v_x$ which derives from the local velocity field $\boldsymbol{v} = (v_x, v_y)$. As was first discussed in the context of classical fluid dynamics [291–293], it is convenient to think of vortices as Coulomb-interacting 'charges' in an effective 'electrostatic' picture where vortices of opposite-sign (like-sign) winding number attract (repel) each other. The dynamics of the GPE vortices is to a good approximation of Hamiltonian character, where the position along one spatial dimension forms the canonical momentum of the position along the other. This forces, in effect, oppositely charged vortices to move in parallel at a fixed distance (Helmholtz law) while equal-sign vortices circulate around each other. The statistics of the vortex distribution contains important information about the temporal and spatial characteristics of the system.

Bogoliubov sound waves form the weak linear excitations of the order parameter field, through which vortices can interact with each other. The interaction with a fluctuating, *e. g.* thermal, background of excitations of the superfluid causes the vortices to show deviations from the Hamiltonian behavior. For instance, a sufficiently strong dissipative force can suppress the Helmholtz pair propagation and make oppositely charged vortices move towards each other. This is well known for defect solutions of Ginzburg–Landau equations which represent the generalization of the GPE with complex parameters [294].

On a mean-field level, aspects of vortex annihilation in a superfluid can also be described in terms of phase-ordering kinetics [295]. In this context, it is assumed that in the 'coarsening regime' the system can be characterized by a single length scale exhibiting a scaling law with respect to time. However, cases have been identified [296, 297] in which systems can deviate from the simple scaling predictions of [295]. In this work, we study non-thermal fixed points [254] of which phase-ordering kinetics represents one possible realization. Note, however, that the concept of non-thermal fixed points reaches beyond phase-ordering kinetics. For example, they can be associated with turbulent processes which can have effects opposite to ordering kinetics. In the language of turbulence, ordering kinetics corresponds to an inverse cascade directed from small to large length scales, building up large-scale correlations in the system. In contrast, a direct cascade transports energy in the opposite direction, creating small-scale fluctuations. In Sec. 11.5, we discuss non-thermal fixed points in the context of our findings. In fact, it is possible that the dynamics we discuss in this work contains both, ordering processes, *i. e.* inverse cascades, and direct turbulent cascades directed from large to small length scales.

We emphasize that not all of the typical properties mentioned above will necessarily be seen in the holographic superfluid that we study here. But we find it helpful to compare our findings to those properties in the following.

11.3 Dynamical Evolution of the Vortex Ensembles in the Holographic Superfluid

We now turn back to our holographic superfluid. In the following we discuss the dynamics of the holographic superfluid for $t > 0$, after imprinting the initial conditions discussed in Sec. 11.1. The vortices start to move around, subject to an effective interaction. When vortices of opposite sign approach each other sufficiently closely they mutually annihilate. There appears to be a strong suppression of Helmholtz pair propagation: The vortex' and the anti-vortex' trajectories only bend slightly in a common direction before annihilating. This is an indication of strong dissipative effects in the holographic superfluid. Annihilations reduce the total vortex number and change length scales of the vortex distribution. This has important implications for the turbulence properties of the system, which we discuss in Sec. 11.4. At the time $t_\mathrm{f} = 4000$ where we end our simulation, only very few vortices are left, typically about 4 to 8 for all types of quenches considered. In our simulations, the non-zero temperature of the black hole is related to dissipation such that sound fluctuations are quickly damped out. The spontaneous generation of vortex–anti-vortex pairs could not be observed. We expect that, after all vortices have annihilated, the excess energy which we initially injected into the superfluid component is completely dissipated into the heat bath. As a consequence, the condensate $\langle \psi(\boldsymbol{x}, t) \rangle$ would relax to a homogeneous, fully ordered state. Within the finite evolution times, our simulations give indications for this behavior.

Snapshots of the full time evolution of the system for the two classes of initial conditions are shown in Fig. 11.2, where the upper (lower) panels correspond to a random, *i. e.*, class-$\mathcal{A}$ (class-$\mathcal{B}$, lattice) initial distribution. We plot the superfluid density $n(\boldsymbol{x}) = |\langle \psi(\boldsymbol{x}) \rangle|^2$ at various times. These snapshots are representative for the different stages encountered in the evolution.[al] In both cases, the main features of the dynamic evolution can be understood as due to the motion and annihilation of vortices. Due to the relatively high initial density of vortices the first stage of the evolution is characterized by a small mean vortex–anti-vortex distance and a high annihilation rate. Each annihilation event releases energy in form of sound waves which is then dissipated into the thermal background [233]. For initial configurations of class $\mathcal{B}$, there is an additional stage in which non-elementary vortices decay. The emerging elementary vortices drift apart for a certain amount of time, thereby expanding like-sign clusters. Naturally, these early stages are highly parameter-dependent and therefore non-universal. The following stage is an evolving dilute vortex gas. Although it is still the annihilation of vortex–anti-vortex pairs which brings the system closer to equilibrium, essential aspects of the time evolution of the system at this stage can be understood from the statistics of the vortex distribution as we will discuss below.

Typical bulk views of aspects of the field configuration in the vortex liquid are

---

[al]http://www.thphys.uni-heidelberg.de/holographic-superfluid links to videos of example evolutions.
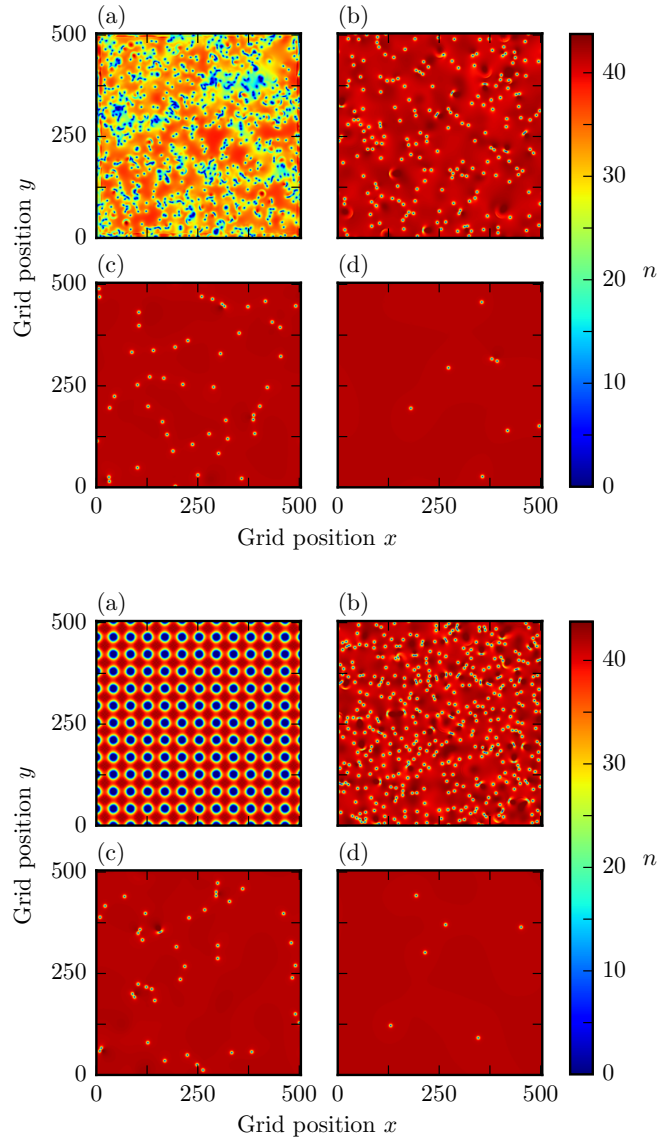
Figure 11.2: Single-run snapshots of the superfluid density $n(\boldsymbol{x}) = |\langle\psi(\boldsymbol{x})\rangle|^2$ showing the characteristic stages of the evolution of the system, after a quench of type $\mathcal{A}\,\mathrm{II}$ (random distribution with 432 elementary vortices of either sign, upper panel) and after a quench of type $\mathcal{B}\,\mathrm{II}$ (vortex lattice with winding numbers ± 6, lower panel). The vortices can be discerned as dips in the density, and one can observe sound waves from vortex annihilation events. The snapshots are taken at times (a) $t = 0$, (b) $t = 100$, (c) $t = 600$, and (d) $t = 4000$. The quenches have been performed at times $t = -5$ (quench $\mathcal{A}\,\mathrm{II}$) and $t = -10$ (quench $\mathcal{B}\,\mathrm{II}$).

shown in Fig. 11.3. The upper panel corresponds to an early to intermediate time $t = 200$, and the lower panel to a late time $t = 4000$. We plot isosurfaces of $|\Phi|^2 /z^4$ (blue surfaces) and of the bulk charge density $\sqrt{-g} \, |J^0|$ (orange surfaces), see Eq. (10.10) for the definition of J^0. The former quantity reduces to the superfluid density $n = |\langle\psi\rangle|^2$ at the boundary, *i.e.*, as $z \to 0$. The slice at $z = 0$ shows n with the same color map as in Fig. 11.2. The vortices in the boundary theory, discernible as dips in the superfluid density, are represented by 'tubes' in the bulk, with the bulk scalar Φ vanishing in their centers. The tubes punch holes through the charge cloud that hovers in the bulk, *cf.* Fig. 10.2 and the discussion in Sec. 10.3, and thus provide an avenue for energy to dissipate into the black hole [233]. A larger defining value of the isosurface of the charge density would lead to an increased width of the holes and a decreased distance between the two sheets of the isosurface. We observe that sound waves in the boundary theory, such as those produced in vortex annihilation events, are reflected in the bulk as perturbations of the charge density. In particular, the isosurfaces of the bulk charge density at $t = 4000$ (lower panel), when the system has evolved to a dilute vortex gas, are much smoother than those at $t = 200$ (upper panel), when the superfluid still exhibits many vortices and a high rate of annihilation events.

Let us now turn to the details of the vortex distribution. At each unit timestep, we determine the position of all vortices and anti-vortices, see Appendix D.1 for details. In Fig. 11.4 we show the total vortex density as a function of time (averages are taken over ten runs for each type of quench). For both classes of initial conditions, annihilation proceeds in a non-universal manner, up to a simulation time of $t \simeq 400$, depending on the particular initial configuration. For initial conditions in class $\mathcal{B}$ (lattice), the vortex density is approximately constant at early times. This stage was referred to as the 'drift stage' above. It arises because the like-sign vortex clusters need to expand and dissolve before vortices of opposite sign can encounter each other. Naturally, this takes longer if the initial number of vortices is lower.[am] At time $t \simeq 400$, starting from any of the initial conditions, a scaling regime is entered, where the vortex density ρ decays algebraically in time, $\rho \sim t^{-1}$. This scaling persists until the end of our simulations at $t_\mathrm{f} = 4000$. We observe that the power-law is the same for all tested initial conditions. Hence, starting at $t \simeq 400$, the vortex density has a universal form. We point out that this decay of vortex density does not exhibit any characteristic time scale. Remarkably, the algebraic decay of the vortex density is characterized by a universal pre-factor. This, together with the value of the exponent, can be explained by a diffusive motion of vortices within a thermal background of sound waves.

To investigate this in more detail we define the following quantities. By $l_=$ we denote the mean distance of nearest-neighbor defects of equal sign, while $l_{\neq}$ is the

---

[am] From our data on the vortex density shown in Fig. 11.4 and the average vortex separations shown in Fig. 11.5 below we can estimate the drift velocity v of the elementary vortices in the initial stage in which the vortex lattice dissolves. We find $v = 0.07, 0.13$, and 0.24, for the quench types $\mathcal{B}\,\mathrm{I}$, $\mathcal{B}\,\mathrm{II}$, and $\mathcal{B}\,\mathrm{III}$, respectively.
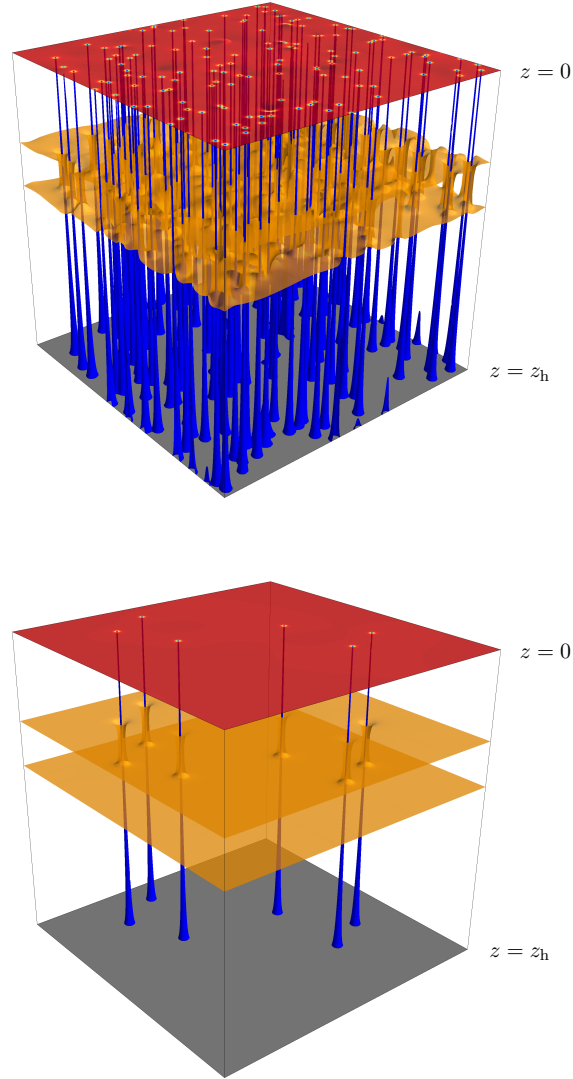
Figure 11.3: Single-run bulk snapshots of isosurfaces of $|\Phi|^2/z^4$ (blue surfaces, defining value 2.2) and the charge density $\sqrt{-g}\,|J^0|$ (orange surfaces, defining value 12.3) after a quench of type $\mathcal{A}$ III (random distribution with 720 elementary vortices of either sign), at the times $t = 200$ (upper panel) and $t = 4000$ (lower panel). At the boundary, $|\Phi|^2/z^4$ reduces to the superfluid density $n = |\langle\psi\rangle|^2$, and we plot n in the top slice using the same color coding as in Fig. 11.2. The plots represent our full simulation domain. Consequently, the vortex tubes in the upper panel that appear to be 'cut' actually close on the opposite side due to periodicity. For an unobstructed view on the isosurfaces of the charge density see Fig. 11.10.
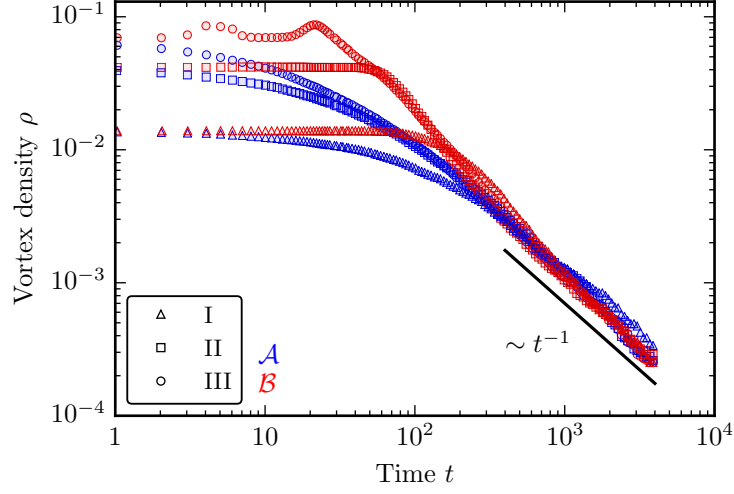
Figure 11.4: Time dependence of the total vortex density, on a double-logarithmic scale. Shown is the averaged vortex density ρ for runs starting from the six different initial conditions summarized in Table 11.1. Class-$\mathcal{A}$ (class-$\mathcal{B}$) runs are drawn in blue (red), while the different choices of total vortex numbers are indicated by different symbols. Note that the apparent initial oscillation of ρ for initial condition $\mathcal{B}$ III is not physical, but rather due to uncertainty in the vortex finding algorithm at the high initial densities associated with $\mathcal{B}$ III.

mean nearest-neighbor distance between vortices and anti-vortices,[an]

$$l_= = \frac{1}{2} \sum_{\alpha=(+,-)} \frac{1}{N} \sum_{i_\alpha=1}^{N} \left| \boldsymbol{x}_{i_\alpha} - \boldsymbol{x}_{\text{nn}_\alpha(i_\alpha)} \right| , \tag{11.1}$$

$$l_{\neq} = \frac{1}{2} \sum_{\alpha=(+,-)} \frac{1}{N} \sum_{i_\alpha=1}^{N} \left| \boldsymbol{x}_{i_\alpha} - \boldsymbol{x}_{\text{nn}_{-\alpha}(i_\alpha)} \right| . \tag{11.2}$$

Here, $\alpha = (+, -)$ denotes the sign of the winding number of the vortex indexed by $i_\alpha = 1, \ldots, N$, and $\boldsymbol{x}_{i_\alpha}$ is its position. The function $\text{nn}_\alpha(i_\beta)$ yields the index of the vortex of sign α nearest to the vortex i_β.

In Fig. 11.5 we show $l_=$ (upper panel) and $l_{\neq}$ (lower panel) as functions of time (averages are taken over ten runs for each type of quench). As the inverse of the square root of the vortex density gives the mean vortex distance, the time evolution of the above length scales is directly related to the density evolution shown in

---

[an]We note that in both $l_=$ and $l_{\neq}$, the two sums corresponding to $\alpha = (+, -)$ need not coincide. However, in the thermodynamic limit, we expect that these two sums coincide because of the symmetry under exchange of vortices and anti-vortices. We have numerically checked that, on average, the two sums are indeed equal.
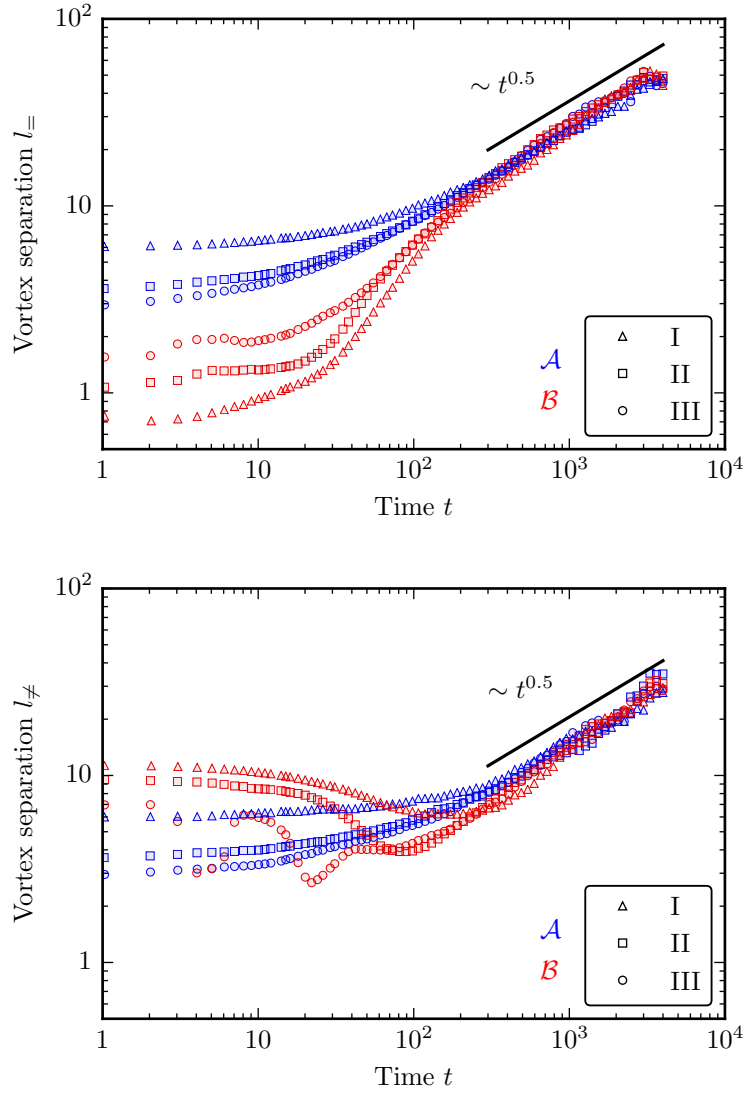
Figure 11.5: Time evolution of the mean nearest-neighbor vortex–vortex distance $l_=$ (upper panel) and vortex–anti-vortex distance $l_{\neq}$ (lower panel), in double-logarithmic scale. The class of initial condition, $\mathcal{A}$ or $\mathcal{B}$, is color-coded, while the different choices of total vortex number are indicated by different symbols, *cf.* Table 11.1.

Fig. 11.4. The panels in Fig. 11.5 show that the nearest-neighbor distances evolve as $l_=(t) = \sqrt{4D_= t}$ and $l_{\neq}(t) = \sqrt{4D_{\neq} t}$ during the universal late-time period, *i. e.*, diffusively. From our data shown in Fig. 11.5, we estimate $D_= \approx 0.16$ and $D_{\neq} \approx 0.05$. The diffusive behavior is a consequence of the effective interaction of vortices with the thermal background in the dual theory. We attribute the fact that $D_=$ and $D_{\neq}$ differ to the influence of the effective vortex–vortex and vortex–anti-vortex interactions. The values of the constants $D_=$ and $D_{\neq}$ can be used to further constrain the parameters controlling the dissipation and the vortex interactions of the boundary theory for a quantitative comparison with conventional models of superfluidity. Finally, note that the universal regime associated with this scaling behavior of both $l_=$ and $l_{\neq}$ is entered at the same time $t \simeq 400$ for all initial conditions.

11.4 Holographic Turbulence

So far we have identified at late times $t \gtrsim 400$ a universal stage of the system's evolution with respect to the effective dynamics of vortices. During this stage, the characteristic length scales of the vortex distribution evolve algebraically, as we have shown in Sec. 11.3. Therefore, their rate of change, $\dot{l}/l$, decreases and approaches zero asymptotically. Thus, at late times the system can be considered quasi-stationary. As we will discuss in the following, during this stage the system bears signatures of turbulence. We will, in particular, analyze momentum-space distributions as statistical observables and find them to exhibit algebraic behavior as it is characteristic for the development of turbulent transport.

   While vortices are the building blocks of superfluid turbulence, one needs to study correlation functions of the superfluid order-parameter field in order to obtain a full understanding of the microscopic dynamics of the superfluid. Here, we concentrate on the equal-time two-point correlation function, $\langle \psi^*(\boldsymbol{x}, t)\psi(\boldsymbol{y}, t) \rangle$. Since our system is spatially homogeneous in a statistical sense this quantity can be analyzed in relative momentum space, *i. e.* with respect to the momentum conjugate to the relative coordinate $\boldsymbol{r} = \boldsymbol{x} - \boldsymbol{y}$, defined via Fourier transform. The (radial) occupation number spectrum is defined as[ao]

$$n(k,t) = \int \frac{\mathrm{d}\Omega_k}{2\pi} \langle \psi^*(\boldsymbol{k},t)\psi(\boldsymbol{k},t) \rangle. \tag{11.3}$$

Due to the isotropy of the underlying model we can perform the angular integration $\int \mathrm{d}\Omega_k/(2\pi)$ without losing information, such that we are left with the radial

---

[ao]A comment is in order here. In practice, we extract the full quantum expectation value $\langle \psi(\boldsymbol{k},t) \rangle$ from the simulations, and compute $\int \langle \psi^*(\boldsymbol{k},t) \rangle \langle \psi(\boldsymbol{k},t) \rangle \, \mathrm{d}\Omega_k/(2\pi)$ from it as an approximation for $n(k,t)$. In addition, we average this quantity over a number of runs [234]. The infrared phenomena we are interested in here are expected to be classical in the statistical sense, and averaging over many realizations washes out, *e. g.*, effects due to the definite positions of the vortices. It would be nonetheless interesting, if numerically demanding, to use the holographic dictionary to extract the full quantum two-point function.

momentum $k = |\boldsymbol{k}|$. We define the radial kinetic energy spectrum as

$$E(k) = \int \frac{\mathrm{d}\Omega_k\, k}{2\pi} |\boldsymbol{k}|^2 \langle \psi^*(\boldsymbol{k}, t)\psi(\boldsymbol{k}, t)\rangle. \qquad (11.4)$$

It is related to the radial occupation number spectrum via $k^3 n(k) = E(k)$. In general $n(k)$ has a well-defined field-theoretic interpretation.

In his seminal work on turbulence ([298–300], see also [301]), Kolmogorov assumed the existence of an inertial range in momentum space, bounded by two characteristic scales, k_{in} and k_{diss}. At the scale k_{in}, energy is injected into the system. It cascades from momentum shell to momentum shell before it is eventually dissipated into heat at the higher scale k_{diss}. Based on the assumption of such a local transport in momentum space, Kolmogorov found that the kinetic energy spectrum of stationary turbulent flow in an incompressible fluid scales as $E(k) \sim k^{-5/3}$ within the inertial range. This result holds also in two spatial dimensions where it is associated with an inverse energy cascade [302]. The essential feature of this so-called Kolmogorov–Richardson cascade is that the system is self-similar, *i.e.* scale-free, within the inertial range.

Here, we take a more general view on turbulence and analyze the occupation number spectra of the holographic superfluid in terms of scaling laws, $n(k) \sim k^{-\zeta}$, previously discussed in [233]. We extract the scaling exponents ζ by fitting power laws to the spectra after averaging them over ten runs for each initial condition. We estimate the uncertainty of the fitted exponents to be 0.1, for details see Appendix D.3. In the following, we relate the scaling seen in the spectra to the statistical properties of the vortex distribution that we discussed in Sec. 11.3. In particular, we want to study whether the universality that emerges in the late-time vortex dynamics is reflected in the occupation number spectra.

In Fig. 11.6, we show the occupation number spectra $n(k)$ for the initial conditions $\mathcal{A}\,\mathrm{II}$ and $\mathcal{B}\,\mathrm{II}$ (averages are taken over ten runs for each type of quench). To illustrate their time evolution the spectra are shown at $t = 0, 200, 600$, and 4000. In both classes, $\mathcal{A}$ (random distributions) and $\mathcal{B}$ (vortex lattices), the spectra for the parameter sets I and III are very similar to the spectra for the sets II of the respective class. For intermediate and late times we observe inertial ranges in k, the corresponding power laws fitted to the spectra at these times are also shown in the figure. Within the uncertainty in our determination of scaling exponents of occupation spectra (*cf.* Appendix D.3), the scaling exponents at intermediate to late times, $t \gtrsim 400$, agree even quantitatively for all quench types within each class. Thus, we can discuss the generic features of the spectra at the examples shown in Fig. 11.6.

First, we note that the initial occupation spectra (corresponding to time $t = 0$ in Fig. 11.6) are indeed similar to the far-from-equilibrium initial momentum distributions considered in various classical statistical simulations of dilute Bose gases [258–260, 281, 282]. Similar initial momentum distributions have also been studied in the relativistic case [257, 303].

During the early to intermediate stage of the system's evolution, for example at $t = 200$, the scaling exponents differ between the various initial conditions, indicating
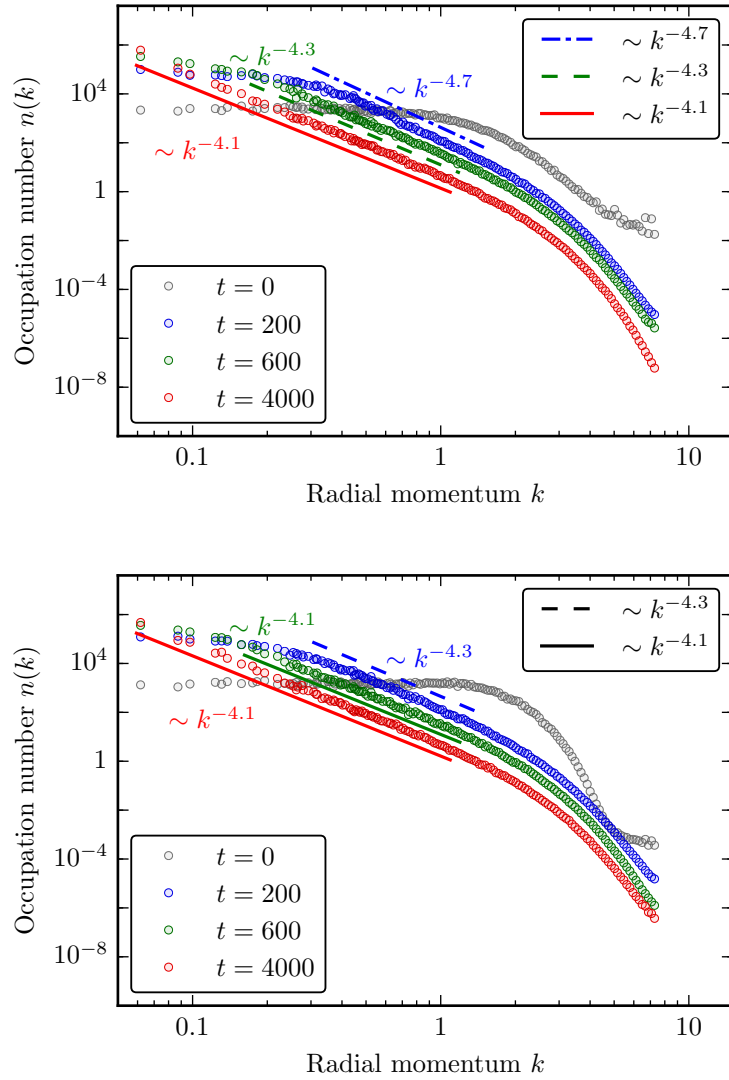
Figure 11.6: Occupation number spectra as functions of the radial momentum k during the different stages of the evolution, on a double-logarithmic scale. Here we show the evolution after quench type $\mathcal{A}$ II (random distribution, upper panel), and the evolution after quench type $\mathcal{B}$ II (vortex lattice, lower panel). Results for the respective parameter sets I and III are similar to the results depicted here, *cf.* the main text.

that this stage is still non-universal. This could be expected from our analysis of the vortex dynamics in Sec. 11.3 where we saw that a dependence on the initial parameters persists until $t \simeq 400$. Specifically, we find, at time $t = 200$, a scaling law at intermediate momenta with exponents $\zeta \approx 4.7$ and $\zeta \approx 4.3$ in class $\mathcal{A}$ and $\mathcal{B}$, respectively, for quench types II and III. The exponents for quench type I in each of the classes $\mathcal{A}$ and $\mathcal{B}$ are slightly larger, $\zeta \approx 4.9$ and $\zeta \approx 4.5$, respectively. The power-law scaling $n(k) \sim k^{-4.7}$ of the occupation number $n(k) = k^{-3}E(k)$ at intermediate times after quenches $\mathcal{A}$ II and $\mathcal{A}$ III (random distributions) is consistent with an $E(k) \sim k^{-5/3}$ Kolmogorov scaling of the radial kinetic energy spectrum. The scaling exponent found in the case of initial condition $\mathcal{A}$ I is slightly larger than the Kolmogorov value.

At this point, let us briefly pause to compare our findings for the intermediate times (at about $200 \lesssim t \lesssim 400$) to the results reported in [233]. There, the evolution of the holographic superfluid was studied starting from an initial condition very similar to our type $\mathcal{B}$ II vortex-lattice configuration. Even though the simulation domain used in [233] was smaller than the one employed here, the initial vortex densities differ by only $10\,\%$. The kinetic energy spectrum was defined in [233], based on hydrodynamic arguments [304], as $\epsilon_{\mathrm{kin}}(k, t) = \frac{1}{2} \int |\boldsymbol{w}(\boldsymbol{k}, t)|^2 \, k \, \mathrm{d}\Omega_k$. Here, $\boldsymbol{w}(\boldsymbol{k}, t)$ is the Fourier transform of the generalized velocity field $\boldsymbol{w}(\boldsymbol{x}, t) = \langle \psi(\boldsymbol{x}) \rangle \boldsymbol{\nabla} \varphi(\boldsymbol{x})$ with $\varphi = \arg(\langle \psi \rangle)$ the phase of the superfluid order parameter. This definition of the kinetic energy spectrum differs from that of our $E(k)$ in Eq. (11.4). In the cited work, the system was propagated up to time $t = 600$, and Kolmogorov scaling of the kinetic energy spectrum, $\epsilon_{\mathrm{kin}}(k, t) \sim k^{-5/3}$, was reported for intermediate evolution times in the range $160 < t < 500$. We have analyzed our data for quench type $\mathcal{B}$ II also in terms of the quantity $\epsilon_{\mathrm{kin}}(k, t)$. We find, within the uncertainty inherent in the fitting procedure, a scaling law $\epsilon_{\mathrm{kin}}(k, t) \sim k^{-1.3}$ during the intermediate stage of the evolution, for example at $t = 200$, differing from Kolmogorov scaling. We will discuss that point in light of our further findings in the summary in Chap. 13.

We now continue with the discussion of our results in Fig. 11.6. During the evolution, the momentum range where $n(k, t)$ obeys a scaling law gradually grows on its lower end, for all initial conditions. Also, the scaling exponents' absolute values decrease. This can be attributed to the increasing diluteness of the vortex gas. The flow field of a single vortex exhibits a scaling $n(k) \sim k^{-4}$ for momenta not resolving the vortex core. The same scaling is expected for randomly distributed vortices and anti-vortices at momenta larger than the mean inverse of the vortex–anti-vortex distance [259]. Hence, the inverse average vortex separation sets a lower cutoff to the scaling regime. As the vortex gas becomes more dilute, the average vortex separation increases, see Fig. 11.5, so that the lower cutoff of the scaling regime decreases. Furthermore, Fig. 11.6 shows that the scaling exponents gradually approach the value for single-vortex scaling.

Let us next turn to the late-time evolution. At time $t = 600$, the scaling exponents of the occupation number spectra are still slightly different for quench classes $\mathcal{A}$ and $\mathcal{B}$. They are fitted by $\zeta \approx 4.3$ and $\zeta \approx 4.1$ for quench types $\mathcal{A}$ II and $\mathcal{B}$ II, respectively. At time $t = 4000$ the scaling exponent is fitted by $\zeta \approx 4.1$ for both quench types $\mathcal{A}$ II
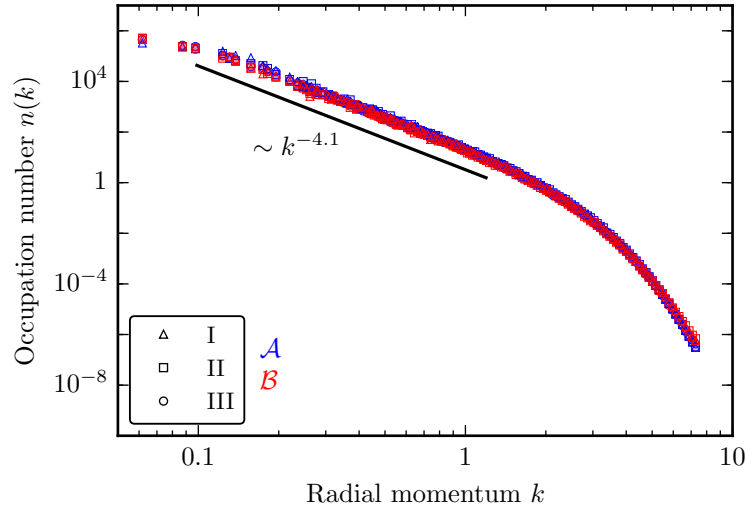
Figure 11.7: Occupation number spectrum as a function of the radial momentum k at time $t = 1000$ during the universal late stage of the evolution, on a double-logarithmic scale. The class of quenches, $\mathcal{A}$ or $\mathcal{B}$, is color-coded, while the different choices of total vortex number are indicated by different symbols, *cf.* Table 11.1. The spectra exhibit scaling $n(k) \sim k^{-\zeta}$ with $\zeta \approx 4.1$ over a large momentum range that gradually expands to the infrared.

and $\mathcal{B}$ II. We recall that the uncertainty in the estimation of these scaling exponents is about 0.1, see Appendix D.3. As discussed above, within each of the classes $\mathcal{A}$ and $\mathcal{B}$ of quenches, at late times both the qualitative and quantitative scaling behavior is unchanged for the alternative choices I and III of the total vortex number. In particular, the scaling exponents in the late stages of the evolution are consistent with $4.1 \lesssim \zeta \lesssim 4.3$ for all initial conditions. To demonstrate this, we plot in Fig. 11.7 the occupation number spectra for all our quenches (averages are taken over ten runs for each type of quench) at $t = 1000$ during the late-time stage. At this time, for all initial conditions, the estimates for the scaling exponents are in fact in the narrower range $4.1 \lesssim \zeta \lesssim 4.2$. This indicates the emergence of a universal scaling law for $n(k, t)$. Thus, in the long run, the system loses all memory of its initial conditions, confirming our findings in Sec. 11.3. Furthermore, the universal scaling law in the occupation number spectra emerges at late times $t \gtrsim 600$. This is to be compared with our findings in Sec. 11.3. There, we identified $t \gtrsim 400$ to roughly mark the onset of the late-time universal scaling behavior with respect to time.

We note that the late-time scaling exponent still appears to deviate slightly from the single-vortex scaling $\zeta = 4$, indicating that effects of vortex interactions are still relevant in this universal regime. Typically, for all initial conditions, we still have 4 to 8 remaining vortex defects at the final time $t_{\mathrm{f}} = 4000$.

11.5 Non-Thermal Fixed Point: The Holographic Perspective

In the following, we concentrate on the universal late-time behavior of the holographic superfluid that we have found in the previous sections for a temperature ratio $T/T_c = 0.68$ of the heat bath. The system exhibits two types of universal scaling laws, one in space and one in time, at late times $t \gtrsim 600$. The first type characterizes spatial correlations of excitations and is reflected by the scaling $n(k) \sim k^{-\zeta}$ of the single-particle occupation number spectrum with the exponent in the range $4.1 \lesssim \zeta \lesssim 4.3$. This scaling is observed within an infrared momentum regime which can be viewed as an inertial range. The power-law behavior terminates in the infrared at a momentum scale that is related to the characteristic length scales of the vortex distribution. The characteristic lengths of the vortex distribution, including the mean vortex separation, follow a scaling law in time, $l \sim t^{1/2}$, see Sec. 11.3. This leads to the observation that the system's time evolution is slowing down algebraically during the universal stage, $\dot{l}/l \sim t^{-1}$. Such a behavior is interpreted as 'critical slowing down' within the context of dynamic critical phenomena well-known from the theory of dynamics near an equilibrium phase transition [305].

Similar scaling features have been observed in numerical calculations of dilute Bose gases far from equilibrium on the basis of a statistical evaluation of Gross–Pitaevskii models [259, 281, 306]. Within that framework, the scaling features have been interpreted in terms of the more general concept of non-thermal fixed points [254–256]. This concept associates stationary points in the time evolution of non-thermally scaling correlation functions with fixed points in a renormalization-group sense [255, 263, 264]. In the vicinity of those fixed points, correlation functions assume spatial and temporal scaling behavior. Non-thermal fixed points thus constitute a generalization of the concept of critical phenomena near thermal equilibrium. *A priori*, this situation allows for new universality classes as compared to those in the classification of Hohenberg and Halperin [305]. But also phase-ordering kinetics as discussed in [295] within the Hohenberg–Halperin classification scheme could probably be interpreted as a realization of a non-thermal fixed point.

In the following, we argue that the holographic superfluid indeed exhibits the presence of a non-thermal fixed point. We use observables which have been introduced in [281] for the purpose of numerically identifying non-thermal fixed points in two-dimensional Bose gases. The state of the system can be characterized by two length scales, the mean nearest-neighbor vortex–anti-vortex distance $l_{\neq}$, see Eq. (11.2), and the coherence length l_C of the superfluid. The latter is defined as

$$l_C(t) = \int g^{(1)}(r,t)\, \mathrm{d}r \tag{11.5}$$

with the autocorrelation function $g^{(1)}$,[ap]

$$g^{(1)}(r,t) = \int \frac{\mathrm{d}^2 x}{A} \int \frac{\mathrm{d}\Omega_r}{2\pi} \frac{\langle \psi^*(\boldsymbol{x},t)\psi(\boldsymbol{x}+\boldsymbol{r},t)\rangle}{\sqrt{n(\boldsymbol{x},t)n(\boldsymbol{x}+\boldsymbol{r},t)}} \ . \tag{11.6}$$

Here, $\int \mathrm{d}^2 x / A$ denotes the average over the simulation domain A, and $\int \mathrm{d}\Omega_r/(2\pi)$ the angular average for the difference vector $\boldsymbol{r}$. The distance $l_{\neq}$ is a measure for the state of the system from the point of view of the effective vortex picture. The coherence length l_{C} measures the degree of spatial correlations of microscopic excitations. The time evolution of both lengths is depicted in Fig. 11.8 (averages are taken over ten runs for each quench type). Both $l_{\neq}$ and l_{C} show universal scaling behavior in the late stage of the evolution. The scaling exponent of $l_{\neq}$ is found to be 0.5, as discussed in Sec. 11.3. The scaling exponent of l_{C} can be narrowed down to a value between 0.5 and 0.6. Thus, it is conceivable that the latter scaling exponent agrees with the scaling exponent of the characteristic length scales of the vortex distribution. This would imply a constancy of ratios of different characteristic length scales typical for the approach to a non-thermal fixed point or a critical point, see for example [307].

The scaling exponents that we have extracted happen to coincide with those predicted by the theory of phase-ordering kinetics [295]. Note that, as the holographic superfluid is a strongly correlated quantum fluid, it is a non-trivial question to what extent the arguments of [295] apply. In addition, going beyond the probe limit could alter these findings.

It is useful to study the time evolution of the system in a reduced configuration space consisting of the two scales $l_{\neq}$ and l_{C}. Fig. 11.9 shows the trajectories of the system for different initial conditions (averages are taken over ten runs for each quench type) in this configuration space. Here we choose to plot the inverse lengths, $1/l_{\neq}$ and $1/l_{\mathrm{C}}$, on the axes because in the thermodynamic limit one generically expects characteristic length scales to diverge at critical points. While the inverse coherence length decreases monotonically for all initial conditions, the behavior of $1/l_{\neq}$ is different for the two classes of initial conditions. Starting from random distributions of vortices (class $\mathcal{A}$), $1/l_{\neq}$ decreases monotonically due to vortex–anti-vortex annihilation. For vortex lattices (class $\mathcal{B}$) $1/l_{\neq}$ increases during the initial drift phase as the vortices of opposite sign move closer to each other. Subsequently, $1/l_{\neq}$ decreases monotonically for all of our initial conditions during the universal stage. Eventually, for all of our initial conditions the system is attracted by the point of maximal coherence and maximal vortex–anti-vortex separation, as marked in the figure. Close to the fixed point, all trajectories meet in a universal curve, indicating that the memory of the initial condition is completely lost and, with that, signaling the universal stage of time evolution. Due to the algebraic slowing-down the system spends a major part of its time evolution near the fixed point. For time $t \to \infty$, all curves would bend over towards $(1/l_{\neq}, 1/l_{\mathrm{C}}) \to (\infty, 0)$ because the last vortex–anti-vortex pair annihilates and the coherence length diverges.[aq] This would

---

[ap]Concerning the expectation value involved in the computation of $g^{(1)}$ *cf.* our remarks in footnote (ao).

[aq]Obviously, in our simulation this happens only to the extent possible on a finite domain.
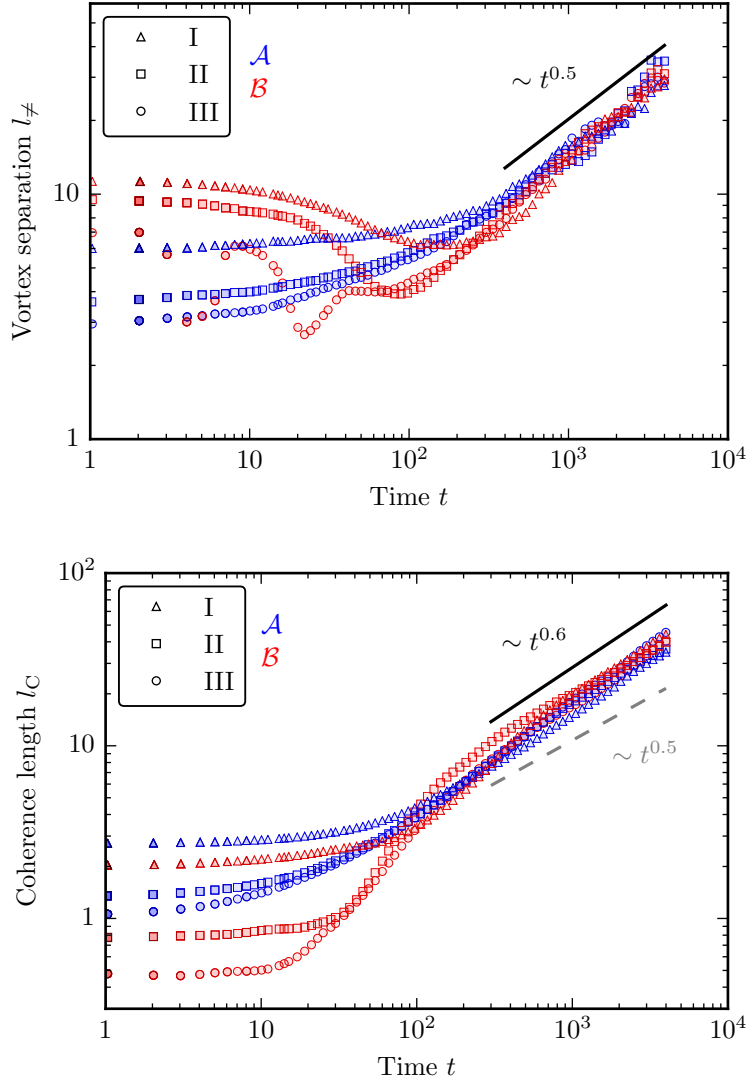
Figure 11.8: Nearest-neighbor vortex–anti-vortex distance $l_{\neq}$ (upper panel) and coherence length l_{C} (lower panel) as functions of time for all initial conditions. The type of initial condition, $\mathcal{A}$ or $\mathcal{B}$, is color-coded, while the different choices of total vortex number are indicated by different symbols, *cf.* Table 11.1.
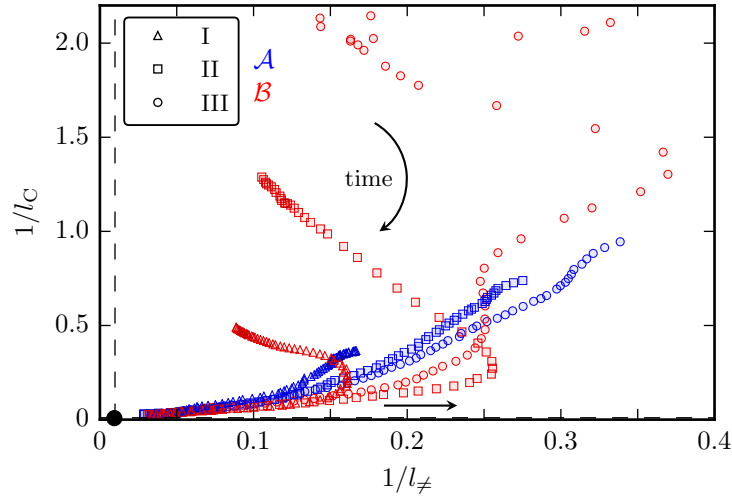
Figure 11.9: Approach to the non-thermal fixed point: Trajectories of the system in the plane spanned by the inverse coherence length $1/l_{\rm C}$ and the inverse mean nearest-neighbor vortex–anti-vortex distance $1/l_{\neq}$. The type of initial condition, $\mathcal{A}$ (random distribution) or $\mathcal{B}$ (vortex lattice), is color-coded, while the different choices of total vortex number are indicated by different symbols, *cf.* Table 11.1. The points are approximately equidistant on a logarithmic time scale: Given the time t_n, the time of the next point is given by $t_{n+1} = 1.1\,t_n$. The first point of each curve represents $t_1 = 1$. The dashed lines correspond to the largest coherence length and vortex–anti-vortex distance possible on the finite simulation domain. For time $t \to \infty$, all curves would bend over towards $(1/l_{\neq}, 1/l_{\rm C}) \to (\infty, 0)$, as indicated by an arrow.

mark the approach to thermal equilibrium. Our findings indicate that the abstract concept of a non-thermal fixed point in the quantum dynamics can be interpreted in a simple way on the gravity side. Specifically, a fixed point corresponds to a time-independent solution of the classical bulk equations of motion (10.8)–(10.10). There is one unique static solution which is completely stable and corresponds to thermal equilibrium, *i. e.* the thermal fixed point. But, as for many systems of non-linear partial differential equations, there will be a series of stationary points with different stability characteristics. The intriguing properties of non-thermal fixed points are reproduced by partially stable stationary points, *i. e.* points which have at least one attractive direction in phase space. This guarantees that the time evolution first approaches such a fixed point – regardless of details of the initial condition – before turning towards thermal equilibrium. Here, we have identified such a partially stable stationary point for the dynamics of the holographic model in the reduced configuration space of Fig. 11.9.

Let us now discuss the picture developed of the non-thermal fixed point in the context of vortices in a superfluid [258, 259, 281]. Precisely at a non-thermal fixed point, scaling of, *e. g.*, the momentum distribution applies by definition at all momenta smaller than some ultraviolet scale, such as the healing length measuring the distance over which a density perturbation 'heals out' in the superfluid. A fixed-point momentum distribution $n(k) \sim k^{-4}$ can be traced to the geometry of the fluid-velocity field around a vortex core, and extending this to $k = 0$ would imply a single vortex at a random position in an infinitely extended system. Hence, vanishing total angular momentum as in the examples discussed above, would require, approaching the fixed point, the 'vortex-behind-the-moon' scenario where the opposite-winding-number vortex is at a large distance from the first one.

Considering this idealized picture, the fixed point can never be exactly reached in a finite system such as on our computer grid. However, the diluting vortex gas approaches a configuration with a few far-separated vortices with vanishing total angular momentum, in fact close to the scenario described above. Notwithstanding these limitations also in a finite geometry metastable vortex configurations exist such as regular lattices of vortices with alternating winding number within a noise-free condensate field.

Finally, we would like to look in more detail at the properties of the non-thermal fixed point in terms of bulk properties in the holographic description. As discussed above, the fixed point itself cannot be reached in our simulations. But it is natural to expect that the quasi-stationary configurations in the late-time stage of the system's evolution should in many respects be close to the fixed point.

We observe that in the early stage of the evolution the bulk fields exhibit strong variation in the x- and y-directions. In particular, these variations are also present away from the vortex cores. In the quasi-stationary late-time regime, in contrast, significant variations are observed only in the direct vicinity of the vortex cores. This characteristic difference is nicely seen in the behavior of the isosurfaces of the quantity $\sqrt{-g}\,|J^0|$ that we show in Fig. 11.3. To exhibit this more clearly, we plot in Fig. 11.10 the same charge-density isosurfaces as in Fig. 11.3, with all other features of the plots removed. In the early stage of the evolution (upper panel), the isosurface of the bulk charge density shows many small ripples and several spikes resulting from vortex annihilation events. On the other hand, in the late-time regime (lower panel) the isosurface appears almost featureless except for the holes due to the vortices. We associate this smoothness of the bulk fields away from the vortex cores with the absence of short-wavelength sound waves. In fact, the almost complete absence of such short-wavelength sound waves appears to be characteristic for all quasi-stationary configurations that we have observed in our simulations. (It also holds for the quasi-stationary lattice configurations that can be constructed as mentioned above.) In the evolution of our systems sound waves of this kind are typically created in annihilation processes of vortices and are then rather rapidly dissipated.[ar] Sound waves of short wavelength have a relatively high

---

[ar]This can be easily seen in our movies of example evolutions, see footnote (al).
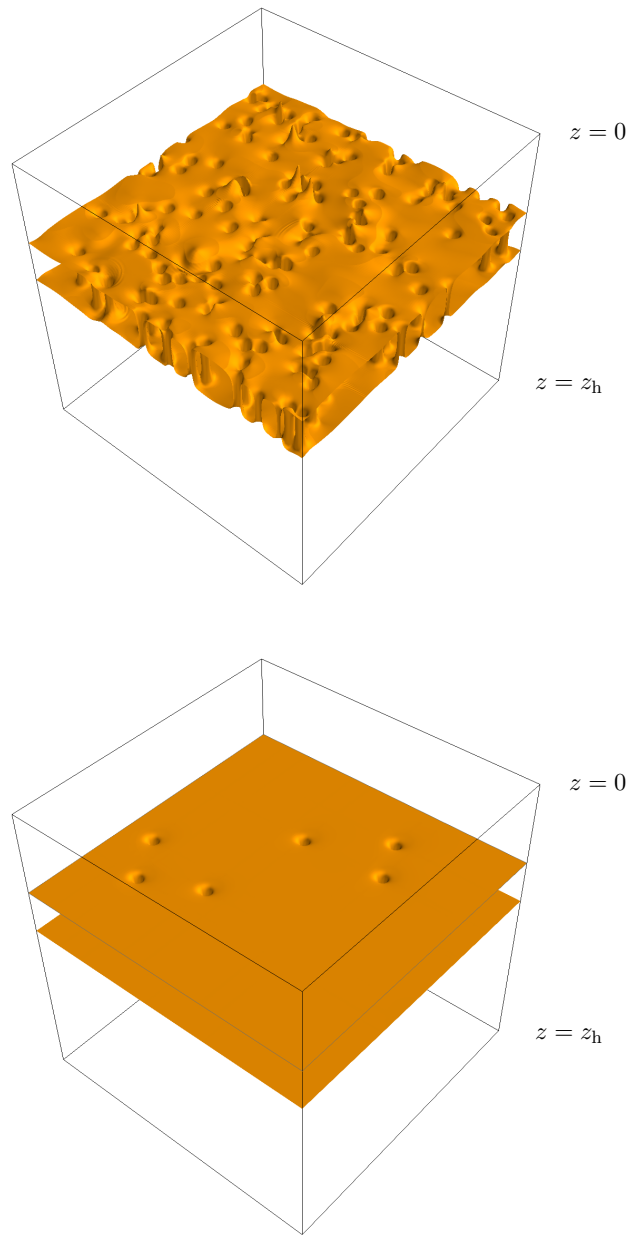
Figure 11.10: Single-run bulk snapshots of isosurfaces of the charge density $\sqrt{-g}\,|J^0|$ at times $t = 200$ (upper panel) and $t = 4000$ (lower panel). The same parameters as in Fig. 11.3 are used. The holes in the charge density indicate the presence of vortices. Note the strong variations of the charge density field at $t = 200$. The isosurface exhibits ripples resulting from vortex annihilation events. In contrast to this, the isosurface at $t = 4000$ is very smooth.

energy density. According to the interpretation of the holographic coordinate z as an inverse energy variable, see Eq. (2.20) in the discussion in Sec. 2.2, one would expect these sound modes to correspond to bulk excitations (more or less) localized close to the boundary. Unfortunately, we did not succeed in extracting this expected behavior from our simulation data. As long as the system still contains vortices, there are bulk excitations spanning a wide range of wavelengths. The said short-wavelength sound waves are only a small contribution relative to this background, and it is therefore difficult to isolate their contribution numerically. Despite this numerical difficulty the bulk perspective offers an attractive way of studying and interpreting the dynamics close to the non-thermal fixed point.

Up to now, our discussion of the non-equilibrium dynamics of the holographic superfluid was based on our simulation data for the choice $T/T_c = 0.68$ of the ratio of the heat bath's temperature and the critical temperature. In the following chapter, we will assess the robustness of our conclusions and the temperature dependence of vortex-related observables such as the constants $D_=$ and $D_{\neq}$ by studying the system at three further values of the ratio T/T_c.

12 Dependence on Temperature and Chemical Potential

In the previous chapter we have investigated the non-equilibrium dynamics of the holographic superfluid starting from quench-like initial conditions. These initial conditions are prepared by perturbing a homogeneous thermal background state with a definite temperature in the superfluid phase, $T/T_c < 1$, by the introduction of vortex defects. We have explored in detail the dynamics starting from a state with $T/T_c = 0.68$. In particular, we have studied large classes of initial conditions, and have found that the system enters a universal stage at late times which is characterized by scaling laws of observables with respect to space (momentum) and time. In this chapter, we study three further choices of T/T_c for the thermal state. As before, these states are perturbed by the introduction of vortex defects. Due to the large numerical cost of the simulations, *cf.* Appendix D.2, in contrast to the previous chapter here we only study one type of initial conditions. Due to our previous findings we expect that this is sufficient to analyze the characteristics of the long-time evolution. The question we want to ask is to what extent our findings regarding the late-time stage in the previous chapter are robust with respect to changes of the temperature of the background state. Moreover, we investigate the temperature dependence of constants related to the evolution of the vortex ensemble.

The simulation parameters and choice of initial conditions are summarized in Table 12.1. In this chapter, we study the three new cases $T/T_c = 0.45, 0.54, 0.90$, and compare the data to that of the case $T/T_c = 0.68$. In practice, T/T_c is tuned by adjusting the chemical potential $\mu = 9, 7.5, 4.5$ in units specified by the condition $z_h = 1$, see Sec. 10.3. The density n_0 of the superfluid order parameter in the corresponding thermal background state is given in the table. For comparison, we have included the details of the case $T/T_c = 0.68$ in the third row. As mentioned above, for the new choices of T/T_c we study one type of initial conditions, namely type $\mathcal{A}$ III, *i. e.* a random distribution of 720 elementary vortices (winding number $+1$) and 720 elementary anti-vortices (winding number -1), *cf.* Table 11.1. As before, we use 504×504 points for the boundary-theory directions (x, y), and 32 for the holographic direction z. Averages are taken for statistical observables over five runs for each set of parameters. For consistency, then, for the data presented in this chapter corresponding to $T/T_c = 0.68$ ($\mu = 6$) with initial condition $\mathcal{A}$ III, we have also averaged over only five of our ten runs. t_f denotes the final time of the simulations (in units set by $z_h = 1$). It is adjusted such that $t_f T_c$ is similar for all parameters, as shown in the table. Finally, a is the grid constant in the aforementioned units. The values of a are chosen, for consistency across different simulations, such that

Table 12.1: Parameters and initial conditions used for the simulations of non-equilibrium dynamics. The quantities in the table are explained in the text. For details on the initial conditions see Table 11.1. In this chapter we investigate the temperature dependence of the non-equilibrium dynamics by studying the system at the given values of T/T_c.

T/T_c	μ	n_0	initial conditions	t_f	a	$t_f T_c$	$L T_c$
0.45	9	265.2	$\mathcal{A}$ III	3000	1/6	1586	44.4
0.54	7.5	120.2	$\mathcal{A}$ III	3500	1/5	1542	44.4
0.68	6	41.7	$\mathcal{A}$ I–III, $\mathcal{B}$ I–III	4000	1/3.5	1410	50.8
0.90	4.5	5.5	$\mathcal{A}$ III	5500	1/1.5	1454	88.8

an isolated elementary vortex is about 13 grid points in diameter, where we define the 'boundary' of the vortex as that point at which the density assumes 95 % of the background density n_0. (Recall that the density vanishes in the center of a vortex. For an isolated vortex, then, the density increases monotonically with the distance from the center.) The choice of a and the grid size of $N \times N = 504 \times 504$ points in the (x, y) direction then leads to a quadratic domain (in the boundary theory) of side length $L = Na$. In the table, we have given the dimensionless product of L and the critical temperature T_c. Note that due our procedure of choosing the grid constant the dimensionless size $(LT_c)^2$ of the simulation domain is larger for the larger temperatures.

In the following sections, we first discuss the time evolution of the vortex ensembles for the different choices of T/T_c. As we will see, a universal stage in which vortex-distribution-related observables obey scaling laws with respect to time arises for all choices of T/T_c. In particular, in that stage the scaling exponents for different T/T_c coincide. Then, we will study the occupation number spectra during the late-time stage and examine their scaling properties. Also here will we find that for different temperatures the scaling exponents coincide in the late-time stage (within the uncertainty in determining them), but they only coincide after a time later than that after which the scaling exponents for the observables related to the vortex distribution coincide.

To be able to properly compare dimensionful quantities evaluated at different values of T/T_c, in the following we generally scale dimensionful quantities by appropriate powers of T_c to make them dimensionless.[as] We thus interpret T_c as fixed and accordingly compare quantities 'measured' at different temperatures.

[as]Considering a quantity $\mathcal{Q}$ with mass dimension n and using Eq. (10.5), the dimensionless quantity $\mathcal{Q}T_c^{-n}$ is given in terms of the dimensionless $\mathcal{Q}z_h^n$ (recall our choice of units $z_h = 1$) by

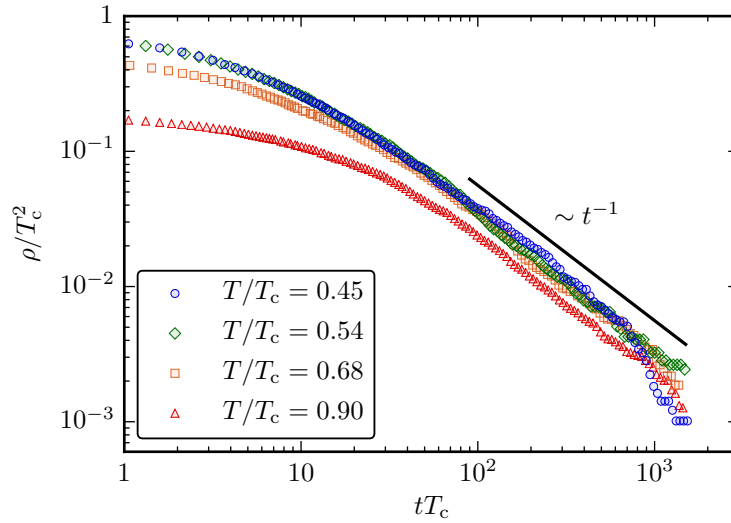$$\mathcal{Q}T_c^{-n} = (\mathcal{Q}z_h^n)\left(\frac{4\pi}{3}\frac{T}{T_c}\right)^n .$$

Figure 12.1: Time dependence of the averaged vortex density for runs with different choices of T/T_{c}, on a double-logarithmic scale. Shown is the scaled vortex density ρ/T_{c}^2 as a function of the scaled time tT_{c}.

12.1 Dynamical Evolution of the Vortex Ensembles at Different Temperatures

We start with a discussion of the time evolution of the vortex ensembles. At the different temperatures considered here, the qualitative picture of the non-equilibrium dynamics of the superfluid after the initial quench is the same as in the case $T/T_{\mathrm{c}} = 0.68$ studied in detail above. The number of vortices in our system is only reduced by vortex–anti-vortex-pair annihilation, and we have never observed spontaneous creation of vortex–anti-vortex pairs or merging of vortices. For $T/T_{\mathrm{c}} = 0.45$, at the final time of the simulations 2 or 4 vortices were left, except for one run out of five in which the last vortex pair annihilated at $t = 2292$ before the end of the simulation at $t_{\mathrm{f}} = 3000$ (in units specified by $z_{\mathrm{h}} = 1$). Next, for $T/T_{\mathrm{c}} = 0.54$ at the final time of the simulations 4 or 6 vortices were left. Finally, for $T/T_{\mathrm{c}} = 0.90$ at the final time of the simulations 8, 10, or 12 vortices were left.

The full time dependence of the vortex density for all four choices of T/T_{c} is shown in Fig. 12.1 (averages are taken over five runs for each choice of T/T_{c}). Both the vortex density and the time are scaled with appropriate powers of the critical temperature T_{c} such that they become dimensionless. Despite the fact that there are initially 1440 elementary vortices in all of the simulations, the initial vortex densities are not all equal since LT_{c} differs for the various choices of T/T_{c}, see Table 12.1. However, this is not too big an issue as we are interested in the late-time behavior where we expect the details of the initial conditions to become unimportant. Roughly for $tT_{\mathrm{c}} \gtrsim 100$ the dimensionless vortex densities ρ/T_{c}^2 exhibit scaling

behavior for all temperatures investigated.[at] The scaling laws are consistent with $\rho \sim t^{-1}$ for all T/T_{c}. For the 'coldest' setup, $T/T_{\mathrm{c}} = 0.45$ (blue circles), on our finite simulation grids at late times $tT_{\mathrm{c}} \gtrsim 700$ the vortex density deviates from the scaling law. As we have mentioned above, in one of the five realizations for $T/T_{\mathrm{c}} = 0.45$ the system was already free of vortices at $t = 2292$ in units specified by $z_{\mathrm{h}} = 1$, corresponding to $tT_{\mathrm{c}} = 1216$. As deviations from scaling appear already for $tT_{\mathrm{c}} \gtrsim 700$, obviously the deviation from scaling cannot be entirely due to one of the five ensemble members already being in a near-thermal vortex-free state. Indeed, even if we average only over the four runs where vortices are present in the system until the end of the simulation a deviation from scaling appears for only slightly later times than when averaging over all five runs, namely for $tT_{\mathrm{c}} \gtrsim 850$. All in all, the effect is most likely due to poor vortex statistics at late times which is most pronounced for $T/T_{\mathrm{c}} = 0.45$ where only very few vortices are left at late times, *cf.* the numbers reported above. The vortex annihilation rate, and thus the vortex density, then becomes sensitively dependent on the definite positions of the remaining vortices. In short, the deviation from scaling is likely an artifact of our finite simulation domain and is expected to vanish in the thermodynamic limit.

Let us express, motivated by the observation of a late-time t^{-1} scaling, the behavior of the vortex density during the late-time stage of the evolution as $\rho(t; T/T_{\mathrm{c}}) \simeq \Gamma(T/T_{\mathrm{c}})^{-1} t^{-1}$ with a vortex decay parameter $\Gamma(T/T_{\mathrm{c}})$ depending on the choice of T/T_{c}. This parameter can be phenomenologically interpreted as follows. The only process that changes the number of vortices in our system is vortex–anti-vortex pair annihilation. Thus, one may argue that the decay rate $\mathrm{d}\rho/\mathrm{d}t$ of the vortex density is proportional to the square of the vortex density as a measure for the probability that vortices meet (see *e. g.* [232, 236]). This leads to the phenomenological equation

$$\frac{\mathrm{d}\rho}{\mathrm{d}t} = -\Gamma\rho^2 \,, \tag{12.1}$$

solved by

$$\rho(t) = \frac{1}{\rho_0^{-1} + \Gamma t} \simeq \frac{1}{\Gamma t} \,, \tag{12.2}$$

where ρ_0 is the initial vortex density and we have approximated $\rho(t)$ for large t. From our data shown in Fig. 12.1 we extract estimates for Γ by multiplying ρ/T_{c}^2 by tT_{c} and computing the mean of the data points in the range at late tT_{c} where $(\rho/T_{\mathrm{c}}^2) \times (tT_{\mathrm{c}})$ is approximately constant, which yields $(\Gamma T_{\mathrm{c}})^{-1}$. As a measure for the statistical uncertainty we compute the standard deviation of these data points.

The resulting estimates for Γ are recorded in Table 12.2. We give the results both in units specified by $z_{\mathrm{h}} = 1$ and in units of T_{c}. We find relative standard deviations between $3\,\%$ and $6\,\%$ due to the noise inherent in the data. However, a larger source

---

[at]The dimensionless product $tT_{\mathrm{c}} \simeq 100$ becomes $t/z_{\mathrm{h}} \simeq 285$ for $T/T_{\mathrm{c}} = 0.68$. In Sec. 11.3 we have found a common scaling law of the vortex densities for different initial conditions for $t/z_{\mathrm{h}} \gtrsim 400$. The earlier time found here is not in conflict with our previous observation since here we consider only a random distribution of vortices as initial condition, which enters the scaling regime more quickly, *cf.* Fig. 11.4.

Table 12.2: Estimates for the decay parameter Γ during the late-time stage of the time evolution. The values are given both in units specified by setting $z_\mathrm{h} = 1$ and in units of the critical temperature T_c. The relative uncertainty is conservatively estimated as $10\,\%$ (see text).

T/T_c	Γ	ΓT_c
0.45	0.03	0.26
0.54	0.04	0.30
0.68	0.05	0.31
0.90	0.09	0.42

of uncertainty is the determination of the range in tT_c on which to compute the average. We address that by varying the endpoints of the range on which the data is averaged, thus producing a range of estimates. As a result of that, a conservative estimate for the relative uncertainty is $10\,\%$ for all four temperatures. A further source of uncertainty would be the fact that here we have used only one type of initial conditions. However, that should introduce only a negligible bias since our previous results for the case $T/T_\mathrm{c} = 0.68$ and using qualitatively different initial conditions indicate that in the late-time regime the dynamics does not depend on the details of the initial condition. From the data given in Table 12.2 we conclude that there is an overall increase of the dimensionless decay parameter ΓT_c with T/T_c.

The vortex decay parameter Γ has also been studied in a holographic superfluid in [236]. However, a quantitative comparison to those results is hindered by the fact that the authors of Ref. [236] only study temperatures $T/T_\mathrm{c} \geq 0.58$, so that we only have two data points overlapping with their results. Moreover, in the cited work only early times are studied whereas we focus on the late-time regime which anyway renders a direct comparison of the results questionable. The qualitative results of the cited work agree with ours, as also there an increase of the decay parameter with temperature is found.

Let us now investigate the statistical properties of the vortex ensembles in more detail by studying the time evolution of the characteristic length scales defined in Eqs. (11.1) and (11.2), *i. e.* the mean nearest-neighbor vortex–vortex distance $l_=$ and vortex–anti-vortex distance $l_{\neq}$. These length scales $l_=$ and $l_{\neq}$, scaled with T_c, are plotted against the scaled time tT_c in Fig. 12.2 (averages are taken over five runs for each choice of T/T_c). For completely uncorrelated vortices, the inverse of the square root of the vortex density ρ gives the mean vortex separation. Therefore, the time evolution of the length scales $l_=$ and $l_{\neq}$ is closely related to the time evolution of the vortex density shown in Fig. 12.1. Like in the case of that observable, the non-monotonic behavior seen in $l_=$ at very late times for $T/T_\mathrm{c} = 0.45$ and $T/T_\mathrm{c} = 0.68$ is most likely an artifact of the finite grid size necessarily employed in the simulation, see our discussion above.

We observe from Fig. 12.2 that a scaling regime compatible with $l_=, l_{\neq} \sim t^{0.5}$ is
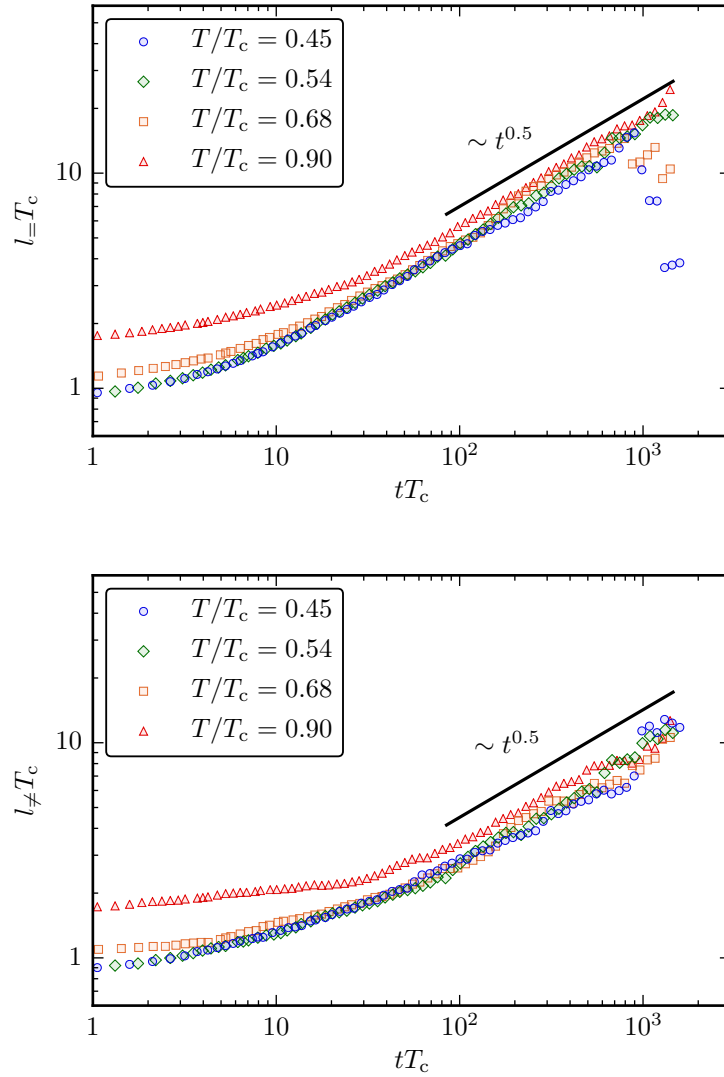
Figure 12.2: Time dependence of the mean nearest-neighbor vortex–vortex distance $l_=$ (upper panel) and vortex–anti-vortex distance $l_{\neq}$ (lower panel) for runs with different choices of T/T_c, on a double-logarithmic scale. Length and time scales are made dimensionless by scaling with T_c. The non-monotonic behavior of $l_=$ at very late times for some T/T_c is likely an artifact of the finite spatial extent of the simulation domain (see text).

Table 12.3: Estimates for the constants $D_=$ and $D_{\neq}$ associated with the diffusive behavior of the vortices during the late-time regime of the time evolution. The values are given both in the units specified by setting $z_{\mathrm{h}} = 1$ and in units of the critical temperature T_{c}. The relative uncertainty is conservatively estimated as $20\,\%$ (see text).

	$D_=$		$D_{\neq}$	
T/T_{c}	$D_=$	$D_= T_{\mathrm{c}}$	$D_{\neq}$	$D_{\neq} T_{\mathrm{c}}$
0.45	0.10	0.05	0.03	0.016
0.54	0.14	0.06	0.04	0.019
0.68	0.19	0.07	0.06	0.020
0.90	0.31	0.08	0.10	0.028

soon entered for all temperatures investigated. We note the tendency that the lower the temperature the earlier in tT_{c} the scaling law applies. Across all choices of T/T_{c}, both $l_=$ and $l_{\neq}$ follow a scaling law for scaled times $tT_{\mathrm{c}} \gtrsim 100$. We thus observe that the diffusive behavior $l_= = \sqrt{4D_= t}$ and $l_{\neq} = \sqrt{4D_{\neq} t}$ in the late-time stage that we have found for $T/T_{\mathrm{c}} = 0.68$ in Sec. 11.3 in fact manifests itself for all temperatures. From the data shown in Fig. 12.2 we estimate the values of the constants $D_= T_{\mathrm{c}}$ and $D_{\neq} T_{\mathrm{c}}$ by averaging $(lT_{\mathrm{c}})^2/(4tT_{\mathrm{c}})$ with $l = l_=$ and $l = l_{\neq}$, respectively, over the range at late tT_{c} where that quotient is approximately constant. We compute the standard deviation as a measure of the statistical uncertainty. The resulting estimates for $D_=$ and $D_{\neq}$ are recorded in Table 12.3. We find relative standard deviations between $4\,\%$ and $10\,\%$. Varying the endpoints of the range in tT_{c} on which we average the data, as discussed above for the determination of Γ, a relative uncertainty of $20\,\%$ is a conservative estimate for both $D_=$ and $D_{\neq}$, and for all temperatures. The estimates for $D_=$ and $D_{\neq}$ in the case $T/T_{\mathrm{c}} = 0.68$ in Table 12.3 are close to the estimates we have obtained in Sec. 11.3 (namely, $D_= \approx 0.16$ and $D_{\neq} \approx 0.05$), and compatible within the uncertainty. Like in the case $T/T_{\mathrm{c}} = 0.68$ discussed in Sec. 11.3, also for the other temperatures T/T_{c} the constants $D_=$ and $D_{\neq}$ differ due to the effective vortex–vortex and vortex–anti-vortex interactions. It is interesting to note from Table 12.3 that $D_= \approx 3D_{\neq}$ for all temperatures investigated. Furthermore, we find that both $D_= T_{\mathrm{c}}$ and $D_{\neq} T_{\mathrm{c}}$ increase with T/T_{c}. It indeed seems reasonable that an increased temperature leads to an increased 'diffusivity' of the vortices, in accordance with our finding of larger decay parameter ΓT_{c} for larger temperature.

Taking our observations for the vortex density and the vortex length scales $l_=$ and $l_{\neq}$ together, we conclude that the universality that we have found in Chap. 11 in the late-time regime of the system's evolution for the choice $T/T_{\mathrm{c}} = 0.68$ extends to the different temperatures explored here. In particular, the scaling exponents of vortex-ensemble-related observables coincide for different values of T/T_{c}. To complete the picture, in the following section we study the occupation number spectrum during

the late-time stage of the system's evolution. This allows us to determine the scaling exponents with respect to momentum and compare them for different choices of temperature T/T_c.

## 12.2 Occupation Number Spectra in the Late-Time Regime at Different Temperatures

We have so far ascertained the presence of a universal regime in the system's non-equilibrium time evolution where for $tT_c \gtrsim 100$ characteristic observables for the vortex distribution exhibit scaling laws in time with a scaling exponent independent of the temperature ratio T/T_c. We now study the occupation number spectrum $n(k, t)$ defined in Eq. (11.3) from the equal-time two-point correlation function of the order-parameter field. As in Sec. 11.4 before, we analyze $n(k, t)$ in terms of scaling laws in an inertial range, $n(k) \sim k^{-\zeta}$, see Appendix D.3 for technical details.

In Fig. 12.3 we show the occupation number spectrum (averages are taken over five runs for each choice of T/T_c) during the late-time stage of the system's evolution. In Fig. 12.3a we plot $n(k, t)$ for the different choices of T/T_c in units specified by $z_h = 1$ in order to clearly exhibit the scaling properties. $n(k, t)$ is shown at times $tT_c = 300$ (left plot) and $tT_c = 400$ (right plot). The reason for the choice of these times will become clear momentarily. In Fig. 12.3b the spectra at $tT_c = 400$ are shown again, now with the occupation number spectra and the momentum made dimensionless by multiplying by appropriate powers of T_c.

We find that the spectra for different choices of the temperature T/T_c exhibit scaling behavior in an inertial range with scaling exponents within some central value ± 0.1 only after a scaled time $tT_c \simeq 300$, which is why we have chosen that time for the left panel in Fig. 12.3a. This time is significantly later than the time $tT_c \simeq 100$ after which the vortex-ensemble-related observables obey universal scaling laws for all temperature investigated. We have already observed this hierarchy of the onset times of the scaling regimes with respect to time and space (momentum) in the case $T/T_c = 0.68$ in Secs. 11.3 and 11.4. The scaling exponent in the late-time regime starting at $tT_c \simeq 300$ are in the range $4.1 \lesssim \zeta \lesssim 4.3$, see Fig. 12.3a. As time progresses, the lower momentum cutoff of the scaling regime decreases toward the infrared, as the vortex gas becomes more dilute.

The time $tT_c = 400$ for the right panel in Fig. 12.3a has been chosen to illustrate the following point. As suggested by the data shown in the two panels in Fig. 12.3a (and backed up by further analysis of the numerical data), the system is slowest in tT_c to enter a universal scaling regime for the occupation number spectrum in the case $T/T_c = 0.90$, *i.e.* the largest temperature we have investigated. Whereas for all other temperatures the scaling exponents relax to smaller values in the course of the evolution from $tT_c = 300$ to $tT_c = 400$, the scaling exponent for $T/T_c = 0.90$ stays at 4.3. This extends our observation in the previous section 12.1 that the characteristic length scales $l = l_=, l_{\neq}$ of the vortex distribution start to obey a universal scaling law $l \sim t^{-0.5}$ at earlier times tT_c for lower temperatures T/T_c. In
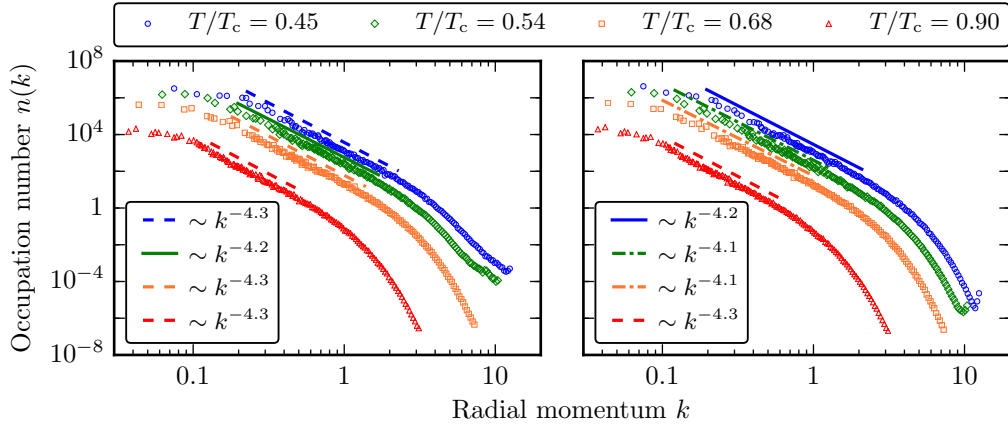
(a) Occupation number spectrum $n(k)$ at the scaled times $tT_c = 300$ (left) and $tT_c = 400$ (right). The units of $n(k)$ and k are specified by the condition $z_h = 1$. Scaling laws with different exponents are shown with different linestyles.
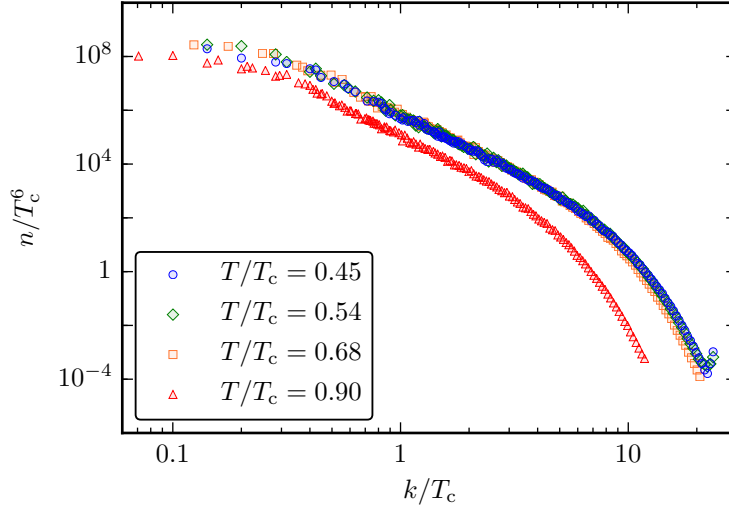
(b) Scaled occupation number spectrum n/T_c^6 at the scaled time $tT_c = 400$ as a function of the scaled radial momentum k/T_c. As the data for each T/T_c are rescaled with constant factors, the scaling exponents of the spectra exactly coincide with those in the upper right panel.

Figure 12.3: Occupation number spectra as functions of the radial momentum during the late stage of the evolution. Note the double-logarithmic scales. The choice of T/T_c is color-coded. The spectra for all choices of T/T_c exhibit scaling behavior $n(k) \sim k^{-\zeta}$ with exponents $4.1 \lesssim \zeta \lesssim 4.3$, see the upper panel.

159

the further evolution, the scaling exponents for all temperatures eventually relax to the range $4.1 \lesssim \zeta \lesssim 4.2$ and remain in that range up to the final times we study in our simulations, see Table 12.1. Thus, apparently effects of the vortex interactions are relevant up to the final times for all temperatures, preventing a complete relaxation to the single-vortex scaling $n(k) \sim k^{-4}$, *cf.* our discussion in Sec. 11.4.

Turning to Fig. 12.3b, it is very interesting to note that the spectra for $T/T_c = 0.45, 0.54, 0.68$ at equal scaled times tT_c are roughly given by a common function after scaling both the spectra and the momenta with appropriate powers of the critical temperature T_c to render them dimensionless. As these spectra characterize non-equilibrium systems coupled to thermal baths of different temperatures, this might be related to non-equilibrium scaling behavior involving rescalings of momenta, time, and temperature (see *e. g.* [295, 308–310]). However, the spectrum for $T/T_c = 0.90$, closest to the equilibrium critical point for all temperatures investigated, clearly deviates from the common curve of the scaled spectra for $T/T_c = 0.45, 0.54, 0.68$. One reason for this might be that the initial vortex density ρ/T_c^2 for $T/T_c = 0.90$ deviates rather strongly from the initial densities ρ/T_c^2 for $T/T_c = 0.45, 0.54, 0.68$. Also the fact that the distance of the temperature to the critical temperature is smaller than for the other values of T/T_c could play a role. With our limited number of values of T/T_c, we cannot clarify these issues further here, so they remain a challenge for further study.

In summary, in this chapter we have found that a universal regime characterized by common scaling behavior of observables with respect to space (momentum) and time is entered at $tT_c \simeq 300$ across a large range of temperatures T/T_c.[au] While the onset time of the universal regime might still depend somewhat on details of the initial conditions (here we have studied the dense distribution $\mathcal{A}$ III of randomly positioned vortices and anti-vortices), for the long-time regime we can robustly conclude that the system is attracted to the same non-thermal fixed point with the same scaling exponents in space (momentum) and time across different values of the temperature ratio T/T_c of the heat bath.

[au]The dimensionless time $tT_c \simeq 300$ becomes $t/z_h \simeq 855$ for $T/T_c = 0.68$ (recall that our units are specified by $z_h = 1$). This is to be compared with the time $t/z_h \simeq 600$ that we have found in Secs. 11.3 and 11.4 for the onset of the universal regime in both the vortex-distribution-related observables and the spectra. The difference is due to the fact that for $T/T_c = 0.90$ the system takes longer in tT_c to reach the universal regime.

13 Summary

In the second part of this thesis, we have studied the far-from-equilibrium dynamics of a holographic superfluid at finite temperature and chemical potential. In the holographic framework, the classical solution of an Einstein–Maxwell–scalar system in 3+1 dimensions is dual to the quantum dynamics of a (2+1)-dimensional superfluid. We have performed a numerical study of the time evolution of the holographic superfluid in its superfluid phase starting from a variety of far-from-equilibrium initial conditions corresponding to quenches of the system. In particular, we have imprinted various kinds of large ensembles of topological defects, $i.\,e.$ quantized vortices and anti-vortices, in the superfluid. We have employed an approximation ('probe approximation') which entails an effective picture in which a superfluid 'component' dynamically evolves on top of and is coupled to a static heat bath. The time evolution of the superfluid can be interpreted in terms of an effective description in which vortices and anti-vortices interact via sound waves. When vortex–anti-vortex pairs annihilate energy is quickly dissipated into the heat bath. We have developed a very fast numerical implementation of the equations of motion that allows to evolve the non-equilibrium states for longer times than studied before in the literature, giving access to a new regime of the system's evolution. We have studied the general properties of the non-equilibrium dynamics for the choice $T/T_c = 0.68$ for the ratio of the heat bath's temperature and the phase transition temperature, using qualitatively different classes of initial conditions (Chap. 11). To assess the robustness of our general conclusions and to estimate the temperature dependence of non-universal coefficients related to the vortex dynamics, we have discussed further simulations (Chap. 12) that were performed for three additional choices of T/T_c.

Let us first summarize our general findings obtained in the case $T/T_c = 0.68$. At early times, the evolution of the system strongly depends on the initial conditions, $i.\,e.$ on the distribution and density of vortices and anti-vortices. We find that the system exhibits a new non-equilibrium universality regime in the late-time stages of the evolution. Starting from any of our initial conditions, that regime is entered at times $t \gtrsim 600$ in units specified by $z_h = 1$. This universal regime is characterized by a dilute 'gas' of vortex defects. The system remains in the universal regime until the final times $t_f = 4000$ we study in our simulations for $T/T_c = 0.68$. In order to obtain more insight into the dynamics of the universal regime, we have analyzed the time evolution of characteristic length scales of the ensemble of topological defects, and have studied spatial correlations of microscopic excitations via the occupation number spectrum. We have observed scaling laws in these observables in the universal regime of the system's evolution and have determined the corresponding scaling exponents. The power-law behavior of the occupation number spectrum can be re-

lated to turbulence. During the universal stage, the occupation number spectrum scales as $n(k,t) \sim k^{-\zeta}$ in an infrared-to-intermediate-momenta inertial range with scaling exponent $4.1 \lesssim \zeta \lesssim 4.3$. This value is close to the scaling $n(k,t) \sim k^{-4}$ observed in classical statistical simulations of two-dimensional Bose gases [258, 259] where it was shown to be related to a dilute random distribution of vortices and anti-vortices and, in turn, to so-called strong wave turbulence [256].

We have made the interesting observation that the evolution of the system exhibits critical slowing-down during the universal regime. This is a natural feature of non-equilibrium dynamics in the vicinity of non-thermal fixed points. Moreover, we have demonstrated that the system exhibits the same long-time dynamics in terms of scaling laws with respect to momentum and time independently of details of the initial conditions (and of the temperature of the heat bath). We have hence found the first evidence for the presence of a non-thermal fixed point in the dynamics of a holographic system. This is particularly interesting as the occurrence of a non-thermal fixed point indicates that the dynamics of the corresponding non-equilibrium state is universal and independent of the microscopic details of the system. The same universal dynamics is then expected to occur in a variety of other quantum systems, thus connecting very different fields of physics, see for example [311–313]. The observation of a non-thermal fixed point not only gives a new perspective on the dynamics of the holographic superfluid. The gauge/gravity duality also adds a new dimension to the understanding of non-thermal fixed points, as it translates quantum dynamics in the boundary theory to classical dynamics in the bulk. Thus, the duality might provide a new avenue for an analytic treatment of non-thermal fixed points, as these are dual to stationary solutions of non-linear partial differential but classical equations of motion.

At an intermediate stage (at about $200 \lesssim t \lesssim 400$) during the evolution of our system we observe a power-law energy spectrum which is consistent with Kolmogorov 5/3-scaling. Such behavior has been reported before in [233] for the same system. However, we find Kolmogorov scaling only for part of the various initial conditions we have chosen. Specifically, Kolmogorov scaling emerges when the evolution starts from random distributions of vortex defects, while this is not the case when we choose vortex lattices as initial configurations, the type of initial conditions used in [233]. At the intermediate times concerned here, the system is still affected by the initial distribution of vortex defects, while soon afterwards it enters the universal regime discussed above which exhibits a different scaling behavior. Kolmogorov scaling thus seems to occur only in a transient way. But it appears that details of the initial conditions can influence the system for a sufficiently long time to completely prohibit the emergence of a transient Kolmogorov scaling. This may also depend on the way in which statistical noise is implemented in the numerical simulation for particular sets of quenches. Further study is needed to understand better the conditions for the occurrence of Kolmogorov scaling.

Finally, we have studied the system with supplementary choices of the temperature ratio T/T_c, both larger and smaller than $T/T_c = 0.68$. The data obtained in these additional simulations corroborate our results regarding the presence and

the details (particularly, scaling exponents) of the universal late-time regime. Both the characteristic vortex-distribution-related length scales and the occupation number spectrum exhibit scaling with universal exponents in the late-time stage for $tT_{\mathrm{c}} \gtrsim 300$ for all choices of T/T_{c} investigated here. We have estimated from our data for different T/T_{c} the values of coefficients appearing in the vortex density and characteristic vortex distance scales during the universal stage. These coefficients can be related to the vortex decay rate and the diffusive motion of vortices, and generally increase with temperature, which indicates a larger 'mobility' of vortices at higher temperatures in the superfluid phase. The occupation number spectra for the lower three of our choices of T/T_{c} appear to be remarkably weakly dependent on T/T_{c} when the time, the momentum, and the spectra themselves are made dimensionless by scaling with appropriate powers of T_{c}. However, the spectrum for our largest choice $T/T_{\mathrm{c}} = 0.90$ deviates strongly from the aforementioned spectra. This may be partly due to differences in the details of the initial conditions, but may also indicate a potential change of behavior close to T_{c}. Further study is needed to clarify these issues.

Besides the demand for further simulations at different values of T/T_{c} and with a still larger variety of initial conditions to corroborate or further refine our results, this last point also clearly highlights an important direction for future study of the non-equilibrium dynamics of the holographic superfluid, namely the exploration of the physics of the system beyond the probe limit that we have used in this work and that has so far been used in all studies of the holographic superfluid's non-equilibrium dynamics. Lifting the probe approximation requires to solve the full dynamics encoded in the action (10.1), in particular including a dynamical metric. While this is numerically demanding, it will potentially also be very rewarding as holographic methods provide an *ab initio* description of certain strongly coupled quantum many-body systems. Moreover (see also the discussion in Ref. [233]), the particular holographic-superfluid model is minimal in the sense that it makes no assumptions about the interaction of the normal and superfluid components of the system, and, in fact, goes beyond an effective description relying on a two-component decomposition. In particular, solving the full dynamics of the model, one would expect modifications in the behavior for smaller temperatures T/T_{c}, *i. e.* 'deeper' in the superfluid phase, where the backreaction of the matter fields onto the metric becomes increasingly important. Our efficient numerical implementation of the probe-limit holographic-superfluid dynamics certainly constitutes a good starting point for this challenging task.

14 Conclusion and Outlook

In this thesis, we have applied a bottom-up holographic approach to two strongly coupled physical systems. Since holographic methods yield a new perspective on the physical systems they are applied to, qualitatively new insights can potentially be gained. Moreover, even with the fact that in bottom-up holography one loses knowledge about the boundary theory to some extent, by systematically studying various holographic models for a given system, universal features might be discovered that apply to the physics of interest. The prime example is the KSS bound [30] on the ratio η/s of the shear viscosity and the entropy density that seems to be obeyed by all fluids in Nature.

In two main parts, we have considered a hot and a cold strongly coupled quantum fluid. More precisely, with the strongly coupled quark–gluon plasma explored in current and future heavy-ion collision experiments in mind, in Part I we have investigated heavy quarks immersed in strongly coupled plasmas with a chemical potential. By studying a large class of non-conformal holographic models our aim has been to find strong-coupling universal behavior. In Part II, we have investigated the real-time non-equilibrium dynamics of a strongly coupled superfluid in two spatial dimensions. Using fast numerical simulations starting from various quench-like initial conditions and exploring different temperatures in the superfluid phase, we have in particular studied non-equilibrium universality in the late-time regime of the system's evolution and its relation to the dynamics of topological vortex defects. We have summarized our detailed findings at the end of the two parts, see Chaps. 8 and 13, respectively. Let us in the following discuss our main results and interesting directions for further study.

Hot: Heavy Quarks in Strongly Coupled Plasmas

We have investigated in detail (Chap. 5) thermodynamic quantities associated with heavy $Q\bar{Q}$ pairs and single quarks, *i. e.*, the free energy, entropy, and internal energy. For $Q\bar{Q}$ pairs, we have in addition studied a quantity that can be interpreted as a binding energy. We have clarified the important distinctions of the free energy and the binding energy, and advocated a general renormalization procedure for the extremal Nambu–Goto action of a bulk string representing a heavy $Q\bar{Q}$ pair that can be used in any asymptotically AdS spacetime to compute the $Q\bar{Q}$ free energy. An analogous procedure can be used to obtain the single-quark free energy. The full implications had not been discussed in the literature before. The renormalization procedure ensures that the $Q\bar{Q}$ free energy, as well as the associated internal energy, become independent of the temperature, chemical potential, and a possible non-

conformal deformation scale for small $Q\bar{Q}$ separation L, as expected on physical grounds. In fact, both the free energy and the internal energy in all our non-conformal deformations of $\mathcal{N} = 4$ SYM approach the vacuum $Q\bar{Q}$ potential of the latter theory, which is analytically known [105], for small L. In contrast, the binding energy manifestly depends on temperature, chemical potential, and a possible non-conformal deformation scale for small L which precludes its interpretation as an effective interaction potential. Comparing the free energy and the internal energy in our non-conformal models with their counterparts in $\mathcal{N} = 4$ SYM, we have made the interesting observation that both the free energy and the internal energy generally increase above their values in $\mathcal{N} = 4$ SYM upon introduction of non-conformality, except for one of our non-conformal models where even for the largest possible deformations both the free and the internal energy show almost no deviation from $\mathcal{N} = 4$ SYM. Thus, the $Q\bar{Q}$ free energy and internal energy are in a large class of non-conformal models for strongly coupled plasma approximately bound from below by their $\mathcal{N} = 4$ SYM counterparts. As these two energies are in principle candidates for model potentials for the interaction of heavy quarks this result should have important implications for QGP phenomenology.

We have shown that the behavior of the free energy qualitatively agrees with lattice QCD data [195, 226] in $\mathcal{N} = 4$ SYM and all our non-conformal models, both with respect to variations of the temperature and of the chemical potential, at least for small values of the latter. In contrast to other strong-coupling methods like lattice QCD, in bottom-up holography the introduction of a chemical potential μ does not introduce additional technical difficulties. While there are more complicated ways of introducing a chemical potential in top-down holographic approaches (see *e. g.* [192, 314]), we have shown in Chap. 6 that the chemical potential we have implemented in our bottom-up models is in fact sufficient to capture essential aspects of the baryon chemical potential in QCD. This result has been achieved by comparing the leading non-trivial coefficient in the small-μ expansion of the heavy quark–anti-quark ($Q\bar{Q}$) free energy in lattice QCD and our holographic models. This coefficient was found to be very robust with respect to the deformation in all our non-conformal models, lending further support to the relevance of 'bottom-up' holographic chemical potentials to QGP physics.

Finally, we have studied (Chap. 7) the running coupling $\alpha_{Q\bar{Q}}(L)$ derived from the $Q\bar{Q}$ free energy. This quantity elucidates the interplay of the non-conformal deformation, which tends to increase $\alpha_{Q\bar{Q}}$, and the screening effects due to the thermal medium, which decrease $\alpha_{Q\bar{Q}}$. In general, these effects combine and lead to a maximum in the running coupling in non-conformal models as is also found in lattice simulations (see *e. g.* [196]). Moving beyond the regime of applicability of lattice QCD, we have studied $\alpha_{Q\bar{Q}}(L)$ in the whole (μ, T)-plane. All previous holographic studies [113, 126] have worked at vanishing chemical potential. While one of our models, in accordance with our findings for other observables, is very robust and deviates only little from $\mathcal{N} = 4$ SYM which as a conformal theory does not exhibit a maximum in $\alpha_{Q\bar{Q}}$, in our other non-conformal models a clear maximum

is found for all deformations and also at non-zero chemical potential. Increasing μ to quite large values $\mu/T \gtrsim 10$ the maximum 'melts' away showing a clear screening effect due to the increased net density associated with μ. We have found that on a range that extends to $\mu/T \gtrsim 20$ and presumably encompasses the range of phenomenological interest, the μ-dependence of the length scale $L_{\max}$ associated with the maximum of $\alpha_{Q\bar{Q}}$ is parametrically weaker than the dependence on T. The overall picture that emerges from this observation and the behavior of the other observables studied in this thesis in various non-conformal holographic models for strongly coupled plasmas is that the impact of the chemical potential on the $Q\bar{Q}$ interaction is generally weaker than that of the temperature.

Our findings show that the bottom-up holographic modeling of strongly coupled deconfined gauge theory plasma akin to the QGP is a very promising approach. In particular, the inclusion of a chemical potential, which is crucial in light of ongoing and future heavy-ion experiments, is technically simple and yields encouraging results. At vanishing chemical potential, where one does not have to deal with the bulk gauge field, more complicated non-conformal bottom-up deformations of $\mathcal{N} = 4$ SYM than those discussed here have been constructed to approximate QCD behavior. Examples include the 2-parameter model of [160] (see *e. g.* [113] for applications with encouraging results) and so-called 'improved holographic QCD' [178, 179]. A very interesting extension of our work would be to construct refined models at non-zero chemical potential along the lines of the cited works. Moreover, holographic methods have been devised [315, 316] to study anisotropic strongly coupled plasma such as the real-world QGP produced in heavy-ion collisions. Based on these methods, a non-conformal model for an anisotropic strongly coupled plasma has already been constructed [214]. It would be very interesting to include a chemical potential into that model. Last but not least, it would also be very interesting to use advanced holographic numerical methods such as those that we employed in Part II to investigate plasmas closer to the real experimental situation where the quark–gluon plasma is not static but rather expanding rapidly and anisotropically. This research direction has already attracted much attention recently (see *e. g.* [317] and references cited therein). However, so far these studies employ $\mathcal{N} = 4$ SYM (and work at vanishing chemical potential). It certainly is important to eventually include non-conformal deformations such as those that we have studied here.

Cold: Non-Equilibrium Dynamics in a Holographic Superfluid

We have studied the real-time dynamics of the standard holographic superfluid model [249, 250, 272] in two spatial dimensions with a special emphasis on universal behavior in the non-equilibrium long-time evolution of the system. To this end, on the basis of our fast numerical implementation of the equations of motion in the probe limit we have studied the system on larger grids and for longer times than previously reported in the literature. We started from various initial conditions characterized by a fixed temperature $T/T_c < 1$ of the background heat bath and ensembles of vortex defects. To investigate the general properties of the dynamics

we have fixed a particular temperature and studied qualitatively different classes of initial conditions, averaging statistical observables over ten runs for each type of initial conditions (Chap. 11). Having found in these simulations the presence of a universal late-time regime in the system's evolution, our results regarding its properties have been corroborated by additional simulations at three further choices of $T/T_c < 1$ (Chap. 12).

For all temperatures investigated, for dimensionless times $tT_c \gtrsim 300$ the system is in a universal regime irrespective of the details of the initial conditions. This universal regime is characterized by a dilute gas of vortices. Moreover, in this regime we observe power-law behavior in time of characteristic observables describing the vortex distribution, as well as power-law behavior in an inertial range of momenta of the occupation number spectrum of microscopic excitations of the superfluid order parameter. We have determined the universal scaling exponents. Specifically, the occupation number spectrum is found to obey scaling $n(k,t) \sim k^{-\zeta}$ in an infrared-to-intermediate-momenta inertial range with scaling exponent $4.1 \lesssim \zeta \lesssim 4.3$, while characteristic length scales l of the vortex distributions scale as $l \sim t^{0.5}$. This indicates a 'critical slowing down' of the dynamics, $\dot{l}/l \sim t^{-1}$. Such behavior in association with scaling in momentum space and time is typical for the approach to a non-thermal fixed point. We have shown that the system is in fact attracted, in a reduced phase space, by the point of maximal phase coherence and maximal vortex–anti-vortex separation, as previously observed in the context of ultracold Bose gases in [258, 259, 281].

Our findings constitute the first evidence for the presence of a non-thermal fixed point in the dynamics of a holographic system. Moreover, due to the new perspective offered by the holographic approach, new insights into non-thermal fixed points in certain strongly correlated quantum many-body systems may be gained. Non-thermal fixed points in such systems should be related to stationary points of the classical dynamical equations in the dual bulk theory, which might provide a new avenue for an analytic treatment of non-thermal fixed points.

There are many open questions to be addressed in order to obtain a full understanding of the holographic superfluid. An interesting point for further investigation concerns the coupling strength of the holographic superfluid. In general, the holographic duality maps a weakly coupled classical gravity system to a strongly coupled quantum system. It would be useful to investigate what exactly that means in relation to other descriptions of superfluids which have the coupling as an explicit parameter. A detailed comparison of the behavior of, for instance, typical length or time scales in the holographic superfluid and in semi-classical (Gross–Pitaevskii) descriptions of superfluidity can give insight into this problem. Furthermore, to complete the picture of the non-equilibrium dynamics of the holographic superfluid it will eventually be necessary to lift the probe approximation and study the full dynamics of the bulk system, which means including a dynamical metric. In particular, then, there would no longer be a static 'heat bath', and one would be able to study a fully non-equilibrium superfluid, with no artificial distinction of normal and superfluid components. As holography allows for an *ab initio* description of certain

strongly coupled quantum many-body systems, this would indeed be very interesting. Our fast numerical implementation of the system's dynamics in the probe approximation provides a solid foundation for this endeavor. Finally, a very important question is the relevance of a holographic description to experiments. Potentially related real-world systems in two spatial dimensions that exhibit superfluidity and vortex excitations include semiconductor-based exciton–polariton condensates (see *e. g.* [243–246]) as well as oblate, quasi-2D Bose–Einstein condensates (see *e. g.* [232]), and it will be very interesting to see what insights into the physics of these systems holographic methods can yield.

Appendix

A Conventions and Identities Used in Gravity

In this appendix, we give the definitions that we use in our calculations involving general relativity, and collect some useful identities.

In any dimension considered we use metric signature $(- + \cdots +)$. We employ the $(+ + +)$ sign conventions ($\mathbf{g}$ sign, Riemann sign, Einstein sign) for gravity as classified and used by Misner, Thorne, and Wheeler [37]. We generically, unless otherwise noted, denote by D the dimension of the AdS-like bulk spacetime, and by $d = D - 1$ the dimension of the boundary theory. We use capital Latin indices for the D bulk coordinates $x^M = (t, \boldsymbol{x}, z)$, Greek indices for the d boundary theory coordinates $x^\mu = (t, \boldsymbol{x})$, and lower-case Latin indices for the $d - 1$ spatial boundary coordinates $x^i = (\boldsymbol{x})$.

Denoting the D-dimensional bulk metric by g_{MN}, the Christoffel symbols Γ^L_{MN}, the Riemann tensor $\mathcal{R}^K{}_{LMN}$, the Ricci tensor $\mathcal{R}_{MN}$, and the Ricci scalar $\mathcal{R}$ are given by

$$\Gamma^L_{MN} = \frac{1}{2} g^{LA} \left(\partial_M g_{AN} + \partial_N g_{MA} - \partial_A g_{MN} \right), \tag{A.1}$$

$$\mathcal{R}^K{}_{LMN} = \partial_M \Gamma^K_{LN} - \partial_N \Gamma^K_{LM} + \Gamma^A_{LN} \Gamma^K_{AM} - \Gamma^A_{LM} \Gamma^K_{AN}, \tag{A.2}$$

$$\mathcal{R}_{MN} = \mathcal{R}^A{}_{MAN}, \tag{A.3}$$

$$\mathcal{R} = g^{MN} \mathcal{R}_{MN}. \tag{A.4}$$

In Part II we deal with the equations of motion of an Abelian Higgs model on a curved background, see Eqs. (10.8)–(10.10). The left-hand sides of Eqs. (10.8) and (10.9) can be simplified as follows by using standard identities from general relativity (see *e.g.* [159]). For the field-strength tensor F_{MN} we use the fact that it is antisymmetric, which implies

$$\nabla_M F^{MN} = \frac{1}{\sqrt{-g}} \partial_M (\sqrt{-g} F^{MN}),$$

where g is the determinant of the metric g_{MN}. For the scalar field Φ we first note that $D^M \Phi$, for the metric- and gauge-covariant derivative $D^M = g^{MN}(\nabla_N - \mathrm{i} A_N)$, is a vector. The covariant divergence of a vector V^M can be expressed as

$$D_M V^M = \frac{1}{\sqrt{-g}} \partial_M \left(\sqrt{-g} V^M \right), \tag{A.5}$$

and since Φ is a scalar we have

$$\left(\nabla_M - \mathrm{i} A_M \right) \Phi = \left(\partial_M - \mathrm{i} A_M \right) \Phi. \tag{A.6}$$

Using these two equations we obtain

$$
\begin{aligned}
0 = \left(-D^2 + m^2\right)\Phi &= -(\nabla_M - \mathrm{i}A_M)D^M\Phi + m^2\Phi \\
&= -\frac{1}{\sqrt{-g}}(\partial_M - \mathrm{i}A_M)\sqrt{-g}D^M\Phi + m^2\Phi \\
&= -\frac{1}{\sqrt{-g}}(\partial_M - \mathrm{i}A_M)\sqrt{-g}g^{MN}(\partial_N - \mathrm{i}A_N)\Phi + m^2\Phi \\
&= -\frac{1}{\sqrt{-g}}\partial_M\left(\sqrt{-g}g^{MN}\partial_N\Phi\right) + \frac{\mathrm{i}}{\sqrt{-g}}\partial_M\left(\sqrt{-g}g^{MN}A_N\Phi\right) \\
&\quad + \mathrm{i}g^{MN}A_M(\partial_N\Phi - \mathrm{i}A_N\Phi) + m^2\Phi\,.
\end{aligned}
$$

B Explicit Form of the 1-Parameter Models

In this appendix, we give the explicit expressions for the 1-parameter models discussed in Sec. 4.1.3. These expressions have been first computed at vanishing chemical potential in [113] and at non-zero chemical potential in [45]. In our presentation in this appendix we closely follow the latter reference. The thermodynamics of the 1-parameter models is discussed in Sec. 4.1.4.

B.1 The 1-Parameter Model with Non-Minimal Gauge Kinetic Function

We first deal with the model that has the gauge kinetic function of DeWolfe *et al.*[158] in the action (4.1), *i. e.*

$$f_{\mathrm{DWGR}}(\phi) = \frac{\cosh\left(\frac{12}{5}\right)}{\cosh\left(\frac{6}{5}(\phi - 2)\right)} \, . \tag{B.1}$$

Recall from Eqs. (4.40) and (4.39) that the *ansätze* for the warp factor A and the scalar ϕ are

$$A(z) = \log\left(\frac{L_{\mathrm{AdS}}}{z}\right) \, , \tag{B.2}$$

$$\phi(z) = \sqrt{\frac{3}{2}}\kappa z^2 \, . \tag{B.3}$$

Using MATHEMATICA we solve the equation of motion (4.34) with the boundary condition (4.12) for B, and the equation of motion (4.36) with the boundary conditions (4.41) and (4.42) for Φ. We find the following closed-form expressions,

$$B(z) = \log\left(\frac{L_{\mathrm{AdS}}}{z}\right) - \frac{1}{4}\kappa^2 z^4 \, , \tag{B.4}$$

$$\Phi(z) = L_{\mathrm{AdS}}\mu \, \frac{\mathrm{e}^{24/5}E_+\left(\kappa z^2\right) - E_-\left(\kappa z^2\right) - \left(\mathrm{e}^{24/5}E_+\left(\kappa z_{\mathrm{h}}^2\right) - E_-\left(\kappa z_{\mathrm{h}}^2\right)\right)}{\mathcal{S}\left(\kappa z_{\mathrm{h}}^2\right)} \, , \tag{B.5}$$

B Explicit Form of the 1-Parameter Models

where we have defined the functions

$$E_{\pm}(x) = \operatorname{erf}\left(\frac{3\sqrt{6}}{5} \pm \frac{x}{2}\right), \tag{B.6}$$

$$\mathcal{S}\left(\kappa z_{\mathrm{h}}^2\right) = \left(\mathrm{e}^{24/5} - 1\right)\operatorname{erf}\left(\frac{3\sqrt{6}}{5}\right) - \left(\mathrm{e}^{24/5}E_+\left(\kappa z_{\mathrm{h}}^2\right) - E_-\left(\kappa z_{\mathrm{h}}^2\right)\right). \tag{B.7}$$

For later use, let us also define

$$\widetilde{E}_{\pm}(x) = \operatorname{erf}\left(\frac{3\sqrt{3}}{5} \pm \frac{x}{\sqrt{2}}\right), \tag{B.8}$$

$$\widetilde{\mathcal{S}}\left(\kappa z_{\mathrm{h}}^2\right) = \left(\mathrm{e}^{24/5} - 1\right)\operatorname{erf}\left(\frac{3\sqrt{3}}{5}\right) - \left(\mathrm{e}^{24/5}\widetilde{E}_+\left(\kappa z_{\mathrm{h}}^2\right) - \widetilde{E}_-\left(\kappa z_{\mathrm{h}}^2\right)\right). \tag{B.9}$$

The error function erf used here is defined by

$$\operatorname{erf}(x) = \frac{2}{\sqrt{\pi}} \int_0^x \mathrm{d}t\, \mathrm{e}^{-t^2}. \tag{B.10}$$

Next, from (4.35) we find the horizon function,

$$
\begin{aligned}
h(z) = {}& \frac{\mathrm{e}^{-\kappa^2 z^4/4}}{\mathrm{e}^{\kappa^2 z_{\mathrm{h}}^4/4} - 1}\, \mathcal{S}^{-2}\left(\kappa z_{\mathrm{h}}^2\right)\Bigg\{ \mathcal{S}^2\left(\kappa z_{\mathrm{h}}^2\right)\left(\mathrm{e}^{\kappa^2 z_{\mathrm{h}}^4/4} - \mathrm{e}^{\kappa^2 z^4/4}\right) \\[2mm]
& + \frac{\mu^2}{\kappa}\Bigg[\alpha\left(\mathrm{e}^{\kappa^2 z_{\mathrm{h}}^4/4} - \mathrm{e}^{\kappa^2 z^4/4}\right) \\[2mm]
& \qquad + \beta\Bigg[\mathrm{e}^{\kappa^2 z^4/4}\left(\mathrm{e}^{24/5}\widetilde{E}_+\left(\kappa z^2\right) - \widetilde{E}_-\left(\kappa z^2\right)\right) \\[2mm]
& \qquad\quad - \sqrt{2}\mathrm{e}^{27/25}\left(\mathrm{e}^{24/5}E_+\left(\kappa z^2\right) - E_-\left(\kappa z^2\right)\right)\Bigg]\left(\mathrm{e}^{\kappa^2 z_{\mathrm{h}}^4/4} - 1\right) \\[2mm]
& \qquad + \beta\Bigg[\sqrt{2}\mathrm{e}^{27/25}\left(\mathrm{e}^{24/5}E_+\left(\kappa z_{\mathrm{h}}^2\right) - E_-\left(\kappa z_{\mathrm{h}}^2\right)\right) \\[2mm]
& \qquad\quad - \mathrm{e}^{\kappa^2 z_{\mathrm{h}}^4/4}\left(\mathrm{e}^{24/5}\widetilde{E}_+\left(\kappa z_{\mathrm{h}}^2\right) - \widetilde{E}_-\left(\kappa z_{\mathrm{h}}^2\right)\right)\Bigg]\left(\mathrm{e}^{\kappa^2 z^4/4} - 1\right)\Bigg]\Bigg\},
\end{aligned}
\tag{B.11}
$$

with the functions $\mathcal{S}$, $E_{\pm}$, and $\widetilde{E}_{\pm}$ as defined in Eqs. (B.7), (B.6), and (B.8), respec-

tively. We have introduced the constants

$$\alpha = \sqrt{\frac{2}{\pi}} e^{-81/25} \left(e^{48/5} - 1 \right) \left(\sqrt{2} e^{27/25} \operatorname{erf}\left(\frac{3\sqrt{6}}{5}\right) - \operatorname{erf}\left(\frac{3\sqrt{3}}{5}\right) \right)$$

$$\approx 1452.9 \,, \tag{B.12}$$

$$\beta = \sqrt{\frac{2}{\pi}} e^{-81/25} \left(1 + e^{24/5} \right) \approx 3.83 \,. \tag{B.13}$$

Finally, the potential $V(\phi)$ can be computed from Eq. (4.38),

$$V(\phi) = -\frac{6}{L_{\text{AdS}}^2} e^{\phi^2/3} \left[h(\phi) \left(2 - \frac{\phi^2}{3} \right) - \phi \frac{\mathrm{d}h(\phi)}{\mathrm{d}\phi} \right.$$

$$\left. + \frac{\mu^2}{\kappa} \nu f(\phi) \phi^3 \frac{e^{-\phi^2/3} e^{-12\phi/5} \left(e^{24/5} + e^{12\phi/5} \right)^2}{\mathcal{S}^2(\phi_{\text{h}})} \right] . \tag{B.14}$$

Here, we have re-expressed all z-dependence in the functions h and $\mathcal{S}$, see Eqs. (B.11) and (B.7), respectively, in terms of the scalar ϕ using the one-to-one relation (B.3). To clarify, we have $h(\phi) = h(z)$ only for $\phi = \sqrt{3/2}\,\kappa z^2$, and analogously for $\mathcal{S}$. Further, we denote by ϕ_{h} the value of ϕ at the horizon and we have defined the constant

$$\nu = \frac{2}{9\pi} \sqrt{\frac{2}{3}} e^{-108/25} \approx 7.68 \times 10^{-4} \,. \tag{B.15}$$

The expression just reported for A, B, h, ϕ, Φ, and V define the Einstein-frame model, *i.e.*, we have not treated the scalar as the dilaton; see the discussion in Sec. 4.1.3. The string-frame model is obtained by transforming the metric according to Eq. (4.48). Effectively this just results in the changes

$$A(z) \to \log\left(\frac{L_{\text{AdS}}}{z}\right) + \frac{1}{2}\kappa z^2 \,, \qquad B(z) \to \log\left(\frac{L_{\text{AdS}}}{z}\right) + \frac{1}{2}\kappa z^2 - \frac{1}{4}\kappa^2 z^4 \,. \tag{B.16}$$

B.2 The 1-Parameter Model with Minimal Gauge Kinetic Function

In this section, we deal with the model that has a trivial gauge kinetic function in the action (4.1), *i.e.*

$$f(\phi) = 1 \,. \tag{B.17}$$

The warp factor A and the scalar ϕ are chosen as before, see Eqs. (B.2) and (B.3), respectively.

B Explicit Form of the 1-Parameter Models

While the result for B is unchanged from the model discussed above, due to the trivial gauge kinetic function the solutions for Φ and h get considerably simpler,

$$B(z) = \log\left(\frac{L_{\mathrm{AdS}}}{z}\right) - \frac{1}{4}\kappa^2 z^4\,, \tag{B.18}$$

$$\Phi(z) = \mu L_{\mathrm{AdS}}\left(1 - \frac{\mathrm{erf}\left(\frac{\kappa z^2}{2}\right)}{\mathrm{erf}\left(\frac{\kappa z_{\mathrm{h}}^2}{2}\right)}\right)\,, \tag{B.19}$$

$$
\begin{aligned}
h(z) = \frac{e^{-\kappa^2 z^4/4}}{e^{\kappa^2 z_{\mathrm{h}}^4/4} - 1}\,\mathrm{erf}^{-2}\left(\frac{\kappa z_{\mathrm{h}}^2}{2}\right)\Bigg\{ &\mathrm{erf}^2\left(\frac{\kappa z_{\mathrm{h}}^2}{2}\right)\left(e^{\kappa^2 z_{\mathrm{h}}^4/4} - e^{\kappa^2 z^4/4}\right) \\
&+ \frac{\mu^2}{\kappa}\sqrt{\frac{2}{\pi}}\Bigg[\left(e^{\kappa^2 z^4/4}\,\mathrm{erf}\left(\frac{\kappa z^2}{\sqrt{2}}\right) - \sqrt{2}\,\mathrm{erf}\left(\frac{\kappa z^2}{2}\right)\right)\left(e^{\kappa^2 z_{\mathrm{h}}^4/4} - 1\right) \\
&+ \left(\sqrt{2}\,\mathrm{erf}\left(\frac{\kappa z_{\mathrm{h}}^2}{\sqrt{2}}\right) - e^{\kappa^2 z_{\mathrm{h}}^4/4}\,\mathrm{erf}\left(\frac{\kappa z_{\mathrm{h}}^2}{\sqrt{2}}\right)\right)\left(e^{\kappa^2 z^4/4} - 1\right)\Bigg]\Bigg\}\,.
\end{aligned}
\tag{B.20}
$$

The error function erf used here has been defined in Eq. (B.10). The scalar potential $V(\phi)$ is

$$V(\phi) = -\frac{6}{L_{\mathrm{AdS}}^2}e^{\phi^2/3}\left[h(\phi)\left(2 - \frac{\phi^2}{3}\right) - \phi\frac{\mathrm{d}h(\phi)}{\mathrm{d}\phi} + \frac{\mu^2}{\kappa}\upsilon\phi^3\frac{e^{-\phi^2/3}}{\mathrm{erf}^2\left(\frac{\phi_{\mathrm{h}}}{\sqrt{6}}\right)}\right] \tag{B.21}$$

with the constant

$$\upsilon = \frac{2}{9\pi}\sqrt{\frac{2}{3}} \approx 0.058\,. \tag{B.22}$$

In the potential, we have re-expressed h in terms of ϕ, as discussed after Eq. (B.14).

Just as in the previous section, these solutions define the Einstein-frame model. The transformation to the string-frame model is unaffected by the different choice of the gauge kinetic function, so Eq. (B.16) still applies to the model discussed here.

C Details on the Computation of the $Q\bar{Q}$ Entropy

In this appendix, we give details on the computation of the $Q\bar{Q}$ entropy $S_{Q\bar{Q}}$ discussed in Sec. 5.4.

The basic thermodynamic formula is $S_{Q\bar{Q}} = -\partial F_{Q\bar{Q}}/\partial T$ where it is understood that the interquark distance L is to be kept constant. An implementation of this formula is not entirely straightforward. The issue that arises is that the free energy $F_{Q\bar{Q}}$, as well as the distance L, are only known as integrals in terms of the bulk length scales z_t and z_h, see Eqs. (5.9) and (4.64), respectively. Therefore, while these integrals can be readily computed numerically (or even analytically for $\mathcal{N} = 4$ SYM), the differentiation with respect to the temperature T while keeping the distance L constant is more involved.

In the following we will make use of a notation well-known from thermodynamics, where a vertical bar with a subscripted variable indicates that this variable is kept constant. We will suppress any dependence on a possible deformation parameter. If present in the model under consideration, the deformation parameter is always assumed to be kept constant. For simplicity, we will furthermore work at vanishing chemical potential.

Under the above assumptions, z_h is in a one-to-one relation with T, so we can straightforwardly obtain $z_h = z_h(T)$. On the other hand, $L = L(z_t, z_h)$, which upon inversion yields $z_t = z_t(L, T)$. Thus,

$$\left.\frac{\partial F_{Q\bar{Q}}(z_t, z_h)}{\partial T}\right|_L = \left.\frac{\partial F_{Q\bar{Q}}}{\partial z_h}\right|_{z_t} \frac{\partial z_h}{\partial T} + \left.\frac{\partial F_{Q\bar{Q}}}{\partial z_t}\right|_{z_h} \left.\frac{\partial z_t}{\partial T}\right|_L , \qquad (C.1)$$

where on $\partial z_h/\partial T$ we may omit the specification of the variable that is to be kept constant because z_h is actually a function of T only. Next, we have to evaluate $\partial z_t/\partial T$ with L kept constant. Using

$$0 \stackrel{!}{=} \mathrm{d}L = \left.\frac{\partial L}{\partial z_t}\right|_{z_h} \mathrm{d}z_t + \left.\frac{\partial L}{\partial z_h}\right|_{z_t} \mathrm{d}z_h = \left.\frac{\partial L}{\partial z_t}\right|_{z_h} \mathrm{d}z_t + \left.\frac{\partial L}{\partial z_h}\right|_{z_t} \frac{\partial z_h}{\partial T} \mathrm{d}T , \qquad (C.2)$$

we derive

$$\left.\frac{\partial z_t}{\partial T}\right|_L = -\frac{\left.\frac{\partial L}{\partial z_h}\right|_{z_t}}{\left.\frac{\partial L}{\partial z_t}\right|_{z_h}} \frac{\partial z_h}{\partial T} . \qquad (C.3)$$

C Details on the Computation of the $Q\bar{Q}$ Entropy

Finally, we obtain

$$S_{Q\bar{Q}} = -\left.\frac{\partial F_{Q\bar{Q}}(z_\mathrm{t}, z_\mathrm{h})}{\partial T}\right|_L = -\left(\left.\frac{\partial F_{Q\bar{Q}}}{\partial z_\mathrm{h}}\right|_{z_\mathrm{t}} - \left.\frac{\partial F_{Q\bar{Q}}}{\partial z_\mathrm{t}}\right|_{z_\mathrm{h}} \frac{\left.\frac{\partial L}{\partial z_\mathrm{h}}\right|_{z_\mathrm{t}}}{\left.\frac{\partial L}{\partial z_\mathrm{t}}\right|_{z_\mathrm{h}}}\right) \frac{\partial z_\mathrm{h}}{\partial T}, \qquad (\text{C.4})$$

which can be directly implemented on the basis of the numerical routines (or analytic expressions) for $F_{Q\bar{Q}} = F_{Q\bar{Q}}(z_\mathrm{t}, z_\mathrm{h})$ and $L = L(z_\mathrm{t}, z_\mathrm{h})$.

D Details on the Numerical Implementation of the Holographic Superfluid

In this appendix, we discuss technical details concerning the numerical algorithms and techniques involved in the solution of the equations of motion of the holographic superfluid studied in Part II, as well as in the analysis of observables in that model. We closely follow the presentation in our publication [235].

D.1 Numerical Methods

The general equations of motion for the $(2+1)$-dimensional holographic superfluid in the probe limit are given in Eqs. (10.8)–(10.10). They are defined on a $(3+1)$-dimensional bulk spacetime with metric (10.6), described by the boundary-theory coordinates t, x, y, and the compact holographic coordinate $0 \leq z \leq z_\mathrm{h}$. Units are specified by setting the horizon radius $z_\mathrm{h} = 1$.

For the z-parts of the equations of motion, we use a collocation method with a basis of Chebyshev polynomials on a Gauß–Lobatto grid with 32 points in the holographic direction (see *e. g.* [273]). After setting $z_\mathrm{h} = 1$, we switch to a new coordinate $\tilde{z} \in [-1, 1]$ defined by

$$z = \frac{1}{2}(\tilde{z} + 1) \,. \tag{D.1}$$

With respect to $\tilde{z}$, we work entirely in real space, implementing $\partial_{\tilde{z}}$-differentiation via matrix multiplication.

We treat the directions x and y as periodic. This enables us to use discrete Fourier transforms to efficiently compute derivatives ∂_x and ∂_y. Our choice of the grid constant a for the (x, y) grid depends on the choice of the temperature ratio T/T_c, or equivalently, on the choice of the chemical potential μ. We choose, in the aforementioned units, $a = 6^{-1}$, 5^{-1}, 3.5^{-1}, and 1.5^{-1} for $T/T_\mathrm{c} = 0.45$, 0.54, 0.68, and 0.90 ($\mu = 9$, 7.5, 6, and 4.5), respectively, *cf.* Table 12.1 and the discussion in Chap. 12. All data shown in this thesis were produced on a $504 \times 504 \times 32$ grid (x, y, z-directions).

To compute the equilibrium configuration of the system we have to solve the boundary-value problem defined by the dynamic equations (10.16)–(10.19) and the boundary values given in Eqs. (10.14) and (10.15). We treat the non-linearity of the equations by using the Newton–Kantorovich iteration procedure. Technically,

we solve the resulting system of linear equations via an LU decomposition with full pivoting, see *e. g.* [318].

To construct the initial conditions for the full equations of motion, we perturb the homogeneous equilibrium solution by putting vortices on top of it at an initial time $t = t_i < 0$. For a vortex of winding number w, this is done by imprinting its winding structure onto the bulk scalar field Φ, locally $\Phi(t_i, \boldsymbol{x}, z) \rightarrow \Phi(t_i, \boldsymbol{x}, z) \cdot \mathrm{e}^{iw\phi_v}$ for every z-slice, where ϕ_v is a polar angle in the xy-plane, centered on the respective vortex. The bulk configuration representing a single vortex carries the phase winding at every z-slice [252]. This follows naturally from the fact that all z-slices contribute to the dual field configuration, and is consistent with continuity of the phase of the bulk scalar field. At the vortex positions $\boldsymbol{x}_v$ the scalar field has to vanish to remain well-defined after the phase winding is imprinted, so we set $\Phi(t_i, \boldsymbol{x}_v, z) = 0$ along all z. At all other grid points we leave the absolute value of Φ at the equilibrium value. Starting the simulation, the system very quickly builds up stationary density profiles around the vortex cores. The duration of this build-up process depends on the choice of T/T_c (or, equivalently, μ); the exact numbers are not important for our purposes as we are particularly interested in the long-time behavior. To give an example, for $T/T_c = 0.68$ ($\mu = 6$) stationary density profiles around the vortex cores are built up approximately within 5 or 10 units of time for quench classes $\mathcal{A}$ and $\mathcal{B}$ (see Table 11.1), respectively. To induce variations in the decay pattern of the vortex lattices (class $\mathcal{B}$), we additionally perturb the phase with noise $\mathrm{e}^{i \, \mathrm{Re}(\zeta(\boldsymbol{x}))}$ at time $t = 0$ (and only there) when the vortex cores are fully formed. $\zeta(\boldsymbol{x})$ is obtained as the inverse discrete Fourier transform of $\zeta(\boldsymbol{k})$. This is in turn constructed by populating the Fourier modes in a disk of radius $N/100$ about the origin in momentum space with $\mathcal{O}(1)$ complex Gaußian noise, where N is the number of grid points along each of the directions x, y. All Fourier modes outside this disk are set to zero. We thus excite the system to a non-equilibrium state, as discussed in Sec. 11.1. Solving the full set of equations of motion, we follow the subsequent evolution of the superfluid order parameter $\langle \psi \rangle$. At every time step, we extract it from the bulk field Φ using (10.13).

For the dynamic evolution described by the full equations of motion we solve the boundary value problems in Eqs. (10.25), (10.26), and (10.27) for $\nabla_+ A_x$, $\nabla_+ A_y$, and $\nabla_+ \Phi$, undo the shifts (10.23) to get the time derivatives, and use a fourth-order/fifth-order Runge–Kutta–Fehlberg algorithm with adaptive timestep size to propagate the fields one timestep forward. We allow the timestep size τ to vary in the range $0.001 \leq \tau \leq 0.1$ in our aforementioned units. We use (10.24) to update A_t in every timestep.

During the simulations, in order to investigate the spatial characteristics of the vortex ensembles, we determine the positions of all vortices and anti-vortices in the superfluid order parameter $\langle \psi(\boldsymbol{x}, t) \rangle$ at every unit timestep. To this end, we iterate over the whole (x, y) grid, measuring the integrated phase of the superfluid order parameter around each elementary plaquette.

D.2 Performance

We implement the algorithm in C++, using the `fftw3` library [319] for Fourier transformations and the `Eigen` library [320] for high-performance linear algebra. We parallelize the numerical code for multicore architectures with `OpenMP` [321].

Propagating a 352×352 grid with 32 points in the holographic direction up to time 600 utilizing 4 threads on a regular desktop computer with an Intel i7 processor takes approximately 8 hours.

Running on the Intel Xeon server architecture using 16 threads, a run up to time 4000 on a 504×504 grid with 32 points in the holographic direction takes around 120 hours.

D.3 Fitting of Scaling Exponents of Occupation Spectra

Scaling laws of occupation number spectra take the simple form $n(k) \sim k^{-\zeta}$ with scaling exponent ζ. In the case of the occupation number spectra discussed in Sec. 11.4, we fit the power law exponents. We employ the Levenburg–Marquardt least-squares fitting algorithm to determine these scaling exponents after choosing a momentum range for the fit by eye.

There are two sources of uncertainty in this: the determination of the momentum range and the uncertainty inherent in estimating the best fit parameters. The fitting algorithm reports an uncertainty of typically 0.03 for the scaling exponents. Fixing the momentum range introduces a larger source of uncertainty. To address this, we vary the endpoints of the momentum range and thus determine a range of estimators for the scaling exponent. As a result of that, we estimate the uncertainty in our determination of scaling exponents of the occupation number spectra to be 0.1. Therefore, we state results for fitted scaling exponents with one decimal digit.

The data on the time dependence of our observables is noisier than the data on occupation number spectra such that using a fitting algorithm is not appropriate in this case. The uncertainty in our determination of scaling exponents with respect to time is difficult to assess.

D.4 Equilibrium Solutions in Poincaré Coordinates

For reference for the interested reader, here we give the explicit equations determining static solutions, homogeneous in x and y, of the equations of motion (10.8)–(10.10) of the holographic superfluid, using the metric given in Eq. (10.3), *i.e.*, employing Poincaré coordinates. These equations can also be found for instance in [322]. In the dynamical simulations, Eddington–Finkelstein (EF) coordinates are used; we give the transformation rule below.

For conciseness, here we immediately set the spatial components of the gauge field to zero $A_i = 0$. With the boundary conditions we impose, see Sec. 10.2, the A_i are

in fact found to vanish in solving the full system defined by Eqs. (10.16)–(10.19). Moreover, we work in axial gauge $A_z = 0$.

Introducing $\tilde{\Phi} = \Phi/z$ for the scalar, the equations for the remaining fields, the gauge-field component A_t and $\tilde{\Phi}$, are found to be

$$hA_t'' = 2\tilde{\Phi}^2 A_t \,, \tag{D.2}$$

$$h^2\tilde{\Phi}'' - 3z^2 h\tilde{\Phi}' - zh\tilde{\Phi} = -A_t^2\tilde{\Phi} \,, \tag{D.3}$$

where the derivative with respect to z is denoted by a prime, $h(z)$ is the horizon function given in Eq. (10.4), and we have already set $z_{\rm h} = 1$ and $m^2 = -2$. The scalar field $\tilde{\Phi}$ can be taken real. The boundary conditions relevant for equilibrium solutions of the holographic superfluid are $A_t(z = 0) = \mu$ and $A_t(z = z_{\rm h} = 1) = 0$ for the gauge field, and $\tilde{\Phi}(z = 0) = 0$ plus the requirement of regularity at the horizon for the scalar, *cf.* our discussion in Sec. 10.2. The boundary-value problem can relatively easily be solved by an expansion of A_t and $\tilde{\Phi}$ in Chebyshev polynomials and a Newton–Kantorovich iteration to treat the non-linearity (see *e. g.* [273]), see Appendix D.1 above.

To discuss the transformation of the solutions of Eqs. (D.2) and (D.3) to EF coordinates we now explicitly use a subscript 'P' for the solutions of Eqs. (D.2) and (D.3), *i. e.* $(A_{\rm P})_M$ (recall that $(A_{\rm P})_i = 0$) and $\tilde{\Phi}_{\rm P}$, and for the Poincaré coordinates themselves, $x_{\rm P}^M$. We denote the EF coordinates and fields by x^M, A_M, and $\tilde{\Phi}$, where $\tilde{\Phi} = \Phi/z$, as used in the full dynamical equations of motion discussed in Sec. 10.4. The only coordinate that differs between Poincaré and EF coordinates is the time, see the relation (10.7). We deduce the Jacobian

$$\frac{\partial x_{\rm P}^M}{\partial x^N} = \begin{pmatrix} 1 & 0 & 0 & \frac{1}{h(z)} \\ 0 & 1 & 0 & 0 \\ 0 & 0 & 1 & 0 \\ 0 & 0 & 0 & 1 \end{pmatrix}, \tag{D.4}$$

and the transformation rules

$$A_M = \frac{\partial x_{\rm P}^N}{\partial x^M}\,(A_{\rm P})_N \,, \tag{D.5}$$

$$\tilde{\Phi} = \tilde{\Phi}_{\rm P} \,. \tag{D.6}$$

After this transformation, the axial gauge $(A_{\rm P})_z = 0$ is lost, $A_z \neq 0$. It can be re-imposed in EF coordinates by a gauge transformation generated by a function $\chi(z)$, requiring one to integrate the differential equation

$$0 \overset{!}{=} A_z + \chi' = \frac{(A_{\rm P})_t}{h(z)} + (A_{\rm P})_z + \chi' = \frac{(A_{\rm P})_t}{h(z)} + \chi' \,. \tag{D.7}$$

The associated gauge transformation of the scalar, $\tilde{\Phi} \to \tilde{\Phi}\mathrm{e}^{\mathrm{i}\chi}$, finally leads to a complex scalar in EF coordinates.

Bibliography

[1] J. M. Maldacena, "The Large-N limit of superconformal field theories and supergravity," *Adv. Theor. Math. Phys.* **2** (1998) 231, `arXiv:hep-th/9711200 [hep-th]`.

[2] S. S. Gubser, I. R. Klebanov, and A. M. Polyakov, "Gauge theory correlators from noncritical string theory," *Phys. Lett.* **B428** (1998) 105, `arXiv:hep-th/9802109 [hep-th]`.

[3] E. Witten, "Anti-de Sitter space and holography," *Adv. Theor. Math. Phys.* **2** (1998) 253, `arXiv:hep-th/9802150 [hep-th]`.

[4] J. Casalderrey-Solana, H. Liu, D. Mateos, K. Rajagopal, and U. A. Wiedemann, *Gauge/String Duality, Hot QCD and Heavy Ion Collisions.* Cambridge Univ. Pr., 2014. `arXiv:1101.0618v1 [hep-th]`.

[5] A. Adams, L. D. Carr, T. Schäfer, P. Steinberg, and J. E. Thomas, "Strongly Correlated Quantum Fluids: Ultracold Quantum Gases, Quantum Chromodynamic Plasmas, and Holographic Duality," `arXiv:1205.5180 [hep-th]`.

[6] S. A. Hartnoll, "Lectures on holographic methods for condensed matter physics," *Class. Quant. Grav.* **26** (2009) 224002, `arXiv:0903.3246 [hep-th]`.

[7] J. McGreevy, "Holographic duality with a view toward many-body physics," *Adv. High Energy Phys.* **2010** (2010) 723105, `arXiv:0909.0518 [hep-th]`.

[8] M. H. Anderson, J. R. Ensher, M. R. Matthews, C. E. Wieman, and E. A. Cornell, "Observation of Bose-Einstein condensation in a dilute atomic vapor," *Science* **269** (1995) 198.

[9] K. B. Davis, M. O. Mewes, M. R. Andrews, N. J. van Druten, D. S. Durfee, D. M. Kurn, and W. Ketterle, "Bose-Einstein condensation in a gas of sodium atoms," *Phys. Rev. Lett.* **75** (1995) 3969.

[10] C. C. Bradley, C. A. Sackett, J. J. Tollett, and R. G. Hulet, "Evidence of Bose-Einstein Condensation in an Atomic Gas with Attractive Interactions," *Phys. Rev. Lett.* **75** (1995) 1687.

[11] B. DeMarco and D. S. Jin, "Onset of Fermi degeneracy in a trapped atomic gas," *Science* **285** (1999) 1703.

[12] A. G. Truscott, K. E. Strecker, W. I. McAlexander, G. B. Partridge, and R. G. Hulet, "Observation of Fermi Pressure in a Gas of Trapped Atoms," *Science* **291** (2001) 2570.

[13] K. M. O'Hara, S. L. Hemmer, M. E. Gehm, S. R. Granade, and J. E. Thomas, "Observation of a Strongly Interacting Degenerate Fermi Gas of Atoms," *Science* **298** (2002) 2179, `arXiv:cond-mat/0212463` `[cond-mat.supr-con]`.

[14] M. Bartenstein, A. Altmeyer, S. Riedl, S. Jochim, C. Chin, J. H. Denschlag, and R. Grimm, "Crossover from a Molecular Bose-Einstein Condensate to a Degenerate Fermi Gas," *Phys. Rev. Lett.* **92** (2004) 120401, `arXiv:cond-mat/0401109` `[cond-mat.other]`.

[15] M. W. Zwierlein, J. R. Abo-Shaeer, A. Schirotzek, C. H. Schunck, and W. Ketterle, "Vortices and superfluidity in a strongly interacting Fermi gas," *Nature* **435** (2005) 1047, `arXiv:cond-mat/0505635` `[cond-mat.supr-con]`.

[16] D. D. Osheroff, R. C. Richardson, and D. M. Lee, "Evidence for a New Phase of Solid He^3," *Phys. Rev. Lett.* **28** (1972) 885.

[17] D. D. Osheroff, W. J. Gully, R. C. Richardson, and D. M. Lee, "New Magnetic Phenomena in Liquid He^3 below 3 mK," *Phys. Rev. Lett.* **29** (1972) 920.

[18] P. Kapitza, "Viscosity of Liquid Helium below the λ-Point," *Nature* **141** (1938) 74.

[19] J. F. Allen and A. D. Misener, "Flow Phenomena in Liquid Helium II," *Nature* **142** (1938) 643.

[20] T. Byrnes, N. Y. Kim, and Y. Yamamoto, "Exciton–polariton condensates," *Nature Phys.* **10** (2014) 803.

[21] **BRAHMS** Collaboration, I. Arsene *et al.*, "Quark gluon plasma and color glass condensate at RHIC? The Perspective from the BRAHMS experiment," *Nucl. Phys.* **A757** (2005) 1, `arXiv:nucl-ex/0410020` `[nucl-ex]`.

[22] **PHOBOS** Collaboration, B. Back *et al.*, "The PHOBOS perspective on discoveries at RHIC," *Nucl. Phys.* **A757** (2005) 28, `arXiv:nucl-ex/0410022` `[nucl-ex]`.

[23] **STAR** Collaboration, J. Adams *et al.*, "Experimental and theoretical challenges in the search for the quark gluon plasma: The STAR Collaboration's critical assessment of the evidence from RHIC collisions," *Nucl. Phys.* **A757** (2005) 102, `arXiv:nucl-ex/0501009` `[nucl-ex]`.

[24] **PHENIX** Collaboration, K. Adcox *et al.*, "Formation of dense partonic matter in relativistic nucleus-nucleus collisions at RHIC: Experimental evaluation by the PHENIX collaboration," *Nucl. Phys.* **A757** (2005) 184, `arXiv:nucl-ex/0410003 [nucl-ex]`.

[25] **ALICE** Collaboration, K. Aamodt *et al.*, "Elliptic flow of charged particles in Pb-Pb collisions at 2.76 TeV," *Phys. Rev. Lett.* **105** (2010) 252302, `arXiv:1011.3914 [nucl-ex]`.

[26] **ATLAS** Collaboration, G. Aad *et al.*, "Measurement of the pseudorapidity and transverse momentum dependence of the elliptic flow of charged particles in lead-lead collisions at $\sqrt{s_{NN}} = 2.76$ TeV with the ATLAS detector," *Phys. Lett.* **B707** (2013) 330–348, `arXiv:1108.6018 [hep-ex]`.

[27] **CMS** Collaboration, S. Chatrchyan *et al.*, "Measurement of the elliptic anisotropy of charged particles produced in PbPb collisions at $\sqrt{s_{NN}}$=2.76 TeV," *Phys. Rev.* **C87** (2013) 014902, `arXiv:1204.1409 [nucl-ex]`.

[28] R. Averbeck, J. W. Harris, and B. Schenke, "Heavy-Ion Physics at the LHC," in *The Large Hadron Collider: Harvest of Run 1*, T. Schörner-Sadenius, ed., pp. 355–420. Springer, 2015.

[29] P. Braun-Munzinger, V. Koch, T. Schäfer, and J. Stachel, "Properties of hot and dense matter from relativistic heavy ion collisions," `arXiv:1510.00442 [nucl-th]`.

[30] P. Kovtun, D. T. Son, and A. O. Starinets, "Viscosity in strongly interacting quantum field theories from black hole physics," *Phys. Rev. Lett.* **94** (2005) 111601, `arXiv:hep-th/0405231 [hep-th]`.

[31] E. D'Hoker and D. Z. Freedman, "Supersymmetric gauge theories and the AdS/CFT correspondence," `arXiv:hep-th/0201253`.

[32] G. 't Hooft, "Dimensional reduction in quantum gravity," `arXiv:gr-qc/9310026 [gr-qc]`.

[33] L. Susskind, "The World as a hologram," *J. Math. Phys.* **36** (1995) 6377, `arXiv:hep-th/9409089 [hep-th]`.

[34] J. D. Bekenstein, "Black Holes and Entropy," *Phys. Rev. D* **7** (1973) 2333.

[35] S. W. Hawking, "Particle Creation by Black Holes," *Commun. Math. Phys.* **43** (1975) 199.

[36] G. 't Hooft, "A Planar Diagram Theory for Strong Interactions," *Nucl. Phys.* **B72** (1974) 461.

[37] C. W. Misner, K. S. Thorne, and J. A. Wheeler, *Gravitation*. WH Freeman & co, 1973.

[38] M. B. Green, J. H. Schwarz, and E. Witten, *Superstring Theory*. Cambridge Monographs on Mathematical Physics. Cambridge Univ. Pr., 1988.

[39] J. Polchinski, *String Theory*. Cambridge Monographs on Mathematical Physics. Cambridge Univ. Pr., 1998.

[40] K. Becker, M. Becker, and J. H. Schwarz, *String theory and M-theory: A modern introduction*. Cambridge Univ. Pr., 2006.

[41] J. Polchinski, "Dirichlet Branes and Ramond-Ramond charges," *Phys. Rev. Lett.* **75** (1995) 4724, `arXiv:hep-th/9510017 [hep-th]`.

[42] D. Tong, "String Theory," `arXiv:0908.0333 [hep-th]`. Lectures in Part III of the Mathematical Tripos at the University of Cambridge.

[43] M. Ammon and J. Erdmenger, *Gauge/Gravity Duality: Foundations and Applications*. Cambridge Univ. Pr., 2015.

[44] O. Aharony, S. S. Gubser, J. M. Maldacena, H. Ooguri, and Y. Oz, "Large N field theories, string theory and gravity," *Phys. Rept.* **323** (2000) 183, `arXiv:hep-th/9905111`.

[45] A. Samberg, "A Holographic View on Screening in Strongly Coupled Plasmas With Chemical Potential," Diploma thesis, Universität Heidelberg, 2012.

[46] E. Witten, "Bound states of strings and p-branes," *Nucl. Phys.* **B460** (1996) 335–350, `arXiv:hep-th/9510135 [hep-th]`.

[47] G. W. Gibbons and P. K. Townsend, "Vacuum interpolation in supergravity via super p-branes," *Phys. Rev. Lett.* **71** (1993) 3754–3757, `arXiv:hep-th/9307049 [hep-th]`.

[48] G. T. Horowitz and A. Strominger, "Black strings and P-branes," *Nucl. Phys.* **B360** (1991) 197.

[49] I. R. Klebanov, "World volume approach to absorption by nondilatonic branes," *Nucl. Phys.* **B496** (1997) 231–242, `arXiv:hep-th/9702076 [hep-th]`.

[50] S. S. Gubser, I. R. Klebanov, and A. A. Tseytlin, "String theory and classical absorption by three-branes," *Nucl. Phys.* **B499** (1997) 217–240, `arXiv:hep-th/9703040 [hep-th]`.

[51] C. Frances, "The conformal boundary of anti-de Sitter space-times," in *IRMA Lectures in Mathematics and Theoretical Physics*, O. Biquard, ed., vol. 8, p. 205. European Mathematical Society, 2005.

[52] J. Polchinski and M. J. Strassler, "The string dual of a confining four-dimensional gauge theory," `arXiv:hep-th/0003136`.

[53] I. R. Klebanov and M. J. Strassler, "Supergravity and a confining gauge theory: Duality cascades and χ-SB resolution of naked singularities," *JHEP* **0008** (2000) 052, `arXiv:hep-th/0007191 [hep-th]`.

[54] J. M. Maldacena and C. Nuñez, "Towards the Large N Limit of Pure $\mathcal{N} = 1$ Super Yang-Mills Theory," *Phys. Rev. Lett.* **86** (2001) 588, `arXiv:hep-th/0008001 [hep-th]`.

[55] L. Susskind and E. Witten, "The holographic bound in anti-de Sitter space," `arXiv:hep-th/9805114`.

[56] A. W. Peet and J. Polchinski, "UV/IR relations in AdS dynamics," *Phys. Rev.* **D59** (1999) 065011, `arXiv:hep-th/9809022`.

[57] I. R. Klebanov and E. Witten, "AdS/CFT correspondence and symmetry breaking," *Nucl. Phys.* **B556** (1999) 89–114, `arXiv:hep-th/9905104 [hep-th]`.

[58] P. Breitenlohner and D. Z. Freedman, "Positive Energy in anti-De Sitter Backgrounds and Gauged Extended Supergravity," *Phys. Lett.* **B115** (1982) 197.

[59] P. Breitenlohner and D. Z. Freedman, "Stability in Gauged Extended Supergravity," *Annals Phys.* **144** (1982) 249.

[60] L. Mezincescu and P. Townsend, "Stability at a Local Maximum in Higher Dimensional Anti-de Sitter Space and Applications to Supergravity," *Annals Phys.* **160** (1985) 406.

[61] V. Balasubramanian, P. Kraus, and A. E. Lawrence, "Bulk vs. boundary dynamics in anti-de Sitter spacetime," *Phys. Rev.* **D59** (1999) 046003, `arXiv:hep-th/9805171`.

[62] V. Balasubramanian, P. Kraus, A. E. Lawrence, and S. P. Trivedi, "Holographic probes of anti-de Sitter space-times," *Phys. Rev.* **D59** (1999) 104021, `arXiv:hep-th/9808017`.

[63] K. Skenderis, "Lecture notes on holographic renormalization," *Class. Quant. Grav.* **19** (2002) 5849–5876, `arXiv:hep-th/0209067 [hep-th]`.

[64] E. Witten, "Anti-de Sitter space, thermal phase transition, and confinement in gauge theories," *Adv. Theor. Math. Phys.* **2** (1998) 505, `arXiv:hep-th/9803131 [hep-th]`.

[65] Y. Aoki, S. Borsanyi, S. Durr, Z. Fodor, S. D. Katz, S. Krieg, and K. K. Szabo, "The QCD transition temperature: results with physical masses in the continuum limit II.," *JHEP* **06** (2009) 088, `arXiv:0903.4155 [hep-lat]`.

[66] A. Bazavov *et al.*, "The chiral and deconfinement aspects of the QCD transition," *Phys. Rev.* **D85** (2012) 054503, `arXiv:1111.1710 [hep-lat]`.

[67] K. G. Wilson, "Confinement of Quarks," *Phys. Rev.* **D10** (1974) 2445.

[68] J. Smit, *Introduction to quantum fields on a lattice*, vol. 15 of *Cambridge Lect. Notes Phys.* Cambridge Univ. Pr., 2002.

[69] E. Laermann and O. Philipsen, "The Status of lattice QCD at finite temperature," *Ann. Rev. Nucl. Part. Sci.* **53** (2003) 163–198, `arXiv:hep-ph/0303042 [hep-ph]`.

[70] P. Petreczky, "Lattice QCD at non-zero temperature," *J. Phys.* **G39** (2012) 093002, `arXiv:1203.5320 [hep-lat]`.

[71] E. V. Shuryak, "Quantum Chromodynamics and the Theory of Superdense Matter," *Phys. Rept.* **61** (1980) 71.

[72] **ALICE** Collaboration, B. Abelev *et al.*, "Charged-particle multiplicity density at mid-rapidity in central Pb-Pb collisions at $\sqrt{s_{NN}} = 2.76$ TeV," *Phys. Rev. Lett.* **105** (2010) 252301, `arXiv:1011.3916 [nucl-ex]`.

[73] **NA50** Collaboration, M. C. Abreu *et al.*, "Observation of a threshold effect in the anomalous J/Ψ suppression," *Phys. Lett.* **B450** (1999) 456.

[74] **NA38** Collaboration, M. C. Abreu *et al.*, "J/Ψ and Ψ' production in p, O and S induced reactions at SPS energies," *Phys. Lett.* **B466** (1999) 408.

[75] **NA50** Collaboration, F. Prino *et al.*, "J/Ψ suppression in Pb-Pb collisions at CERN SPS," `arXiv:hep-ex/0101052 [hep-ex]`.

[76] L. Kumar, "Review of Recent Results from the RHIC Beam Energy Scan," *Mod. Phys. Lett.* **A28** (2013) 1330033, `arXiv:1311.3426 [nucl-ex]`.

[77] **ALICE** Collaboration, K. Aamodt *et al.*, "Higher harmonic anisotropic flow measurements of charged particles in Pb-Pb collisions at $\sqrt{s_{NN}}$=2.76 TeV," *Phys. Rev. Lett.* **107** (2011) 032301, `arXiv:1105.3865 [nucl-ex]`.

[78] **ATLAS** Collaboration, G. Aad *et al.*, "Measurement of the azimuthal anisotropy for charged particle production in $\sqrt{s_{NN}} = 2.76$ TeV lead-lead collisions with the ATLAS detector," *Phys. Rev.* **C86** (2012) 014907, `arXiv:1203.3087 [hep-ex]`.

[79] **ALICE** Collaboration, K. Aamodt *et al.*, "Suppression of Charged Particle Production at Large Transverse Momentum in Central Pb-Pb Collisions at $\sqrt{s_{NN}} = 2.76$ TeV," *Phys. Lett.* **B696** (2011) 30, `arXiv:1012.1004 [nucl-ex]`.

[80] **CMS** Collaboration, S. Chatrchyan *et al.*, "Study of high-pT charged particle suppression in PbPb compared to *pp* collisions at $\sqrt{s_{NN}} = 2.76$ TeV," *Eur. Phys. J.* **C72** (2012) 1945, `arXiv:1202.2554 [nucl-ex]`.

[81] **ATLAS** Collaboration, G. Aad *et al.*, "Observation of a Centrality-Dependent Dijet Asymmetry in Lead-Lead Collisions at $\sqrt{s_{NN}} = 2.77$ TeV with the ATLAS Detector at the LHC," *Phys. Rev. Lett.* **105** (2010) 252303, `arXiv:1011.6182 [hep-ex]`.

[82] **CMS** Collaboration, S. Chatrchyan *et al.*, "Observation and studies of jet quenching in PbPb collisions at nucleon-nucleon center-of-mass energy = 2.76 TeV," *Phys. Rev.* **C84** (2011) 024906, `arXiv:1102.1957 [nucl-ex]`.

[83] M. Gyulassy and L. McLerran, "New forms of QCD matter discovered at RHIC," *Nucl. Phys.* **A750** (2005) 30, `arXiv:nucl-th/0405013`.

[84] B. Müller, "From Quark-Gluon Plasma to the Perfect Liquid," *Acta Phys. Polon.* **B38** (2007) 3705, `arXiv:0710.3366 [nucl-th]`.

[85] P. Braun-Munzinger, B. Friman, and J. Stachel (eds.), "Proceedings of the 24th International Conference on Ultra-Relativistic Nucleus–Nucleus Collisions (Quark Matter 2014)," *Nucl. Phys.* **A931** (2014) 1.

[86] C. Gale, S. Jeon, and B. Schenke, "Hydrodynamic Modeling of Heavy-Ion Collisions," *Int. J. Mod. Phys.* **A28** (2013) 1340011, `arXiv:1301.5893 [nucl-th]`.

[87] D. T. Son and A. O. Starinets, "Viscosity, Black Holes, and Quantum Field Theory," *Ann. Rev. Nucl. Part. Sci.* **57** (2007) 95, `arXiv:0704.0240 [hep-th]`.

[88] **ATLAS** Collaboration, G. Aad *et al.*, "Measurement of the centrality dependence of J/ψ yields and observation of Z production in lead–lead collisions with the ATLAS detector at the LHC," *Phys. Lett.* **B697** (2011) 294–312, `arXiv:1012.5419 [hep-ex]`.

[89] **ALICE** Collaboration, B. Abelev *et al.*, "J/ψ suppression at forward rapidity in Pb-Pb collisions at $\sqrt{s_{NN}} = 2.76$ TeV," *Phys. Rev. Lett.* **109** (2012) 072301, `arXiv:1202.1383 [hep-ex]`.

[90] **CMS** Collaboration, S. Chatrchyan *et al.*, "Suppression of non-prompt J/ψ, prompt J/ψ, and $\Upsilon(1S)$ in PbPb collisions at $\sqrt{s_{NN}} = 2.76$ TeV," *JHEP* **05** (2012) 063, `arXiv:1201.5069 [nucl-ex]`.

[91] **ALICE** Collaboration, B. B. Abelev *et al.*, "Centrality, rapidity and transverse momentum dependence of J/ψ suppression in Pb-Pb collisions at $\sqrt{s_{NN}}$=2.76 TeV," *Phys. Lett.* **B734** (2014) 314–327, `arXiv:1311.0214 [nucl-ex]`.

[92] T. Matsui and H. Satz, "*J/ψ* Suppression by Quark-Gluon Plasma Formation," *Phys. Lett.* **B178** (1986) 416.

[93] P. Braun-Munzinger and J. Stachel, "(Non)thermal aspects of charmonium production and a new look at *J/ψ* suppression," *Phys. Lett.* **B490** (2000) 196, `arXiv:nucl-th/0007059 [nucl-th]`.

[94] R. L. Thews, M. Schroedter, and J. Rafelski, "Enhanced *J/ψ* production in deconfined quark matter," *Phys. Rev.* **C63** (2001) 054905, `arXiv:hep-ph/0007323 [hep-ph]`.

[95] C. Wetterich, "Exact evolution equation for the effective potential," *Phys. Lett.* **B301** (1993) 90.

[96] J. Berges, N. Tetradis, and C. Wetterich, "Nonperturbative renormalization flow in quantum field theory and statistical physics," *Phys. Rept.* **363** (2002) 223, `arXiv:hep-ph/0005122 [hep-ph]`.

[97] J. M. Pawlowski, "Aspects of the functional renormalisation group," *Annals Phys.* **322** (2007) 2831–2915, `arXiv:hep-th/0512261 [hep-th]`.

[98] H. Gies, "Introduction to the functional RG and applications to gauge theories," *Lect. Notes Phys.* **852** (2012) 287–348, `arXiv:hep-ph/0611146 [hep-ph]`.

[99] F. J. Dyson, "The *S* Matrix in Quantum Electrodynamics," *Phys. Rev.* **75** (1949) 1736.

[100] J. Schwinger, "On the Green's Functions of Quantized Fields. I," *PNAS* **37** (1951) 452.

[101] C. D. Roberts and S. M. Schmidt, "Dyson-Schwinger equations: Density, temperature and continuum strong QCD," *Prog. Part. Nucl. Phys.* **45** (2000) S1–S103, `arXiv:nucl-th/0005064 [nucl-th]`.

[102] C. S. Fischer, "Infrared properties of QCD from Dyson-Schwinger equations," *J. Phys.* **G32** (2006) R253, `arXiv:hep-ph/0605173 [hep-ph]`.

[103] N. Christiansen, M. Haas, J. M. Pawlowski, and N. Strodthoff, "Transport Coefficients in Yang–Mills Theory and QCD," *Phys. Rev. Lett.* **115** (2015) 112002, `arXiv:1411.7986 [hep-ph]`.

[104] P. de Forcrand, "Simulating QCD at finite density," *PoS* **LAT2009** (2009) 010, `arXiv:1005.0539 [hep-lat]`.

[105] J. M. Maldacena, "Wilson loops in large N field theories," *Phys. Rev. Lett.* **80** (1998) 4859, `arXiv:hep-th/9803002`.

[106] H. Liu, K. Rajagopal, and U. A. Wiedemann, "An AdS/CFT calculation of screening in a hot wind," *Phys. Rev. Lett.* **98** (2007) 182301, `arXiv:hep-ph/0607062`.

[107] H. Liu, K. Rajagopal, and U. A. Wiedemann, "Wilson loops in heavy ion collisions and their calculation in AdS/CFT," *JHEP* **0703** (2007) 066, `arXiv:hep-ph/0612168`.

[108] E. Caceres, M. Natsuume, and T. Okamura, "Screening length in plasma winds," *JHEP* **0610** (2006) 011, `arXiv:hep-th/0607233`.

[109] H. Liu, K. Rajagopal, and Y. Shi, "Robustness and Infrared Sensitivity of Various Observables in the Application of AdS/CFT to Heavy Ion Collisions," *JHEP* **0808** (2008) 048, `arXiv:0803.3214 [hep-ph]`.

[110] K. Schade, "Gone with the Wind: Heavy Meson and Baryon Screening in Hot Moving Plasmas," Diploma thesis, Universität Heidelberg, 2009.

[111] C. Ewerz and K. Schade, "Screening in Strongly Coupled Plasmas: Universal Properties from Strings in Curved Space," in *Proc. Gribov-80 Memorial Workshop*. 2010. `arXiv:1010.1138 [hep-th]`.

[112] K. B. Fadafan, "Heavy quarks in the presence of higher derivative corrections from AdS/CFT," *Eur. Phys. J.* **C71** (2011) 1799, `arXiv:1102.2289 [hep-th]`.

[113] K. Schade, *Applications of Holography to Strongly Coupled Plasmas*. PhD thesis, Universität Heidelberg, 2012.

[114] C. P. Herzog, A. Karch, P. Kovtun, C. Kozcaz, and L. G. Yaffe, "Energy loss of a heavy quark moving through $\mathcal{N} = 4$ supersymmetric Yang-Mills plasma," *JHEP* **0607** (2006) 013, `arXiv:hep-th/0605158`.

[115] S. S. Gubser, "Drag force in AdS/CFT," *Phys. Rev.* **D74** (2006) 126005, `arXiv:hep-th/0605182`.

[116] E. Nakano, S. Teraguchi, and W.-Y. Wen, "Drag force, jet quenching, and AdS/QCD," *Phys. Rev.* **D75** (2007) 085016, `arXiv:hep-ph/0608274 [hep-ph]`.

[117] C. P. Herzog, "Energy Loss of Heavy Quarks from Asymptotically AdS Geometries," *JHEP* **0609** (2006) 032, `arXiv:hep-th/0605191 [hep-th]`.

[118] E. Caceres and A. Guijosa, "On Drag Forces and Jet Quenching in Strongly Coupled Plasmas," *JHEP* **0612** (2006) 068, `arXiv:hep-th/0606134 [hep-th]`.

[119] K. B. Fadafan, "R^2 curvature-squared corrections on drag force," *JHEP* **0812** (2008) 051, `arXiv:0803.2777 [hep-th]`.

[120] J. F. Vázquez-Poritz, "Drag force at finite 't Hooft coupling from AdS/CFT," `arXiv:0803.2890 [hep-th]`.

[121] U. Gürsoy, E. Kiritsis, G. Michalogiorgakis, and F. Nitti, "Thermal Transport and Drag Force in Improved Holographic QCD," *JHEP* **0912** (2009) 056, `arXiv:0906.1890 [hep-ph]`.

[122] A. Ficnar, J. Noronha, and M. Gyulassy, "Non-conformal Holography of Heavy Quark Quenching," *Nucl.Phys.* **A855** (2011) 372, `arXiv:1012.0116 [hep-ph]`.

[123] J. F. Fuini III and A. Karch, "Energy Loss Calculations of Moving Defects for General Holographic Metrics," *Phys. Rev.* **D85** (2012) 066006, `arXiv:1112.2747 [hep-th]`.

[124] C. Ewerz, L. Lin, and A. Samberg, *in preparation.*

[125] N. Brambilla, A. Pineda, J. Soto, and A. Vairo, "Effective field theories for heavy quarkonium," *Rev. Mod. Phys.* **77** (2005) 1423, `arXiv:hep-ph/0410047 [hep-ph]`.

[126] S. S. Gubser, "Comparing the drag force on heavy quarks in $\mathcal{N} = 4$ super-Yang–Mills theory and QCD," *Phys. Rev.* **D76** (2007) 126003, `arXiv:hep-th/0611272`.

[127] A. Karch and E. Katz, "Adding flavor to AdS/CFT," *JHEP* **0206** (2002) 043, `arXiv:hep-th/0205236 [hep-th]`.

[128] T. Sakai and S. Sugimoto, "Low energy hadron physics in holographic QCD," *Prog. Theor. Phys.* **113** (2005) 843, `arXiv:hep-th/0412141`.

[129] T. Sakai and S. Sugimoto, "More on a holographic dual of QCD," *Prog. Theor. Phys.* **114** (2005) 1083, `arXiv:hep-th/0507073`.

[130] D. J. Gross and H. Ooguri, "Aspects of large N gauge theory dynamics as seen by string theory," *Phys. Rev.* **D58** (1998) 106002, `arXiv:hep-th/9805129 [hep-th]`.

[131] M. Kruczenski, D. Mateos, R. C. Myers, and D. J. Winters, "Towards a holographic dual of large-N_c QCD," *JHEP* **0405** (2004) 041, `arXiv:hep-th/0311270 [hep-th]`.

[132] A. Karch, E. Katz, D. T. Son, and M. A. Stephanov, "Linear Confinement and AdS/QCD," *Phys. Rev.* **D74** (2006) 015005, `arXiv:hep-ph/0602229`.

[133] O. Andreev and V. I. Zakharov, "Heavy-quark potentials and AdS/QCD," *Phys. Rev.* **D74** (2006) 025023, `arXiv:hep-ph/0604204`.

[134] H. Boschi-Filho, N. R. Braga, and C. N. Ferreira, "Heavy quark potential at finite temperature from gauge/string duality," *Phys. Rev.* **D74** (2006) 086001, `arXiv:hep-th/0607038 [hep-th]`.

[135] C. P. Herzog, "A Holographic Prediction of the Deconfinement Temperature," *Phys. Rev. Lett.* **98** (2007) 091601, `arXiv:hep-th/0608151 [hep-th]`.

[136] K. Kajantie, T. Tahkokallio, and J.-T. Yee, "Thermodynamics of AdS/QCD," *JHEP* **0701** (2007) 019, `arXiv:hep-ph/0609254`.

[137] S. S. Gubser and A. Nellore, "Mimicking the QCD equation of state with a dual black hole," *Phys. Rev.* **D78** (2008) 086007, `arXiv:0804.0434 [hep-th]`.

[138] S. S. Gubser, A. Nellore, S. S. Pufu, and F. D. Rocha, "Thermodynamics and bulk viscosity of approximate black hole duals to finite temperature quantum chromodynamics," *Phys. Rev. Lett.* **101** (2008) 131601, `arXiv:0804.1950 [hep-th]`.

[139] J. Alanen, K. Kajantie, and V. Suur-Uski, "A gauge/gravity duality model for gauge theory thermodynamics," *Phys. Rev.* **D80** (2009) 126008, `arXiv:0911.2114 [hep-ph]`.

[140] E. Megias, H. J. Pirner, and K. Veschgini, "QCD thermodynamics using five-dimensional gravity," *Phys. Rev.* **D83** (2011) 056003, `arXiv:1009.2953 [hep-ph]`.

[141] D. Li, S. He, M. Huang, and Q.-S. Yan, "Thermodynamics of deformed AdS$_5$ model with a positive/negative quadratic correction in graviton-dilaton system," *JHEP* **1109** (2011) 041, `arXiv:1103.5389 [hep-th]`.

[142] M. Natsuume, "String theory and quark-gluon plasma," `arXiv:hep-ph/0701201`.

[143] T. Springer, "Hydrodynamics of strongly coupled non-conformal fluids from gauge/gravity duality," `arXiv:0908.1587 [hep-th]`.

[144] G. Policastro, D. T. Son, and A. O. Starinets, "Shear Viscosity of Strongly Coupled $\mathcal{N} = 4$ Supersymmetric Yang-Mills Plasma," *Phys. Rev. Lett.* **87** (2001) 081601, `arXiv:hep-th/0104066 [hep-th]`.

[145] C. P. Herzog, "The Hydrodynamics of M theory," *JHEP* **0212** (2002) 026, `arXiv:hep-th/0210126 [hep-th]`.

[146] P. Kovtun, D. T. Son, and A. O. Starinets, "Holography and hydrodynamics: Diffusion on stretched horizons," *JHEP* **0310** (2003) 064, `arXiv:hep-th/0309213 [hep-th]`.

[147] A. Buchel and J. T. Liu, "Universality of the shear viscosity from supergravity duals," *Phys. Rev. Lett.* **93** (2004) 090602, `arXiv:hep-th/0311175 [hep-th]`.

[148] A. Buchel, J. T. Liu, and A. O. Starinets, "Coupling constant dependence of the shear viscosity in $\mathcal{N} = 4$ supersymmetric Yang–Mills theory," *Nucl. Phys.* **B707** (2005) 56, `arXiv:hep-th/0406264 [hep-th]`.

[149] M. Brigante, H. Liu, R. C. Myers, S. Shenker, and S. Yaida, "Viscosity Bound Violation in Higher Derivative Gravity," *Phys. Rev.* **D77** (2008) 126006, `arXiv:0712.0805 [hep-th]`.

[150] Y. Kats and P. Petrov, "Effect of curvature squared corrections in AdS on the viscosity of the dual gauge theory," *JHEP* **0901** (2009) 044, `arXiv:0712.0743 [hep-th]`.

[151] M. Brigante, H. Liu, R. C. Myers, S. Shenker, and S. Yaida, "The Viscosity Bound and Causality Violation," *Phys. Rev. Lett.* **100** (2008) 191601, `arXiv:0802.3318 [hep-th]`.

[152] J. Mas, "Shear viscosity from R-charged AdS black holes," *JHEP* **0603** (2006) 016, `arXiv:hep-th/0601144 [hep-th]`.

[153] D. T. Son and A. O. Starinets, "Hydrodynamics of R-charged black holes," *JHEP* **0603** (2006) 052, `arXiv:hep-th/0601157 [hep-th]`.

[154] O. Saremi, "The Viscosity bound conjecture and hydrodynamics of M2-brane theory at finite chemical potential," *JHEP* **0610** (2006) 083, `arXiv:hep-th/0601159 [hep-th]`.

[155] P. Benincasa, A. Buchel, and R. Naryshkin, "The shear viscosity of gauge theory plasma with chemical potentials," *Phys. Lett.* **B645** (2007) 309, `arXiv:hep-th/0610145 [hep-th]`.

[156] C. Gale, S. Jeon, B. Schenke, P. Tribedy, and R. Venugopalan, "Event-by-event anisotropic flow in heavy-ion collisions from combined Yang-Mills and viscous fluid dynamics," *Phys. Rev. Lett.* **110** (2013) 012302, `arXiv:1209.6330 [nucl-th]`.

[157] B. Schenke and R. Venugopalan, "Eccentric protons? Sensitivity of flow to system size and shape in p+p, p+Pb and Pb+Pb collisions," *Phys. Rev. Lett.* **113** (2014) 102301, `arXiv:1405.3605 [nucl-th]`.

[158] O. DeWolfe, S. S. Gubser, and C. Rosen, "A holographic critical point," *Phys. Rev.* **D83** (2011) 086005, `arXiv:1012.1864 [hep-th]`.

[159] S. Weinberg, *Gravitation and Cosmology: Principles and Applications of the General Theory of Relativity.* John Wiley & Sons, 1972.

[160] O. DeWolfe and C. Rosen, "Robustness of Sound Speed and Jet Quenching for Gauge/Gravity Models of Hot QCD," *JHEP* **0907** (2009) 022, `arXiv:0903.1458 [hep-th]`.

[161] B. Galow, E. Megias, J. Nian, and H. Pirner, "Phenomenology of AdS/QCD and Its Gravity Dual," *Nucl. Phys.* **B834** (2010) 330, `arXiv:0911.0627 [hep-ph]`.

[162] S. He, M. Huang, and Q.-S. Yan, "Logarithmic correction in the deformed AdS$_5$ model to produce the heavy quark potential and QCD beta function," *Phys. Rev.* **D83** (2011) 045034, `arXiv:1004.1880 [hep-ph]`.

[163] F. Brümmer, A. Hebecker, and E. Trincherini, "The Throat as a Randall-Sundrum model with Goldberger-Wise stabilization," *Nucl. Phys.* **B738** (2006) 283, `arXiv:hep-th/0510113 [hep-th]`.

[164] M. Cvetic and S. S. Gubser, "Phases of R-charged black holes, spinning branes and strongly coupled gauge theories," *JHEP* **9904** (1999) 024, `arXiv:hep-th/9902195`.

[165] M. Cvetic, M. Duff, P. Hoxha, J. T. Liu, H. Lu, *et al.*, "Embedding AdS black holes in ten-dimensions and eleven-dimensions," *Nucl. Phys.* **B558** (1999) 96, `arXiv:hep-th/9903214 [hep-th]`.

[166] S. S. Gubser, "Thermodynamics of spinning D3-branes," *Nucl. Phys.* **B551** (1999) 667, `arXiv:hep-th/9810225 [hep-th]`.

[167] K. Behrndt, M. Cvetic, and W. A. Sabra, "Non-extreme black holes of five dimensional $\mathcal{N} = 2$ AdS supergravity," *Nucl. Phys.* **B553** (1999) 317, `arXiv:hep-th/9810227`.

[168] A. Chamblin, R. Emparan, C. V. Johnson, and R. C. Myers, "Charged AdS black holes and catastrophic holography," *Phys. Rev.* **D60** (1999) 064018, `arXiv:hep-th/9902170`.

[169] A. Chamblin, R. Emparan, C. V. Johnson, and R. C. Myers, "Holography, thermodynamics and fluctuations of charged AdS black holes," *Phys. Rev.* **D60** (1999) 104026, `arXiv:hep-th/9904197 [hep-th]`.

[170] M. Panero, "Thermodynamics of the QCD Plasma and the Large-N Limit," *Phys. Rev. Lett.* **103** (2009) 232001, `arXiv:0907.3719 [hep-lat]`.

[171] O. Andreev and V. I. Zakharov, "The Spatial String Tension, Thermal Phase Transition, and AdS/QCD," *Phys. Lett.* **B645** (2007) 437, `arXiv:hep-ph/0607026`.

[172] O. Andreev and V. I. Zakharov, "On Heavy-Quark Free Energies, Entropies, Polyakov Loop, and AdS/QCD," *JHEP* **0704** (2007) 100, `arXiv:hep-ph/0611304`.

[173] P. Colangelo, F. Giannuzzi, and S. Nicotri, "Holography, Heavy-Quark Free Energy, and the QCD Phase Diagram," *Phys. Rev.* **D83** (2011) 035015, `arXiv:1008.3116 [hep-ph]`.

[174] C. Park, D.-Y. Gwak, B.-H. Lee, Y. Ko, and S. Shin, "The Soft Wall Model in the Hadronic Medium," *Phys. Rev.* **D84** (2011) 046007, `arXiv:1104.4182 [hep-th]`.

[175] P. Colangelo, F. Giannuzzi, S. Nicotri, and V. Tangorra, "Temperature and quark density effects on the chiral condensate: An AdS/QCD study," *Eur. Phys. J.* **C72** (2012) 2096, `arXiv:1112.4402 [hep-ph]`.

[176] P. Colangelo, F. Giannuzzi, and S. Nicotri, "In-medium hadronic spectral functions through the soft-wall holographic model of QCD," *JHEP* **1205** (2012) 076, `arXiv:1201.1564 [hep-ph]`.

[177] P. Colangelo, F. Giannuzzi, S. Nicotri, and F. Zuo, "Temperature and chemical potential dependence of the gluon condensate: a holographic study," *Phys. Rev.* **D88** (2013) 115011, `arXiv:1308.0489 [hep-ph]`.

[178] U. Gürsoy and E. Kiritsis, "Exploring improved holographic theories for QCD: Part I," *JHEP* **0802** (2008) 032, `arXiv:0707.1324 [hep-th]`.

[179] U. Gürsoy, E. Kiritsis, and F. Nitti, "Exploring improved holographic theories for QCD: Part II," *JHEP* **0802** (2008) 019, `arXiv:0707.1349 [hep-th]`.

[180] A. Stoffers and I. Zahed, "Improved AdS/QCD Model with Matter," *Phys. Rev.* **D83** (2011) 055016, `arXiv:1009.4428 [hep-th]`.

[181] S. He, S.-Y. Wu, Y. Yang, and P.-H. Yuan, "Phase Structure in a Dynamical Soft-Wall Holographic QCD Model," *JHEP* **1304** (2013) 093, `arXiv:1301.0385 [hep-th]`.

[182] R. Rougemont, A. Ficnar, S. Finazzo, and J. Noronha, "Energy loss, equilibration, and thermodynamics of a baryon rich strongly coupled quark-gluon plasma," `arXiv:1507.06556 [hep-th]`.

[183] S. Nicotri, "Phenomenology Of The Holographic Soft-Wall Model Of QCD With 'Reversed' Dilaton," *AIP Conf. Proc.* **1317** (2011) 322, `arXiv:1009.4829 [hep-ph]`.

[184] A. Karch, E. Katz, D. T. Son, and M. A. Stephanov, "On the sign of the dilaton in the soft wall models," *JHEP* **1104** (2011) 066, `arXiv:1012.4813 [hep-ph]`.

[185] T. Gutsche, V. E. Lyubovitskij, I. Schmidt, and A. Vega, "Dilaton in a soft-wall holographic approach to mesons and baryons," *Phys. Rev.* **D85** (2012) 076003, `arXiv:1108.0346 [hep-ph]`.

198

[186] M. Cheng *et al.*, "The QCD equation of state with almost physical quark masses," *Phys. Rev.* **D77** (2008) 014511, `arXiv:0710.0354 [hep-lat]`.

[187] A. Bazavov *et al.*, "Equation of state and QCD transition at finite temperature," *Phys. Rev.* **D80** (2009) 014504, `arXiv:0903.4379 [hep-lat]`.

[188] J. Noronha-Hostler, J. Noronha, and C. Greiner, "Particle Ratios and the QCD Critical Temperature," *J. Phys.* **G37** (2010) 094062, `arXiv:1001.2610 [nucl-th]`.

[189] P. Braun-Munzinger, K. Redlich, and J. Stachel, "Particle production in heavy ion collisions," `arXiv:nucl-th/0304013 [nucl-th]`.

[190] J. Stachel, A. Andronic, P. Braun-Munzinger, and K. Redlich, "Confronting LHC data with the statistical hadronization model," *J. Phys. Conf. Ser.* **509** (2014) 012019, `arXiv:1311.4662 [nucl-th]`.

[191] S. W. Hawking and D. N. Page, "Thermodynamics of black holes in anti-de Sitter space," *Commun. Math. Phys.* **87** (1983) 577.

[192] J. Erdmenger, N. Evans, I. Kirsch, and E. Threlfall, "Mesons in Gauge/Gravity Duals - A Review," *Eur. Phys. J.* **A35** (2008) 81, `arXiv:0711.4467 [hep-th]`.

[193] S.-J. Rey, S. Theisen, and J.-T. Yee, "Wilson-Polyakov loop at finite temperature in large-N gauge theory and anti-de Sitter supergravity," *Nucl. Phys.* **B527** (1998) 171, `arXiv:hep-th/9803135`.

[194] A. Brandhuber, N. Itzhaki, J. Sonnenschein, and S. Yankielowicz, "Wilson loops in the large N limit at finite temperature," *Phys. Lett.* **B434** (1998) 36, `arXiv:hep-th/9803137`.

[195] O. Kaczmarek, F. Karsch, F. Zantow, and P. Petreczky, "Static quark anti-quark free energy and the running coupling at finite temperature," *Phys. Rev.* **D70** (2004) 074505, `arXiv:hep-lat/0406036 [hep-lat]`.

[196] O. Kaczmarek and F. Zantow, "Static quark anti-quark interactions in zero and finite temperature QCD. I. Heavy quark free energies, running coupling and quarkonium binding," *Phys. Rev.* **D71** (2005) 114510, `arXiv:hep-lat/0503017 [hep-lat]`.

[197] D. Bak, A. Karch, and L. G. Yaffe, "Debye screening in strongly coupled $\mathcal{N} = 4$ supersymmetric Yang-Mills plasma," *JHEP* **0708** (2007) 049, `arXiv:0705.0994 [hep-th]`.

[198] T. Appelquist, M. Dine, and I. J. Muzinich, "The Static Potential in Quantum Chromodynamics," *Phys. Lett.* **B69** (1977) 231.

[199] W. Fischler, "Quark-Antiquark Potential in QCD," *Nucl. Phys.* **B129** (1977) 157.

[200] L. D. McLerran and B. Svetitsky, "A Monte Carlo study of SU(2) Yang-Mills theory at finite temperature," *Phys. Lett.* **B98** (1981) 195.

[201] M. Laine, O. Philipsen, P. Romatschke, and M. Tassler, "Real-time static potential in hot QCD," *JHEP* **03** (2007) 054, `arXiv:hep-ph/0611300 [hep-ph]`.

[202] A. Beraudo, J.-P. Blaizot, and C. Ratti, "Real and imaginary-time Q anti-Q correlators in a thermal medium," *Nucl. Phys.* **A806** (2008) 312–338, `arXiv:0712.4394 [nucl-th]`.

[203] Y. Burnier, O. Kaczmarek, and A. Rothkopf, "Static quark-antiquark potential in the quark-gluon plasma from lattice QCD," *Phys. Rev. Lett.* **114** (2015) 082001, `arXiv:1410.2546 [hep-lat]`.

[204] S.-J. Rey and J.-T. Yee, "Macroscopic strings as heavy quarks: Large-*N* gauge theory and anti-de Sitter supergravity," *Eur. Phys. J.* **C22** (2001) 379, `arXiv:hep-th/9803001`.

[205] J. L. Albacete, Y. V. Kovchegov, and A. Taliotis, "Heavy Quark Potential at Finite Temperature in AdS/CFT Revisited," *Phys. Rev.* **D78** (2008) 115007, `arXiv:0807.4747 [hep-th]`.

[206] Z.-q. Zhang, D.-f. Hou, Y. Wu, and G. Chen, "Heavy quark potential from a deformed AdS$_5$ model," `arXiv:1507.07263 [hep-ph]`.

[207] O. Kaczmarek, F. Karsch, P. Petreczky, and F. Zantow, "Heavy quark anti-quark free energy and the renormalized Polyakov loop," *Phys. Lett.* **B543** (2002) 41, `arXiv:hep-lat/0207002 [hep-lat]`.

[208] S. I. Finazzo and J. Noronha, "Estimates for the Thermal Width of Heavy Quarkonia in Strongly Coupled Plasmas from Holography," *JHEP* **11** (2013) 042, `arXiv:1306.2613 [hep-ph]`.

[209] S. I. Finazzo and J. Noronha, "Debye screening mass near deconfinement from holography," *Phys. Rev.* **D90** (2014) 115028, `arXiv:1411.4330 [hep-th]`.

[210] Y. Yang and P.-H. Yuan, "Confinement-Deconfinement Phase Transition for Heavy Quarks," `arXiv:1506.05930 [hep-th]`.

[211] Y. Kinar, E. Schreiber, and J. Sonnenschein, "Q anti-Q potential from strings in curved space-time: Classical results," *Nucl.Phys.* **B566** (2000) 103, `arXiv:hep-th/9811192 [hep-th]`.

[212] D. Giataganas, "Probing strongly coupled anisotropic plasma," *JHEP* **07** (2012) 031, `arXiv:1202.4436 [hep-th]`.

[213] A. Rebhan and D. Steineder, "Probing Two Holographic Models of Strongly Coupled Anisotropic Plasma," *JHEP* **08** (2012) 020, `arXiv:1205.4684 [hep-th]`.

[214] E. Brehm, "Application of Gauge/String Duality to Anisotropic Strongly Coupled Plasmas," Master thesis, Universität Heidelberg, 2014.

[215] S. D. Avramis, K. Sfetsos, and D. Zoakos, "On the velocity and chemical-potential dependence of the heavy-quark interaction in $\mathcal{N} = 4$ SYM plasmas," *Phys. Rev.* **D75** (2007) 025009, `arXiv:hep-th/0609079`.

[216] J. J. Friess, S. S. Gubser, G. Michalogiorgakis, and S. S. Pufu, "Stability of strings binding heavy-quark mesons," *JHEP* **0704** (2007) 079, `arXiv:hep-th/0609137`.

[217] O. Kaczmarek and F. Zantow, "Static quark anti-quark interactions at zero and finite temperature QCD. II. Quark anti-quark internal energy and entropy," `arXiv:hep-lat/0506019 [hep-lat]`.

[218] N. Brambilla, J. Ghiglieri, A. Vairo, and P. Petreczky, "Static quark-antiquark pairs at finite temperature," *Phys. Rev.* **D78** (2008) 014017, `arXiv:0804.0993 [hep-ph]`.

[219] P. Petreczky, "Heavy quark potentials and quarkonia binding," *Eur. Phys. J.* **C43** (2005) 51, `arXiv:hep-lat/0502008`.

[220] Y. Burnier, O. Kaczmarek, and A. Rothkopf, "Quarkonium at finite temperature: Towards realistic phenomenology from first principles," `arXiv:1509.07366 [hep-ph]`.

[221] I. Iatrakis and D. E. Kharzeev, "Holographic entropy and real-time dynamics of quarkonium dissociation in non-Abelian plasma," `arXiv:1509.08286 [hep-ph]`.

[222] J. Noronha, "The Heavy Quark Free Energy in QCD and in Gauge Theories with Gravity Duals," *Phys. Rev.* **D82** (2010) 065016, `arXiv:1003.0914 [hep-th]`.

[223] M. Abramowitz and I. A. Stegun, *Handbook of Mathematical Functions with Formulas, Graphs, and Mathematical Tables.* Dover Publications, 1964.

[224] P. Petreczky and K. Petrov, "Free energy of a static quark anti-quark pair and the renormalized Polyakov loop in three flavor QCD," *Phys. Rev.* **D70** (2004) 054503, `arXiv:hep-lat/0405009 [hep-lat]`.

[225] A. Bazavov and P. Petreczky, "Polyakov loop in 2+1 flavor QCD," *Phys. Rev.* **D87** (2013) 094505, arXiv:1301.3943 [hep-lat].

[226] M. Döring, S. Ejiri, O. Kaczmarek, F. Karsch, and E. Laermann, "Screening of heavy quark free energies at finite temperature and non-zero baryon chemical potential," *Eur.Phys.J.* **C46** (2006) 179, arXiv:hep-lat/0509001 [hep-lat].

[227] **WHOT-QCD** Collaboration, S. Ejiri *et al.*, "Equation of State and Heavy-Quark Free Energy at Finite Temperature and Density in Two Flavor Lattice QCD with Wilson Quark Action," *Phys. Rev.* **D82** (2010) 014508, arXiv:0909.2121 [hep-lat].

[228] J. Takahashi, K. Nagata, T. Saito, A. Nakamura, T. Sasaki, *et al.*, "Color screening potential at finite density in two-flavor lattice QCD with Wilson fermions," *Phys. Rev.* **D88** (2013) 114504, arXiv:1308.2489 [hep-lat].

[229] C. R. Allton, S. Ejiri, S. J. Hands, O. Kaczmarek, F. Karsch, E. Laermann, C. Schmidt, and L. Scorzato, "The QCD thermal phase transition in the presence of a small chemical potential," *Phys. Rev.* **D66** (2002) 074507, arXiv:hep-lat/0204010 [hep-lat].

[230] M. E. Peskin and D. V. Schroeder, *An Introduction to Quantum Field Theory.* Westview Press, 1995.

[231] O. Kaczmarek, "Screening at finite temperature and density," *PoS* **CPOD07** (2007) 043, arXiv:0710.0498 [hep-lat].

[232] W. J. Kwon, G. Moon, J.-y. Choi, S. W. Seo, and Y.-i. Shin, "Relaxation of superfluid turbulence in highly oblate Bose-Einstein condensates," *Phys. Rev.* **A90** (2014) 063627, arXiv:1403.4658 [cond-mat.quant-gas].

[233] A. Adams, P. M. Chesler, and H. Liu, "Holographic Vortex Liquids and Superfluid Turbulence," *Science* **341** (2012) 368, arXiv:1212.0281 [hep-th].

[234] P. M. Chesler, A. M. Garcia-Garcia, and H. Liu, "Defect Formation beyond Kibble-Zurek Mechanism and Holography," *Phys. Rev.* **X5** (2015) 021015, arXiv:1407.1862 [hep-th].

[235] C. Ewerz, T. Gasenzer, M. Karl, and A. Samberg, "Non-Thermal Fixed Point in a Holographic Superfluid," *JHEP* **1505** (2015) 070, arXiv:1410.3472 [hep-th].

[236] Y. Du, C. Niu, Y. Tian, and H.-b. Zhang, "Holographic Vortex Pair Annihilation in Superfluid Turbulence," arXiv:1412.8417 [hep-th].

[237] B. P. Anderson, P. C. Haljan, C. A. Regal, D. L. Feder, L. A. Collins, C. W. Clark, and E. A. Cornell, "Watching Dark Solitons Decay into Vortex Rings in a Bose-Einstein Condensate," *Phys. Rev. Lett.* **86** (2001) 2926, `arXiv:cond-mat/0012444 [cond-mat]`.

[238] B. Eiermann, T. Anker, M. Albiez, M. Taglieber, P. Treutlein, K.-P. Marzlin, and M. K. Oberthaler, "Bright Bose-Einstein gap solitons of atoms with repulsive interaction," *Phys. Rev. Lett.* **92** (2004) 230401, `arXiv:cond-mat/0402178 [cond-mat.other]`.

[239] L. E. Sadler, J. M. Higbie, S. R. Leslie, M. Vengalattore, and D. M. Stamper-Kurn, "Spontaneous symmetry breaking in a quenched ferromagnetic spinor Bose-Einstein condensate," *Nature* **443** (2006) 312, `arXiv:cond-mat/0605351 [cond-mat.stat-mech]`.

[240] A. Weller, J. P. Ronzheimer, C. Gross, J. Esteve, M. K. Oberthaler, D. J. Frantzeskakis, G. Theocharis, and P. G. Kevrekidis, "Experimental Observation of Oscillating and Interacting Matter Wave Dark Solitons," *Phys. Rev. Lett.* **101** (2008) 130401, `arXiv:0803.4352 [quant-ph]`.

[241] C. N. Weiler, T. W. Neely, D. R. Scherer, A. S. Bradley, M. J. Davis, and B. P. Anderson, "Spontaneous vortices in the formation of Bose-Einstein condensates," *Nature* **455** (2008) 948, `arXiv:0807.3323 [cond-mat.other]`.

[242] T. W. Neely, E. C. Samson, A. S. Bradley, M. J. Davis, and B. P. Anderson, "Observation of Vortex Dipoles in an Oblate Bose-Einstein Condensate," *Phys. Rev. Lett.* **104** (2010) 160401, `arXiv:0912.3773 [cond-mat.quant-gas]`.

[243] J. Kasprzak *et al.*, "Bose–Einstein condensation of exciton polaritons," *Nature* **443** (2006) 409.

[244] K. G. Lagoudakis, M. Wouters, M. Richard, A. Baas, I. Carusotto, R. André, L. S. Dang, and B. Deveaud-Plédran, "Quantized vortices in an exciton–polariton condensate," *Nature Phys.* **4** (2008) 706, `arXiv:0801.1916 [cond-mat.other]`.

[245] K. G. Lagoudakis, T. Ostatnický, A. V. Kavokin, Y. G. Rubo, R. André, and B. Deveaud-Plédran, "Observation of Half-Quantum Vortices in an Exciton–Polariton Condensate," *Science* **326** (2009) 974, `arXiv:0911.2555 [cond-mat.quant-gas]`.

[246] A. Amo *et al.*, "Polariton Superfluids Reveal Quantum Hydrodynamic Solitons," *Science* **332** (2011) 1167, `arXiv:1101.2530 [cond-mat.quant-gas]`.

[247] J. Berges, J.-P. Blaizot, and F. Gelis, "EMMI Rapid Reaction Task Force on 'Thermalization in Non-abelian Plasmas'," *J. Phys.* **G39** (2012) 085115, `arXiv:1203.2042 [hep-ph]`.

[248] S. S. Gubser, "Breaking an Abelian gauge symmetry near a black hole horizon," *Phys. Rev.* **D78** (2008) 065034, `arXiv:0801.2977 [hep-th]`.

[249] S. A. Hartnoll, C. P. Herzog, and G. T. Horowitz, "Building a Holographic Superconductor," *Phys. Rev. Lett.* **101** (2008) 031601, `arXiv:0803.3295 [hep-th]`.

[250] C. Herzog, P. Kovtun, and D. Son, "Holographic model of superfluidity," *Phys. Rev.* **D79** (2009) 066002, `arXiv:0809.4870 [hep-th]`.

[251] O. J. C. Dias, G. T. Horowitz, N. Iqbal, and J. E. Santos, "Vortices in holographic superfluids and superconductors as conformal defects," *JHEP* **1404** (2014) 096, `arXiv:1311.3673 [hep-th]`.

[252] V. Keranen, E. Keski-Vakkuri, S. Nowling, and K. Yogendran, "Inhomogeneous Structures in Holographic Superfluids: II. Vortices," *Phys. Rev.* **D81** (2010) 126012, `arXiv:0912.4280 [hep-th]`.

[253] M. J. Bhaseen, J. P. Gauntlett, B. D. Simons, J. Sonner, and T. Wiseman, "Holographic Superfluids and the Dynamics of Symmetry Breaking," *Phys. Rev. Lett.* **110** (2013) 015301, `arXiv:1207.4194 [hep-th]`.

[254] J. Berges, A. Rothkopf, and J. Schmidt, "Non-thermal fixed points: Effective weak-coupling for strongly correlated systems far from equilibrium," *Phys. Rev. Lett.* **101** (2008) 041603, `arXiv:0803.0131 [hep-ph]`.

[255] J. Berges and G. Hoffmeister, "Nonthermal fixed points and the functional renormalization group," *Nucl. Phys.* **B813** (2009) 383, `arXiv:0809.5208 [hep-th]`.

[256] C. Scheppach, J. Berges, and T. Gasenzer, "Matter-wave turbulence: Beyond kinetic scaling," *Phys. Rev.* **A81** (2010) 033611, `arXiv:0912.4183 [cond-mat.quant-gas]`.

[257] J. Berges and D. Sexty, "Strong versus weak wave-turbulence in relativistic field theory," *Phys. Rev.* **D83** (2011) 085004, `arXiv:1012.5944 [hep-ph]`.

[258] B. Nowak, D. Sexty, and T. Gasenzer, "Superfluid Turbulence: Nonthermal Fixed Point in an Ultracold Bose Gas," *Phys. Rev.* **B84** (2011) 020506(R), `arXiv:1012.4437 [cond-mat.quant-gas]`.

[259] B. Nowak, J. Schole, D. Sexty, and T. Gasenzer, "Nonthermal fixed points, vortex statistics, and superfluid turbulence in an ultracold Bose gas," *Phys. Rev.* **A85** (2012) 043627, `arXiv:1111.6127 [cond-mat.quant-gas]`.

[260] M. Karl, B. Nowak, and T. Gasenzer, "Tuning universality far from equilibrium," *Scientific Reports* **3** (2013) 2394, `arXiv:1302.1122` `[cond-mat.quant-gas]`.

[261] T. Gasenzer, B. Nowak, and D. Sexty, "Charge separation in Reheating after Cosmological Inflation," *Phys. Lett.* **B710** (2012) 500, `arXiv:1108.0541` `[hep-ph]`.

[262] T. Gasenzer, L. McLerran, J. M. Pawlowski, and D. Sexty, "Gauge turbulence, topological defect dynamics, and condensation in Higgs models," *Nucl. Phys.* **A930** (2014) 163, `arXiv:1307.5301 [hep-ph]`.

[263] T. Gasenzer and J. M. Pawlowski, "Towards far-from-equilibrium quantum field dynamics: A functional renormalisation-group approach," *Phys. Lett.* **B670** (2008) 135, `arXiv:0710.4627 [cond-mat.other]`.

[264] S. Mathey, T. Gasenzer, and J. M. Pawlowski, "Anomalous scaling at non-thermal fixed points of Burgers' and Gross-Pitaevskii turbulence," *Phys. Rev.* **A92** (2015) 023635, `arXiv:1405.7652 [cond-mat.quant-gas]`.

[265] T. Albash and C. V. Johnson, "Vortex and Droplet Engineering in Holographic Superconductors," *Phys. Rev.* **D80** (2009) 126009, `arXiv:0906.1795 [hep-th]`.

[266] P. M. Chesler and L. G. Yaffe, "Numerical solution of gravitational dynamics in asymptotically anti-de Sitter spacetimes," *JHEP* **1407** (2014) 086, `arXiv:1309.1439 [hep-th]`.

[267] V. Cardoso *et al.*, "NR/HEP: roadmap for the future," *Class. Quant. Grav.* **29** (2012) 244001, `arXiv:1201.5118 [hep-th]`.

[268] L. Tisza, "Transport Phenomena in Helium II," *Nature* **141** (1938) 913.

[269] D. R. Tilley and J. Tilley, *Superfluidity and Superconductivity*. Institute of Physics Publishing, 2003.

[270] J. Sonner and B. Withers, "A gravity derivation of the Tisza-Landau Model in AdS/CFT," *Phys. Rev.* **D82** (2010) 026001, `arXiv:1004.2707 [hep-th]`.

[271] D. T. Son and A. O. Starinets, "Minkowski space correlators in AdS/CFT correspondence: Recipe and applications," *JHEP* **0209** (2002) 042, `arXiv:hep-th/0205051 [hep-th]`.

[272] S. A. Hartnoll, C. P. Herzog, and G. T. Horowitz, "Holographic Superconductors," *JHEP* **0812** (2008) 015, `arXiv:0810.1563 [hep-th]`.

[273] J. P. Boyd, *Chebyshev and Fourier Spectral Methods*. Dover Publications, 2nd ed., 2001.

[274] K. Maeda, M. Natsuume, and T. Okamura, "Universality class of holographic superconductors," *Phys. Rev.* **D79** (2009) 126004, `arXiv:0904.1914 [hep-th]`.

[275] N. D. Mermin and H. Wagner, "Absence of ferromagnetism or antiferromagnetism in one-dimensional or two-dimensional isotropic Heisenberg models," *Phys. Rev. Lett.* **17** (1966) 1133.

[276] D. Anninos, S. A. Hartnoll, and N. Iqbal, "Holography and the Coleman-Mermin-Wagner theorem," *Phys. Rev.* **D82** (2010) 066008, `arXiv:1005.1973 [hep-th]`.

[277] S. Franco, A. Garcia-Garcia, and D. Rodriguez-Gomez, "A General class of holographic superconductors," *JHEP* **04** (2010) 092, `arXiv:0906.1214 [hep-th]`.

[278] S. Franco, A. M. Garcia-Garcia, and D. Rodriguez-Gomez, "A Holographic approach to phase transitions," *Phys. Rev.* **D81** (2010) 041901, `arXiv:0911.1354 [hep-th]`.

[279] C. P. Herzog, "An Analytic Holographic Superconductor," *Phys. Rev.* **D81** (2010) 126009, `arXiv:1003.3278 [hep-th]`.

[280] J. Sonner, A. del Campo, and W. H. Zurek, "Universal far-from-equilibrium Dynamics of a Holographic Superconductor," `arXiv:1406.2329 [hep-th]`.

[281] J. Schole, B. Nowak, and T. Gasenzer, "Critical Dynamics of a Two-dimensional Superfluid near a Non-Thermal Fixed Point," *Phys. Rev.* **A86** (2012) 013624, `arXiv:1204.2487 [cond-mat.quant-gas]`.

[282] M. Karl, B. Nowak, and T. Gasenzer, "Universal scaling at non-thermal fixed points of a two-component Bose gas," *Phys. Rev.* **A88** (2013) 063615, `arXiv:1307.7368 [cond-mat.quant-gas]`.

[283] C. Raman, J. R. Abo-Shaeer, J. M. Vogels, K. Xu, and W. Ketterle, "Vortex Nucleation in a Stirred Bose-Einstein Condensate," *Phys. Rev. Lett.* **87** (2001) 210402, `cond-mat/0106235`.

[284] J. R. Abo-Shaeer, C. Raman, J. M. Vogels, and W. Ketterle, "Observation of Vortex Lattices in Bose-Einstein Condensates," *Science* **292** (2001) 476.

[285] T. W. Neely *et al.*, "Characteristics of Two-Dimensional Quantum Turbulence in a Compressible Superfluid," *Phys. Rev. Lett.* **111** (2013) 235301, `arXiv:1204.1102 [cond-mat.quant-gas]`.

[286] R. J. Donnelly, *Quantized Vortices in Liquid He II*. Cambridge Univ. Pr., 1991.

[287] M. Inguscio, S. Stringari, and C. E. Wieman, eds., *Bose-Einstein Condensation in Atomic Gases: Proceedings of the International School of Physics 'Enrico Fermi', Varenna 1998.* IOS Press, 1999.

[288] M. Tsubota, K. Kasamatsu, and M. Kobayashi, "Quantized vortices in superfluid helium and atomic Bose-Einstein condensates," `arXiv:1004.5458 [cond-mat.quant-gas]`.

[289] E. P. Gross, "Structure of a quantized vortex in boson systems," *Nuovo Cim.* **20** (1961) 454.

[290] L. P. Pitaevskii, "Vortex Lines in an Imperfect Bose gas," *Sov. Phys. JETP* **13** (1961) 451. [Zh. Eksp. Teor. Fiz. **40** (1961) 646].

[291] M. Lagally, "Über ein Verfahren zur Transformation ebener Wirbelprobleme," *Math. Z.* **10** (1921) 231.

[292] C. Lin, "On the motion of vortices in 2D—I. Existence of the Kirchhoff-Routh function," *Proc. Nat. Acad. Sci.* **27** (1941) 570.

[293] L. Onsager, "Statistical hydrodynamics," *Nuovo Cim. Suppl.* **6** (1949) 279.

[294] I. S. Aranson and L. Kramer, "The world of the complex Ginzburg-Landau equation," *Rev. Mod. Phys.* **74** (2002) 99, `cond-mat/0106115`.

[295] A. J. Bray, "Theory of phase-ordering kinetics," *Adv. Phys.* **43** (1994) 357, `arXiv:cond-mat/9501089 [cond-mat]`.

[296] K. Damle, S. N. Majumdar, and S. Sachdev, "Phase ordering kinetics of the Bose gas," *Phys. Rev.* **A54** (1996) 5037, `arXiv:cond-mat/9511058 [cond-mat]`.

[297] S. Nazarenko and M. Onorato, "Wave turbulence and vortices in Bose-Einstein condensation," *Physica* **D219** (2006) 1, `arXiv:nlin/0507051 [nlin.CD]`.

[298] A. N. Kolmogorov, "The local structure of turbulence in incompressible viscous fluid for very large Reynolds numbers," *Dokl. Akad. Nauk. SSSR* **30** (1941) 299. [Proc. R. Soc. Lond. **A434** (1991) 9].

[299] A. N. Kolmogorov, "On the degeneration of isotropic turbulence in an incompressible viscous fluid," *Dokl. Akad. Nauk. SSSR* **31** (1941) 538.

[300] A. N. Kolmogorov, "Dissipation of Energy in Locally Isotropic Turbulence," *Dokl. Akad. Nauk. SSSR* **32** (1941) 16.

[301] U. Frisch, *Turbulence: The Legacy of A. N. Kolmogorov.* Cambridge Univ. Pr., 2004.

[302] R. H. Kraichnan, "Inertial Ranges in Two-Dimensional Turbulence," *Phys. Fl.* **10** (1967) 1417.

[303] J. Berges and D. Sexty, "Bose condensation far from equilibrium," *Phys. Rev. Lett.* **108** (2012) 161601, `arXiv:1201.0687 [hep-ph]`.

[304] C. Nore, M. Abid, and M. E. Brachet, "Decaying Kolmogorov turbulence in a model of superflow," *Phys. Fl.* **9** (1997) 2644.

[305] P. C. Hohenberg and B. I. Halperin, "Theory of Dynamic Critical Phenomena," *Rev. Mod. Phys.* **49** (1977) 435.

[306] B. Nowak, J. Schole, and T. Gasenzer, "Universal dynamics on the way to thermalisation," *New J. Phys.* **16** (2014) 093052, `arXiv:1206.3181 [cond-mat.quant-gas]`.

[307] J. Berges, S. Borsanyi, and C. Wetterich, "Prethermalization," *Phys. Rev. Lett.* **93** (2004) 142002, `arXiv:hep-ph/0403234 [hep-ph]`.

[308] A. Lamacraft, "Quantum Quenches in a Spinor Condensate," *Phys. Rev. Lett.* **98** no. 16, (2007) 160404, `arXiv:cond-mat/0611017 [cond-mat.stat-mech]`.

[309] E. G. Dalla Torre, E. Demler, and A. Polkovnikov, "Universal Rephasing Dynamics after a Quantum Quench via Sudden Coupling of Two Initially Independent Condensates," *Phys. Rev. Lett.* **110** (2013) 090404, `arXiv:1211.5145 [cond-mat.quant-gas]`.

[310] E. Nicklas, M. Karl, M. Höfer, A. Johnson, W. Muessel, H. Strobel, J. Tomkovič, T. Gasenzer, and M. Oberthaler, "Observation of scaling in the dynamics of a strongly quenched quantum gas," `arXiv:1509.02173 [cond-mat.quant-gas]`.

[311] J. Berges, K. Boguslavski, S. Schlichting, and R. Venugopalan, "Universal attractor in a highly occupied non-Abelian plasma," *Phys. Rev.* **D89** (2014) 114007, `arXiv:1311.3005 [hep-ph]`.

[312] J. Berges, K. Boguslavski, S. Schlichting, and R. Venugopalan, "Universality far from equilibrium: From superfluid Bose gases to heavy-ion collisions," *Phys. Rev. Lett.* **114** (2015) 061601, `arXiv:1408.1670 [hep-ph]`.

[313] J. Berges, B. Schenke, S. Schlichting, and R. Venugopalan, "Turbulent thermalization process in high-energy heavy-ion collisions," *Nucl. Phys.* **A931** (2014) 348, `arXiv:1409.1638 [hep-ph]`.

[314] C. P. Herzog and A. Vuorinen, "Spinning Dragging Strings," *JHEP* **0710** (2007) 087, `arXiv:0708.0609 [hep-th]`.

[315] D. Mateos and D. Trancanelli, "The anisotropic N=4 super Yang-Mills plasma and its instabilities," *Phys. Rev. Lett.* **107** (2011) 101601, `arXiv:1105.3472 [hep-th]`.

[316] D. Mateos and D. Trancanelli, "Thermodynamics and Instabilities of a Strongly Coupled Anisotropic Plasma," *JHEP* **07** (2011) 054, `arXiv:1106.1637 [hep-th]`.

[317] P. M. Chesler and W. van der Schee, "Early thermalization, hydrodynamics and energy loss in AdS/CFT," `arXiv:1501.04952 [nucl-th]`.

[318] J. F. Epperson, *An introduction to numerical methods and analysis.* John Wiley & Sons, 2013.

[319] M. Frigo and S. G. Johnson, "The design and implementation of FFTW3," in *Proceedings of the IEEE*, p. 216. 2005.

[320] G. Guennebaud, B. Jacob, *et al.*, "Eigen v3," 2010. `http://eigen.tuxfamily.org`.

[321] L. Dagum and R. Menon, "OpenMP: an industry standard API for shared-memory programming," *Computational Science Engineering, IEEE* **5** (Jan, 1998) 46.

[322] C. P. Herzog, "Lectures on Holographic Superfluidity and Superconductivity," *J. Phys.* **A42** (2009) 343001, `arXiv:0904.1975 [hep-th]`.

Danksagung

In den letzten Jahren haben viele Menschen zur Entstehung dieser Arbeit beigetragen, denen ich im Folgenden herzlich danken möchte.

Zuerst und im Besonderen bedanke ich mich bei meinem Doktorvater Prof. Dr. Carlo Ewerz, von dem ich seit Beginn meiner Diplomarbeit sehr viel über Physik und auch viel Außerfachliches gelernt habe. Durch zahllose Diskussionen hat er hat meine Art, Forschung zu betreiben, maßgeblich geprägt. Vielen Dank für die hervorragende Zusammenarbeit, organisatorische Unterstützung und viele wertvolle physikalische Einsichten.

Für die Übernahme des Zweitgutachtens bedanke ich mich herzlich bei Prof. Dr. Jan Martin Pawlowski. Ihm und Prof. Dr. Johanna Stachel sowie Prof. Dr. Björn Malte Schäfer möchte ich außerdem für ihr Interesse an meiner Arbeit und ihre Teilnahme an meiner Prüfung danken.

Bei Dr. Olaf Kaczmarek bedanke ich mich für hilfreiche Diskussionen im Zusammenhang mit der Renormierung der freien Energie und dafür, dass er mir freundlicherweise die Gitter-Daten zu Ref. [226] zur Verfügung gestellt hat.

Vielen Dank an meine aktuellen und früheren Kollegen Dr. Sebastian Bock, Isara Chantesana, Ling Lin, Alexander Liluashvili, Enrico Brehm, Dr. Konrad Schade, Markus Karl, Thorge Müller, Simon Sailer, Dr. Boris Nowak, Sebastian Erne, Dr. Steven Mathey, Fabian Brock, Dr. Mariele Motta, Sebastian Heupts und Anselm Klenner für viele Diskussionen über Physik und für eine immer gute Atmosphäre. Insbesondere Markus Karl gebührt großer Dank für die hervorragende persönliche und wissenschaftliche Zusammenarbeit, viele Diskussionen über Physik und numerische Methoden sowie auch für das Korrekturlesen der Arbeit.

Bei Prof. Dr. Thomas Gasenzer möchte ich mich für die sehr gute Zusammenarbeit an den holographischen Supraflüssigkeiten bedanken.

I would like to thank Prof. Dr. Steven S. Gubser, Dr. Nele Callebaut, and Dr. Chiara Toldo for great collaboration and many discussions during my research stay in Princeton.

Furthermore, I am very grateful for exciting and insightful scientific discussions with Prof. Dr. Martin Ammon and his group in Jena, Dr. Paul Chesler, Prof. Dr. Christopher Herzog, Dr. Óscar J. C. Dias, Dr. Will A. Horowitz, Ben Meiring, Prof. Dr. Jan M. Pawlowski, Dr. Alexander Rothkopf, Dr. Hayder Salman, Prof. Dr. Michael G. Schmidt, Prof. Dr. Johanna Stachel, Prof. Dr. Derek Teaney, Prof. Dr. Stefan Theisen, and Prof. Dr. Hongbao Zhang.

Dr. Eduard Thommes sowie dem Sekretariatsteam des Instituts für Theoretische Physik danke ich für Unterstützung in allen organisatorischen Belangen und für die viele Arbeit hinter den Kulissen, die die hervorragende Atmosphäre am Institut erst

ermöglicht.

Zu guter Letzt danke ich von Herzen meiner ganzen Familie und insbesondere meiner Frau Cristina, die mich zu allen Phasen dieser Arbeit immer unterstützt hat.